Delft University of Technology

From bioreactors to bubbles to bacteria: on multi-scale interactions in gas fermentations

Puiman, L.

DOI
10.4233/uuid:e68fcc5d-f349-4f52-ad66-89f1a5e6187d

Publication date
2024

Document Version
Final published version

Citation (APA)
Puiman, L. (2024). *From bioreactors to bubbles to bacteria: on multi-scale interactions in gas fermentations*. [Dissertation (TU Delft), Delft University of Technology]. https://doi.org/10.4233/uuid:e68fcc5d-f349-4f52-ad66-89f1a5e6187d

Important note
To cite this publication, please use the final published version (if applicable).
Please check the document version above.

Copyright
Other than for strictly personal use, it is not permitted to download, forward or distribute the text or part of it, without the consent of the author(s) and/or copyright holder(s), unless the work is under an open content license such as Creative Commons.

Takedown policy
Please contact us and provide details if you believe this document breaches copyrights.
We will remove access to the work immediately and investigate your claim.

This work is downloaded from Delft University of Technology.
For technical reasons the number of authors shown on this cover page is limited to a maximum of 10.

From bioreactors to bubbles to bacteria

on multi-scale interactions in gas fermentations

Lars Puiman

From bioreactors to bubbles to bacteria

on multi-scale interactions in gas fermentations

From bioreactors to bubbles to bacteria

on multi-scale interactions in gas fermentations

Proefschrift

ter verkrijging van de graad van doctor
aan de Technische Universiteit Delft,
op gezag van de Rector Magnificus prof. dr. ir. T.H.J.J. van der Hagen,
voorzitter van het College voor Promoties,
in het openbaar te verdedigen op vrijdag 31 mei 2024 om 12:30 uur

door

Lars PUIMAN

Master of Science in Life Science and Technology,
Technische Universiteit Delft, Nederland,
geboren te Stadskanaal, Nederland.

Dit proefschrift is goedgekeurd door de promotoren.

Samenstelling promotiecommissie:

Rector Magnificus	voorzitter
Prof.dr.ir. H.J. Noorman	Technische Universiteit Delft, *promotor*
Prof.dr.ir. C. Picioreanu	King Abdullah University of Science and Technology, Saudi Arabië, *promotor*
Dr.ir. C. Haringa	Technische Universiteit Delft, *copromotor*
Onafhankelijke leden:	
Prof.dr.-ing. R. Takors	University of Stuttgart, Duitsland
Prof.dr.ir. J.A.M. Kuipers	Technische Universiteit Eindhoven
Prof.dr.ir. C.A. Ramírez Ramírez	Technische Universiteit Delft
Prof.dr.ir. A.A. Kiss	Technische Universiteit Delft
Prof.dr. F. Hollmann	Technische Universiteit Delft, reservelid

This work is part of the MicroSynC research programme (project number P16-10/5) and is (partly) financed by the Netherlands Organization for Scientific Research (NWO). This work used the Dutch national e-infrastructure with the support of the SURF Cooperative using grant no. EINF-4918.

Printed by: Ridderprint | `www.ridderprint.nl`
Cover: Futuristic bioreactors with highlighted multi-scale interactions.
AI-generated using `www.bing.com/images/create`.
ISBN: 978-94-6366-858-3

Copyright © 2024 by L. Puiman
An electronic version of this dissertation is available at
`http://repository.tudelft.nl/`.
A selection of models is available at
`https://github.com/larspuiman`.
All research data and models are publicly available at
`https://doi.org/10.4121/aba6e9f8-d65e-486f-b1ae-a3fd1635b6c8`.

So you found your solution
What will be your last contribution?
"Live it up, rip it up, why so lazy?
Give it out, dish it out, let's go crazy!"

Roger Hodgson in *Fool's Overture*

Contents

Samenvatting xi

Summary xiii

Nomenclature xv

1 Introduction **3**

1.1 The potential of gas fermentation 4

1.2 Commercialisation of gas fermentation 5

1.3 Concerns on gas fermentation scale-up 7

1.4 The craftsmanship of fermentation modelling 9

1.5 Thesis scope and outline 13

2 Mass transfer in industrial-scale gas fermentation **17**

2.1 Introduction 19

2.2 Methods 23

2.3 Results and discussion 27

2.3.1 Pilot-scale flow pattern 27

2.3.2 Large-scale flow pattern 29

2.3.3 Mass transfer. 33

2.3.4 Outlook 37

2.4 Conclusion 39

3 The impact of broth components on mass transfer **41**

3.1 Introduction 43

3.2 Materials and methods 45

3.3 Results and discussion 48

3.3.1 Influence of ethanol on $k_L a$ 48

3.3.2 $k_L a$ determination in different mixtures with ethanol 49

3.3.3 k_L as function of biomass concentration 52

3.3.4 Comparison with empirical correlations 52

3.3.5 Implications and future studies 54

3.4 Conclusion 55

4 Downscaling gas fermentation by taking the microbial perspective 57
4.1 Introduction 59
4.2 Methods 61
4.3 Results and discussion 66
 4.3.1 Eulerian concentration gradients 66
 4.3.2 Lifeline analysis 69
 4.3.3 Development of scale-down simulator 73
 4.3.4 Outlook 77
4.4 Conclusion 79

5 Influence of dissolved gas concentration and its gradient 81
5.1 Introduction 83
5.2 Methods 86
5.3 Results and discussion 90
 5.3.1 Mass balances in the biomass phase 90
 5.3.2 Spatial distribution of energy conservation 91
 5.3.3 Analysis of characteristic times 93
 5.3.4 Influence of dissolved CO on product spectrum 94
 5.3.5 Metabolism during dynamic conditions 98
 5.3.6 Emerging hypotheses 101
 5.3.7 Towards better gas fermentation bioreactors 104
5.4 Conclusion 105

6 Conclusions 107

7 Moving forwards 113
7.1 The landscape of gas fermentation 114
7.2 Bioreactor operation for gas fermentation 116
7.3 Concentration gradients and scale-down 119
7.4 Gas-to-liquid mass transfer 120
7.5 Gas fermenting bacteria 122
7.6 The end in mind 124

References 127

A Supplement Chapter 2 141

B Supplement Chapter 3 149

C Supplement Chapter 4 157

D Supplement Chapter 5 169
D.1 Detailed CRD model description 169
 D.1.1 Metabolic kinetic model 169

D.1.2 Increasing the model stability 172
D.1.3 Model verification as a batch process 173
D.1.4 Lifeline reconstruction 174
D.1.5 Choice of Δt_f and N_p 175
D.1.6 Mass balance during a lifeline 178
D.2 Relationship between dissolved CO and H_2 179
D.3 CO and H_2 uptake kinetics and inhibition by ferredoxin 180
D.4 Formate production 181
D.5 Ethanol production during lifelines 182
D.6 Metabolism 184

Acknowledgements / Dankwoord 187

List of Publications 193

Curriculum Vitae 197

Samenvatting

Momenteel staat we voor grote uitdagingen, waaronder het aanpakken van klimaatverandering. Industriële processen die moeilijk te verduurzamen zijn, zoals staalproductie, (olie)raffinage en afvalverwerking, veroorzaken een aanzienlijke uitstoot van broeikasgassen. De reststromen van deze processen kunnen echter worden verwerkt met behulp van gasfermentatie, een recent ontwikkelde technologie. De kern van het gasfermentatie proces is de omzetting van synthesegas, bestaande uit koolmonoxide CO, kooldioxide CO_2, en waterstof H_2, tot ethanol en azijnzuur door bacteriën zoals *Clostridium autoethanogenum*. Deze stoffen kunnen vervolgens dienen als grondstof voor nuttige producten zoals brandstoffen, plastics en cosmetica.

Hoewel gasfermentatie al wordt toegepast op industriële schaal, bestaan er onzekerheden over de opschaling van dit proces, met name omtrent de interacties van verschillende schalen binnen de bioreactor, bellen en bacteriën. Onder meer vertragen de lage oplosbaarheid van CO en H_2, samen met het samenvloeien van bellen, de massaoverdracht van de gas- naar de vloeistoffase, gebruikelijkerwijs aangegeven middels een lage k_La-waarde. Daarnaast verloopt de menging in grootschalige bioreactoren ($500\,\mathrm{m}^3$), veel trager dan in kleinschalige lab-schaal bioreactoren (0,5 tot 2 L). Gecombineerd met een aanzienlijke gasomzetting leidt dit tot grote variaties in concentraties van opgelost gas. De concentratievariaties die bacteriën in de bioreactor ervaren, worden vaak gerelateerd aan onverwachte productiviteitsverliezen. Dit proefschrift onderzoekt

- *i*) de relevante factoren voor het verkrijgen van voldoende massaoverdracht op industriële schaal,
- *ii*) de omvang en duur van de concentratiefluctuaties en hun nabootsing op laboratoriumschaal, evenals
- *iii*) de mogelijke impact hiervan op *C. autoethanogenum*.

Deze kwesties worden uitgebreid geïntroduceerd in hoofdstuk 1.

In hoofdstuk 2 wordt de massaoverdracht in industriële gasfermentatiereactoren (gaslift bioreactoren met externe lus) nader bekeken. Empirische correlaties die vaak voor opschaling worden gebruikt, voorspelden te lage massaoverdrachtswaarden voor CO (0,3 tot $2\,\mathrm{g\,L^{-1}\,h^{-1}}$), terwijl op industriële schaal 7 tot $8{,}5\,\mathrm{g\,L^{-1}\,h^{-1}}$ verwacht wordt. Met een numeriek model, dat de gas- en vloeistofstromen binnen een industriële bioreactor voorspelt, kon de invloed van relevante variabelen voor massaoverdracht, zoals de druk, de temperatuur, en de beldiameter, worden nagegaan. Hieruit bleek dat vooral kleine bellen (< 2 mm) nodig zijn om de benodigde waarden te behalen, wat deels te danken is aan het geproduceerde ethanol, die het samenvloeien van bellen vermindert.

Vervolgens wordt in hoofdstuk 3 experimenteel uitgezocht in welke mate ethanol en componenten van fermentatiebeslagen (zoutig kweekmedium en biomassa) het samenvloeien van bellen verhinderen en de $k_L a$-waarden verhogen. Uit deze experimenten bleek dat ethanol aanzienlijk bijdraagt aan het verkleinen van gasbellen (van 3 naar 1 mm), en de $k_L a$-waarden 2 tot 6 keer kan verhogen. Ook het zout in het medium zorgt voor kleinere bellen. Het geproduceerde ethanol speelt een substantiële rol in het aanzienlijk verhogen van de massaoverdracht op industriële schaal. Bovendien werd vastgesteld dat dat de empirische correlaties, doorgaans ontwikkeld met metingen van lucht in gezuiverd water, onvoldoende rekening houden met de complexiteit van fermentatiebeslagen.

Met het ontwikkelde stromingsmodel wordt in hoofdstuk 4 de grootte en frequentie van de concentratiefluctuaties in grootschalige gasfermentatiereactoren in kaart gebracht. Dit gebeurt door massaoverdracht en gasconsumptie door bacteriën mee te nemen in het bioreactormodel, voor verschillende biomassaconcentraties. Hieruit bleek dat bacteriën, ongeacht de hoeveelheid biomassa in de reactor, concentratiefluctuaties ervaren van ongeveer één orde van grootte. De tijd die bacteriën doorbrengen in gebieden met hoge en lage concentraties is onregelmatig en varieert tussen de 5 en 30 seconden. Om de invloed van deze concentratiefluctuaties op *C. autoethanogenum* te onderzoeken, werd voorgesteld om een neerschalingsstudie uit te voeren waarbij deze fluctuaties worden nagebootst in het laboratorium. Dit kan worden bereikt door onregelmatige variaties aan te brengen in de roersnelheid van een continu werkende bioreactor, met de eerder genoemde tijdsduur.

In hoofdstuk 5 is een eerste voorspelling gemaakt van het effect van de concentratiefluctuaties. Hiervoor werd een numeriek model van het metabolisme van *C. autoethanogenum*, wat de belangrijkste reacties binnenin de cel beschrijft, gekoppeld aan het stromings- en massaoverdrachtsmodel van de industriële bioreactor. Deze bevindingen zijn vergeleken met experimentele resultaten en beide lieten zien dat de opgeloste CO-concentratie een cruciale rol speelt bij de productie van azijnzuur of ethanol: een hoge CO-concentratie leidt tot azijnzuurproductie, terwijl een lage concentratie de ethanolproductie stimuleert. Bovendien werd er verwacht dat de concentratiefluctuaties ook zouden resulteren in een versterkte ethanolproductie.

Ter afsluiting worden de onderzoeksvragen uitvoerig beantwoord in hoofdstuk 6, en worden aanknopingspunten voor vervolgonderzoek uitgewerkt in hoofdstuk 7. Over het geheel genomen concluderen we dat het beschouwen van de interacties tussen de verschillende schalen (bioreactor, bellen en bacteriën) van essentieel belang is voor succesvolle opschaling van gasfermentatiebioreactoren. Meer onderzoek, waaronder bestudering van de gasopnamesnelheid van *C. autoethanogenum*, is vereist om dit proces nauwkeuriger te kunnen voorspellen.

Dit proefschrift biedt niet alleen nieuwe fundamentele inzichten in gasfermentatie, maar draagt ook bij aan verdere implementatie ervan in de industrie, waarmee het bijdraagt aan de strijd tegen klimaatverandering.

Summary

One of the major challenges mankind faces nowadays is combating climate change. A substantial fraction of greenhouse gases are released by industrial processes, as steelmaking, (oil)refinery and waste processing. Emissions from these processes can partly be prevented with a recently developed technology called gas fermentation. Within this process, synthesis gas – a mixture containing CO, CO_2 and H_2 – is converted into ethanol and acetic acid by bacteria such as *Clostridium autoethanogenum*. These products could be used in a wide range of applications, like fuels, plastics and cosmetics.

Whilst gas fermentation is already applied at commercial-scale, challenges in scale-up persists due to complex multi-scale interactions among the bioreactor, gas bubbles, and bacteria. The poor solubility of CO and H_2 alongside gas bubble coalescence, leads to low gas-to-liquid mass transfer rates (typically denoted via $k_L a$). Slow mixing in industrial bioreactors ($500\,\mathrm{m}^3$), and high gas conversion rates, result in large spatial variations in dissolved gas concentrations. Bacteria experiencing concentration fluctuations have often been related to decreased process performance. This dissertation explores

i) the relevant factors to obtain high mass transfer rates at industrial-scale,
ii) the magnitude and duration of the concentration fluctuations, and how these can be resembled at laboratory-scale, and
iii) the possible impact of these concentration fluctuations on *C. autoethanogenum*.

Chapter 1 serves as a comprehensive introduction into these themes.

Mass transfer in industrial-scale gas fermentation reactors (primarily external-loop gas-lift bioreactors) is extensively studied in Chapter 2. The engineering correlations that are often used for bioreactor scale-up, predicted insufficient CO mass transfer capacities ($0.3 – 2\,\mathrm{g\,L^{-1}\,h^{-1}}$), while at scale $7 – 8.5\,\mathrm{g\,L^{-1}\,h^{-1}}$ is expected. With a computational fluid dynamics (CFD) model of an industrial-scale gas-lift bioreactor, the influence of the most relevant variables regarding mass transfer, i.e., pressure, temperature, and bubble diameter, have been studied. The model revealed that predominantly small bubbles (< 2 mm) are required to obtain the industrial-scale performance. The produced ethanol was expected to inhibit coalescence, facilitating the creation of such small bubbles.

Chapter 3 focuses on experimental investigations regarding the impact of ethanol and broth components (mineral medium and biomass) on bubble coalescence and $k_L a$ enhancement. The findings indicated that ethanol substantially reduces the gas bubble diameter (from 3 to 1 mm) and thereby amplifies $k_L a$ between 2 to 6 times. The salts in the medium demonstrated a similar effect in reducing bubble size. The study emphasises the key role of ethanol in achieving industrial-scale mass transfer rates, and highlighted that the engineering correlations, which were mostly developed in air-water mixtures, are not suitable to describe the complex interactions within fermentation broths.

The CFD model is expanded in Chapter 4 to explore the magnitude and duration of the concentration fluctuations that the bacteria experience in the large-scale bioreactor. This was done by modelling mass transfer and gas consumption for a wide range of biomass concentrations. Irrespective of the biomass concentration, bacteria experienced concentration fluctuations of approximately one order of magnitude. The duration in concentration peaks and valleys varied irregularly, spanning between 5 and 30 seconds. To assess the impact of such concentration variations on *C. autoethanogenum*, a downscaling study was proposed to simulate these fluctuations at laboratory-scale gas fermentation conditions. It was proposed to irregularly modulate the stirring speed of a continuously operated bioreactor for periods of the aforementioned duration.

An initial evaluation of the impact of the concentration fluctuations is made in Chapter 5. This was done by coupling a metabolic kinetic model of *C. autoethanogenum* to the CFD and mass transfer model of the industrial-scale bioreactor. Comparison of simulation results with experimental data, uncovered that the dissolved CO concentration influences the product spectrum: elevated dissolved CO concentrations favours acetic acid production, while ethanol production is stimulated at lower concentrations. The simulations suggested that the concentration fluctuations led to escalated ethanol production rates at the expense of acetic acid production.

In Chapter 6, the research questions will extensively be answered, while future research suggestions will be elaborated in Chapter 7. Ultimately, this dissertation concludes that accounting for multi-scale interactions – amongst bioreactor, bubbles and bacteria – is crucial for successful scale-up of gas fermentation bioreactors. Further research, including investigation of gas uptake kinetics of *C. autoethanogenum*, is required to refine the accuracy of gas fermentation modelling.

This dissertation provides novel fundamental insights into gas fermentation field, it also contributes to furthering its implementation in the industry, thereby contributing to the fight against climate change.

Nomenclature

Mathematical symbols

Symbol	Description	Unit
Latin		
a	Specific surface area	$\mathrm{m^{-1}}$
A	Area	$\mathrm{m^{2}}$
c	Concentration	$\mathrm{mol\,m^{-3}}$ or $\mathrm{g\,L^{-1}}$
d_b	Bubble diameter	m
d_{32}	Sauter mean bubble diameter	m
D	Diameter	m
D_L	Liquid-phase diffusion coefficient	$\mathrm{m^{2}\,s^{-1}}$
D_{ax}	Axial dispersion coefficient	$\mathrm{m^{2}\,s^{-1}}$
D_r	Dilution rate	$\mathrm{h^{-1}}$
D_{KL}	Kullback-Leibler divergence	nat
e	Eccentricity	-
E	Enhancement factor	-
f	Correction factor	-
F	Flow rate	$\mathrm{m^{3}\,s^{-1}}$
g	Gravitational acceleration	$\mathrm{m\,s^{-2}}$
ΔG	Gibbs free energy	$\mathrm{kJ\,mol^{-1}}$
h	Height	m
H	Henry coefficient	$\mathrm{kg\,m^{-3}\,Pa^{-1}}$
I	Turbulence intensity	%
I	Ionic strength	$\mathrm{mol\,L^{-1}}$
J	Metabolic rate	$\mathrm{mol\,mol_x^{-1}\,h^{-1}}$
k	Turbulent kinetic energy	$\mathrm{m^{2}\,s^{-2}}$
k_L	Liquid-side mass transfer coefficient	$\mathrm{m\,s^{-1}}$
k_La	Volumetric mass transfer coefficient	$\mathrm{s^{-1}}$
K_I	Inhibition constant	$\mathrm{mol\,m^{-3}}$
K_S	Half-saturation constant	$\mathrm{mol\,m^{-3}}$
L	Length	m
$\dot{m}$	Mass flow rate	$\mathrm{kg\,s^{-1}}$
MTC	Mass transfer capacity	$\mathrm{kg\,m_L^{-3}\,h^{-1}}$
MTR	Mass transfer rate	$\mathrm{kg\,m_L^{-3}\,h^{-1}}$
n	Stirring speed	rot/s

$\dot{n}$	Molar flow rate	$\mathrm{mol\,s^{-1}}$
N_y	Number of y	-
N_p	Number of particles	-
N_Po	Power number	-
N_{t_c}	Number of circulation times	-
p	Probability	-
p	Pressure	Pa
$P(y)$	Distribution of y	-
P	Power	W
q	Biomass-specific uptake rate	$\mathrm{mol\,mol_X^{-1}\,h^{-1}}$
r	Reaction rate	$\mathrm{kg\,m_L^{-3}\,h^{-1}}$
$\tilde{r}_i$	Particle-specific rate	$\mathrm{mol\,h^{-1}}$
r_a	Radius of semi-major axis	m
r_c	Radius of semi-minor axis	m
r	Radial position	m
R	Radius	m
R	Universal gas constant	$\mathrm{J\,mol^{-1}\,K^{-1}}$
R_rec	Recirculation ratio	-
t	Time	s
t_c	Circulation time	s
t_m	95% mixing time	s
Δt	Time step	s
T	Temperature	K
u	Velocity	$\mathrm{m\,s^{-1}}$
$\vec{u}$	Velocity magnitude	$\mathrm{m\,s^{-1}}$
u_s	Superficial velocity	$\mathrm{m\,s^{-1}}$
v_b^∞	Bubble rise velocity	$\mathrm{m\,s^{-1}}$
v_slip	Slip velocity	$\mathrm{m\,s^{-1}}$
V	Volume	$\mathrm{m^3}$
X	Conversion	%
y	Mole fraction	$\mathrm{mol\,mol_G^{-1}}$
$Y_\mathrm{i/j}$	Molar yield	$\mathrm{mol_i\,mol_j^{-1}}$
z	Axial position	m
z	Ionic charge	-

Greek

ϵ	Energy dissipation rate	$\mathrm{m^2\,s^{-3}}$
ε_G	Gas hold-up	$\mathrm{m_G^{-3}\,m_L^{-3}}$
ε_L	Liquid hold-up	$\mathrm{m_L^{-3}\,m_L^{-3}}$
ε_{ij}	Elasticity coefficient	-
η	Dynamic viscosity	$\mathrm{kg\,m^{-1}\,s^{-1}}$
θ	Normalised time	s

μ	Growth rate	h^{-1}
ν	Kinematic viscosity	$m^2\,s^{-1}$
ρ	Density	$kg\,m^{-3}$
σ	Surface tension	$N\,m^{-1}$
$\sigma(y)$	Standard deviation of$y$	-
τ	Characteristic time	s

Sub- and superscripts

0	Initial
∞	Final
ax	Axial
b	bubble
c	Circulation
con	Connector
d	Downcomer
D	Dispersion
e	Exposure
EC	Extracellular
f	Flow
G	Gas
H	Headspace
i	Species
IC	Intracellular
in	Inlet
j	Reaction
L	Liquid
ll	lin-log
m	Molar
MT	Mass transfer
out	Outlet
p	Particle
prod	product
prot	protein
ref	Reference
rxn	Reaction
r	Riser
sat	Saturation
s	Superficial
SD	Scale-down
t	Tracer
VE	Volume element
x	Biomass

Abbreviations

General	
ALR	Airlift reactor
BCR	Bubble column reactor
CFD	Computational fluid dynamics
CRD	Cellular reaction dynamics
EL	External-loop
FBA	Flux Balance Analysis
GEM	Genome-scale metabolic model
GLR	Gaslift reactor
OD	Optical density
STR	Stirred tank reactor
VE	Volume element
VSS	Volatile suspended solids

(Bio)chemical species	
AcT	Total acetate
Ac^-	Acetate
AcCoA	Acetyl-coA
ATP	Adenosine triphosphate
BDO	2,3-butanediol
CO	Carbon monoxide
CO_2	Carbon dioxide
EtOH	Ethanol
Fd	Ferredoxin
For^-	Formate
H_2	Hydrogen
HAc	Acetic acid
N_2	Nitrogen
NADH	Nicotinamide adenine dinucleotide
NADPH	Nicotinamide adenine dinucleotide phosphate
O_2	Oxygen

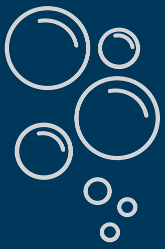

Chapter 1

Introduction

The implementation of biotechnology, in terms of process scale-up and operation, would not have been possible without application of mathematical concepts and methods which lie at the heart of modern engineering and education.

James Edward Bailey [1]

This chapter has been written to provide the reader background information for each chapter. Each chapter contains its own introduction.

Biotechnology is fundamental to our society. Humanity has mastered the act of using microorganisms for multiple purposes: from cleaning our wastewater to brewing beer, from cultivating food to generating fuels and plastics, even to save lives by producing pharmaceuticals and preventing pandemics using vaccines. The miraculous microbial world enables us to solve many of the urgent challenges society faces: from preventing food shortages to mitigating climate change, to changing our meat industry. One of the solutions the microbial world offers us is called *gas fermentation*.

1.1. The potential of gas fermentation

In the late 1980's, early 1990's, microorganisms were discovered that were able to use synthesis gas (syngas), a gas mixture containing carbon monoxide (CO), hydrogen (H_2) and carbon dioxide (CO_2), as carbon and electron sources to produce useful products as ethanol and acetate [2, 3]. The workhorses of this process, acetogenic bacteria like *Clostridium ljungdahlii* and *C. autoethanogenum*, were isolated shortly afterwards from chicken yard waste and rabbit feces [4, 5]. Since the late 2000's, research into this technology has skyrocketed, with tens of research articles and many[1] review papers being published every year [6].

The potential of the gas fermentation process is founded in its versatility: syngas can be produced from a wide range of feedstocks, while also a wide range of products can be produced (Figure 1.1). The products range from acetate and ethanol, to longer chain carboxylic acids and alcohols [7], proteins and precursors for polymers [8], while the production of acetone and isopropanol have been demonstrated at pilot-scale [9]. Current commercial applications convert industrial off-gases towards ethanol, which can be upgraded to a wide range of products like car fuel, plastics (as polyethylene), detergents, clothing, and cosmetics [8–11].

Syngas has been used in the chemical industry for many years. With fossil carbon as input, it has mainly been used in Fisher-Tropsch Synthesis for hydrocarbon production and in catalytic conversion to methanol [12, 13]. In some industries, such as the steelmaking and the ferroalloy industry, syngas is typically considered as a waste stream and only used for energy generation. By fermentation these fossil-based waste streams can be valorised [14]. Potential circular processes can be obtained by gasification of waste streams such as lignocellulosic biomass residues and municipal solid waste [15]. Lastly, efforts are being made to use atmospheric CO_2 and green hydrogen as feedstocks for the syngas fermentation process, using CO_2 and/or water electrolysis [11].

Compared to the catalytic (e.g., Fisher-Tropsch and syngas-to-methanol) processes for syngas conversion, the biological process offers several advantages [11, 13–15]: *i)* operation at ambient temperatures and pressure (saving energy costs), *ii)* microbes are

---

[1] Too many, according to the authors opinion: around 22% (93 out of 425 hits) of the Web of Science article collection on "syngas fermentation" published between 2019 and 2023 has been marked as a review paper, while other areas average around 10% (dated October 23rd 2023).

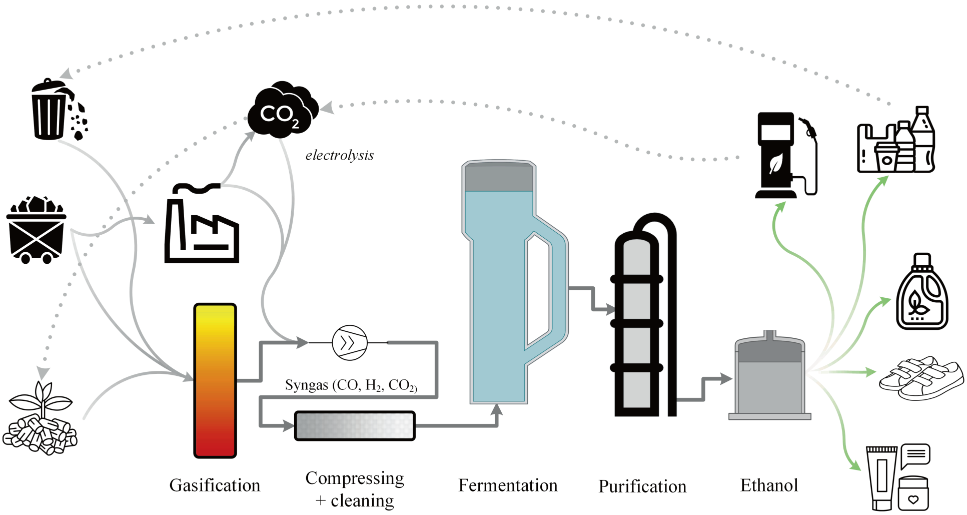

Figure 1.1: Schematic representation of the syngas fermentation process, feedstocks and end-products.

cheap catalysts and offer high resistance to contaminants (sulfur, tars), *iii)* no fixed ratio between CO and H_2 is required, and *iv)* higher specificity and carbon-to-product yields can be obtained. However, biological processes take place in water, leading to low volumetric productivity (or space-time-yield) although productivity per gram biomass and catalyst are similar [13], and the low product concentration challenges product separation [16]. These advantages offer syngas fermentation the potential to become more attractive and environmental-friendly than the competing chemical processes for the production of fuels from syngas.

Figure 1.1 schematically illustrates the syngas fermentation process. After production of the syngas, the gas is being compressed and cleaned to remove impurities such as tars, nitrogen oxides and sulphates [17, 18]. The separation and purification of ethanol after fermentation is commonly done via distillation and pressure swing absorption, although more efficient and sustainable downstream processes have been proposed [16].

1.2. Commercialisation of gas fermentation

As was recently demonstrated with their initial public offering, the company LanzaTech successfully scaled-up the syngas fermentation process. They were founded in 2005 in New Zealand, and opened their first full-scale plant in 2018 in Shougang, China, where they produce ~50 kton ethanol per year using off-gases from a neighbouring steel-mill (Figure 1.2a). Currently, LanzaTech is expanding its operations and building facilities across the world, amongst others in India, South-Africa, and in Ghent, Belgium, in the Steelanol project with ArcelorMittal (Figure 1.2b) [10].

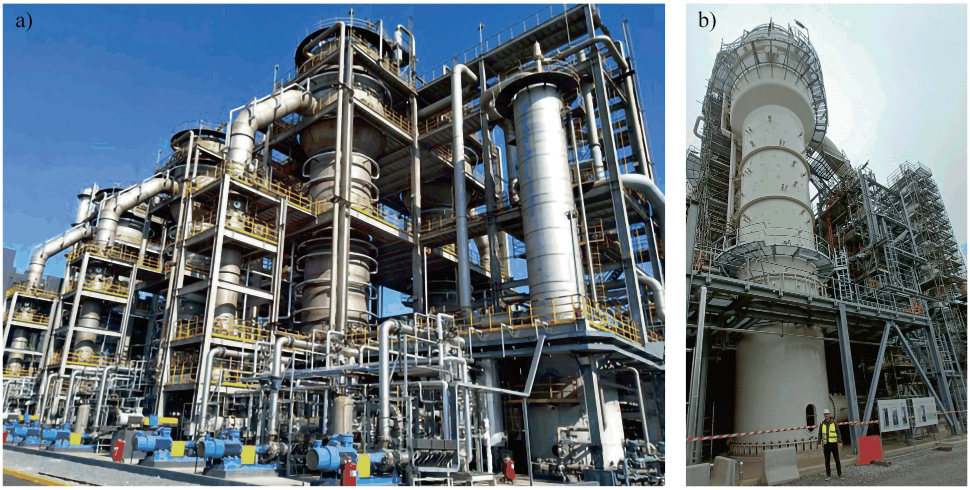

Figure 1.2: Photographs of industrial-scale syngas fermentation plants, depicting LanzaTech's external-loop gas-lift reactors. a) Shougang-LanzaTech plant near Beijing, China[2], b) Steelanol plant near Ghent, Belgium, the author is visible for scale.

At scale, the syngas fermentation process is performed in an external-loop gas-lift reactor (EL-GLR) (see Figure 1.1 for a schematic and Figure 1.2 for photographs of their industrial-scale EL-GLRs). Based on these photographs, the reactor is approximately 30 metre tall and 5 to 7 m wide, and encompasses a volume of more than 500 m^3 [10]. This reactor is similar to the well-known bubble column, but it contains an external-loop to force (a part of) the liquid back to the bottom, where pressurised gas is injected. Due to its density difference with the fermentation broth (the liquid mixture containing water, biomass and the liquid products), the gas and, consequentially, the broth rise upwards, which is recirculated via an external-loop aside of the reactor [19, 20]. The external-loop can be used, amongst others, for cooling, liquid feeding and withdrawal, while a (multiphase) pump can be installed to regulate the mixing time (and mass transfer). LanzaTech claims an ethanol specificity of 95% [8], near-complete gas conversion (~90%) [10], and an ethanol concentration of 50 $\mathrm{g\,L^{-1}}$ [8] (similar to beer).

Compared to other bioreactor types that are used in commercial-scale processes (mainly stirred tank reactors), the EL-GLR offers low capital and operational costs (no stirring required) and decent mixing characteristics [14, 15, 21]. Other reactors that are frequently studied (at lab-scale) for gas fermentations include hollow fibre membrane reactors (with limitations like clogging) [21–23] and trickle bed bioreactors (with low working volumes and flow rates) [21, 23], which both require biofilm formation.

---

[2] source: `https://www.mitsui.com/jp/en/topics/2019/1230078_11243.html`.

1.3. Concerns on gas fermentation scale-up

In the scientific literature, there are many concerns on the scalability of the gas fermentation process and the EL-GLR. These relate to gas-to-liquid mass transfer, biomass and product concentrations, and the existence of dissolved gas concentration gradients. As will be shown here, all these issues relate to the interactions between the operational parameters of the bioreactor, the physical phenomena in the EL-GLR (such as mass transfer and mixing) and the microorganisms and their metabolism. In this work, these concerns will be studied, while aiming to find solutions to overcome or alleviate these.

Mass transfer

Transport of the syngas components from the gas phase to the liquid phase, gas-to-liquid mass transfer, is often regarded as the major limitation in syngas fermentation due to the low solubility of CO and H_2 [2, 13–15, 17, 22]. The mass transfer rate depends on a mass transfer coefficient k_L, the gas fraction ε_G the bubble diameter d_b (both combined into the volume-specific surface area a of the gas phase), and the solubility of the compound. This large number of parameters means that the mass transfer rate is influenced by many different factors, such as the broth composition, the pressure p, the temperature T, and the local turbulent energy dissipation rate ϵ [24–26].

The standard engineering correlations for bubble column and gas-lift bioreactors, could not predict the high mass transfer performance of industrial-scale EL-GLRs. For example, as a rule of thumb in columns with coarse bubbles, an oxygen depletion rate of 0.55% per metre liquid height can be assumed [26]. Translating this to a 30 m tall syngas fermentor, this would maximally lead to 16.5% CO conversion, significantly lower than the 90% advocated by LanzaTech. To achieve this 90%, a depletion rate of at least 3% per metre is needed, which could for example be in columns with very small bubbles [26]. As gas sources can be costly, high gas conversion rates and thus high mass transfer rates are paramount design parameters for competitive gas-based bioprocesses at scale (e.g., using syngas, oxygen, methane, H_2, and CO_2 [27–30]).

Productivity

Another major hurdle in syngas fermentation experiments is the low volumetric productivity (or: space-time yield), which can be attributed to the low microbial growth rate μ [13, 17, 22]. Typically, a low μ leads to low biomass concentrations c_x and thus low product concentrations c_{prod}. Biomass retention has been identified as a tool to increase the volume-specific ethanol productivity and gas conversion rates [22, 31].

High biomass concentrations might cause significant mass transfer limitations, and therefore thermodynamically unfavourably low concentrations of dissolved gases [32]. In contrast, a too low c_x could increase the dissolved gas concentrations so much that CO becomes inhibiting [33, 34]. This results into a narrow operational window, governed by the mass transfer rate and the biomass concentration. Furthermore, high ethanol concentrations could inhibit growth and product formation [35, 36], but might also lead to increased mass transfer rates by decreasing d_b [37].

Within the scientific community, there is some variability in understanding of the gas fermentation product spectrum. So far, usually acetate is regarded as the main acetogenic gas fermentation product [38–40], and it is unclear at which conditions high ethanol specificity prevail, although several influential factors have been identified. For example, low pH [38], high (extracellular) acetate concentrations [31, 39, 41], addition of nitrate [42], and specific medium optimisation [43] could enhance the ethanol production rates. Increased ethanol production rates were obtained in chemostats by increasing the biomass concentration [44], by increasing the dilution rate [45], or by H_2 supplementation [45, 46]. 2,3-butanediol and lactate can be considered as by-products due to their low product concentrations (1:10 ethanol) [47]. It should be noted, however, that the conducted chemostat lab-studies with CO as main electron source never reached the 90% specificity as is obtained in industry with CO-rich syngas.

Concentration gradients

In industrial-scale continuous or fed-batch bioreactors, spatial gradients in substrate (e.g., glucose, O_2 or CO) concentration are frequently observed. They typically arise due to poor mixing in the liquid phase and too slow mass transfer from the gas phase [48, 49]: When mass transfer or mixing are slower than consumption of the gas, then such gradients are likely to occur [50]. As mixing in lab-scale (~2 L) is usually much faster, these gradients are usually identified at industrial-scale (~500 000 L). As most industrial microorganisms were characterised at lab-scale, and the scaled-up performance was typically estimated from the lab-scale performance, these concentration gradients got associated with significant performance losses [51–53]. Studying how these concentration gradients influence the microbial metabolism (i.e., all the reactions that occur within the cell [54]) is therefore paramount for successful scale-up.

In large-scale reactors for syngas fermentations, the existence of a spatial dissolved gas concentration gradient is expected due to the varying hydrostatic pressure, bubble size, gas fraction and gas composition [32, 55, 56]. From *lifeline* analysis (i.e., the concentration variations from the perspective of the microorganism [57, 58]) decreased product yields and growth rates were expected based on analogy with *E. coli* [56] in a modelling study. Currently, there is no (experimental or modelling) information on how the metabolism of acetogens is affected by the the environmental fluctuations, and thus how these would influence gas uptake and the product spectrum.

Scaling-up by scaling-down

The existence of concentration gradients has often been related to (unexpected) performance losses after scale-up [52], with as consequence that successful bioreactor scale-up has often been regarded as "both art and science" [59–61].

One successful scale-up strategy is the “begin with the end in mind”-concept [62, 63]. This implies that lab-scale experiments should consider the industrial environment from the perspective of the cell. By mimicking the industrial conditions in a so-called scale-down simulator, the microbial response to these conditions (i.e., temperature, product concentration, pH, but most importantly, the relevant concentration gradients) can be assessed [64, 65]. This should, first of all, lead to less surprises while scaling-up but it can also enable the selection of more resilient microbial strains and the development of metabolic models [66, 67]. In the scientific literature, no scale-down experiments have been done for syngas fermentation. Such experiments could determine whether decreased yields (as mentioned above) would occur and how the cellular metabolism would respond in terms of product spectrum.

Bioreactor modelling has been proven as a viable tool to design scale-down experiments from the cellular perspective [64, 66, 68]. Despite several drawbacks of modelling, it is the best alternative as long as large-scale data is unavailable [69].

1.4. The craftsmanship of fermentation modelling

All models are wrong, but some are useful - George Box [70]

Every model is a representation of reality, and it is therefore possible to decide on the level of reality representation. Typically, implementing more physical and (bio)chemical phenomena increase the model accuracy, at the cost of the model complexity and simulation time, whereas the model could also be simpler and faster by neglecting more phenomena, and thus limiting the model resolution and accuracy. In fermentation modelling, one has to decide on simulation purpose (what is its use?), the level of accuracy (which phenomena should be included?) and resource requirement (how many CPU hours can we spend, or how long can we wait?). As such personal choices have to be made during fermentation model development, fermentation modelling should be regarded as a *craft*.

Fermentation models typically contain sets of balances (of mass, chemical species, energy and/or momentum) for various phases (gas, liquid, biomass), with transport and source terms for inter-phase transport and reaction. To solve these balances, assumptions have to be made on the physical description of the bioreactor and of the microorganism. Models for gas fermentation bioreactors (e.g., the EL-GLR), have to cover a wide range of multi-scale phenomena: One should consider the interrelationships between geometry and operational conditions (e.g., pressure and temperature, gas inflow) of the bioreactor (at the metre-scale), mass transport from the gas to the broth via the bubbles (at the millimetre-scale), and gas consumption and product formation by the microorganisms (at the micrometre-scale). The interactions between phenomena at all these different scales are visually represented in Figure 1.3.

In this section, the various types of models typically used for modelling bioreactors and microorganisms will be discussed.

Models for bioreactors

The reactor model with the lowest amount of complexity is the zero-dimensional *ideal-mixing* model. The bioreactor is assumed to be well-mixed, thereby neglecting the existence of concentration gradients [71]. These models can be complemented by engineering relations for predicting phenomena such as the gas hold-up, bubble diameter, and the mass transfer rate more accurately [19, 25, 26]. For continuous (chemostat) bioreactors, these models are typically solved in a *steady-state* situation, wherein equilibrium is obtained between the in- and outgoing streams. Models that consider variations over time (e.g., how is the equilibrium obtained?) are referred to as *dynamic* models and could also be used to simulate full batch and fed-batch bioprocesses.

More details can be acquired using one-dimensional convection-dispersion models, which could predict how variables (e.g., the gas hold-up, mass transfer rate and dissolved gas concentrations) would vary along height and time, and have often been applied in bubble column and gas-lift modelling [72–74]. The advantage of these models is that they are fast: They can be used to estimate liquid and gas flow rates and the resulting concentration gradients, and allow coupling to detailed metabolic models [75]. Since these models are only 1D, they do not describe the turbulence inside the bioreactor, nor lack the fundamental equations to predict a detailed gas and liquid flow pattern inside the reactor, which is partly responsible for both mass transfer and the concentration gradient.

In contrast, *Computational Fluid Dynamics* (CFD) models can be used to obtain a high-resolution flow field in the bioreactor. By dividing the reactor into small volume-elements (a mesh) the equations for continuity (mass balance), momentum (Navier-Stokes), turbulence and chemical species transport can be solved. There are many different models for solving multiphase flow behaviour; the Volume of Fluid model (for separated or stratified flows), the mixture model (approximating multiphase flow patterns by solving only a single momentum equation describing the mixture), and Eulerian models where separate momentum equations are solved for each phase. A seemingly large variation of models is available for turbulence modelling. Of these, the RANS $k-\epsilon$ (Reynolds-Averaged Navier-Stokes) model is currently the workhorse for CFD modelling in large-scale bioreactors, although the more detailed LES (Large Eddy Simulation) models are gaining popularity [76]. The most detailed model is the DNS (Direct Numerical Simulation) model, wherein the Navier-Stokes equations are solved explicitly in each volume element [77].

Environmental dynamics from the cellular perspective can be studied by releasing virtual, Lagrangian, particles that follow the liquid flow in the bioreactor. These particles can represent (a package of) individual cells. By coupling the Lagrangian particles with the Eulerian model, the environmental fluctuations (in for example dissolved gas concentration) can be recorded, resulting into a lifeline. This Euler-Lagrangian model allows us to record the history of the microbe, while potentially considering the intracellular state by coupling a metabolic model [58, 78].

Practical details concerning the modelling setup are provided in later chapters. For an extensive overview of the equations and underlying model assumptions in CFD modelling, the interested reader is referred to [77, 79], while for gas-liquid interactions (such as drag, lift, bubble-induced turbulence, and turbulent dispersion), choices have to be made dependent on the physical phenomena in the system [80–82].

Models for microorganisms

A *black-box* model is the simplest model to describe microorganisms. This model assumes simultaneous import of substrates and product export, using a process reaction, that can be based on experimentally derived yields, or based on thermodynamics [83, 84]. The major disadvantage of black-box modelling is that it is unclear what happens inside the microbe as mechanisms for carbon and electron storage are not included. This hampers its applicability for predicting the influence of the dissolved gas concentration gradients on the microbe and its metabolism. One step further is the inclusion of cell maintenance and growth using the Herbert-Pirt relation [85], wherein substrate uptake can be related to the substrate concentration using a kinetic equation, with special emphasis to the one developed by Monod [86], while still assuming an instant equilibrium between the intra- and extracellular environment.

To predict the metabolic fluxes, genome-scale metabolic models (GEMs) of *C. autoethanogenum* have been constructed [87, 88], and applied to chemostat reactors for syngas fermentation [45, 46, 89, 90]. Such models are reconstructed from genome information, and can be supplemented with experimental data or with an objective and a set of constraints (Flux Balance Analysis, FBA), to predict intracellular as well as import and export fluxes, while assuming a metabolic steady-state [54]. One should note that the selection of the constraints and objective (which could be maximum growth or minimum uptake) is challenging and condition-specific. Due to the assumption of metabolic steady-state the applicability of FBA in a dynamic environment is weak, although dynamic FBA approaches have been suggested that couple FBA outputs to a dynamic extracellular environment [91]. GEMs usually contain hundreds to thousands of reactions, making model solving expensive and hamper its ability to couple it with CFD.

In between the black-box and the GEMs are so-called (pooled) kinetic metabolic models [40, 92–94]. These models do not consider the entire genome or metabolism but focus on a smaller reaction network, possibly by lumping several metabolic reactions and/or metabolites into pools. The models are called *Cellular Reaction Dynamics* (CRD) models, as they are able to predict the metabolic dynamics in time scales from seconds to days [94]. They are also called structured metabolic models, while the black-box description is said to be unstructured [1, 95]. These CRD models can be solved by integrating a more limited set of differential equations, making it possible to couple it with CFD [78] using the Lagrangian particle model, and elucidate the impact of substrate gradients on the metabolism, and on the reactor performance as a whole.

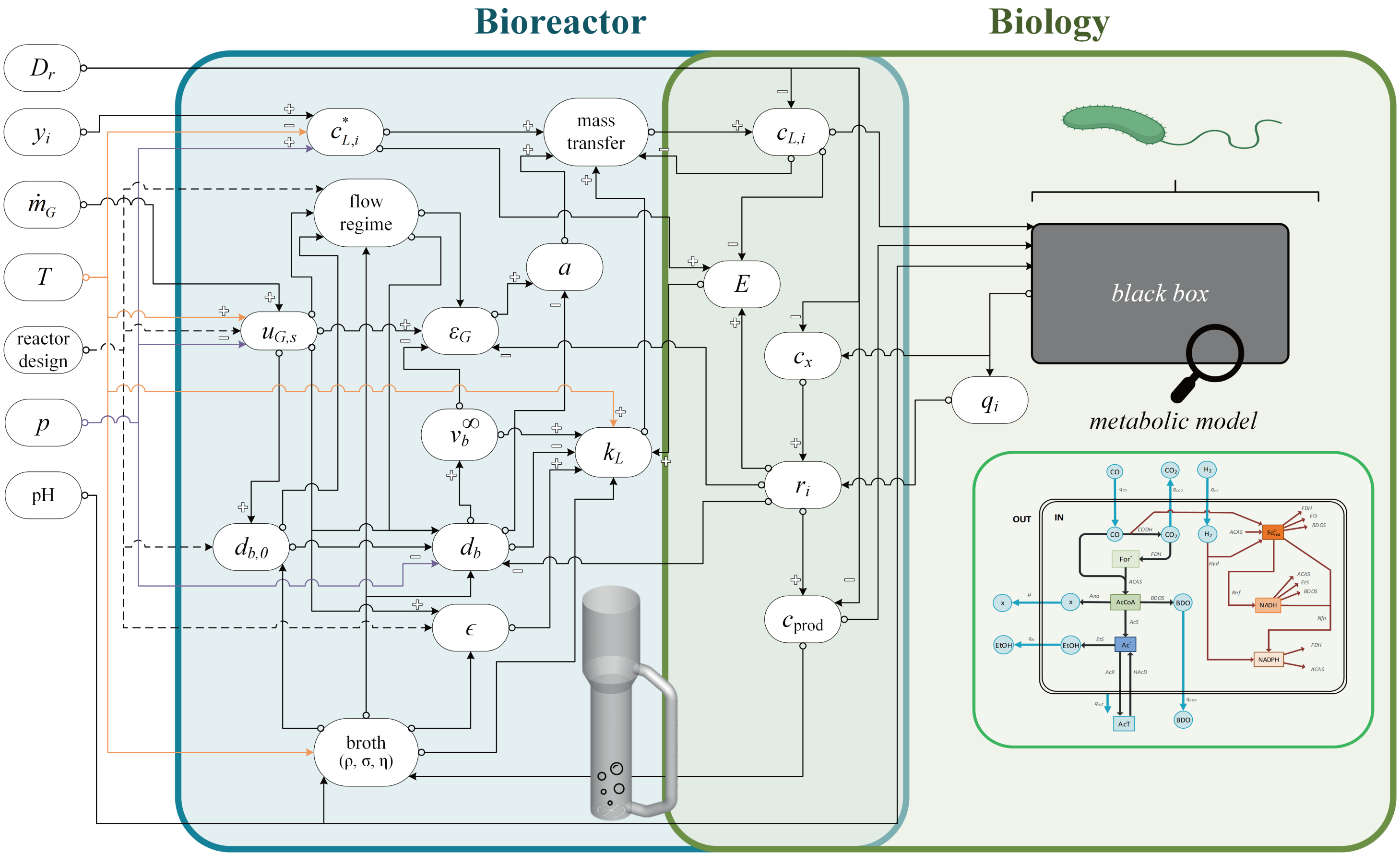
Bioreactor
Biology
D_r
y_i
$\dot{m}_G$
T
reactor design
p
pH
$c^*_{L,i}$
mass transfer
$c_{L,i}$
flow regime
a
E
$u_{G,s}$
ε_G
c_x
v_b^∞
k_L
r_i
$d_{b,0}$
d_b
ϵ
c_prod
broth (ρ, σ, η)
q_i
black box
metabolic model
OUT
IN
CO
CO_2
H_2
CODH
For
FDH
ACAS
AcCoA
BDO
BDOS
x
μ
Ana
EtOH
EtS
Ac
AcS
AcX
HAcD
AcT
Hyd
Rnf
NADH
NADPH
Nfn

Figure 1.3: Schematic overview of the interactions between operational parameters, the physics in bubble column-type bioreactors, and microorganisms. The complexity of the hydrodynamics in the bioreactor is provided on the left, while the various biological modelling approaches are provided at the right part of the scheme. The key elements regarding the microbial experience, at various scales, are provided in the middle part of the scheme. The operational parameters are provided at the left side, outside of the graph.

Population balance modelling has been done to describe population heterogeneity. For example, such a model was used to describe the variations in μ among a cell population in a bioreactor [96], and has been coupled to a μ-dependent intracellular model at various scales [97]. Although these models can be used to predict variations in one or two states, they cannot be used to gather intracellular details as in CFD-CRD modelling [66].

The first CFD-CRD coupling was published in the noteworthy works of Lapin et al. [58, 98], and was applied later on to industrial-scale fermentations [99, 100]. Since then, many reviews and perspective papers have exemplified the use of this method [63, 66, 67, 101, 102], but the actual execution seems to be challenging given the lack of actual research output using this method. The challenge probably arises due to the complexity of CFD modelling, and difficulties on developing trustworthy kinetic pool models.

1.5. Thesis scope and outline

The liquid phase concentrations of the dissolved gases, biomass and products are at centre of the complex multi-scale interrelationships in bioreactors. Figure 1.3 clearly shows them at the intersection between the reactor physics and the microorganism, depicting that they are fundamental parameters for bioprocess performance and scale-up.

This work explores the multi-scale interactions between bioreactor, bubbles and bacteria in the context of gas fermentation and how these should be addressed for scale-up, considering the concerns raised in Section 1.3 (i.e., low mass transfer rates, low (ethanol) productivity, the dissolved gas concentration gradient and the lack of scale-down studies). This will be done in a step-by-step fashion, by gradually zooming in (and sometimes out) on an industrial-scale EL-GLR, while aiming to answer the following questions in the end:

- What are the factors that should be considered to achieve sufficient mass transfer rates for successful operation of a commercial-scale gas fermentation process?
- What is an effective way to represent industrial-scale gas fermentation conditions at bench-scale?
- What is the influence of the dissolved gas concentration and its gradient on the metabolism and product spectrum of *C. autoethanogenum*?

The common engineering correlations used to describe gas-to-liquid mass transfer [25], significantly underpredicted the required mass transfer rate for commercial-scale operation (see Appendix 7.6, Table 2.1), highlighting the scientific concern regarding mass transfer in gas fermentation scale-up. The factors that could induce sufficient mass transfer in an industrial-scale EL-GLR will be investigated in **Chapter 2**. This will be done by developing and validating a CFD model which could describe the gas and liquid flow inside a pilot-scale external-loop airlift bioreactor. This model will then be applied in the large-scale EL-GLR and used to test strategies to obtain commercial-scale mass transfer performance.

In **Chapter 3**, the identified strategies (or: hypotheses) from Chapter 2 to obtain high mass transfer rates in the EL-GLR will be tested in a lab-scale bubble column. First, the influence of the produced ethanol and its concentration on the bubble size distribution and the $k_L a$ will be studied. Next to this, the fermentation medium (containing salts and vitamins) and the whole broth (containing biomass will be studied. By determining the physical properties of each mixture (surface tension σ, viscosity η and density ρ) the accuracy of the empirical mass transfer correlations will be assessed.

After understanding how high mass transfer rates could be obtained, it will be studied how the biomass concentration relates to gas uptake rates (and thus productivity) and the dissolved gas concentration gradient in **Chapter 4**. This will be done by implementing a mass transfer model and a Monod-type, black-box, kinetic model for CO and H_2-uptake in *C. autoethanogenum* in the CFD framework developed in Chapter 3. From Euler-Lagrangian simulations, a scale-down simulator will be proposed to replicate the industrial-scale environment at lab-scale. The developed scale-down simulator should enable experimentalists to study the influence of the dissolved gas concentration gradient on cellular metabolism.

The impact of the dissolved gas concentration and its gradient on the cellular metabolism and the product spectrum will be investigated in **Chapter 5**. Here, a metabolic kinetic model of *C. autoethanogenum* will be coupled to the CFD model developed in the previous chapters. This will enable a full coupling between the phenomena in the bioreactor and the metabolism (see Figure 1.3). It will be studied how high ethanol production rates may be obtained and how that is influenced by multi-scale (from hydrodynamic to enzymatic) phenomena.

After wrapping up our results in **Chapter 6**, the research questions will be answered. Perspectives towards future work will be provided in **Chapter 7**.

Please keep seated for an amazing journey from bioreactors to bubbles to bacteria, across the wonderful world of gas fermentation!

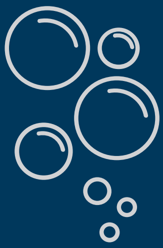

Chapter 2

Hydrodynamics and mass transfer in external-loop gas-lift reactors

Perfect is the enemy of good

Voltaire

This chapter has been published as:
Puiman, L., Abrahamson, B., Van der Lans, R. G. J. M., Haringa, C., Noorman, H. J., & Picioreanu, C. (2022). Alleviating mass transfer limitations in industrial external-loop syngas-to-ethanol fermentation. *Chemical Engineering Science*, 259, 117770.

Abstract

Mass transfer limitations in syngas fermentation processes are mostly attributed to poor solubility of CO and H_2 in water. Despite these assumed limitations, a syngas fermentation process has recently been commercialised. Using large-sale external-loop gas-lift reactors (EL-GLR), CO-rich off-gases are converted into ethanol, with high mass transfer performance ($7-8.5\,\mathrm{g\,L^{-1}\,h^{-1}}$). However, when applying established mass transfer correlations, a much poorer performance is predicted ($0.3-2.7\,\mathrm{g\,L^{-1}\,h^{-1}}$). We developed a CFD model, validated on pilot-scale data, to provide detailed insights on hydrodynamics and mass transfer in a large-scale EL-GLR. As produced ethanol could increase gas hold-up (+ 30%) and decrease the bubble diameter (< 2 mm) compared to air-water mixtures, we found with our model that a high volumetric mass transfer coefficient ($650-750\,\mathrm{h^{-1}}$) and mass transfer capacity ($7.5-8\,\mathrm{g\,L^{-1}\,h^{-1}}$) for CO are feasible. Thus, the typical mass transfer limitations encountered in air-water systems can be alleviated in the syngas-to-ethanol fermentation process.

Graphical abstract

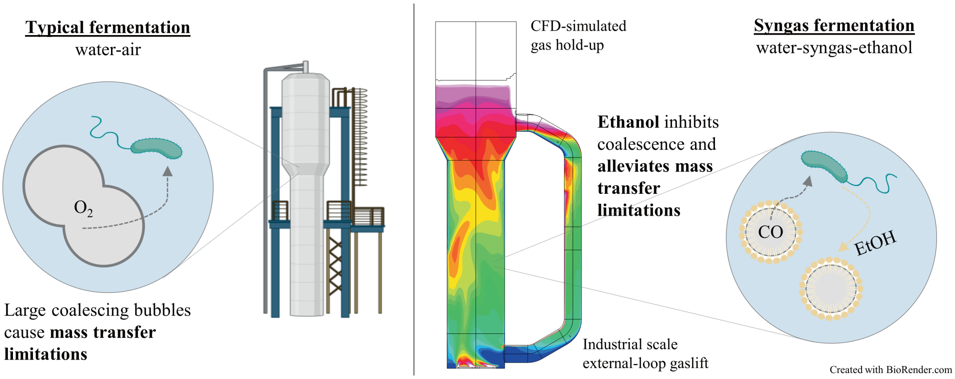
Typical fermentation
water-air
O2
Large coalescing bubbles cause **mass transfer limitations**
CFD-simulated gas hold-up
Ethanol inhibits coalescence and **alleviates mass transfer limitations**
Industrial scale external-loop gaslift
Syngas fermentation
water-syngas-ethanol
CO
EtOH
Created with BioRender.com

2.1. Introduction

The conversion of waste gases by synthesis gas (syngas) fermentation has advanced to industrial scale in the last decade. In this process, a gas mixture containing CO, CO_2 and H_2 can be converted by microbes (predominantly *Clostridium* spp.) into a range of chemicals, e.g., acetic acid, ethanol, acetone and isopropanol [103]. The company LanzaTech has been able to commercialise the process of converting CO-rich off-gases from steel-mills into ethanol. Currently they deploy ethanol production facilities in China, while expanding their manufacturing network to other countries [8, 10, 103].

Details of the full-scale operation are unknown in the scientific literature due to the proprietary nature of this process. It is expected that syngas conversion takes place in a gas-lift reactor with an external circulation loop [104]. This reactor configuration, also known as the external loop gas-lift reactor (EL-GLR) is like a conventional air-lift loop reactor as applied in waste-water treatment and industrial bioprocesses. Compared to the more established bubble column reactors (BCRs), in external-loop airlift reactors (EL-ALRs) there is forced liquid recirculation (potentially but not necessarily via pump action) through the downcomer (the external-loop), causing high liquid velocities, a more defined (plug) flow pattern and a shorter mixing time [20, 105]. The external-loop might also be used for heat exchange, introduction of fresh feed and broth withdrawal [106].

The increased liquid velocity in the riser is known to decrease the gas residence time and thus the gas hold-up (ε_G) and the volumetric mass transfer coefficient ($k_L a$) compared to a bubble column [107, 108]. At the same time, gas-liquid mass transfer is generally known to be one of the limiting factors in syngas fermentation processes [2, 22, 23, 109, 110]. For industrial ethanol production, it was determined that a $k_L a$ of at least 580 h^{-1} should be reached for commercial success [111]. Our preliminary calculations, based on publicly available data reported by LanzaTech, show that a mass transfer capacity (MTC) of 7 – 8.5 $g L^{-1} h^{-1}$ should be reached, which results in a $k_L a$ between 600 and 750 h^{-1}, based on a headspace pressure of 1 bar and 50% CO in the inlet gas (Figure A.1).

For estimation of $k_L a$ in air-water systems, many relationships have been provided in the literature for different reactor types [25]. With these relations the most likely $k_L a$ was estimated at industrial conditions and compared to the $k_L a$ from our preliminary calculations (Table 2.1), resulting into a MTC between 0.3 and 2.7 $g L^{-1} h^{-1}$. A clear discrepancy between the $k_L a$ obtained by these relations and the supposed industrial performance was found, as all engineering correlations predict a substantially lower $k_L a$. Although it is widely known that electrolytes, organic molecules (such as the produced ethanol), biomass, and the reactor geometry influence $k_L a$ [25, 26], the impact of these factors are not comprehensively considered with the correlations in Table 2.1. Furthermore, empirical relations obtained for ALRs were derived at smaller scales and their validity for larger scales bears uncertainties. The non-standard reactor geometry and irregular flow pattern in industrial reactors complicate the prediction of the mass transfer per-

Table 2.1: Relationships used for the prediction of $k_L a$ in Newtonian media in a large-scale EL-GLR, as well as typical $k_L a$ values for industrial operation. See Tables A.1 and A.2 for the meaning, units and calculation of variables in these equations. The empirical correlations were developed for air-water systems, and would require a small correction (around 5% lower) for CO due to its lower diffusion coefficient compared to oxygen [113].

Reference	**Equation**	$\boldsymbol{k_L a}$ (h^{-1})
LanzaTech estimation (Figure A.1)		600 – 750
Empirical correlations		
External-loop airlift		
Bello et al. [114]	$k_L a = 0.76 \cdot \left(1 + \frac{A_d}{A_r}\right)^{-2} \cdot u_{G,s}^{0.8}$	~130
Chisti et al. [115]	$k_L a = \varepsilon_L \left(1 + \frac{A_d}{A_r}\right)^{-1} u_{G,s}^{0.899} \cdot (0.349 - 0.102 c_{\text{solids}})$	~40
Chisti and Moo-Young [105]	$k_L a = 1.27 \cdot 10^{-4} \cdot \left(\frac{P_\text{G}}{V_\text{D}}\right)^{0.925}$	~75
Bubble column		
Deckwer et al. [72]	$k_L a = 0.5 \cdot u_{G,s}^{0.884}$	~80
Deckwer et al. [116]	$k_L a = 0.467 \cdot u_{G,s}^{0.82}$	~90
Jackson and Shen [117]	$k_L a = 0.53 \cdot u_{G,s}^{1.15}$	~30
Heijnen and Van't Riet [26]	$k_L a = 0.32 \cdot u_{G,s}^{0.7} \cdot 1.024^{(T-293)}$	~140
Dimensionless relations		
Akita and Yoshida [118]	$(Sh)\, a \cdot D_r = 0.6 Eo^{0.62} Ga^{0.3} Sc^{0.5} \varepsilon_G^{1.1}$	~170
Nakanoh and Yoshida [119]	$(Sh)\, a \cdot D_r = 0.09 Eo^{0.75} Ga^{0.4} Sc^{0.5} Fr^{1}$	~230
Kawase et al. [120]	$(Sh)\, a \cdot D_r = 0.452 Eo^{0.62} Ga^{0.3} Sc^{0.5} Fr^{1} Re^{1}$	~15
Uchida et al. [121]	$(Sh)\, a \cdot D_r = 0.17 Eo^{0.62} Ga^{0.3} Sc^{0.5} \varepsilon_G^{1.1}$	~50
Vatai and Tekić [122]	$(Sh)\, a \cdot D_r = 0.031 Eo^{0.75} Ga^{0.4} Sc^{0.5} Fr^{1}$	~80
Kawase and Hashiguchi [123]	$(Sh)\, a \cdot D_r = 0.142 Eo^{0.6} Sc^{0.5} Fr^{0.075} Re^{0.875} \left(1 + \frac{A_d}{A_r}\right)^{-97/80}$	~170

formance using common correlations, which are normally valid for a narrow range of conditions and were derived in shorter columns (influencing $u_{G,s}$) while assuming ideal mixing. Spatio-temporal variations complicate the *a priori* estimation of ε_G, $k_L a$ and MTC as particular geometry configurations strongly influence the hydrodynamics in ALRs (e.g., riser width/height, separator dimensions and the particular connection of the downcomer). For example, while the liquid and gas velocities are expected to be high in the riser, these should decrease in the wider separator section in the top of the vessels and consequently increase the local ε_G [112].

Several models have been developed to describe hydrodynamics of pilot- and full-scale airlift bioreactors. The model by Van der Lans [74] predicted the axial mean values of liquid circulation velocity and gas fraction in a pilot-scale external-loop bioreactor well. Van Benthum et al. [124] modelled three-phase hydrodynamics (liquid velocity, gas and solid hold-up) in a biofilm airlift suspension extension reactor, wherein the liquid velocity in a gas-free downcomer is controlled independently from the gas flow velocity. While neglecting spatial variations of gas, liquid and solids concentrations in the internal

Table 2.2: The different relations that are used for predicting the liquid-side mass transfer coefficient, k_L.

Eq.	Reference	Equation	
Bubble-based models			
(2.1)	Higbie [127]	$k_L = 2\sqrt{\frac{D_{L,\mathrm{CO}}}{\pi t_e}} = 2\sqrt{\frac{D_{L,\mathrm{CO}} v_\mathrm{slip}}{\pi d_b}}$	$d_b > 2$ mm [26]
(2.2)	Calderbank and Moo-Young [128]	$k_L = 0.42\left(\frac{\Delta\rho v_L g}{\rho_L}\right)^{\frac{1}{3}}\left(\frac{D_{L,\mathrm{CO}}}{v_L}\right)^{\frac{1}{2}}$	Non-rigid bubbles
Eddy-based models			
(2.3)	Kaštánek [129]	$k_L = 2\sqrt{\frac{D_{L,\mathrm{CO}}}{\pi t_e}} = 1.13 D_{L,\mathrm{CO}}^{\frac{1}{2}}\left(\epsilon/\nu_L\right)^{\frac{1}{4}}$	Theoretical
(2.4)	Linek et al. [130]	$k_L = 0.45 D_{L,\mathrm{CO}}^{\frac{1}{2}}\left(\epsilon/\nu_L\right)^{\frac{1}{4}}$	Empirical
(2.5)	Lamont and Scott [131]	$k_L = 0.4 D_{L,\mathrm{CO}}^{\frac{1}{2}}\left(\epsilon/\nu_L\right)^{\frac{1}{4}}$	Empirical
(2.6)	Kawase and Moo-Young [132]	$k_\mathrm{L} = 0.3 D_{L,\mathrm{CO}}^{\frac{1}{2}}\left(\epsilon/\nu_L\right)^{\frac{1}{4}}$	Empirical

regions, the model was well able to predict the pilot-scale hydrodynamics. Earlier, Heijnen et al. [125] described the liquid circulation velocity and gas hold-up in an industrial-scale biofilm internal-loop airlift suspension reactor, based on mass and momentum balances. This model is applicable to three hydrodynamic regimes: gas-free downcomer (regime 1), entrained gas in downcomer (regime 2) and gas back-circulation via downcomer (regime 3). We argue that in the LanzaTech case, operation in regime 1 or 2 may be preferred compared to regime 3 as the latter could reduce the CO partial pressure and thus its saturation concentration in the riser.

Convection-dispersion and tanks-in-series (1D) models have been proposed to understand mixing and mass transfer phenomena in small-scale airlift reactors [126], but it is unclear how the flow pattern deviates from these simple mixing models for the large-scale EL-GLR. It is generally known that large-scale BCRs show high axial dispersion coefficients [26] but that EL-ALRs studied at lab and pilot-scale display more plug-flow behaviour [108]. As the axial dispersion behaviour is unclear in an industrial EL-GLR, the convection-dispersion models turned out to be unsuitable for the prediction of the large-scale flow pattern and gas-liquid mass transfer rates. Furthermore, several relations have been developed to describe the mass transfer coefficient k_L, based on local conditions such as the slip velocity and the eddy dissipation rate (Table 2.2). These relations require a high spatial resolution, which cannot be provided by the 0D and 1D models.

With 3D computational fluid dynamics (CFD) models a high spatio-temporal resolution can be obtained, albeit with a much greater computational effort than when applying simple mixing models. For EL-ALRs, several authors used CFD to study the hydrodynamics and the mixing behaviour [133–135]. Hydrodynamics and oxygen mass transfer in a lab-scale sectionalized EL-ALR has been studied recently; it was demonstrated that the $k_L a$ predicted with Equation 2.5 (Table 2.2) matched the experimental data better than predictions from Equation 2.1 and 2.3 [136]. Similar work was done earlier, wherein it was observed that Equation 2.3 showed a strikingly good agreement with experimental results [137]. Most of these models were developed for lab and pilot-scale EL-ALRs, with riser diameters smaller than 0.14 m, where wall effects can be significant [105].

A CFD model for syngas fermentation in a BCR with a population balance model for the gas phase was developed recently [56]. Low $k_L a$ values and thus low CO transfer rates, low dissolved CO concentrations and low CO uptake rates were obtained as more than 50% of the bubbles had a relatively high bubble diameter ($d_b > 8$ mm). Several one-dimensional models have been presented for syngas fermentation in large-scale BCRs as well. de Medeiros et al. [138] developed such a model for the optimisation of different process conditions. They determined that strategies needed to be obtained to enhance the $k_L a$ with at least a factor three, relative to air-water correlations, to decrease the minimum ethanol selling price to \$0.7/L and reach high (70%) thermodynamic efficiency. Another BCR model was coupled with a black-box stoichiometric model for *C. autoethanogenum* based on thermodynamics in order to estimate the ethanol productivity in such a reactor. High productivities were obtained $4.25\ \mathrm{g_{EtOH}\,L^{-1}\,h^{-1}}$, but this was at the expense of the gas utilisation (only 17%) as high gas flow rates were used [32]. In another 1D model, with kinetics reported by LanzaTech, a genome-scale metabolic model for a proprietary *C. autoethanogenum* strain was coupled to bubble column hydrodynamics. In their model $k_L a$ and microbial CO uptake rate varied axially between 350 and 425 $\mathrm{h^{-1}}$ and 0 and $7\ \mathrm{g\,L^{-1}\,h^{-1}}$, respectively, by assuming d_b below 1.5 mm and constant k_L of $1 \times 10^{-4}\ \mathrm{m\,s^{-1}}$ [55]. However, detailed analyses how the low d_b and high MTC could be accomplished in industrial reactors are lacking.

Thus far, no CFD model has been developed for describing the hydrodynamics and CO mass transfer in a large-scale external-loop gas-lift reactor, for studying the required conditions to minimise the gas-liquid mass transfer limitations in an industrial syngas fermentation process. Next to that, the results of such a model would provide information to be used for subsequent reactor design and optimisation. The model that we have developed in this study for hydrodynamics and mass transfer in an EL-ALR was first tested and validated by comparing local axial gas and liquid flow velocities in the riser and the downcomer, gas hold-up, and turbulence intensity with pilot-scale results obtained by Young et al. [139]. Then, using the same model equations, the large-scale EL-GLR hydrodynamics and gas transfer were simulated and compared with correlations and observations from literature. For varying bubble diameters (between 1 and 7 mm), higher temperatures and gas hold-up, and a range of headspace pressures, $k_L a$ and MTC were determined using different relations (Table 2.2), in order to establish the best operation window for high industrial performance.

2.2. Methods

Reactor geometry and mesh

In this work, two reactor geometries were considered: A pilot-scale geometry to compare CFD model predictions with experimental results and a full-scale reactor for the subsequent mass transfer study. The hydrodynamic CFD model was applied to data obtained by Young et al. [139] for a pilot-scale external-loop reactor (2.95 m high, riser and downcomer diameter of 19 and 14 cm, 260 L reactor volume, 160 L liquid volume). This reactor configuration was chosen as it was found that the gas hold-up was independent of the riser diameter when wider than 14 cm [105]. The 3D geometry was developed using ANSYS Design Modeller. A polyhedral mesh (400000 cells, 0.27 minimum orthogonal quality) with a higher resolution in the dispersed-phase domain was developed in ANSYS Meshing (Figure A.2).

The dimensions of the industrial-scale reactor were estimated from openly available pictures of the Shougang-LanzaTech plant (Figure 1.2), and are schematically represented in Figure 2.1. The 3D geometry has been developed using cylindrical bodies, with a ring sparger [139] mounted at 0.1 m above the reactor base. The total volume of the reactor equals 840 m^3, with an ungassed liquid volume of 565 m^3, which roughly corresponds to the 500 m^3 volume presented by LanzaTech [10]. A mesh with 370,000 polyhedral cells, 0.3 minimum orthogonal quality, 20 cm cell size and three refined boundary layers near all walls (including sparger), was constructed in Fluent Meshing. A mesh refinement study done using meshes with 1.6 and 1.9 million cells established that the 370,000-cell mesh was sufficient for determining $k_L a$ and MTC within 10% accuracy (Figure A.2, Table A.3).

Fluid dynamic model

The transient gas-liquid flow was computed within ANSYS Fluent 2020R1 with the Eulerian multiphase flow model, with implicit volume fraction formulation, dispersed RNG k-ϵ turbulence model, which is the recommended choice for bubble column modelling [140], and standard wall functions. The forces involved in the two-phase interaction were surface tension (continuum surface force), drag (Fluent's universal-drag model) and gravity. A model with a similar set of forces was used before for syngas fermentation modelling in BCRs [56].

In the pilot-scale ALR, mean air bubble diameters ranged from 4 to 6 mm [139], therefore as dispersed phase 5 mm bubbles were modelled. For the large-scale reactor, the mean bubble diameter is unknown and could range between 1 and 7 mm, based on the liquid properties and operating conditions [26]. Because coalescence inhibition can be expected due to the salt and ethanol-rich fermentation broth, 3 mm bubbles were modelled in the large-scale hydrodynamic model, according to [141], by assuming a sparger orifice size of 0.75 mm.

A mass-flow inlet was used on the sparger surface at the bottom of the reactor, providing a fixed mass flow rate of gas (Table 2.3). A pressure-outlet with gas backflow was

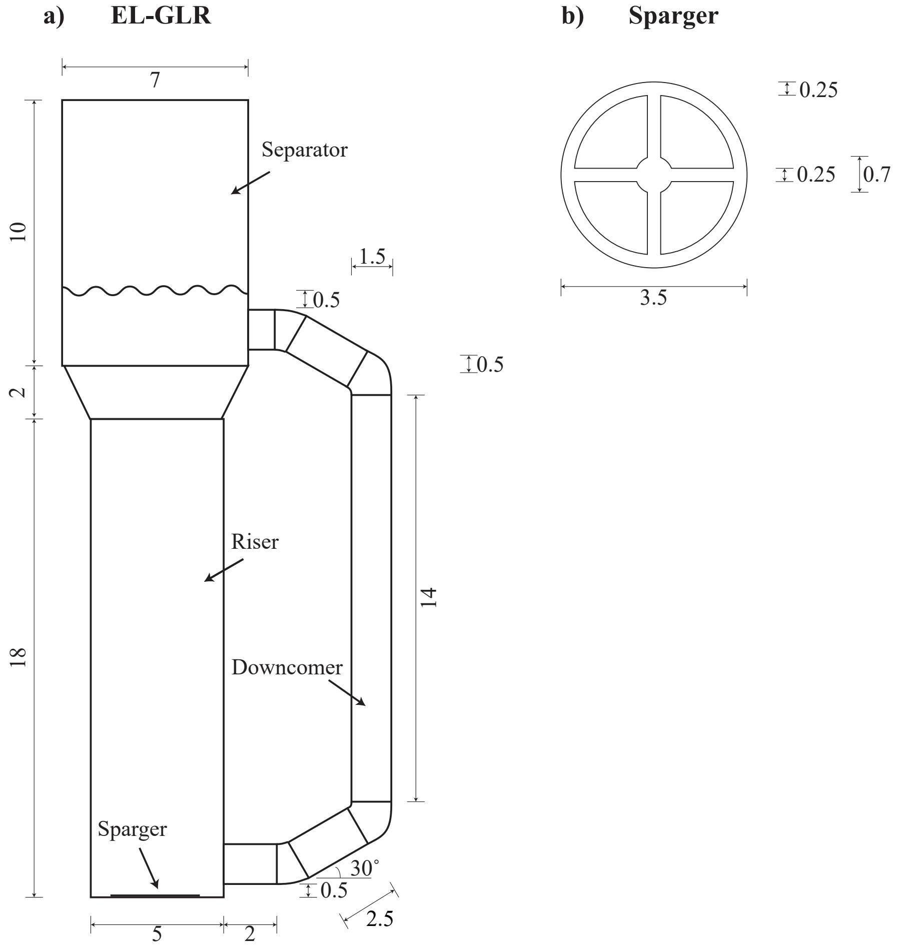

Figure 2.1: Schematic representation of a) the industrial-scale external-loop gas-lift reactor and b) the sparger geometry. The wavy line represents the initial (ungassed) liquid height. All dimensions are in meters.

assumed at the top of the column, with the headspace pressure of 101 kPa in both reactors. Sensitivity analyses were done with 304 kPa and 608 kPa headspace pressure for the large-scale reactor. Boundary conditions considered a turbulence intensity of 5% and the local vessel diameter. To all the walls standard no-slip conditions were assigned.

As the precise liquid medium properties are unknown due to the presence of variable concentrations of cells and ethanol, the properties of water at 25°C were assumed for the liquid phase (Table 2.4). Gas density differences were accounted for using the ideal gas law. Both reactor models contained a gas headspace, by initialising the headspace gas fraction to be 1.

Table 2.3: Values uses for the mass flow inlet boundary condition in the various models. The superficial gas velocity for the EL-GLR was calculated by determining the gas flow rate ($\mathrm{m^3\,s^{-1}}$) using the local pressure at the sparger (Table A.1). For scale comparison, the gas mass flow per volume liquid is provided.

Superficial gas-velocity ($\mathrm{cm\,s^{-1}}$)	**Mass flow per volume liquid** ($\mathrm{kg\,m_L^{-3}\,s^{-1}}$)	**Mass flow inlet** ($\mathrm{kg\,s^{-1}}$)
Pilot-scale reactor		
0.96	2.37×10^{-3}	3.96×10^{-4}
2.1	5.19×10^{-3}	8.66×10^{-4}
4.7	1.14×10^{-2}	1.90×10^{-3}
8.4	2.04×10^{-2}	3.4×10^{-3}
Industrial-scale reactor		
2.8	3.73×10^{-3}	2.11

Table 2.4: Parameters used in the CFD models.

Symbol	**Description**	**Pilot-scale**	**Industrial-scale**	**Unit**
g	Gravitational acceleration	-9.81	-9.81	$\mathrm{m\,s^{-2}}$
T	Temperature	293.15	310.15	K
p_0	Operating pressure	101325	101325	Pa
d_b	Bubble diameter	5×10^{-3}	3×10^{-3}	m
σ	Surface tension	0.072	0.072	$\mathrm{N\,m^{-1}}$
Gas phase		*air*	*syngas*	
ρ_G	Gas density	ideal gas law	ideal gas law	$\mathrm{kg\,m^{-3}}$
η_G	Gas viscosity	1.78×10^{-5}	1.72×10^{-5}	$\mathrm{kg\,m^{-1}\,s^{-1}}$
$y_{\mathrm{CO,in}}$	Inlet mole fraction	-	0.5	$\mathrm{mol_{CO}\,mol_G^{-1}}$
Liquid phase		*water*	*water*	
ρ_L	Water density	998	998	$\mathrm{kg\,m^{-3}}$
η_L	Liquid viscosity	1×10^{-3}	1×10^{-3}	$\mathrm{kg\,m^{-1}\,s^{-1}}$

Mass transfer model

The mass transfer studies in the large-scale bioreactor were performed after a statistically stationary ("steady") flow field was established (after 1000 seconds simulation time, using 3 mm bubbles). For an additional 200 s, dynamic flow data was exported every second for time-averaging and processed in Tecplot 360 EX 2018 R1. Based on the computed flow field, $k_L a$ and MTC were calculated via six different relations for k_L (Table 2.1). Spherical bubbles were assumed because of the small bubble diameter and bubble-stabilizing effects of dissolved solutes (Equation 2.7) as well as a linear gradient in axial gas phase CO mole fraction y_{CO} (considering 90% CO conversion (Figure A.1)) (Equation 2.8). The

Table 2.5: Parameters used for mass transfer calculations.

Symbol	Description	20 °C	37 °C	Unit	Source
ν_L	Kinematic viscosity	1.018×10^{-6}	7.121×10^{-7}	$\mathrm{m^2\,s^{-1}}$	Reid et al. [142]
$D_{L,\mathrm{CO}}$	CO diffusion coefficient	1.78×10^{-9}	2.71×10^{-9}	$\mathrm{m^2\,s^{-1}}$	Cussler [143]
H_{CO}	Henry coefficient	2.93×10^{-7}	2.29×10^{-7}	$\mathrm{kg\,m^{-3}\,Pa^{-1}}$	Sander [144]

impact of the bubble size was studied in the 1 – 7 mm range. The influence of the operating temperature was considered as it affects the liquid viscosity, CO diffusion coefficient and Henry constant (Table 2.5). For the calculation of MTC, microbial CO uptake kinetics are not required, instead a dissolved CO concentration of $0\,\mathrm{g\,L^{-1}}$ was assumed in all grid cells.

$$MTC = k_L a \cdot c^{\mathrm{sat}}_{L,\mathrm{CO}} = k_L \cdot \frac{6\varepsilon_G}{d_b \varepsilon_L} \cdot H_{\mathrm{CO}}\, p\, y_{\mathrm{CO}} \tag{2.7}$$

$$y_{\mathrm{CO}}(z) = -\frac{(y_{\mathrm{CO,in}} - 0.9\,y_{\mathrm{CO,in}})}{h_D} z + y_{\mathrm{CO,in}} \tag{2.8}$$

Model solution

The transient models were solved using ANSYS Fluent 2020R1. For the pilot-scale models, a time step of 0.01 s was used with a maximum of 30 iterations per time step, wherein the residuals decreased to $O(10^{-3})$. The results presented here were obtained by storing flow data at the positions mentioned by Young et al. [139] every 0.01 s, starting at 50 s (when a steady flow field was reached) until 110 s flow time.

For the industrial reactor, the time step dt was gradually increased from an initial 0.01 s until 0.65 s, $dt = 0.025$ s until 3 s, $dt = 0.05$ s until 5 s and $dt = 0.1$ s from 5 seconds on. This time-stepping strategy was required to keep solution convergence (residuals $< O(10^{-3})$) within 10 – 25 iterations per time step, and found to be crucial to achieving convergence near the mesh-refined sparger location. The solution methods, spatial discretization and relaxation factors for both reactor models are given in Table A.4.

2.3. Results and discussion

In this section, the flow pattern predicted by the CFD model will first be compared with the pilot-scale data obtained by Young et al. [139] (section 2.3.1). After this, the results at the large-scale are discussed (section 2.3.2) in terms of the gas hold-up, flow pattern and hydrodynamic regime. Then, results on mass transfer and strategies for relieving the gas-liquid mass transfer limitations will be discussed (section 2.3.3), before we sketch the implications of this research in the outlook (section 2.3.4).

2.3.1. Pilot-scale flow pattern

The computed liquid velocity in the riser was compared with the velocity profiles along the radius obtained experimentally by Young et al. [139] (Figure 2.2). The computed mean liquid velocity in the riser approximates the measured one with maximum deviations of 36% (Table A.5). However, the computed velocity gradients along the column radius were consistently smaller (i.e., flatter velocity profiles) than those measured (i.e., showing usually a sharp maximum at the axis at $r/R = 0$). The radial profiles of the turbulence intensities in both the riser and downcomer are quite similar to the data, but the model underestimates the turbulence intensity in the riser, while overestimating in the downcomer. This is probably a result of the simplified set of forces considered in the model. Roy et al. [135] were able to model the radial liquid velocity profile by using the standard k-ϵ model and taking the turbulence dispersion and lift forces into account, together with a conveniently chosen bubble size. On the other hand, liquid velocity measurement errors up to 10% for the riser were noted from a liquid phase mass balance by Young et al. [139], which could possibly explain part of the deviation between model and measurements. The (gas-free) downcomer velocity profile, however, showed good correspondence, as well as the profiles predicted for the gas hold-up and gas velocity. The trends for increasing superficial gas velocities were modelled correctly for all variables.

By simulated injection of a liquid tracer (with the same properties as water) just above the sparger, it was determined that the model can predict the typical circulating liquid mixing behaviour as often shown in airlift reactors [105, 145]. The tracer concentration profile over time c_t extracted from the CFD simulations was normalised with the final (steady state) concentration $c_{t,\infty}$. This normalised tracer concentration over time t was fitted with Equation 2.9 [105] expressing the fluctuations of concentration over a normalised time θ ($\theta = t/t_c$, with t_c the circulation time), as function of the Bodenstein number ($Bo = u_{L,\mathrm{ax}} L_c / D_{\mathrm{ax}}$ with L_c the circulation length and the axial dispersion coefficient D_{ax}).

$$\frac{c_t}{c_{t,\infty}} = \left(\frac{Bo}{4\pi\theta}\right)^{1/2} \sum_{n=1}^{\infty} \exp\left[\frac{-(n-\theta)^2 Bo}{4\theta}\right] \tag{2.9}$$

In this way, Bo and t_c for the EL-ALR were determined at several locations in the reactor (Figure 2.3). The model predicted Bo values around 45, which are typical estimations for Bo in an ALR [146, 147], indicating the dominance of the plug-flow in the

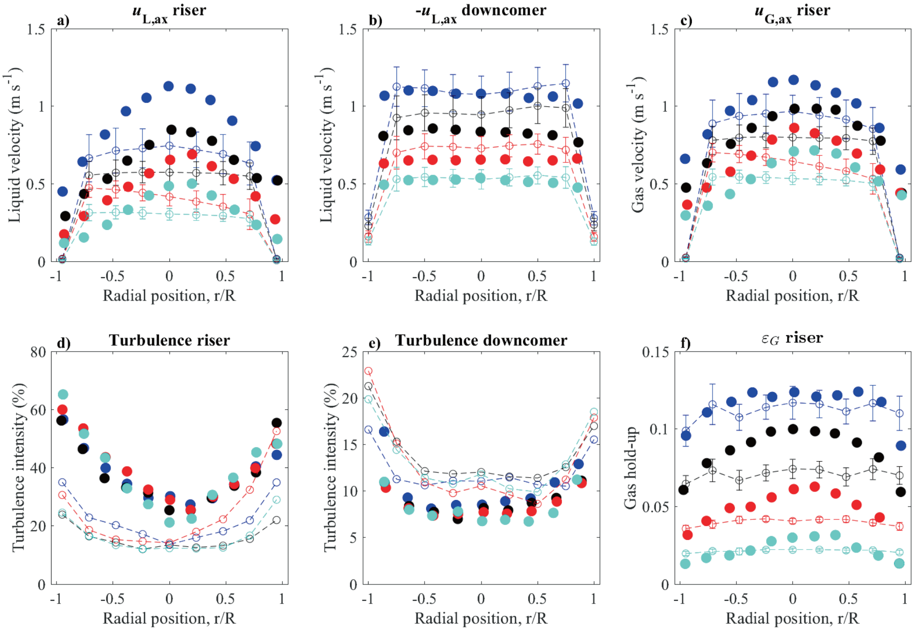

Figure 2.2: Comparison of radial profiles obtained by experiments in a pilot-scale EL-ALR [139] (filled circles) and mean values of CFD results (open circles with dashed lines) for different $u_{G,s}$ (8.4 (blue), 4.7 (black), 2.1 (red) and 0.96 cm s^{-1} (cyan). a) the axial liquid velocity in the riser ($u_{L,\mathrm{ax}}$), b) the axial liquid velocity in the downcomer ($-u_{L,\mathrm{ax}}$), c) the axial gas velocity in the riser ($u_{G,\mathrm{ax}}$)), d) the turbulence intensity in the liquid in the riser and e) downcomer, and f) the gas hold-up in the riser. Error bars: the standard deviation of the CFD results during 60 s simulation time (data stored every 0.01 s).

reactor. A mean circulation time of about 7.6 s resulted from the tracer model with a $u_{G,s}$ of 8.4 cm s^{-1}.

Considering that most of the flow parameters were determined to be within a 25% range of experimental values (Table A.5) and the good correspondence with mixing theory, we considered the model appropriate for engineering calculations. Furthermore, the most important variable concerning mass transfer, the gas hold-up, was reasonably well predicted. In order to be sure that the radial liquid velocity profile is properly predicted, it will be compared with theoretical predictions for this profile in large-scale EL-ALRs in the upcoming section.

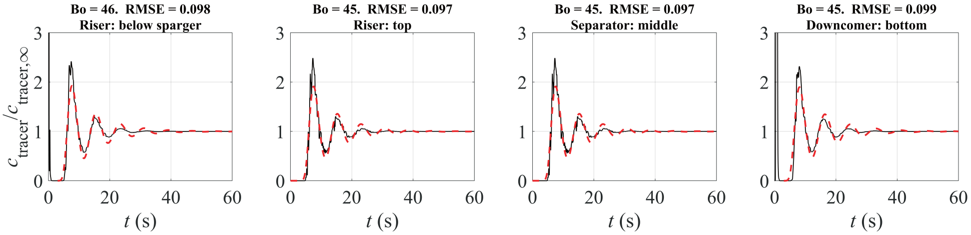

Figure 2.3: The normalised concentration of a tracer obtained from the CFD model (black lines) and concentration according to the axial dispersion model for ALR (Equation 2.9) (red lines), compared at four locations in the pilot-scale reactor. For all locations, the Bodenstein number was ~45 with the root-mean-square-error (RMSE) smaller than 0.1. The CFD data has been obtained at $u_{G,s}$ of 8.4 cm s^{-1}.

2.3.2. Large-scale flow pattern

In this section, the results of the large-scale reactor CFD model are presented. First, its ability to predict the gas fraction is discussed, since this is a key variable regarding mass transfer. Then the gas and liquid velocity-fields are analysed in detail. Lastly, the radial profiles of the liquid velocity in the riser and the observed time-variations are discussed.

The simulated gas hold-up in the EL-GLR was on average 0.13 at a superficial gas velocity of 2.8 cm s^{-1}. This value was in good agreement with the values obtained from several correlations available in literature for BCRs and EL-ALRs (Table 2.6).

The local values of the instantaneous gas hold-up (Figure 2.4a) were averaged in time over 200 seconds (Figure 2.4c). The CFD simulations indicate that at the bottom of the reactor, the freshly sparged gas is strongly pushed towards the wall of the riser, which might result in bubble coalescence, by the liquid exiting the downcomer. This is also visible in the liquid flow patterns (Figure 2.4b, d). When the gas is pushed towards the left side, the local liquid velocity increases, creating a circulation loop around the downcomer outlet. Similar behaviour has been observed experimentally for bottom-plate spargers

Table 2.6: The 200 s time- and volume-averaged gas hold-up ε_G determined by CFD in the EL-GLR, riser and downcomer, compared with values from established correlations. The values of $u_{G,s,r}$ and $u_{L,s,r}$ used in the correlations were the averages of the time-averaged axial superficial velocities computed in six horizontal planes across the riser. 1: $v_b^\infty = 0.25\,\mathrm{m\,s^{-1}}$, 2: $L_{\text{con}} = 0.5$ m and $L_d = 19.5$ m. Other parameters in Table A.1.

Study	**Reactor type**	**Equation**	$\boldsymbol{\varepsilon_G}$
This study	EL-GLR	3D CFD model	0.126
Zuber and Findlay [148] [1]	BCR	$\varepsilon_{G,r} = \frac{u_{G,s,r}}{1.08(u_{G,s,r}+u_{L,s,r})+v_b^\infty}$	0.137
Heijnen and Van't Riet [26] [1]	BCR	$\varepsilon_{G,r} = \frac{u_{G,s}}{v_b^\infty}$ (homogeneous flow)	0.112
Chisti and Moo-Young [105]	EL-ALR	$\varepsilon_{G,r} = \frac{u_{G,s,r}}{0.24+1.35(u_{G,s,r}+u_{L,s,r})^{0.93}}$	0.124
Bello et al. [114]	EL-ALR	$\varepsilon_G = 0.16\left(\frac{u_{G,s,r}}{u_{L,s,r}}\right)^{0.56}\left(1+\frac{A_d}{A_r}\right)^{-1}$	0.149
Choi and Lee [149] [2]	EL-ALR	$\varepsilon_{G,r} = 0.288u_{G,s,r}^{0.504}\left(\frac{A_d}{A_r}\right)^{-0.098}\left(\frac{L_{\text{con}}}{L_d}\right)^{-0.094}$	0.112

[105] and also from CFD models developed for different EL-ALRs [135].

Halfway the riser the instantaneous gas hold-up shows an asymmetric distribution (Figure 2.4a), while the time-averaged gas hold-up (Figure 2.4c) is more symmetrical with high values along the riser axis, indicating an oscillating gas plume. This is also apparent from the velocity plots, with liquid moving back and forth between the sides (Figure 2.4b). Such oscillating behaviour has been observed experimentally in internal-loop airlift reactors [150]. However, by time-averaging these movements cancelled-out and a quasi-symmetric velocity profile was obtained (Figure 2.4d). While the liquid mostly rises, the negative values observed near the riser wall indicate a certain degree of back-mixing, which has also been observed experimentally in ALRs [20, 151]. This internal liquid recirculation contributes to the overall mixing in the riser and creates axial and radial dispersion.

Approaching the gas-liquid separator at the top of the riser, the gas hold-up tends to increase as gas expansion (decreasing hydrostatic pressure) and the wider separator diameter (decreasing the local liquid velocity) increase the gas residence time. This particular section of the reactor could become advantageous for mass transfer because the expected lower CO saturation concentration (due to the lower hydrostatic pressure and a lower CO fraction in the gas) can be compensated by the increase in gas hold-up.

Just above and in the downcomer inlet, high ε_G as well as high liquid flow velocities were predicted. While the liquid flow is directed horizontally and downwards, the bubbles dragged into the downcomer will rise. This causes a sharp separation between gas and liquid and consequently high ε_G. Similar behaviour was found by modelling EL-ALRs with comparable geometry [133, 134, 137]. Degassing geometries might prevent the gas to flow into the downcomer [152]. At the left side of the downcomer, the drag by the liquid and buoyancy of the gas bubbles are in equilibrium and therefore a stable gas hold-up is obtained over time (Figure 2.4c). This corresponds to the second gas entrainment regime [125], wherein the gas bubbles entrained in the downcomer do not reach the bottom and only partially fill the downcomer. Higher local gas hold-up in the downcomer close to the riser wall was also observed in internal-loop airlift reactors [153].

The question emerges on how high the recirculation through the downcomer is in the EL-GLR compared with the internal recirculation in the riser. From the velocity field it was determined that, in this particular reactor geometry, about 14% of the liquid goes down via the downcomer while the rest flows downwards near the riser walls. This indicates that axial mixing in the riser is significant and plug-flow behaviour cannot be assumed for the liquid phase. Although the downcomer appears to be poorly used for the liquid circulation in the studied operation regime, it clearly increases the liquid flow rates in the riser compared to a bubble column (with zero net axial liquid velocity). Such results highlight the added value of CFD predictions as this behaviour could not be predicted with simpler 1D models.

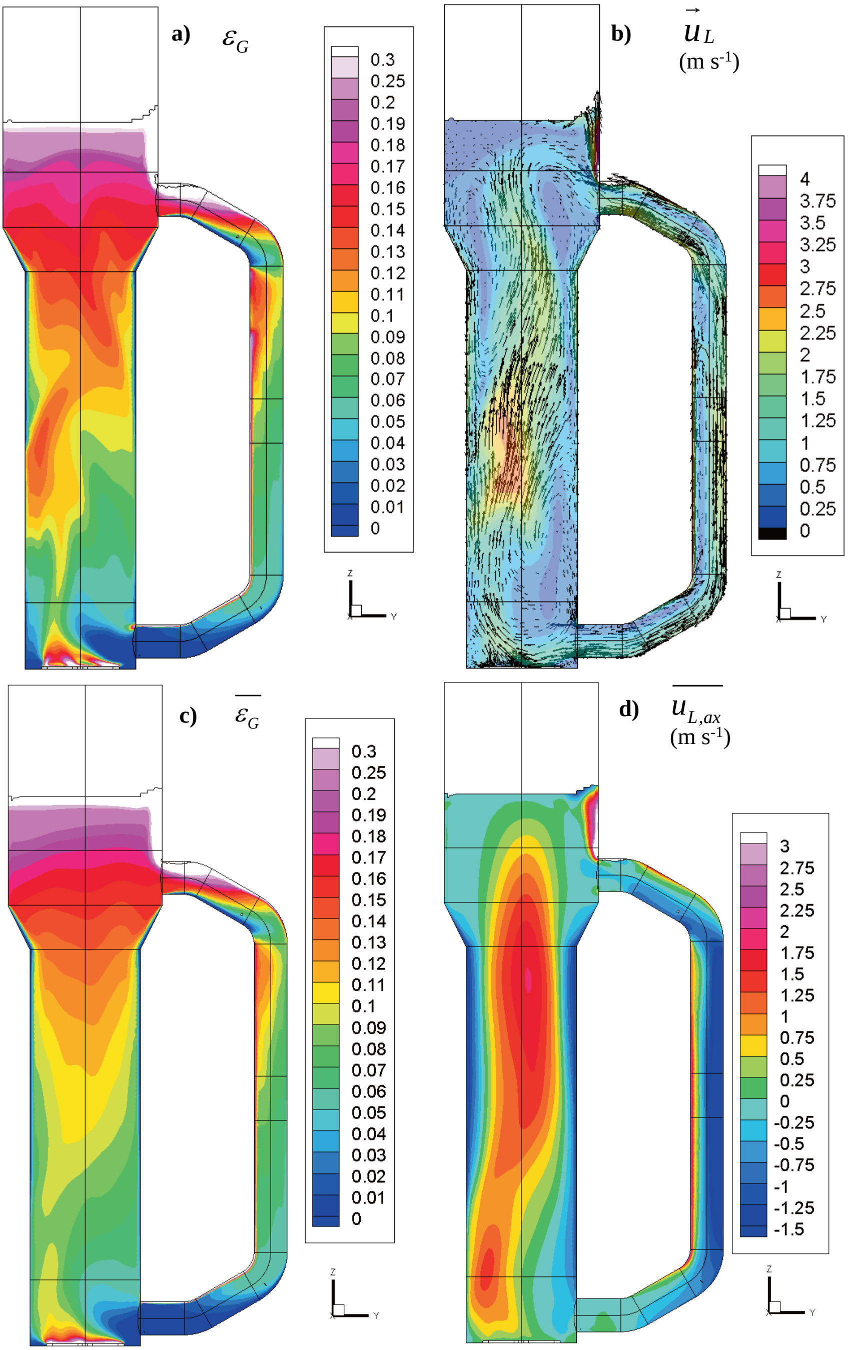

Figure 2.4: Surface plots in the yz-plane ($x = 0$) of the EL-GLR ($u_{G,s} = 0.028\,\mathrm{m\,s^{-1}}$). a), b) gas hold-up and liquid velocity magnitude at a certain moment in time after establishing the flow field ($t = 1100$ s), with arrows indicating the velocity vectors. c), d) gas hold-up and axial liquid velocity averaged over 200 s.

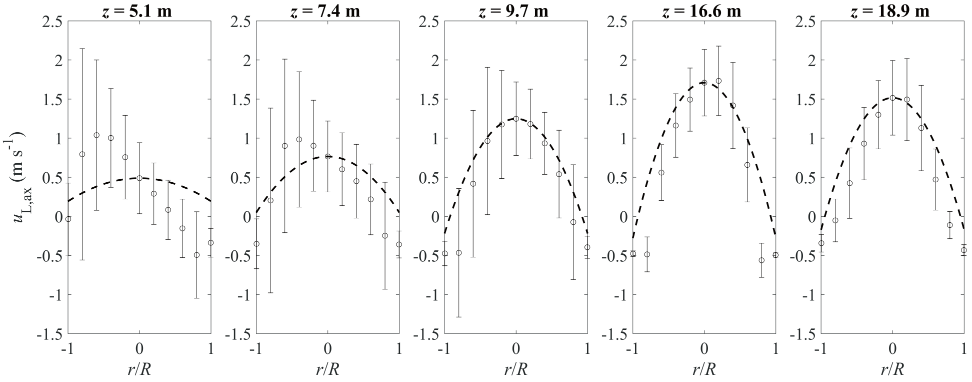

Figure 2.5: Radial profiles for the axial liquid velocity in the EL-GLR (with $u_{G,s} = 0.028\,\mathrm{m\,s^{-1}}$). Open circles: 200 s time-averaged mean velocities; error bars: time-variations observed via the standard deviation; dashed lines: parabolic profile calculated with Equation 2.10.

In the pilot-scale model, a parabolic velocity profile was not observed (Figure 2.2) therefore the large-scale model needed to simulate local axial and radial velocity variations. At several heights in the riser, the profile of axial liquid velocity along the whole riser diameter was calculated over time, then compared with a parabolic profile (Equation 2.10, Figure 2.5) characteristic for BCRs and ALRs [154]. Both parameters of the parabolic profiles, velocity at the riser axis $u_{L,\mathrm{ax}}(r=0)$ and superficial liquid velocity $u_{L,s,\mathrm{ax}}$, were taken from time-averaged CFD results.

$$u_{L,\mathrm{ax}}(r) = \left(u_{L,\mathrm{ax}}(r=0) - u_{L,s,\mathrm{ax}}\right)\left(1 - 2\left(\frac{r}{R}\right)^2\right) + u_{L,s,\mathrm{ax}} \qquad (2.10)$$

At the lower locations (5.1 m and 7.4 m) the liquid velocity profile is skewed towards the left side, due to the liquid entering from the downcomer. However, the liquid velocity profile shifts towards the central axis at higher locations in the riser, where it matches the proposed parabolic profile. It should be noted that there are large time-variations, which should be taken into account when analysing mass transfer in EL-GLRs, for example by time-averaging for 200 s (Figure A.3).

Many phenomena found at pilot-scale were also predicted by the simulations to occur in the large-scale external-loop reactor. Moreover, the predicted overall gas hold-up and liquid flow velocities showed a good match with literature relations. From all these indicators it can be concluded that with a CFD model the large-scale hydrodynamic behaviour can be described properly. With this hydrodynamic model, subsequent calculations on $k_L a$ and MTC will be performed and are discussed in the next section.

2.3.3. Mass transfer

Gas fermentation processes are developed towards a multitude of products, e.g., acids, alcohols, ketones, glycols, aromatics, dienes, esters and terpenes [8]. Although the literature is very scarce on their influence on mass transfer in fermentation broths, it is known that hydrophilic products inhibit bubble coalescence in water, thereby decreasing the Sauter mean bubble diameter (d_{32}) [37], and increasing $k_L a$ [155]. In a pilot-scale bubble column (3 m high, 20 cm width), Keitel and Onken [37] found decreases in d_{32} from 4 to 1 mm and doubling of ε_G from 2 to 4%, for a variety of alcohols. By increasing hydrophobic chain length, stronger effects (i.e., occurring at lower concentrations) were reported, for d_{32}, ε_G, and $k_L a$ [37, 155]. Similar results (<1 mm bubbles and highly increased ε_G) in tall bubble columns were obtained with ethanol [156–159], while Krishna et al. [160] found that the ethanol stabilises the homogeneous flow regime (i.e., bubbly flow at higher $u_{G,s}$).

In ALRs, however, organics increased ε_G up to a modest 30% [161, 162]. The smaller influence of organics on ε_G in ALRs compared to BCRs was explained by, amongst others, the higher velocities of the axial liquid flow [107]. The expected ethanol concentration in the LanzaTech reactor ($50\,\mathrm{g\,L^{-1}}$) [111] is much higher than the minimum concentrations for coalescence inhibition ($1-10\,\mathrm{g\,L^{-1}}$) [37]. Therefore, we can assume a low d_{32} (optimistic scenario: about 1 mm; pessimistic scenario: 3 mm) in the scenario with ethanol, whereas scale-independent d_{32} between 5 and 7 mm are observed in BCRs with air-water mixtures [25, 26, 163]. Likewise, it may be assumed that the produced ethanol could increase the local gas hold-up by at least 30% compared to solutions without ethanol.

Furthermore, temperature dependencies of the physical properties show a significant influence on the mass transfer. By operating at a temperature of 37°C, $k_L a$ is estimated to be around 1.44 times higher than at 20°C [26], mainly due to an increased CO diffusion coefficient (+150%) and decreased liquid kinematic viscosity (-45%). However, the effect of this elevated temperature will be counteracted by a lower CO solubility through its Henry coefficient (-28%), which in turn negatively influences MTC. The net effect of a higher temperature, however, will still be positive.

Thus, for different models describing k_L (Table 2.1), the impact of the bubble diameter (varied between 1 and 7 mm) and the mutual impact of increased hold-up and temperature were examined (Figure 2.6). It was found that with a bubble diameter of 3 mm, most correlations predicted $k_L a$ and MTC lower than those required by the process (Figure A.1), even with an increased hold-up and temperature. However, with 2 mm bubbles, sufficient $k_L a$ and MTC were predicted using the relations from Higbie [127] and Kaštánek [129]. In addition, when including hold-up and temperature effects with 2 mm bubbles, also the relations from Calderbank and Moo-Young [128] and Linek et al. [130] led to adequate $k_L a$ and MTC. If the bubble diameter would be 5 to 7 mm, which is expected for air-water mixtures in industrial BCRs [25, 26], then all correlations predict insufficient $k_L a$ and MTC, causing mass transfer limitations. These values correspond with the values from Table 2.1, stressing the validity of these relations in air-water dispersions.

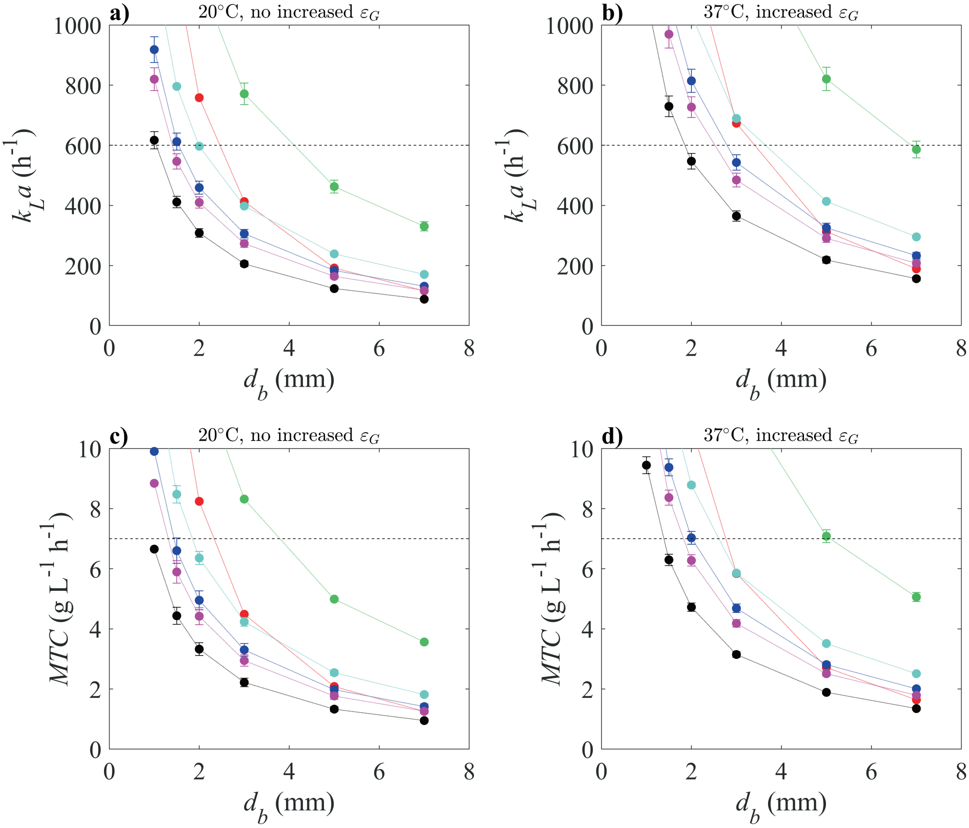

Figure 2.6: $k_L a$ (a, b) and mass transfer capacity MTC (c, d), calculated using different k_L-relations (1 to 6 in Table 2.2) for varying bubble diameters, while considering the effect of produced ethanol on the gas hold-up and the higher temperature (b, d). Red: Higbie [127], cyan: Calderbank and Moo-Young [128], green: Kaštánek [129], blue: Linek et al. [130], magenta: Lamont and Scott [131], black: Kawase and Moo-Young [132]. Error bars: standard deviation during a 200 s period with statistically stationary flow field; Black dashed line: lower value of the estimated range of the industrial process.

From this sensitivity analysis we can conclude that industrial-scale syngas fermentation in the EL-GLR requires small bubble diameters (≤ 2 mm), which should be obtained in combination with a high gas-hold up at 37°C. Ethanol presence promotes these conditions, while in air-water conditions (5 to 7 mm bubbles) the mass transfer limitations would not be alleviated. Therefore, our results indicate that in an industrial syngas fermentation process towards bubble-stabilising products, e.g., ethanol, the typical mass transfer limitations that are present in air-water systems can significantly be alleviated.

It is noted that there are large differences among the $k_L a$ values predicted using the different k_L-relations. The relations based on eddy energy dissipation rate (2.3–2.6) predict lower values than the bubble-based relations (2.1, 2.2). The deviations with relations 2.1 and 2.2 could be due to underestimation of ε by the k-ε turbulence model

[164]. Accounting for this with a scaling factor, based on the overall minimum power input [165, 166], would result in a 22% increase in k_La. Moreover, it has been noted that relation 2.3 has a too high proportionality constant [132] compared to the similar relations 2.4–2.6. Generally, sensitivity analyses with different k_L-relations should be done in future modelling work on gas-liquid mass transfer. Experiments in EL-ALRs could determine which relation describes k_L the best in the specific reactor and how the produced ethanol and the higher temperature would influence the k_La.

In some cases the k_La was predicted to be sufficient, while the MTC was not (e.g., relations 2.5 and 2.6). This indicates that the ideal-mixing assumption (Figure A.1) may not hold and, instead, the *local* values of k_La and solubility should be taken into consideration when computing MTC. Although high k_La values were obtained at certain locations (such as in the separator), the contribution of these volumes to the overall mass transfer rate was found to be low because of the decreased CO saturation concentration (Figure 2.7). However, the high k_La at the reactor top could be beneficial for CO depletion such that the off-gas only contains residual amounts of CO. As LanzaTech patented a method with the aim of, amongst others, increasing mass transfer in the headspace via a so-called ‘showerhead’ [104], it is expected that these local high k_La values at the top of the reactor are indeed required for maximising gas conversion. Although significant CO mass transfer was predicted in the downcomer, when microbial consumption takes place, only marginal transfer is expected as the relative volume of the downcomer is small and as the EL-GLR is operated in the second hydrodynamic regime.

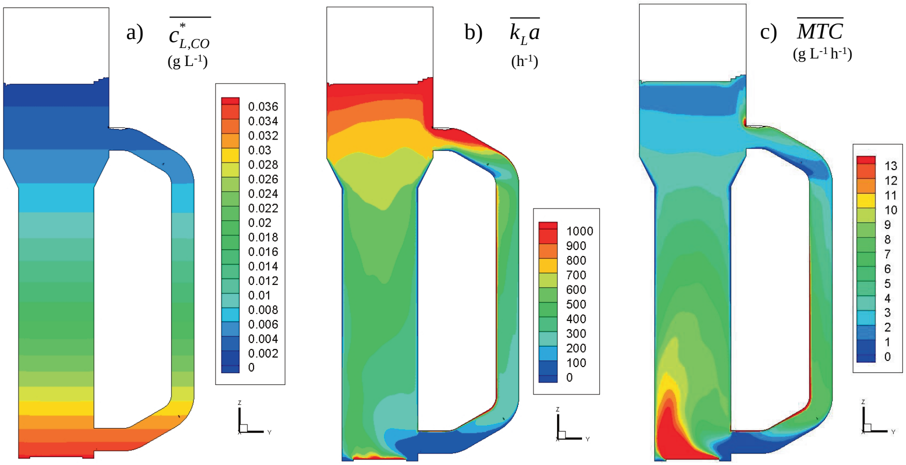

Figure 2.7: Surface plots on the yz-plane of the EL-GLR ($x = 0$), showing 200 s time-averaged values for a) the CO saturation concentration in the liquid, b) the k_La as predicted using the Higbie relation (Equation 2.1, c) the mass transfer capacity, assuming d_b of 3 mm, a 30% increase in gas-hold up compared to water due to the presence of ethanol and a temperature of 37°C.

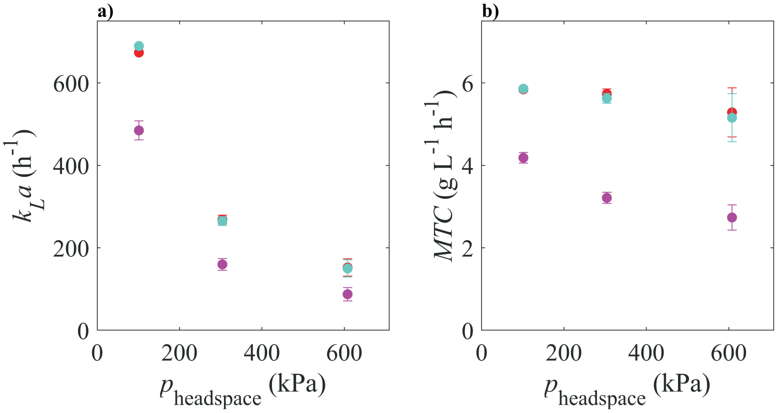

Figure 2.8: Volume-averaged values of a) k_La and b) MTC in the EL-GLR for different headspace pressures, calculated via different k_L-relationships (Table 2.2) assuming d_b of 3 mm, a 30% increase in gas-hold up compared to water due to the presence of ethanol and a temperature of 37°C. Red: Higbie [127], blue: Calderbank and Moo-Young [128], magenta: Lamont and Scott [131]. Bars: standard deviation during a 200 s period with statistically stationary flow field.

High pressure fermentation has been mentioned as a promising strategy to increase the mass transfer rate of poorly soluble gases [113]. Patents indicate that in lab experiments with higher operating pressures (304 and 608 kPa) increased ethanol titre and productivity was obtained [167, 168]. However, in the scientific literature, no beneficial effect was found on the productivity, while *C. ljungdahlii*'s product spectrum shifted from acetate and ethanol towards formate at increased pressures [169]. Inhibitory effects were observed for CO with an inhibition constant of 60 kPa [34], so that increased pressures could decrease the CO consumption rate. The gas saturation concentration increases proportionally with the pressure (Equation 2.7), but the gas hold-up would decrease (ideal gas law) with a constant gas (mass) flow rate. In order to study these opposing phenomena, the effect of increasing the headspace pressure on the k_La and MTC was investigated by running CFD simulations with 304 and 608 kPa headspace pressure.

It was observed that increased headspace pressures decrease the k_La significantly (Figure 2.8). This is due to the decrease in ε_G, which decreased from 0.13 to 0.054 and 0.033, at 304 and 608 kPa respectively. Similar values of MTC at increased pressure were observed when it was calculated using the relations of Higbie [127] and Calderbank and Moo-Young [128], while a slight decrease was observed with the eddy-based equation. Thus, the decrease in ε_G was neutralised by the solubility-increase. One should note that the compressor power requirement [113] increases sharply for increased pressures.

At elevated pressures, one could increase the gas mass flow rate linearly with pressure to obtain a constant superficial gas velocity and thus k_La, without changing the hydrodynamic regime. In our study, the mass flow rate was assumed constant at 2.11 $\text{kg}\,\text{s}^{-1}$, causing decreasing superficial gas velocities and hold-up at elevated pressured. As is it expected that LanzaTech operates six reactors to produce in total 48 kton a^{-1} ethanol (Figure A.1), a higher gas mass flow rate at higher pressures was not likely. If the gas flow rate would be increased proportionally with pressure (to obtain constant $k_L a$), a near-linear relationship between MTC and the compressor power requirement is obtained (Figure A.4), making operating at overpressures an economical choice. Moreover, considering CO-uptake kinetics, with high affinity and inhibiting effect at high dissolved CO concentrations [138], we would not recommend operation at higher pressures.

2.3.4. Outlook

The hydrodynamics and gas-liquid mass transfer in an industrial-scale reactor for the conversion of CO-rich steel-mill off-gases by syngas fermentation were studied by computational fluid dynamics. Simulation results indicated that conditions could be reached for industrially-sufficient specific mass transfer rates ($k_L a$) and mass transfer capacities (MTC). High *MTC* was found possible when the operating temperature is 37°C and by producing ethanol, which inhibits bubble coalescence to maintain relatively small bubbles ($d_b \leq 2$ mm), and increases riser gas hold-up (~30%). We recognise that other factors (e.g., particular medium components or process engineering strategies) might also be deployed to obtain such mass transfer capacities. Since most of the $k_L a$ relations from literature (Table 2.1) were derived in air-water systems, without considering any enhancing effects, further research is needed on the development of mass transfer correlations representing real fermentation conditions. Especially, these relations should consider the presence of bubble-stabilising compounds such as ethanol, acetone, and acetic acid, as well as the presence of salts, antifoam agents and microbial biomass. The addition of fine particles (e.g., kieselguhr, silica) can also increase $k_L a$ substantially [170], possibly by minimising bubble coalescence [171], and could be included in such relations, which are pertinent for the development of more realistic CFD and process models.

The two-phase flow pattern in the large-scale reactor was found to be very dynamic, with large variations in the movement of the gas plume. As the local values of the gas solubility and $k_L a$ determine MTC, the high spatio-temporal resolution that can be obtained via CFD was necessary for predicting the reactor performance and for determination of the main factors influencing mass transfer. Since the main limitation of CFD is its high computational demand, further research should focus on the development of coarse-grained computational models (such as compartment models) to determine $k_L a$ and MTC in a faster way and as function of several variables such as the gas flow rate, media composition (enhancement agents), pressure and reactor scale and geometry.

The strong dynamics of the computed flow patterns in the large-scale reactor will determine the trajectories of microorganisms performing the syngas conversion. Consequently, the microorganisms would experience peaks and valleys in dissolved CO concentrations in an irregular fashion. By implementing CO-uptake kinetics, CO concentration profiles can be obtained for the different operating conditions. Euler-Lagrangian simulations can then reveal what conditions microbes experience over time (*lifelines*) and how that would influence their (dynamic) behaviour [58]. Coupling the flow field with a metabolic model of *C. autoethanogenum* could reveal the influence of these dynamic conditions on the bioprocess performance and (by)product spectrum and guide the development of scale-down simulators and optimised reactor geometries [99].

To develop an optimal bioreactor, spatial homogenization of mass transfer is imperative [111], requiring high $k_L a$ in zones with lower solubility (e.g., separator section) and low $k_L a$ in zones with high solubility (e.g., lower riser section). Controlling the liquid flow rate in the riser, which determines the riser gas hold-up, could be done to fine-tune the local mass transfer capacity. Reducing the liquid backmixing could for example be accomplished by adding internal surfaces, such as perforated plates [20], which would additionally promote local bubble-break up [136], or by increasing the resistance in the downcomer [107, 172] by decreasing its diameter or adding a pump, to force the flow at the optimal rate. By decreasing the liquid flow rate in the riser, the riser gas hold-up can be increased, possibly leading to an increased mass transfer capacity. As this may increase the mixing time [146], one should balance the impact of the mass transfer time with the liquid mixing time when designing large-scale EL-GLRs. Using the downcomer, the liquid velocity and thus the gas velocity and hold-up can be adjusted, which cannot be done in a bubble column. The downcomer can also be used for product removal towards the distillation section, inflow of fresh medium or nutrients, heat transfer, and as source for supplying the showerhead [104].

Alternatively, by positioning the sparger above the downcomer inlet, the gas flow could be better distributed in the riser [105]. In this case, less bubble coalescence is expected as the gas is less likely to be pushed towards the wall opposite to the downcomer. Although the CO solubility is larger in the riser bottom, the higher sparger position would lead to a CO-depleted zone below the sparger, which decreases the overall mass transfer capacity. CFD simulations with a sparger above the downcomer inlet confirm a 4-6% decrease in MTC, due to the low gas hold-up below the sparger (Figure A.5, Table A.6). Further research on the sparger position and how the downcomer (and its position) influence bubble coalescence in ethanol-rich media could be helpful for designing industrial-scale EL-GLRs with higher productivity.

In this study, all the CO transferred to the liquid phase was assumed to be instantaneously consumed by the microbes. In practice, there will be CO dissolved in the liquid phase, thus decreasing the driving force for mass transfer. The dissolved CO concentration is determined not only by the local flow conditions and mass transfer rates, but also by the local microbial CO uptake rate, governed by the uptake kinetics (especially the affinity). The literature is very scarce on studies of CO uptake kinetics by *Clostridia* (e.g., [34]). Detailed CO uptake kinetics using dissolved CO concentration measurements should be developed with priority.

Many authors [2, 22, 110] explain the low mass transfer capacity obtained in syngas fermentation partly by the low solubility of CO. Solubility can also be affected by the ethanol fraction in the solution, and this effect has been mostly studied for O_2 dissolution. Shchukarev and Tolmacheva [173] determined little impact of ethanol on the O_2 solubility in the water-ethanol mixture for ethanol mole fractions below 0.2. Therefore, it is not expected that the CO solubility would be affected by the produced ethanol in the studied reactor conditions ($50\,\mathrm{g\,L^{-1}}$ ethanol or mole fraction ~0.02 [111]). Since O_2 and CO have comparable Henry coefficients at 37°C (9.6×10^{-6} and $8.2\times10^{-6}\,\mathrm{mol\,m^{-3}\,Pa^{-1}}$, respectively [144] and the CO fraction in syngas is often higher than the O_2 fraction in air, we argue that the challenges that have to be addressed in aeration processes should be faced in syngas fermentation as well. Instead of attributing the poor performance to the solubility, research should focus on ways to enhance $k_L a$ in the bioreactor, e.g., by the presence of organic products.

Promising processes for the conversion of syngas towards other products, such as fatty acids [7], acetone, iso-propanol and 2,3-butanediol [8] have been developed. For successful commercialisation of such processes, one could benefit a lot if the produced products are mass transfer-enhancing, like ethanol, or even better.

2.4. Conclusion

With a CFD model, which was validated using published data from a pilot-scale reactor, we investigated the hydrodynamics of a large-scale external-loop gas-lift reactor. With this model, the gas-liquid mass transfer was studied for an industrial CO-to-ethanol fermentation process. Several relations describing the mass transfer coefficient were evaluated and $k_L a$ and mass transfer capacity were computed for varying process conditions.

At an operating temperature of 37°C, with increased gas hold-up compared to air-water and smaller bubbles (≤ 2 mm instead of 5 to 7 mm), most available mass transfer relations predicted sufficient $k_L a$ and MTC for an industrially viable syngas fermentation process, in line with data published by LanzaTech. We argue that this is possible since the produced ethanol inhibits bubble coalescence, causing smaller bubbles and increased gas hold-up. This indicates that typical mass transfer limitations encountered in air-water systems can be alleviated under industrial syngas fermentation conditions.

In spite of being computationally intensive, CFD can also be used for determining high-resolution process conditions that could not be accurately computed using simpler models. The developed hydrodynamic and mass transfer model can be used to advance research into reactor design for industrial syngas fermentation, for determination of the microbial response in such reactors using Euler-Lagrange modelling, and the development of scale-down simulators operated in a representative window.

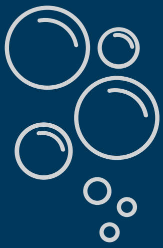

Chapter 3

The impact of broth components on mass transfer

Scientific theories are never fully justifiable or verifiable, but are testable

Karl Popper

This chapter has been published as:
Puiman, L.*, Elisiário, M. P.*, Crasborn, L. M., Wagenaar, L. E., Straathof, A. J., & Haringa, C. (2022). Gas mass transfer in syngas fermentation broths is enhanced by ethanol. *Biochemical Engineering Journal*, 185, 108505.
* These authors contributed equally to this work.

Abstract

In gas fermentations (using O_2, CO, H_2S, CH_4 or CO_2), gas-to-liquid mass transfer is often regarded as one of the limiting processes. However, it is widely known that components in fermentation broths (e.g., salts, biomass, proteins, antifoam, and organic products such as alcohols and acids) have tremendous impact on the volumetric mass transfer coefficient k_La. We studied the influence of ethanol on mass transfer in three fermentation broths derived from syngas fermentation. In demineralized water, we observed that the addition of ethanol, the expected product, increased k_La two-fold in the $0 - 5\,\mathrm{g\,L^{-1}\,h^{-1}}$ range, after which near-constant k_La values were obtained. In the fermentation broths, k_La was increased significantly (2 – 4 fold compared to water) by ethanol supplementation, and to be highly influenced by broth salinity. Our results indicate that k_La is a dynamic parameter in gas fermentation experiments and can be significantly increased due to broth components.

Graphical abstract

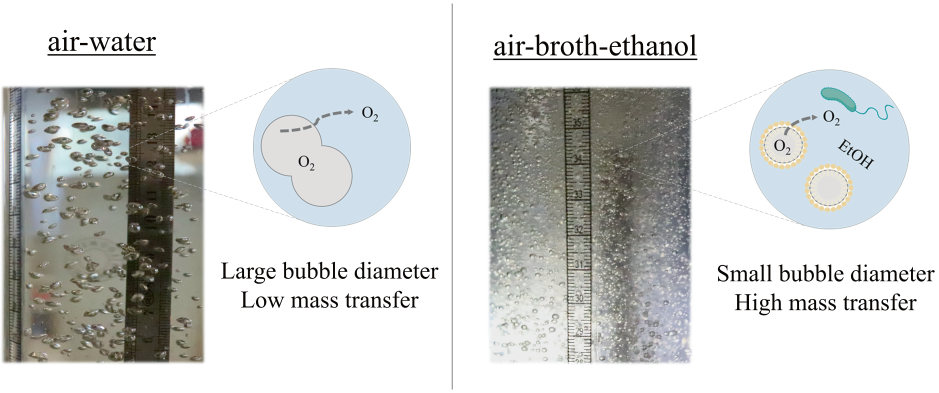
air-water
O_2
O_2
Large bubble diameter
Low mass transfer
air-broth-ethanol
O_2
O_2
EtOH
Small bubble diameter
High mass transfer

3.1. Introduction

Many fermentations with gaseous substrates (e.g., O_2, CO, H_2S, CO_2, CH_4) are considered as promising conversion processes for a multitude of useful products (e.g., succinic acid, ethanol, butanol, hexanoic acid, lactic acid) [103, 174, 175], of which several are established in industrial practice [8, 28]. For many of these processes, poor gas-to-liquid mass transfer and low dissolved gas concentrations have been identified as a limiting factor [22, 25, 176, 177]. Based upon that, a lot of research, for example in syngas fermentation, is focused on increasing the volumetric mass transfer coefficient ($k_L a$) by developing innovative reactor configurations [22, 23, 178]. Understanding of the $k_L a$ values obtained is essential in the gas fermentation field.

For a long time, it has been known that medium components and products (such as salts, acids, alcohols, surfactants, biomass and antifoam) can significantly affect $k_L a$ [155, 179–182]. For a broad range of alcohols in water, a fivefold increase in $k_L a$ was observed in a narrow concentration range [155], which was explained by a decrease in Sauter mean bubble diameter (d_{32}) (from 4 to 1 mm) and a twofold increase in the gas hold-up (ε_G) [37]. The presence of alcohol decreases the surface tension and stabilises low-diameter gas bubbles, leading to repulsions and thereby inhibiting coalescence [37, 157]. Similar effects on mass transfer were not only observed for alcohols, but also for organic acids, ketones and compounds like lactic acid [37, 182, 183]. Changes in the gas solubility at alcohol concentrations relevant for gas fermentations were, however, expected to be negligible [173].

Similar effects have been noticed for electrolytes. Lessard and Zieminski [180] observed significant coalescence inhibition (more than 90%) for different salt solutions with ionic strength above $0.3\,\mathrm{mol\,L^{-1}}$, resulting in increases in $k_L a$ values [155]. The presence of biomass, however, may decrease $k_L a$ by absorption to the bubble surface (the so-called "blocking effect"), as well as by increasing the viscosity, which stimulates coalescence [179] and reduces the diffusion coefficient [143]. Dissolved proteins are known to improve mass transfer as they stabilise bubbles and prevent coalescence [181]. Furthermore, in air-water systems, the mass transfer coefficient (k_L) is known to be, amongst others, a function of the bubble diameter: Small bubbles (d_b around 1 mm) have a rigid surface with a k_L around $1 \times 10^{-4}\,\mathrm{m\,s^{-1}}$, while larger bubbles ($d_b > 2$ mm) have a mobile surface and k_L between 3 and $5 \times 10^{-4}\,\mathrm{m\,s^{-1}}$ [26].

Typically, biomass, salts, proteins, products, and substrates are jointly present in fermentation broth, and might change the medium physical properties (i.e., surface tension, viscosity, density) with respect to pure water. Some empirical relations (Table B.1) predict the influence of these properties on $k_L a$ [25, 118–122]. As these relations have been developed using air-water mixtures without taking into account biomass and salts concentrations, their validity for fermentation broths remains unclear.

The aforementioned studies on mass transfer mostly focus on mixtures with water and one compound of interest, while the joint influence of different compounds has hardly been studied. Studies with fermentation broths have only been performed to characterise the effect of the biomass concentration on k_La [179] and on d_{32} [184]. In wastewater technology, however, it is common to measure aeration performance in process water (with contaminants and biomass sludge), which is often characterised with the alpha-factor, which relates the k_La in process water with clean water [185]. Analyses on the joint influence of broth components in gas fermentations on mass transfer are lacking in the scientific literature, making it challenging to estimate. Knowledge on the most influential parameters and their respective ranges would be essential for accurate prediction in real fermentation broths, both during experiments and modelling. With the growing interest in fermentation and bioprocess design, understanding on the most influential parameters and their respective ranges would be essential for accurate k_La prediction.

In this study, we aim to determine mass transfer characteristics (k_La, d_{32}, ε_G, k_L) in different fermentation broths to show that there are complex interactions between the compounds present and that this has significant consequences in gas fermentation processes. Syngas fermentation is used as an example of a gas fermentation process, as it is a frequently studied process wherein mass transfer is often mentioned as a factor for poor performance [22, 23]. For safety and analytical reasons, oxygen mass transfer is studied, but the same trends are expected for other gases that also have a very low solubility in water, such as CO, H_2S, and CH_4. The very low concentration of dissolved O_2 is expected not to change k_La, d_{32}, ε_G, or k_L. The investigated product is ethanol, since it is a major product in the commercialised syngas fermentation process [10]. First, we will determine the range wherein ethanol addition affects k_La. After that, we will study the influence of ethanol on the mass transfer characteristics in five mixtures (water, fermentation medium, and three syngas fermentation broths). The experimentally obtained k_La values will be compared with k_La values from published empirical relations, after determining the physical properties of the mixtures.

3.2. Materials and methods

Influence of ethanol concentration on $k_L a$

$k_L a$ was determined in water-ethanol solutions using the dynamic absorption method [25] in a 1.5 L temperature-controlled stirred tank reactor (STR) with 1 L working volume (Applikon Biotechnology, the Netherlands). After desaturation with pure nitrogen, dissolved oxygen (DO) was measured every second with an AppliSens Dissolved Oxygen probe (Applikon Biotechnology, the Netherlands) while supplying 1 vvm of air at 800 rpm stirring rate. Experiments were performed at 20 °C and 37 °C and at least in threefold for all demineralized water-ethanol mixtures (with 0, 2.5, 5, 10, 15, 25 and 50 $\mathrm{g\,L^{-1}}$).

Mass transfer characteristics of different mixtures

Several mixtures were tested in a bubble column reactor (BCR): demineralized water, mineral fermentation medium ("medium"), and three fermentation broths derived from syngas fermentation experiments (e.g., "broth-1"). A BCR was used since it enables more detailed analyses on d_b and ε_G than a STR does. The influence of ethanol on the mass transfer characteristics was determined by supplementing with the industrially obtained ethanol concentration (50 $\mathrm{g\,L^{-1}}$) [111], after experiments without supplemented ethanol. The Supplementary material provides the composition of the mineral fermentation medium as well as the media and methods for cultivation of the fermentation broths (Table B.2).

Mass transfer characteristics of the different mixtures were determined in a lab-scale glass bubble column (7 cm internal diameter, 70 cm liquid height) with a multi-orifice sparger (0.6 mm orifice diameter). Experiments were performed with air at a low superficial gas flow velocity of 1.8 $\mathrm{mm\,s^{-1}}$ to ensure that flow was homogeneous and that the individual bubbles could be pictured for bubble size determination. The liquid temperature was kept at 37 °C. Gas hold-up was determined by measuring the ratio between aerated and unaerated volumes [156] using a ruler at the column wall. $k_L a$ was determined using the same method as described above, with the oxygen probe located 42 cm above the sparger, at least in triplicate for each mixture.

The bubble size was analysed using two methods, one for the small bubbles in mixtures with supplemented ethanol and another for larger bubbles in the mixtures without ethanol. During aeration, pictures of the small bubbles were made with a photo-optical endoscopic probe (SOPAT-VF GX 2750) (SOPAT, Germany) with the focal plane at 0.5 mm, located 47 cm above the sparger. From 600 images, between 100 and 1400 bubbles (depending on the mixture) were captured with the Hough circle detection method in the Python OpenCV package, and their diameters were calculated using a camera-specific pixel-to-mm conversion factor. As these bubbles were spherical, the Sauter mean bubble diameter d_{32} was calculated using Equation 3.1, in which $V_{b,i}$ is the volume of bubble i, $A_{b,i}$ its surface area and $d_{b,i}$ its diameter.

$$d_{32} = 6\frac{\sum_i V_{b,i}}{\sum_i A_{b,i}} = 6\frac{\frac{4}{3}\pi \sum_i \left(\frac{1}{2}d_{b,i}\right)^3}{4\pi \sum_i \left(\frac{1}{2}d_{b,i}\right)^2} \tag{3.1}$$

To obtain the (equivalent) diameter of the larger bubbles, pictures were made with a CANON EOS 200D camera. A metal ruler was placed inside the column to decrease the influence of light refraction and to obtain a pixel-to-mm ratio. With image analysis software (ImageJ) d_b was measured for spherical bubbles, and for spheroidal bubbles the radii of the semi-major r_a and semi-minor axes r_c were measured to determine their eccentricity e and equivalent diameter d_{eq} of bubble i (Equation 3.2). Subsequently, d_{32} was calculated with the obtained (equivalent) diameters of the spherical and spheroidal bubbles using Equation 3.1. The two bubble size determination methods were cross-validated using broth-4, see Figure B.1 and Table B.3.

$$d_{\mathrm{eq},i} = 6\frac{V_{b,i}}{A_{b,i}} = 6\frac{\frac{4}{3}\pi r_a^2 r_c}{2\pi r_a^2 + \pi\frac{r_c^2}{e}\ln\left(\frac{1+e}{1-e}\right)} \text{ with } e = \sqrt{1-\frac{r_c^2}{r_a^2}} \tag{3.2}$$

After determining d_{32}, $k_L a$ and ε_G, Equation 3.3 was used to calculate k_L.

$$k_L = \frac{k_L a}{a} \text{ with } a = \frac{6\varepsilon_G}{d_{32}} \tag{3.3}$$

The standard deviation σ of k_L was evaluated using classical error propagation (Equation 3.4). The unpaired t-test with Welch's correction was used to determine statistical significance for all mass transfer characteristics.

$$\sigma_{k_L} = k_L\sqrt{\frac{\sigma_{k_L a}^2}{k_L a} + \frac{\sigma_a^2}{a}} \text{ with } \sigma_a = a\sqrt{\frac{\sigma_{\varepsilon_G}^2}{\varepsilon_G} + \frac{\sigma_{d_b}^2}{d_{32}}} \tag{3.4}$$

Determination of mixture properties

After aeration in the BCR, the mixtures' physical properties were determined at 37 °C. Density was measured with a benchtop density meter (DMA 5000, Anton Paar, Austria). The dynamic viscosity was determined with a Haake Viscotester 500 (Thermo Fisher Scientific, US) with NV sensor system. Dynamic surface tension was measured using a BPT Mobile tensiometer (KRÜSS Scientific, Germany), at least in duplicate.

The biomass concentration for fermentation broth-2, broth-3 and broth-4 was measured by determination of volatile suspended solids (VSS) concentration in the broth, from 150 mL broth samples [186]. For broth-1, the biomass concentration was obtained by measuring its optical density at 660 nm (OD_{660}). This was converted to VSS concentration using calibration curves previously obtained during cultivation. Acetate and ethanol concentrations in filtered broth samples (0.22 µm pore size, Millipore, Millex-GV, Ireland) were determined using ultra high performance liquid chromatography (UPLC) with an Aminex HPX-87H column (BioRad, United States) at 50 °C coupled to a refractive index

(RI) detector RefractoMax 520 (Thermo Fisher Scientific, US), using 1.5 $\mathrm{mmol\,L^{-1}}$ aqueous phosphoric acid as eluent. Lastly, protein concentrations were determined with the Pierce™ BCA Protein Assay Kit (Thermo Fisher Scientific, US) according to the manufacturer recommendations. From the cultivation media composition (Table B.2), ionic strength I was calculated (Equation 3.5), from each ion concentration c and charge z.

$$I = \frac{1}{2}\sum_i c_i z_i^2 \tag{3.5}$$

3.3. Results and discussion

In this section, we will first present the influence of the concentration of ethanol in water on the $k_L a$, which was determined in a stirred tank reactor (section 3.3.1). After that, detailed results for the different mixtures in a bubble column reactor will be presented (section 3.3.2), which will be followed by a discussion on k_L for fermentation broths (section 3.3.3). Lastly, a comparison with empirical correlations (sections 3.3.4) will be performed with the determined physical properties.

3.3.1. Influence of ethanol on $k_L a$

The influence of the ethanol concentration in water on $k_L a$ has been determined in a stirred tank (Figure 3.1). Sharp increases in $k_L a$ values were observed in the lower concentration range, until a plateau was reached (between 5 – 10 g L^{-1}, independent from the temperature). For both temperatures, the maximum $k_L a$ value was about twice as large as it would be without ethanol. Visually, we observed a significant reduction in bubble size upon the addition of ethanol, explaining the increased $k_L a$ value (Figure B.4.

The $k_L a$ value increases roughly 40% between 20 and 37°C, which corresponds with predictions for this temperature-increase [26, 117]. The results obtained for these two temperatures indicate that the temperature-increase and the ethanol addition most likely show an independent influence on $k_L a$. This temperature increase predominantly causes an increase in k_L (by increasing the diffusion coefficient, and reducing the kinematic viscosity [142, 143]).

In STRs with added ethanol, similar increases in $k_L a$ have been observed before [187], but not with such a clear plateau formation. The plateau formation in $k_L a$ has been observed for other organic compounds in STRs [155], and has been explained by the constant bubble diameter beyond a certain concentration range [37]. Similar results on plateau formation have been seen in a plunging jet contactor with propanol [188] and in an external-loop airlift reactor with methanol, ethanol and propanol [189].

The ethanol concentration range in which the steep change in $k_L a$ values was observed (0 – 5 g L^{-1}) corresponds to the range of ethanol titres achieved in lab-scale syngas fermentation experiments, for example [17, 22, 90]. The rapid ethanol concentration change within this range indicates that $k_L a$ is not a constant but a dynamic parameter during gas fermentation processes. For example, during batch operation, different values of $k_L a$ may apply. Moreover, we recommend to obtain $k_L a$ values using representative fermentation conditions rather than using water, to compare reactor configurations [178, 190] or to determine dissolved gas concentrations [191].

Consequently, we expect that $k_L a$ differs between fermentation broths derived from syngas fermentation experiments and synthetic aqueous solutions containing some broth solutes. As more detailed analyses on d_b and ε_G can be performed in BCRs, we will use BCRs in the upcoming sections. Due to the plateau formation by ethanol addition, we will perform experiments with the expected industrial c_{EtOH} of 50 g L^{-1} [111].

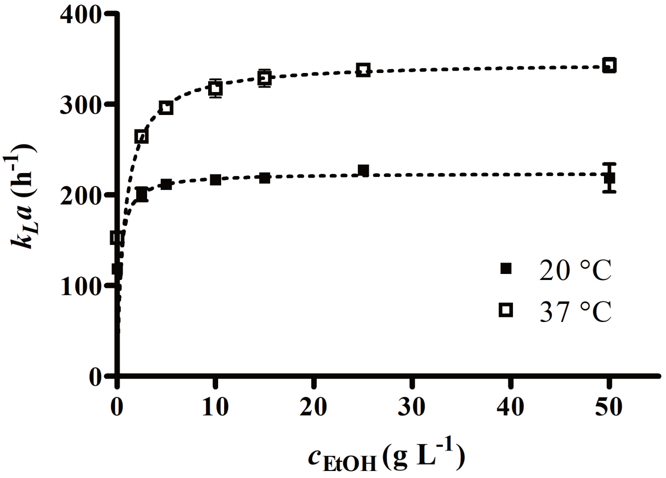

Figure 3.1: Influence of the ethanol concentration on k_La, data obtained at 20 °C (filled squares) and 37 °C (open squares) in the stirred tank. Error bars: standard deviations from triplicates.

Table 3.1: Physical properties of the different mixtures that were analysed in this study. All properties were measured at 37 °C. Provided are the liquid-phase density (ρ_L), liquid-phase viscosity (η_L), surface tension (σ), ionic strength (I), and the concentrations of biomass (c_X), proteins (c_{prot}), total acetic acid (c_{AcT}), and ethanol (c_{EtOH}) of each mixture.

	ρ_L kgm^{-3}	η_L mPas	σ mNm^{-1}	I molL^{-1}	c_X gL^{-1}	c_{prot} gL^{-1}	c_{AcT} gL^{-1}	c_{EtOH} gL^{-1}
Water	992.91	0.768	69.02	N/A	N/A	N/A	0	0.00
Mineral medium	996.28	0.768	68.62	0.296	N/A	N/A	0	0.00
Broth-1	997.97	0.821	70.43	0.296	0.061	0.369	1.14	0.00
Broth-2	997.62	0.732	68.82	0.171	0.246	1.278	2.22	0.18
Broth-3	996.60	0.763	69.08	0.136	0.087	0.062	1.37	0.12
Water + 5% ethanol	984.36	0.827	52.20	N/A	N/A	N/A	0	49.20
Mineral medium + 5% ethanol	986.63	0.825	51.49	0.277	N/A	N/A	0	49.20
Broth-1 + 5% ethanol	989.28	0.815	51.66	0.277	0.057	0.345	1.07	49.20
Broth-2 + 5% ethanol	988.06	0.840	51.83	0.160	0.230	1.196	2.07	49.37
Broth-3 + 5% ethanol	987.93	0.759	51.76	0.127	0.082	0.058	1.28	49.32

3.3.2. k_La determination in different mixtures with ethanol

The determined physical properties of the mixtures are shown in Table 3.1. As the fermentation broths contain only little amounts of ethanol, we supplemented the mixtures with ethanol to reach the industrially relevant concentration (50 gL^{-1}). A clear decrease in surface tension occurs upon supplementation of ethanol. Broth-4 was not included in the table as there was possible interference with the reducing agent during the k_La-

determination (see section 3.3.5), such that the $k_L a$ and k_L values could not be predicted reliably.

For all other mixtures, a significant increase in $k_L a$ is observed (Figure 3.2a) upon the addition of ethanol ($p = 0.038$). In water, a sixfold higher $k_L a$ is encountered after adding ethanol. Such increases have been obtained before with ethanol [155, 158]. This is explained by the decrease in d_{32} (from 2.7 mm to 0.7 mm) and the doubling of the gas hold-up due to the addition of ethanol.

The mineral medium and broth-1 show an increased $k_L a$ compared to the demineralized water. This might be due to their high ionic strength (0.3 $\mathrm{mol\,L^{-1}}$, Table 3.1) since little coalescence was expected when ionic strength is above 0.2 $\mathrm{mol\,L^{-1}}$ [180]. This suggests that $k_L a$ might easily be increased in fermentation broths by increasing ionic strength by slightly changing the mineral medium composition.

Although ethanol decreases the bubble size and makes the bubbles more spherical and rigid (Figure B.3), the beneficial effect of ethanol on $k_L a$ is less pronounced in the mineral medium than in pure water. This lower increase in $k_L a$ can be attributed to a decrease in k_L, which might be due to unresolved complex interactions between salts and ethanol in the boundary layers.

For all fermentation broths, $k_L a$ is observed to be lower than in the mineral medium. As d_{32} and ε_G remain similar in broth-1 and broth-2, the decrease in $k_L a$ is attributed to a decrease in k_L (see section 3.3.3), resulting in broth-2 and broth-3 having a similar $k_L a$ as water (without ethanol). Hence, the presence of biomass in these broths seems to diminish the beneficial effects of salts on $k_L a$. Supplemented ethanol causes a decrease in d_{32}, but the net increase in $k_L a$ is less pronounced than for the mineral medium. Still, the $k_L a$ values in the ethanol-rich broths are two to four times larger than the value in water without ethanol, indicating that the mass transfer properties of these broths can neither be represented by those of pure water, nor by those of water with added ethanol only.

In all cases with ethanol, a significant decrease in bubble diameter is observed ($p = 0.023$), as well as a narrower bubble size distribution by analysing the standard deviations (Figure 3.2b) and the bubble size distribution plots (Figure B.4). This confirms that ethanol stabilises the homogeneous flow regime [156, 160], while the coalescence inhibition causes a hold-up increase (Figure 3.2c) [157].

In the mineral medium and fermentation broths, d_{32} does not change much, except for some decrease with broth-3. This implies that the biomass, acetate and proteins have little effect on the bubble size at the observed concentrations. Broth-3 also shows a remarkably low d_{32} without ethanol, compared to the other mixtures. This effect cannot be explained, because more data are required to achieve correlation to the physical properties or the concentration of components.

The addition of ethanol significantly ($p = 0.0003$) increases the gas hold-up for all media (Figure 3.2c). Increases in gas hold-up have been explained by coalescence inhibition:

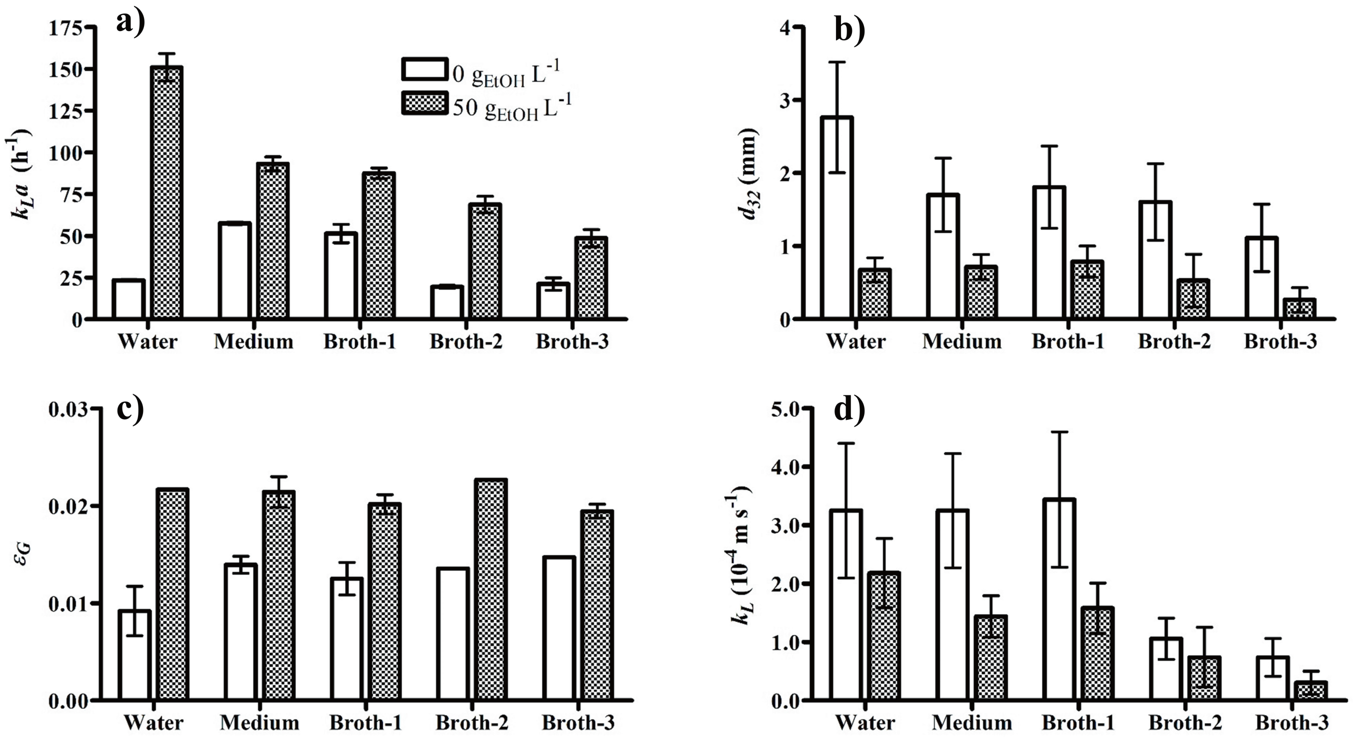

Figure 3.2: Mass transfer characteristics obtained in a bubble column ($u_{G,s}$ = 1.8 mm s^{-1}) for different mixtures (see Table 1) without (white bars) and with supplemented ethanol (patterned bars). a) Volumetric mass transfer coefficient k_La, b) Sauter mean bubble diameter d_{32}, c) gas hold-up ε_G, and d) mass transfer coefficient k_L. Error bars: standard deviations between at least three measurements.

smaller bubbles rise slower, thereby increasing the gas residence time in the reactor and thus the hold-up [157]. The same applies for the mineral medium and broths: salts and surface-active compounds decrease d_{32} by inhibiting coalescence and thus increase the hold-up. For more details about the underlying mechanisms, one is referred to Keitel and Onken [37] and Jamialahmadi and Müller-Steinhagen [157].

The obtained data hint at a decrease in k_L due to supplemented ethanol (Figure 3.2d), but this was not statistically significant ($p = 0.10$). A decrease would be explained by an ethanol layer causing extra mass transfer resistance around the gas bubble, or by increasing surface rigidity due to the small and spherical bubbles.

3.3.3. k_L as function of biomass concentration

From the different mixtures, it was observed that the fermentation broths have a lower k_L than water. This weakly correlates (Pearson's r = -0.57) with the biomass concentration in the broth (Figure 3.3). It has been argued [25] that biomass increases broth viscosity and thus decreases k_L. However, the viscosities of the measured samples are in such a narrow range that a viscosity-based k_L-model cannot adequately describe these changes [131] (Figure B.5). Any such reduction might be explained by a bubble surface blocking effect of the biomass, creating additional mass transfer resistance, even though direct oxygen consumption was not expected for syngas fermenting bacteria [25]. We expect that there are complex interactions between the (type of) microbe, salts and nutrients in the medium, and the products that influence the value of k_L. Unfortunately, at this moment, we are not able to provide general guidelines for prediction of k_L in fermentation broths without further experiments.

3.3.4. Comparison with empirical correlations

Empirical relations (Table B.1) are often used for the prediction of k_La in bubble column fermentations [25]. After determining surface tension, density and viscosity for all the different media (with and without ethanol) (Table 3.1), the k_La values were calculated using these equations (Figure 3.4). However, a large discrepancy is visible between the experimental and predicted values. These relations systematically underestimate k_La since they do not consider the influence of biomass, the salts and ethanol on the bubble properties. For example, the decrease in surface tension by ethanol has a smaller influence on k_La in the empirical relations than observed in our experiments. As we saw that variables such as ionic strength, ethanol and biomass concentration are important regarding mass transfer in fermentation broths, these variables should also be part of such relationships.

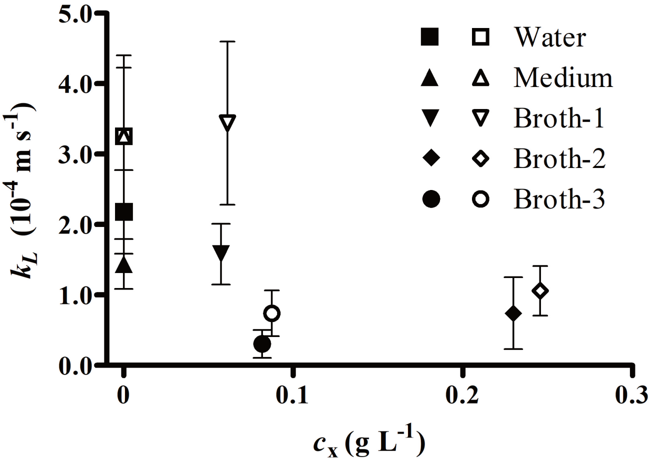

Figure 3.3: Mass transfer coefficient k_L for different values of the biomass concentration in the studied mixtures. Open symbols: mixtures without ethanol, filled: mixtures with 50 g L^{-1} ethanol. Error bars: standard deviations.

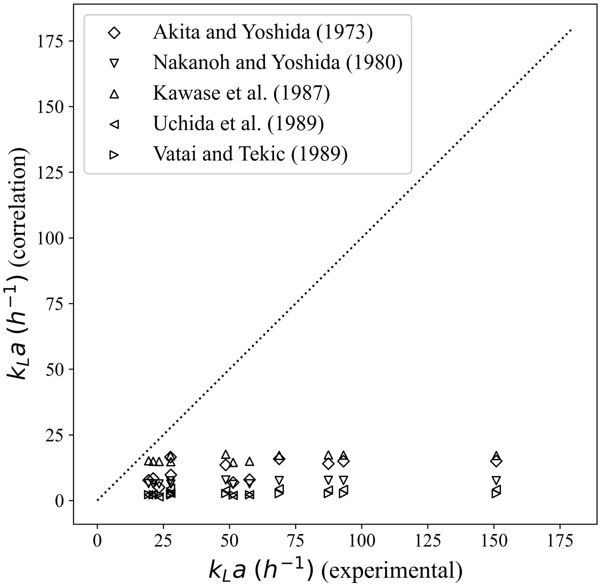

Figure 3.4: Parity plot of experimental k_La data in the different mixtures vs. the values calculated using empirical relations: Akita and Yoshida [118], Nakanoh and Yoshida [119], Kawase et al. [120], Uchida et al. [121], Vatai and Tekić [122].

3.3.5. Implications and future studies

This study shows several mass transfer characteristics obtained in different liquid mixtures relevant for gas fermentations. The obtained results show that the influence of medium components is significant and should be considered in future experimental and modelling work in gas fermentations. Our results are highly applicable to (industrial) practitioners of gas fermentation experiments as these can be beneficial for accurate determination of $k_L a$ and provides means to increase the $k_L a$ value by tuning medium composition.

Although it is widely known that antifoam promotes coalescence [25, 181] and decreases mass transfer by creating a monolayer around the bubbles [192], and that dissolved solids (e.g., silica) can both improve and worsen mass transfer (depending on the concentration) [170], we did not consider their presence. Furthermore, only one mass transfer enhancing agent was studied (ethanol) for only one type of gas fermentation broths (derived from syngas) with a limited range of biomass concentrations ($0 - 0.5\,\mathrm{g\,L^{-1}}$).

To reduce the redox potential, which is required for anaerobic (syngas) fermentation, a reducing agent was added to the fermentation broths (Table B.2). Reaction of oxygen and the reducing agent (sodium sulphide) might have disturbed the dynamic absorption method for $k_L a$ determination (for broth-4), such that this broth had to be left out from the aforementioned evaluation. In such a case the method might be adapted to, for example, the method proposed by Bandyopadhyay et al. [193]. Future studies should also note that the dynamic absorption method for $k_L a$ determination has low validity at high power inputs ($P/V > 1000\,\mathrm{W\,m^{-3}}$ [194]. Considering that in air-water systems P/V is a critical variable determining the $k_L a$ value [25, 195], further research should be done to determine the influence of P/V in cases with ethanol. Therefore the influence of variable superficial gas velocities (in BCRs and STRs) and stirrer speeds could be studied (STRs).

Industrial syngas fermentation requires higher biomass concentrations (around $10\,\mathrm{g\,L^{-1}}$) [32] than the concentrations achieved in our experiments. Such high biomass concentrations are expected to influence the broth viscosity and thus the k_L. Furthermore, the used bubble column (7 cm diameter) is not representative for an industrial fermentation. To represent a large-scale bubble column, the column diameter should be more than 15 cm to exclude wall effects for mild viscous liquids [196]. For an industrial-scale syngas fermentation, a significantly higher gas flow velocity can be expected. We noted by using such gas velocities in this column, determination of d_{32} in media without ethanol would be challenging due to the regime change to slug flow. To prevent slugs, we decided to compare d_{32} and $k_L a$ at low gas flow velocities. In literature, at higher gas flow rates and in wider and higher columns, the beneficial effect of ethanol on gas hold-up [156, 160] and $k_L a$ has been observed [189]. Therefore, we think that the phenomena reported in this paper will also be present in large-scale reactors.

Our research indicates that other aspects of broth composition (next to ethanol content) influence mass transfer that is currently not well understood. Further research is needed to quantitatively predict the relevant parameters (e.g., k_L, d_{32}) in order to develop more realistic mass transfer models for fermentations. Although the exact mechanism might remain unknown, systematic experiments and technologies like machine learning might be used to develop algorithms for reliable prediction of mass transfer properties in fermentation broths of various compositions. Unravelling the mechanisms behind our observations (e.g., why k_La is lower in the mixture with mineral medium and ethanol compared to the water-ethanol mixture) will require additional and more fundamental studies, which could guide the development of mechanistic models.

Although our results were only obtained with supplemented ethanol, we stress that similar phenomena have been obtained with other compounds (longer alcohols, acids, ketones) [37, 155, 182]. This indicates that similar deviations in mass transfer characteristics can be expected in a wide range of gas fermentations [174], e.g., syngas fermentation (to alcohols/acids), microbial electrosynthesis (to acids) [176] as well as aerobic sugar-based fermentations (e.g., 1,4-butanediol production [27]). As there are methods available to measure mass transfer characteristics (k_La, d_{32}, ε_G, k_L, a) easily, we highly recommend to perform these experiments with realistic broths to prevent underestimation of mass transfer rates.

3.4. Conclusion

By supplementing ethanol to water, k_La sharply and significantly increases, primarily by decreasing d_{32}. This effect is also present, but weaker, in the studied syngas fermentation broths. Broth salinity (ionic strength) and biomass concentration seem to affect k_La in fermentation broth as well. Future mass transfer studies should consider the influence of broth components because literature models fail to predict their effects.

Chapter 4

Downscaling gas fermentation by taking the microbial perspective

Waar de werkelijkheid ontbreekt, daar is de schijn het beste

Desiderius Erasmus

This chapter has been published as:
Puiman, L., Almeida Benalcázar, E., Picioreanu, C., Noorman, H. J., & Haringa, C. (2023). Downscaling industrial-scale syngas fermentation to simulate frequent and irregular dissolved gas concentration shocks. *Bioengineering*, 10(5), 518.

Abstract

In large-scale syngas fermentation, strong gradients in dissolved gas (CO, H_2) concentrations are very likely to occur due to locally varying mass transfer and convection rates. Using Euler-Lagrangian CFD simulations, we analysed these gradients in an industrial-scale external-loop gaslift reactor (EL-GLR) for a wide range of biomass concentrations, considering CO inhibition for both CO and H_2 uptake. Lifeline analyses showed that microorganisms are likely to experience frequent (5 to 30 s) oscillations in dissolved gas concentrations with one order of magnitude. From the lifeline analyses we developed a conceptual scale-down simulator (stirred-tank reactor with varying stirrer speed) to replicate industrial-scale environmental fluctuations at bench-scale. The configuration of the scale-down simulator can be adjusted to match a broad range of environmental fluctuations.

Our results suggest a preference for industrial operation at high biomass concentrations as this would strongly reduce inhibitory effects, provide operational flexibility, and enhance the product yield. The peaks in dissolved gas concentration were hypothesised to increase the ethanol yield due to the fast CO-uptake mechanisms in *C. autoethanogenum*. The proposed scale-down simulator can be used to validate such results and to obtain data to parameterise lumped kinetic metabolic models that describe such short-term responses.

Graphical abstract

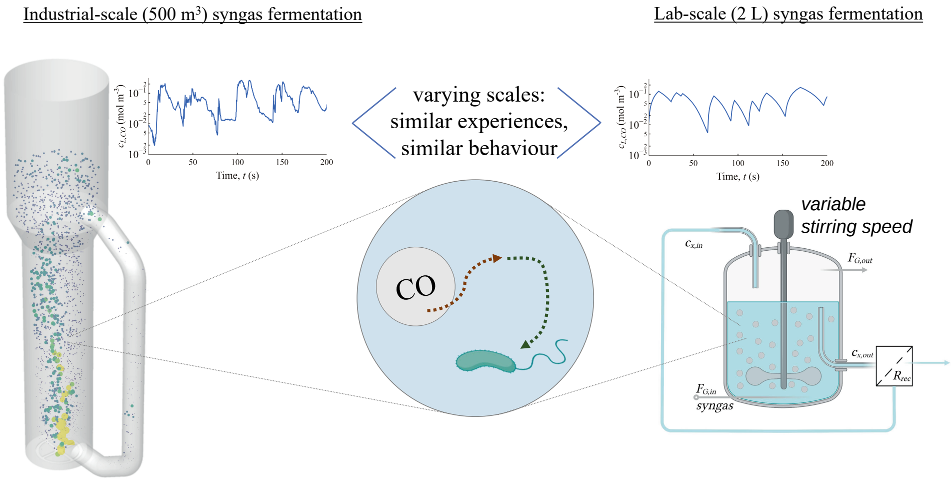
Industrial-scale (500 m³) syngas fermentation
Lab-scale (2 L) syngas fermentation
$c_{L,CO}$ (mol m^{-3})
10^{-1}
10^{-2}
10^{-3}
0
50
100
150
200
Time, t (s)
varying scales: similar experiences, similar behaviour
$c_{L,CO}$ (mol m^{-3})
10^{-1}
10^{-2}
10^{-3}
0
50
100
150
200
Time, t (s)
CO
variable stirring speed
$c_{x,in}$
$F_{G,out}$
$c_{x,out}$
R_{rec}
$F_{G,in}$
syngas

4.1. Introduction

Syngas fermentation is nowadays an established process for the conversion of waste gases into chemicals [8, 10]. The company LanzaTech successfully commercialises the fermentation of synthesis gas (containing CO, H_2 and CO_2) into ethanol, and is currently exploring other products such as acetone and isopropanol [9]. Although mass transfer limitations have often been accounted as a limiting factor for scale-up of syngas fermentation, such limitations could highly be relieved by making products which are bubble coalescence-suppressing, such as ethanol [197].

High product specificity towards ethanol (> 90%) is required for successful commercialisation [8]. In a process called solventogenesis, *Clostridium autoethanogenum*, the workhorse of industrial-scale syngas fermentation, produces ethanol from syngas (e.g., using Reaction 4.1 and 4.2), while during acetogenesis syngas is converted into acetate [14, 198]. Solventogenesis can be triggered by low extracellular pH [11], by high extracellular concentrations of acetate [199], or by H_2 supplementation [46].

$$6\,CO + 3\,H_2O \longrightarrow C_2H_6O + 4\,CO_2 \tag{4.1}$$

$$6\,H_2 + 2\,CO_2 \longrightarrow C_2H_6O + 4\,H_2O \tag{4.2}$$

Since industrial-scale reactors are of considerable size (e.g., 5 m diameter by 25 m height, or ~500 m^3, is not exceptional), the occurrence of spatial gradients is more of a rule than an exception. Usually substrate gradients occur when the characteristic time of reaction τ_{rxn} is significantly lower than the characteristic time of transport, which is related to mixing for substrates in the liquid phase via the circulation time (t_c), and to mass transfer for gaseous-phase substrates (τ_{MT}) [48, 49]. For large-scale syngas fermentation, τ_{rxn} is expected to be much lower (~0.3 s; [40]) than τ_{MT} (around 10 – 20 s; [197]) and t_c (~40 s; Figure C.1). Furthermore, both hydrostatic pressure differences (3.5 bar at the bottom vs. 1 bar near the headspace) and gas mole fraction differences (e.g., y_{CO} decreases from 50% to 5% from bottom to top due to consumption) cause a gradient of around factor 35 in saturation concentration, while the volumetric mass transfer coefficient $k_L a$ might be locally varying due to turbulent fluctuations, differences in bubble size and gas hold-up [197]. We hypothesise that all of this leads to sizeable dissolved CO and H_2 concentration gradients which might have implications on the syngas fermentation performance.

The impact of such concentration differences on *C. autoethanogenum* can be studied with Euler-Lagrangian CFD modelling. This way environmental changes, for example in substrate concentration, temperature, and shear stress, can be recorded from the perspective of the microbe (the so-called *lifeline*) [62, 64, 66]. The cells are simulated as Lagrangian flow-followers (particles) and, when they do not interact with the flow or concentration field (one-way coupling), are used for analysing the environmental fluctuations occurring in the bioreactor [56, 57, 200]. Such analyses could be used for the development of scale-down simulators [165, 201] or to study cell population heterogeneity [202]. Two-way coupling has to be realised when studying the influence of biomass on the flow or concentration fields [58, 99]. This method requires the use of a structured metabolic-kinetic model that could be coupled with the CFD model in a computationally viable fashion [66]. Although very detailed genome-scale metabolic models and kinetic ensemble models are currently available for *C. autoethanogenum* and other acetogens [46, 62, 203], two-way coupling of these models is currently too computationally intensive for practical application. Development of less-detailed, yet structured kinetic models by metabolite lumping [67, 68, 94] is key to study the influence of *C. autoethanogenum* on the flow and concentration fields more accurately.

Siebler et al. [56] studied how *C. ljungdahlii* would respond to CO gradients in a severely mass transfer limited bubble column reactor. They hypothesised based upon their Euler-Lagrangian results and in analogy with *Escherichia coli* that in their case transcriptional changes were very likely (>84%) to occur because long-lasting CO limitations would lead to a maintenance-dominated metabolism. Redox-controlled oscillations in biomass-specific uptake and production rates were observed in *C. autoethanognum* [204], within the timescale of hours, while substrate fluctuations in the order of seconds ($\sim t_c$) or minutes are expected in the large-scale. With scale-down simulators (e.g., based on a single-vessel, multiple vessels such as stirred tank reactors coupled with plug flow reactors, or microfluidics) the physiological cell response on such short-term fluctuations could be studied so that the large-scale environment as experienced by the cell is reproduced at bench-scale [48, 64–66, 205]. The obtained metabolite fluctuations can be used for parametrisation of the lumped metabolic models [67].

Several scale-down simulators have been developed and used in the past decades, but the requirements of a scale-down simulator for syngas fermentation have not been identified yet. Since there are many unknowns in the scientific literature regarding kinetics and short-term cell responses, the execution of scale-down experiments that are representative of the large-scale behaviour is crucial for advancing the syngas fermentation field. In this study, we propose a scale-down simulator to study industrial-scale syngas fermentation at lab-scale. To exemplify the distinctive applicability of the proposed scale-down simulator, a wide range of industrial biomass concentrations were studied, since this is a major determinant for the dissolved gas concentration. The impact of gas (CO_2) production on the dissolved gas concentration gradients and thus possible fluctuations for the microbe was studied. We used our previous CFD model of an industrial-scale external-loop gaslift reactor (EL-GLR) and our lab observations to develop and analyse lifelines representative for large-scale syngas fermentation [197, 206].

4.2. Methods

Eulerian concentration field

Geometry and flow field

As a starting point for the simulations, the 3D reactor geometry and computed flow field of the EL-GLR were used, for which the modelling approach was validated on pilot-scale data as described in [197]. The only change was the syngas composition from a 50% CO, 50% N_2 mixture to a 50% CO, 20% H_2, 30% CO_2 (v/v) mixture [204]. Since the average molar mass of these compositions is similar and the ideal gas law applies, the mass-flow inlet boundary condition of 2.11 $\mathrm{kg\,s^{-1}}$ was kept the same, as well as the headspace pressure of 101 kPa.

Next to the equations for gas and liquid flow, volume fraction, and turbulence, the species equations were solved transiently for both phases for obtaining the concentration fields, by implementing user-defined functions (UDFs) for both mass transfer and biological reaction (Figure 4.1), in ANSYS Fluent 2021R1.

Mass transfer model

The mass transfer coefficient k_L was computed by taking the maximum value derived from either the Higbie [127] (Equation 4.3) or the Lamont-Scott relation [131], the result of the latter was corrected for the underestimation of the energy dissipation rate ϵ by the

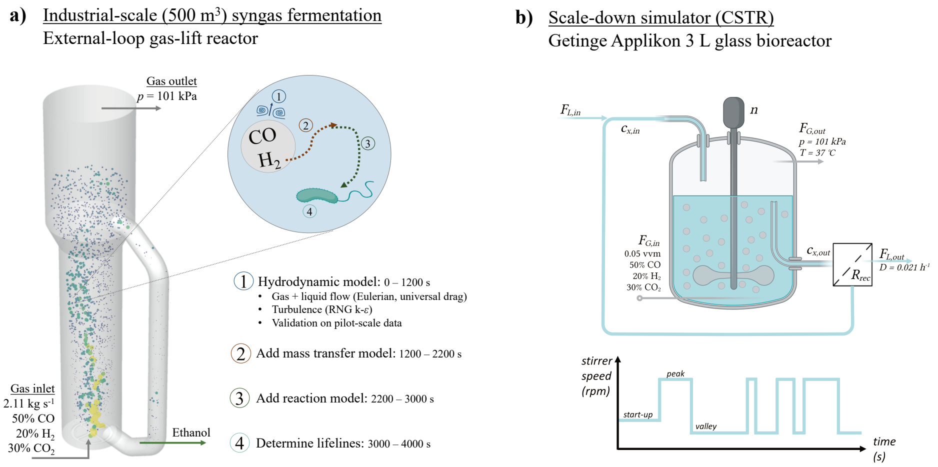
a) Industrial-scale (500 m³) syngas fermentation
External-loop gas-lift reactor
Gas outlet
p = 101 kPa
CO
H₂
①
②
③
④
Gas inlet
2.11 kg s⁻¹
50% CO
20% H₂
30% CO₂
Ethanol
① Hydrodynamic model: 0 – 1200 s
• Gas + liquid flow (Eulerian, universal drag)
• Turbulence (RNG k-ε)
• Validation on pilot-scale data
② Add mass transfer model: 1200 – 2200 s
③ Add reaction model: 2200 – 3000 s
④ Determine lifelines: 3000 – 4000 s
b) Scale-down simulator (CSTR)
Getinge Applikon 3 L glass bioreactor
F_L,in
c_x,in
n
F_G,out
p = 101 kPa
T = 37 °C
F_G,in
0.05 vvm
50% CO
20% H₂
30% CO₂
c_x,out
R_rec
F_L,out
D = 0.021 h⁻¹
stirrer speed (rpm)
peak
start-up
valley
time (s)

Figure 4.1: Conceptual representation of the modelling procedure for both a) the industrial-scale reactor and b) the scale-down simulator. The 3D geometry, based on publicly available pictures of the Shougang-LanzaTech plant, the hydrodynamic model CFD of the EL-GLR and its validation on pilot-scale data are extensively described in our previous work [197]. The scale-down simulator is based upon a 3 L bioreactor (2 L liquid volume), with varying duration of high and low stirrer speed after the start-up phase. See Table C.1 for details on the geometry of this reactor [207]. Created with `BioRender.com`.

k-ϵ model [165] using the pneumatic power input derived from standard correlations [166] and the liquid volume integral of ϵ (Equation 4.4). The maximum k_L of species i was used to account for both surface layer renewal mechanisms, since high k_L might be obtained in zones with high energy dissipation [164], but transfer in low-turbulent conditions is better approximated by the Higbie relation [26].

$$k_{L,i} = 2\sqrt{\frac{D_{L,i}\, v_{\text{slip}}}{\pi d_b}} \tag{4.3}$$

$$k_{L,i} = 0.45 D_{L,i}{}^{\frac{1}{2}} \left(\epsilon_{\text{cor}}/\nu_L\right)^{\frac{1}{4}} \text{ with } \epsilon_{\text{cor}} = f_{\text{cor}}\epsilon_{\text{local}} \text{ and } f_{\text{cor}} = \frac{P_{\text{in}}}{\int_{V_L} \epsilon_{\text{local}}\, dV_L} \tag{4.4}$$

In order to obtain a realistic mass transfer rate for industrial-scale syngas fermentation, spherical bubbles with constant diameter (3 mm) were assumed based upon our previous work [197] (Equation 4.5). Since coalescence could be suppressed by the presence of surface-active compounds (e.g., ethanol, salts) in syngas-to-ethanol fermentations, small bubbles can be obtained, leading to high mass transfer rates [157, 181, 200, 206].

While our multiphase model accounted for mass loss through interphase mass transfer and gas expansion using the ideal gas law in Fluent's volume fraction equation [79], we acknowledge that bubble coalescence, break-up, shrinkage by consumption, and pressure-based bubble expansion were not considered by assuming a constant bubble size. Although these factors could have potentially improved the accuracy of the gas phase description, we chose to prioritise obtaining realistic gas mass transfer rates and focusing on the biological aspects of our study. Therefore, we opted for a simplified set of equations, similar to Siebler et al. [56], that were within the scope of our work.

The saturation concentration was calculated considering the local gas phase mole fraction. The pH equilibrium of CO_2 with carbonate species could increase the gas-to-liquid mass transfer rate in neutral (pH 6 - 8) and basic conditions (pH > 8), however this effect can be neglected as the syngas fermentation process is operated at pH 5. To ensure complete saturation of CO, H_2, and CO_2, and achieve steady-state conditions (i.e., statistically stationary) in the average flow and concentration fields, the mass transfer model was run for 1000 s. Although short-time fluctuations occurred, there were no long-term dynamics, as evidenced by the constant rolling average of the global gas hold-up and dissolved gas concentrations.

$$MTR_i = k_{L,i}\, a \Delta c_{L,i} = k_{L,i}\, 6\frac{\varepsilon_G}{d_b}\left(H_i p y_i - c_{L,i}\right) \tag{4.5}$$

Biological reaction modelling

The biomass-specific CO and H_2 uptake rates (q_i) were modelled using a recently derived kinetic model [40]. Both CO- and H_2-uptake models account for CO inhibition (Equation 4.6 and 4.7), and are based on models derived by Mohammadi et al. [34] and de Medeiros et al. [208], respectively.

Table 4.1: Parameters used for the simulation of the Eulerian concentration field.

Name	**Symbol**	**CO**	**H_2**	**CO_2**	**Unit**	**Source**
Inlet gas fraction	$y_{i,\mathrm{in}}$	0.5	0.2	0.3	$\mathrm{mol}_i\ \mathrm{mol}_G^{-1}$	[204]
Henry coeff.	H_i	2.30×10^{-7}	1.47×10^{-8}	1.06×10^{-5}	$\mathrm{kg\,m^{-3}\,Pa^{-1}}$	[144]
Diffusion coeff.	$D_{L,i}$	2.71×10^{-9}	6.01×10^{-9}	2.56×10^{-9}	$\mathrm{m^2\,s^{-1}}$	[143]
Maximum uptake rate	$q_i^{\max}$	1.459	2.565	-	$\mathrm{mol\ mol}_x^{-1}\mathrm{h}^{-1}$	[40]
Half-saturation coeff.	$K_{S,i}$	0.042	0.025	-	$\mathrm{mol\,m^{-3}}$	[40]
Inhibition coeff.	K_I	0.246	-	-	$\mathrm{mol\,m^{-3}}$	[40]
	$K_{I,\mathrm{CO}}$	-	0.025	-	$\mathrm{mol\,m^{-3}}$	[40]

$$q_{\mathrm{CO}} = q_{\mathrm{CO}}^{\max}\left(\frac{c_{L,\mathrm{CO}}}{K_{S,\mathrm{CO}} + c_{L,\mathrm{CO}} + \frac{c_{L,\mathrm{CO}}^2}{K_I}}\right) \tag{4.6}$$

$$q_{\mathrm{H_2}} = q_{\mathrm{H_2}}^{\max}\left(\frac{c_{L,\mathrm{H_2}}}{K_{S,\mathrm{H_2}} + c_{L,\mathrm{H_2}}}\right)\left(\frac{1}{1 + \frac{c_{L,\mathrm{CO}}}{K_{I,\mathrm{CO}}}}\right) \tag{4.7}$$

The overall reaction rate r_i is the product of q_i and the biomass concentration c_x, the latter was assumed to be spatio-temporally constant as a continuous process is considered in steady state. The reaction rates were enabled once CO and H_2 concentrations reached a steady saturation value. Once statistically stationary flow and concentration fields were obtained (after 600 s the rolling averages of the global dissolved gas concentrations and hold-up remained constant), time-averaged fields were collected over an averaging period of 200 s. Parameters used for computing the Eulerian concentration fields are provided in Table 4.1.

The influence of microbial CO_2 production was examined by modelling two extreme cases at $25\,\mathrm{g\,L^{-1}}$ biomass: *i)* only CO_2 consumption by H_2 catabolism, $q_{\mathrm{CO_2}} = -\frac{1}{3}q_{\mathrm{H_2}}$, and *ii)* also including production by CO catabolism: $q_{\mathrm{CO_2}} = \frac{4}{6}q_{\mathrm{CO}} - \frac{1}{3}q_{\mathrm{H_2}}$. The case with the most extensive dissolved gas concentration gradient was subsequently used to study a wide range of industrially relevant conditions, by running simulations with varying biomass concentrations (2, 5, 7.5, 10 and $25\,\mathrm{g\,L^{-1}}$).

The obtained dissolved gas concentrations from the Eulerian simulations for the different biomass concentrations were compared to approximations obtained by a simple ideal-mixing model ($c_{L,i}$ from Equation 4.8), wherein it was assumed that all transferred gas is directly consumed. The ideal-mixing model used the same parameters (Table 4.1) and uptake kinetics (Equations 4.6 and 4.7), an average pressure (274 kPa), and the volume-average $k_L a$ obtained from the CFD simulations.

$$MTR_i = (k_L a)_i\left(H_i p y_i - c_{L,i}\right) = q_i c_x = r_i \tag{4.8}$$

Lifeline analysis

Microbial lifelines were obtained for three cases with different biomass concentrations (5, 10 and 25 $\mathrm{g\,L^{-1}}$). Massless Lagrangian particles were injected at the sparger and tracked for a certain number of circulation times N_{t_c} and particles N_p. To account for turbulence effects, Fluent's discrete random walk model was enabled. While tracking the particles, the current time, position, concentrations, and biomass-specific uptake rates were stored in text format every 0.1 s. Data obtained for the first 90 s (approximately one 95% mixing time t_m, Figure C.1) were discarded to ensure that the particles were evenly dispersed over the whole reactor volume during the entire analysis.

The lifelines revealed distinct periods of maxima and minima (i.e., peaks and valleys) in both dissolved CO and H_2 concentrations. *Peak* and *valley* periods were defined from the lifelines by comparing the transient concentrations in the lifeline with the Eulerian average dissolved gas concentration: in case the transient concentration was 2 times (for the 5 $\mathrm{g\,L^{-1}}$ case) or 1.5 time (for the other cases) higher or lower than the Eulerian average concentration for at least 1 s, then a peak or valley was assigned, for which the residence time and the average gas concentration were stored. Probability-normalised histograms were calculated subsequently using 100 linearly distributed bins over the whole parameter space (e.g., residence time or average concentration in peak), except for time in the valleys where the maximum value was capped at 150 s. The circulation time t_c was calculated as the average time between two peaks (Equation 4.9):

$$t_c = N_p \frac{t_{\text{lifeline}}}{N_{\text{peaks}}} \tag{4.9}$$

For the case with 5 $\mathrm{g\,L^{-1}}$ biomass, lifelines were obtained during $t_{\text{lifeline}} = 1000$ seconds (around 23 circulation times) and for $N_p = 160{,}000$ Lagrangian trajectories. This resulted into extensive simulation time and data usage so that the analysis of the full dataset was computationally unwieldy. Therefore, we had to determine how many Lagrangian trajectories (N_p) and circulation times (N_{t_c}) were needed to ensure statistical independence using the Kullback-Leibler divergence (see Appendix B, Figure C.2).

Design of a scale-down simulator

The scale-down simulator was designed based on the results of the lifeline analysis (i.e., the probability density functions of concentrations and residence times in peaks and valleys). The goal of this scaled-down system is to reproduce to the best possible degree the residence times and concentrations experienced by microbes in the full-scale system. The starting point was a continuously operated bench-scale stirred tank reactor (CSTR) (see Figure 4.1 and Table C.1), for which operational conditions were varied to mimic the large-scale environment at several biomass concentrations.

Mass transfer, dilution and consumption rates were modelled for CO, H_2, CO_2 and biomass while assuming ideal mixing in the liquid phase (Equation 4.10). The evolution of the gas (CO, H_2 and CO_2) composition in the dispersed phase $y_{D,i}$ and in the headspace

$y_{H,i}$ were also considered (Equation 4.11, 4.12) since these could be highly variable during operation at low gas flow rates. The dispersed gas volume $V_{G,D}$ was determined by approximating the gas hold-up using the method proposed by [25], while volume balancing was done to calculate the headspace gas volume $V_{G,H}$.

$$\frac{dc_{L,i}}{dt} = D_r\left(c_{L,i,\text{in}} - c_{L,i}\right) + (k_L a)_i\left(H_i p y_i - c_{L,i}\right) + q_i c_x \tag{4.10}$$

$$\begin{gathered}\frac{dy_{D,i}}{dt} = \frac{F_{G,\text{in}}}{V_{G,D}} y_{i,\text{in}} - \frac{F_{G,\text{out}}}{V_{G,D}} y_{D,i} - \frac{V_L}{V_{G,D}} (k_L a)_i \left(c^{\text{sat}}_{L,i} - c_{L,i}\right) \frac{RT}{p} \\ \text{with } F_{G,\text{out}} = F_{G,\text{in}} - \sum_{i=\text{all gases}} \left[(k_L a)_i \left(c^{\text{sat}}_{L,i} - c_{L,i}\right)\right] V_L \frac{RT}{p}\end{gathered} \tag{4.11}$$

$$\frac{dy_{H,i}}{dt} = \frac{F_{G,\text{out}}}{V_{G,H}} \left(y_{D,i} - y_{H,i}\right) \tag{4.12}$$

The volumetric mass transfer coefficient $k_L a$ of compound i is dependent on the superficial gas velocity and the stirrer speed [71] and was estimated by considering mass transfer enhancement by the broth composition ($f_{\text{broth}} = 1.5$, [206]), the temperature and the compound-specific diffusion coefficient in water (Equation 4.13). The power input was estimated for a Rushton impeller with $P_0 = N_{\text{Po}} n^3 d^5_{\text{imp}}$ and the used geometry [25, 209].

$$\begin{gathered}(k_L a)_i = f_{\text{broth}} \cdot \left[0.026 \left(\frac{P}{V_L}\right)^{0.4} \left(u_{G,s}\right)^{0.5}\right] \left(1.022^{(T-293.15)}\right) \sqrt{\frac{D_{L,i}}{D_{L,O_2}}} \\ \text{with } P = \alpha \left(\frac{P_0^2 n d^3_{\text{imp}}}{{F_{G,\text{in}}}^{0.56}}\right)^{\beta}\end{gathered} \tag{4.13}$$

The overall gas consumption rate was determined using the local concentrations in the liquid phase via Equations 4.6 and 4.7 and the biomass concentration. The total biomass growth rate $\left(\mu \cdot c_x\right)$ was determined using the model parameters derived by [32] for solventogenic conditions (Equation 4.14), while neglecting the maintenance requirements of the biomass. Biomass retention in the system was assumed (e.g., [31]) and varied by adjusting the biomass recycling rate R_{rec}.

$$\mu = q_{\text{CO}} Y_{x/\text{CO}} + q_{\text{H}_2} Y_{x/\text{H}_2} \tag{4.14}$$

The modelled bench-scale reactor was operated with a constant dilution rate of $0.021\,\text{h}^{-1}$, inlet gas flow of 0.05 vvm, temperature of 37 °C, pressure of 101 kPa and a stirrer speed during start-up of 75 rpm. Initial concentrations of CO, H_2, CO_2 and biomass in the liquid from Table 4.2 were assumed to solve the system with the ode15s function in MATLAB. After the start-up period the concentration oscillations were repeatedly imposed by varying the stirrer speed. The obtained scale-down lifelines were analysed using the same routine as for the industrial-scale reactor but considering no threshold factor to discriminate between the peaks and valleys, since these were manually imposed.

Table 4.2: Parameters specifically used for the design of the scale-down simulator. The other parameters as in Table 4.1.

Name	**Symbol**	**CO**	**H_2**	**CO_2**	**Biomass**	**Unit**	**Source**
Inlet gas fraction	$y_{i,\mathrm{in}}$	0.5	0.2	0.3	-	$\mathrm{mol}_i\ \mathrm{mol}_G^{-1}$	-
Inlet liquid conc.	$c_{L,i,\mathrm{in}}$	0	0	0	$c_{L,x,\mathrm{out}} R_{\mathrm{rec}}$	$\mathrm{mol\ m}_L^{-3}$	-
Biomass yield	$Y_{x/i}$	0.041	0.0070	-	-	$\mathrm{mol}_x\ \mathrm{mol}_i^{-1}$	[32]
Initial liquid conc.	$c_{L,i,0}$	0.1	0.03	7.4	2.03	$\mathrm{mol\ m}_L^{-3}$	-

4.3. Results and discussion

4.3.1. Eulerian concentration gradients

Influence of gas production

The results of Eulerian simulations with 25 $\mathrm{g\,L^{-1}}$ biomass in two CO_2 production cases were compared in terms of the dissolved CO concentration $c_{L,\mathrm{CO}}$ distribution in the reactor (Figure 4.2a,b). Although the dissolved gas concentrations in both simulations were in the same range (as expected since the biomass concentration was kept constant), the spatial distribution of $c_{L,\mathrm{CO}}$ within the riser was completely different. In both cases, the highest CO concentrations appeared at the base of the riser, where the mass transfer rates are high due to the hydrostatic pressure and high CO and H_2 gas fractions. As the gas rises, the pressure and gas fractions decrease, leading to lower mass transfer rates. More mass transfer was observed in the top separator due to the locally increased gas hold-up (Figure C.3), leading to increased $c_{L,\mathrm{CO}}$. In the downcomer, the long biomass residence time and poor gas renewal caused low CO concentrations.

The gas plume is pushed towards the left side by the liquid exiting the downcomer, resulting in high dissolved gas concentrations at the left side in the case without CO_2 production, which is due to reduced oscillations in the gas plume. When CO_2 is considered, the gas, and thus the dissolved syngas, concentrate towards the middle (Figure 4.2a, b) similar to the case without gas consumption [197]. Additional gas is generated halfway the riser by microbial reaction and is transferred back to the gas phase due to CO_2 oversaturation at decreased hydrostatic pressure. The additional gas in the riser (cf. Figure C.3a, b) leads to transport of dissolved CO towards the right side of the riser (cf. Figure 4.2a, b) and homogenises the dissolved gas distribution (i.e., the variation of $c_{L,\mathrm{CO}}$ and $c_{L,\mathrm{H_2}}$) within the whole reactor volume (Figure C.4).

Next to $c_{L,\mathrm{CO}}$, the evolution of gas hold-up ε_G and consequently $k_L a$ in the EL-GLR are highly affected by gas consumption (Figure 4.2c, d). As the mass transfer simulation starts without dissolved gas at $t = 1200$ s, there is an initial drop in ε_G due to gas dissolution. The lower ε_G causes a drop in $k_L a$ because of their linear dependence (Equation 4.5). After about 400 s the liquid saturates with dissolved gas and ε_G and $k_L a$ stabilise. When the reaction is switched on at $t = 2200$ s, both ε_G and $k_L a$ suffer a significantly drop in the cases with high biomass concentration, since high amounts of gas are being consumed (Figure C.3), even when CO_2 production is included. Similar decreases in ε_G were also

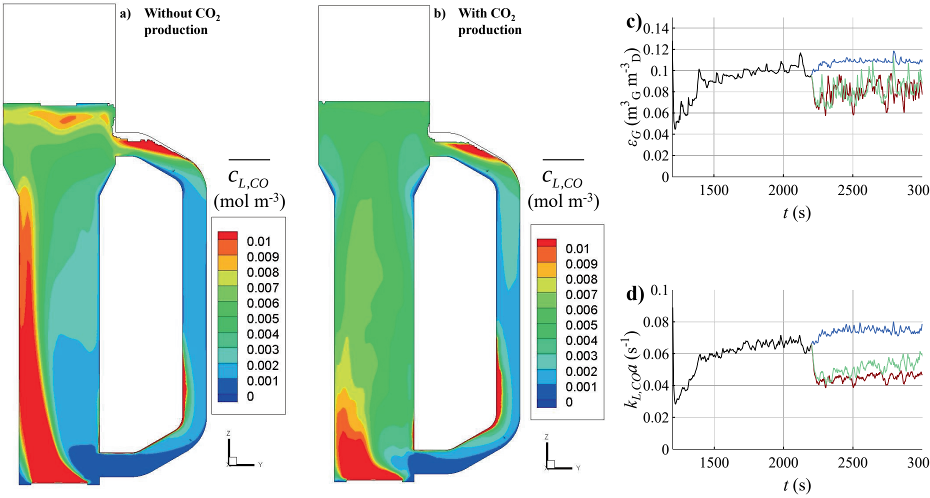

Figure 4.2: Effect of CO_2 production on mass transfer and dissolved gas distribution. Time-averaged (200 s) dissolved CO concentrations $c_{L,\mathrm{CO}}$ in the zy-plane ($x = 0$) of the EL-GLR for 25 $\mathrm{g\,L^{-1}}$ biomass a) without CO_2 production and b) by considering CO_2 production. Time-dependence of the dispersion volume-averaged c) ε_G and d) $k_L a$ during the CFD-simulations. Until 2200 s only gas-liquid mass transfer was included (black line). At 2200 s gas consumption was switched on in the model in three cases: 2 $\mathrm{g\,L^{-1}}$ biomass without CO_2 production (blue line), 25 $\mathrm{g\,L^{-1}}$ biomass without CO_2 production (red line), 25 $\mathrm{g\,L^{-1}}$ biomass including CO_2 production (green line).

visible in the model by Siebler et al. [56]. Interestingly, with little biomass in the reactor (2 $\mathrm{g\,L^{-1}}$) the gas conversion is highly decreased (from 0.67 $\mathrm{kg\,s^{-1}}$ at 25 $\mathrm{g\,L^{-1}}$ to 0.16 $\mathrm{kg\,s^{-1}}$) due to inhibiting CO concentrations (Figure C.5), increasing ε_G and $k_L a$ compared to the cases with more biomass.

Although ε_G could be well predicted with empirical relations in cases without gas consumption [197], the 33% decrease in ε_G by microbial gas consumption makes the prediction of ε_G and thus $k_L a$ even more challenging in operational EL-GLRs. This observation is especially relevant for gases rich in carbon source or electron donors, like the used syngas, in contrast to air where the dilution with inert N_2 and typically near equimolar conversion of O_2 into CO_2 results in negligible volume changes due to mass transfer.

The reduced gradients when considering CO_2 production, would decrease the impact of $c_{L,\mathrm{CO}}$ variations on microorganisms. Due to uncertainties on the metabolism, e.g., the possibility of simultaneous CO and H_2 consumption [44], the modelled cases would either under- or overestimate the CO_2 production rate. Since the case without CO_2 production appears to generate larger fluctuations and thus complicate the design of the scale-down simulator (and this is, dependent on the syngas composition, the ideal gas fermentation process from an environmental point of view), we further examined this scenario.

Influence of biomass concentration

Dissolved gas concentration fields in the large-scale reactor were computed with 2, 5, 7.5, 10, and $25\,\mathrm{g\,L^{-1}}$ biomass, as shown in Figure C.6 and Figure C.7. The variability that the microbes experience in dissolved CO and H_2 concentrations, as well as the corresponding biomass-specific uptake rates q_{CO} and $q_{\mathrm{H_2}}$, are displayed in Figure 4.3.

The mean values for the Eulerian fields follow the same trend as the ideal-mixing model (Equation 4.8), indicating that the concentration range is predominantly $c_{L,i} < K_{S,i}$. For c_x below $5\,\mathrm{g\,L^{-1}}$, the high potential mass transfer capacity compared to the reaction rate leads to strong CO inhibition, while in the $5 – 10\,\mathrm{g\,L^{-1}}$ range the mass transfer rate is in equilibrium with microbial syngas consumption at lower dissolved gas concentrations. At high c_x ($25\,\mathrm{g\,L^{-1}}$) gas uptake is fast, leading to low $c_{L,i}$ and thus also low uptake rates. This decrease in q_i is compensated by the greater c_x, causing the volumetric reaction rate and gas conversion to remain similar to cases with less biomass and higher biomass-specific uptake rates (Figure C.5). The ideal-mixing model suggests that an optimum q_i could be obtained at a certain biomass concentration, but the exact biomass concentration remains challenging to be determined using the CFD models considering the wide concentration distribution, the non-linear kinetics, and that iteratively running these models is very time-consuming. As there is less inhibition at higher c_x, there could be a possibility to increase gas conversion by supplying more gas, providing that coalescence remains suppressed by broth components [206].

There is a large volumetric spread in the dissolved gas concentrations obtained by the CFD models. The highest quartile of concentrations is often a factor 10 higher than the concentrations in the second quartile (e.g., at $5\,\mathrm{g\,L^{-1}}$ Q2 of $c_{L,\mathrm{CO}}$ starts around $1 \times 10^{-2}\,\mathrm{mol\,m^{-3}}$, while Q4 starts at $1 \times 10^{-1}\,\mathrm{mol\,m^{-3}}$). This would imply that the microorganism could experience regular concentration fluctuations of around one order of magnitude. However, due to the non-linear nature of the CO and H_2 uptake kinetics, such fluctuations only lead to minor oscillations in biomass-specific uptake rates. Here, the observed concentration gradients are significantly smaller than those in sugar fermentations with similar τ_{rxn} [57], due to the continuous gaseous substrate supply. However, the spread in the concentration fields may cause an overestimation of uptake rates by the ideal mixing models.

Overall, the ideal mixing model was able to describe the concentration range reasonably well, especially in the limitation regime, and could still be used for quick estimations of dissolved gas concentrations at varying conditions (e.g., increased mass transfer, pressure, or with different kinetics). The spatio-temporal variations in $c_{L,i}$, which can only be obtained by CFD modelling, are then to be estimated as ± half-an-order of magnitude around the derived concentrations from the ideal mixing model.

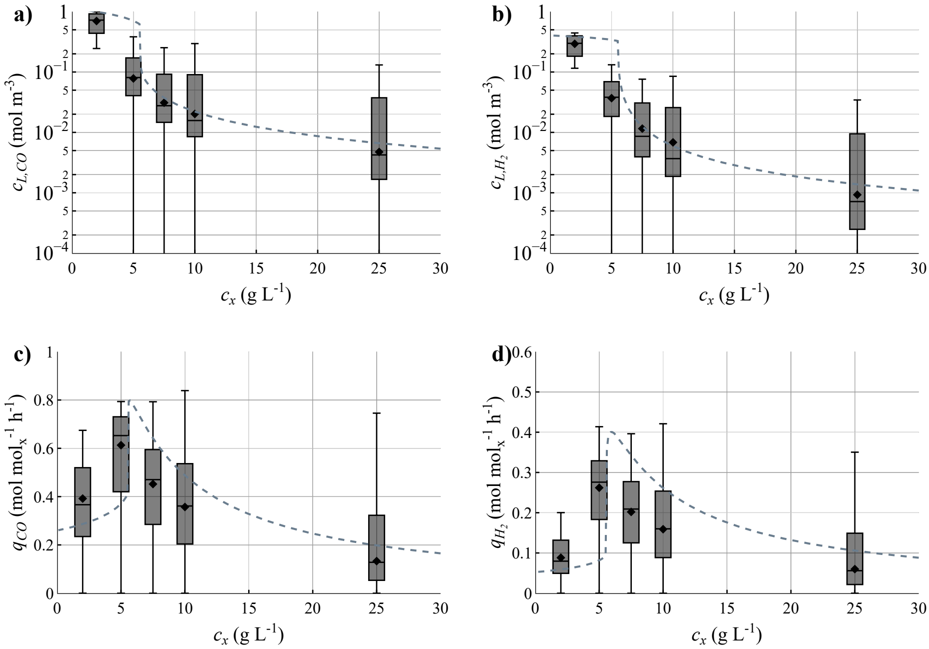

Figure 4.3: Spatial variations in (a, b) dissolved CO and H_2 concentrations and (c, d) biomass-specific uptake rates, represented in boxplots, for varying biomass concentrations. The boxplots were obtained from the 200 s time-averaged results of the CFD simulations and depict the spread around the mean values, with each quartile representing 25% of the reactor volume, while the diamond symbol represents the volume-averaged mean value. The dashed line is the result of a simple ideal-mixing model, using the volume-averaged $k_L a$ from the CFD model (0.050 s^{-1} for CO and 0.074 s^{-1} for H_2).

4.3.2. Lifeline analysis

From the lifelines obtained in cases with 5, 10 and 25 $g L^{-1}$ biomass it appears that the microorganisms could experience frequent fluctuations in solute concentrations (in 5 to 30 seconds), as visible from Video S1. To quantify the microbial experience, the residence times in the peaks and valleys of substrate concentrations were determined, as well as the average dissolved CO and H_2 concentration during a peak or valley. From the resulting probability density functions, we determined the joint probability of observing a specific residence time and concentration in a peak or valley (Figure 4.4).

The dynamic behaviour of the EL-GLR causes a large spread in the observed concentrations and residence time. This makes it impossible to standardise a concentration profile of a lifeline. The difference in concentration between the peaks and valleys are around a factor of 5, but within these there are significant deviations (up to 50%) around their specific mean values.

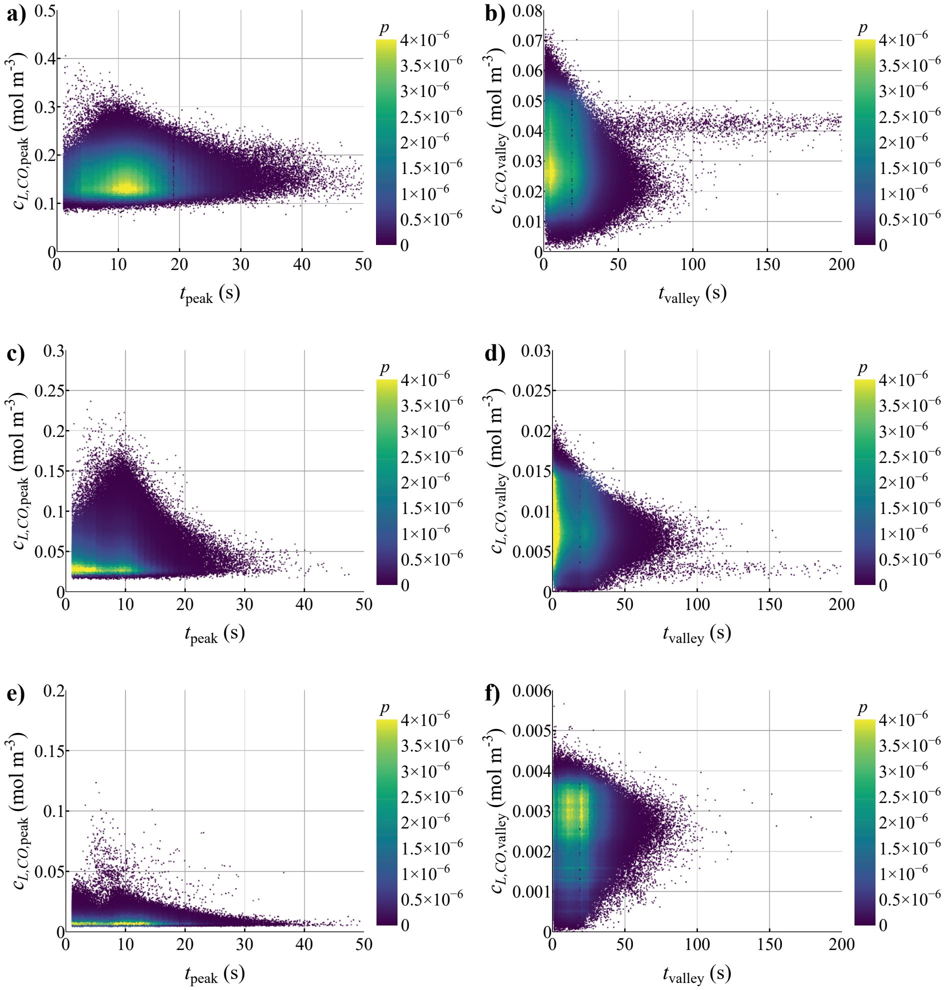

Figure 4.4: Scatter plots representing the likelihood of a microbe to experience peaks or valleys with a certain combination of $c_{L,\mathrm{CO}}$ and duration. Each dot represents a peak or valley with a concentration and residence time, and is colored by the probability of occurrence of that specific combination in the whole set of lifelines. Each row of plots represents data obtained with a specific biomass concentration: (a, b) 5, (c, d) 10 and (e, f) 25 g L^{-1}. Peaks are in the left column of plots (a, c, e) and the valleys are at the right (b, d, f). A similar figure was made for H_2 (Figure C.8).

Although the average gas concentrations during the oscillations are very different for the three biomass concentrations, the microbial residence time distributions are quite similar. This is caused by the similar hydrodynamic behaviour in the three cases, resulting from similar superficial gas flow velocity and gas conversion rates while neglecting the influence of biomass concentration on fluid properties (density and viscosity). Interestingly, in the cases with 5 and 10 $\mathrm{g\,L^{-1}}$ the dips in concentration lasted sometimes very long (> 100 s). This could be due to a recirculation pattern in the downcomer. Since in the 25 $\mathrm{g\,L^{-1}}$ case the concentration difference is small between peaks and valleys, and still some gas pockets with relative high CO concentration exist, such moments were not observed.

During the CO peaks at 5 $\mathrm{g\,L^{-1}}$, cells can spend short moments (between 5 and 15 s) at inhibitory concentrations (since $K_I = 0.25$ mol $\mathrm{m^{-3}}$. In this case $c_{L,\mathrm{CO}}$ still remains around the values needed for an optimum q_{CO}, so that strong inhibition would not be expected since $t_{\mathrm{peak}} < t_c \approx 40$ s, based upon the used kinetic model. The precise microbial response to such short moments of potential inhibition is unclear.

Similar results were obtained for H_2 (Figure C.8). The residence times in peaks and valleys were in the same ranges as for CO, with high concentration fluctuations of about a factor 5 noticed. Because H_2 uptake was inhibited at a relatively low $c_{L,\mathrm{CO}}$ ($K_{I,\mathrm{CO}} = 0.025\,\mathrm{mol\,m^{-3}}$), this resulted in high levels of CO inhibition during peaks. When interested in H_2 (and thus CO_2) conversion, CO levels should be kept well below the inhibitory values, which could be achieved by adjusting the inlet gas composition (e.g., by green hydrogen supplementation) and/or by increasing the biomass concentration. Due to the strong fluctuations in $c_{L,\mathrm{CO}}$ and the inhibiting effect of CO on H_2 uptake, $q_{\mathrm{H_2}}$ was significantly influenced, highlighting the need to study the mutual effect of CO and H_2 fluctuations on $q_{\mathrm{H_2}}$.

The ratio between the average dissolved concentrations of CO and H_2 ($c_{L,\mathrm{CO}}/c_{L,\mathrm{H_2}}$) increases with an increased biomass concentration: $c_{L,\mathrm{CO}}/c_{L,\mathrm{H_2}} \approx 2$ at 5 $\mathrm{g\,L^{-1}}$, 3 at 10 $\mathrm{g\,L^{-1}}$ and 6 at 25 $\mathrm{g\,L^{-1}}$. This is caused by the faster decrease of q_{CO} compared to $q_{\mathrm{H_2}}$ with biomass concentration (cf. Figure 4.3 c, d) due to decreased CO inhibition. To inspect the level of inhibition by CO in the determined ranges for peaks and valleys, the biomass-specific CO and H_2 uptake rates were calculated for each case using its respective $c_{L,\mathrm{CO}}/c_{L,\mathrm{H_2}}$ ratio (Figure 4.5).

From determining the specific gas uptake rates, it became clear that the reactor should be operated in the limitation regime, when increasing $c_{L,i}$ would result in a greater q_i (e.g., at 25 $\mathrm{g\,L^{-1}}$) while inhibitory concentrations are avoided. At low biomass concentration (5 $\mathrm{g\,L^{-1}}$), CO inhibition is already problematic, leading to decreased H_2 uptake rates in the peaks. With 10 $\mathrm{g\,L^{-1}}$ a significant increase in q_{CO} is observed when transitioning from a valley to a peak (from 0.3 to 0.8 mol $\mathrm{mol_x^{-1}h^{-1}}$), but small increases in $c_{L,\mathrm{CO}}$ during the peaks could worsen overall performance since q_{CO} is close to optimum. From the oscillatory dataset of Mahamkali et al. [204] was derived that fluctuations in q_{CO} and $q_{\mathrm{H_2}}$ in the timescale of hours lead to large increases in q_{EtOH} and thus the ethanol yield [40]. Scale-down experiments with imposed concentration fluctuations could inform whether this observation holds for the circulation timescale as well.

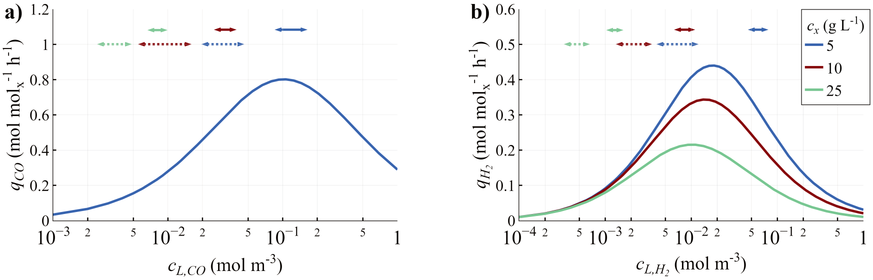

Figure 4.5: Overall biomass-specific a) CO and b) H_2 uptake rates computed for biomass concentrations of 5 (blue), 10 (red), and 25 g L^{-1} (green). $c_{L,\mathrm{CO}}$ in the H_2 uptake kinetics was calculated by using a $c_{L,\mathrm{CO}}/c_{L,\mathrm{H_2}}$ of 2, 3 and 6 for each respective case. The full arrows indicate the concentration ranges of the peaks, while the dashed arrows indicate the ranges for the valleys. CO-uptake is independent of the biomass concentration, hence the single line.

Too low dissolved gas concentrations would cause a thermodynamically infeasible catabolism and thus no syngas uptake at all. Such concentrations were estimated to be around 4×10^{-4} and 3×10^{-3} mol m^{-3} for CO and H_2, respectively, assuming independent consumption of CO and H_2/CO_2 for solventogenesis [32]. Since such low $c_{L,\mathrm{CO}}$ was not obtained in our analysis, we did not expect such problems for CO consumption. However, for H_2, values below the thermodynamic limit were attained in the valleys for 10 and 25 g L^{-1} biomass, so that a coupling with CO consumption is potentially required to supply enough electrons for H_2 uptake. As this may come at the expense of the product yield, further scale-down studies are required to determine how *C. autoethanogenum* may react to such short-term fluctuations in H_2 concentration.

Siebler et al. [56] estimated that a starvation regime could occur when $c_{L,\mathrm{CO}} < 3 \times 10^{-3}$ mol m^{-3}. Since in this regime a major portion of the energy might be spend on maintenance catabolism, lower growth rates can be expected, leading to higher product yield. In the configuration they studied, such CO shortages were highly likely to occur, causing a probable shift towards a starvation regime. In our simulations, this situation may only occur in the valleys when operating with high c_x. Due to higher $c_{L,\mathrm{CO}}$ in our other cases, reaching the maintenance catabolism was very unlikely to occur, since $k_L a$ of the EL-GLR was a factor 5 higher than in the BCR studied by Siebler et al. [56] (with $k_L a \sim 0.01$ s^{-1} and $c_x = 10$ g L^{-1}).

Our results suggest that even higher c_x may be advantageous, considering the current operation in the limitation regime and that high mass transfer could be obtained due to bubble coalescence suppression in the fermentation broths. Operation at very low $c_{L,\mathrm{CO}}$ would enable operational flexibility and a high product yield, without sacrificing gas conversion. Caution is needed to prevent that the dissolved gas concentrations do not get so low that the reaction becomes thermodynamically unfeasible, or that the high c_x hampers mass transfer and mixing by increasing broth viscosity [179].

In the LanzaTech process, $k_{L,\mathrm{CO}}a$ could well be around 3-4 times higher [197] than the final one obtained in our model ($650\,\mathrm{h}^{-1}$ vs. $180\,\mathrm{h}^{-1}$). This could be due to mass transfer intensification (e.g., by introduction of perforated plates [20]) or by achieving smaller bubbles (~1 mm). Although bubbles would become more rigid in such a case, mass transfer might still be enhanced by cell monolayers around the bubbles, especially in case of operating at high biomass concentrations [25]. In such high mass transfer cases, substantial CO inhibition might be expected, stressing the need to operate at high ($> 25\,\mathrm{g}\,\mathrm{L}^{-1}$) biomass concentrations.

4.3.3. Development of scale-down simulator

Based upon the analysis of the CFD data, we used numerical simulations to propose a conceptual design of a scale-down simulator to experimentally replicate the dissolved gas concentrations which were estimated to be experienced by microorganisms in the industrial-scale syngas fermentation. A single-vessel system, being a 2 L working volume CSTR, was chosen as basis for the scale-down simulator. Since rapid and irregular fluctuations in peaks and valleys should be obtained, we did not consider multi-vessel systems with forced circulation because rapid consumption of dissolved gas in the tubes connecting the vessels would be detrimental for the performance. In addition to the advantage of no substrate depletion in the tubes, clogging or high shear stress by pump action could also be avoided. In a well-mixed stirred-tank, there are little spatial variations in dissolved gas concentration (unlike plug-flow systems) so that the dissolved gas concentrations can be better controlled. Another potential scale-down system would be a two-stage STR with a perforated plate separating two well-mixed zones [210]. This way the dynamic interchange between two concentrations could be reproduced, although the step transitions might be unrealistic for the observed large-scale behaviour. A significant disadvantage of using a single-vessel is the lack of population heterogeneity in cellular experience, which would definitely be present in multi-vessel systems, as well as the poor incorporation of dead (or low concentration) zones such as the downcomer [211, 212]. Furthermore, slow mixing at low power input might possibly lead to local concentration gradients [71]. Operation at smaller scales with better mixing (e.g., 200 mL) might, however, lead to practical problems regarding sampling.

To mimic the large-scale successfully, we should make sure that the microbes experience similar peak/valley duration and concentration differences as in the large-scale bioreactor. Although we could argue from Figure 4.4 that most peaks last between 5 and 15 seconds, and valleys 10 to 30 seconds, this argument does not account for frequently occurring irregularities. There are peaks and valleys that largely exceed these times, e.g., peaks of 25 s and valleys of 60 s are not exceptional, and the scale-down simulator should replicate such outliers in terms of time and concentration. With the probability distributions of the residence times derived from the CFD lifelines, variations in the stirrer speed were imposed to obtain corresponding peaks and valleys in the scale-down simulator. It

Table 4.3: Operational conditions of the scale-down simulator to obtain an acceptable fit of the lifelines obtained by the scale-down simulator with the CFD-derived lifelines.

	Peak			**Valley**			**Recycle**	
$c_{x,\mathrm{EL-GLR}}$ ($\mathrm{g\,L^{-1}}$)	n (rpm)	$k_{L,\mathrm{CO}}a$ ($\mathrm{h^{-1}}$)	P/V ($\mathrm{W\,m^{-3}}$)	n (rpm)	$k_{L,\mathrm{CO}}a$ ($\mathrm{h^{-1}}$)	P/V ($\mathrm{W\,m^{-3}}$)	R_{rec} (-)	$c_{x,\mathrm{SD}}$ ($\mathrm{g\,L^{-1}}$)
5	910	153	23,000	20	1.3	0.11	0.5	0.54
10	900	150	2200	150	15	70	0.91	1.44
25	500	71	3400	70	5.6	6.1	0.96	3.27

was determined that around 2000 oscillations, lasting ~15 h in total, should be applied in the scale-down simulator to make sure that enough variation in peak or valley residence time is imposed (Figure C.2). To account for the varying biomass concentrations from the three CFD cases (5, 10 and 25 $\mathrm{g\,L^{-1}}$), the biomass recycling rate R_{rec} was altered between the different cases to adjust the reaction rate.

With this computational set-up and the iteratively derived operational conditions (Table 4.3), lifelines were simulated in the conceptual bench-scale reactor for the three different c_x that roughly correspond to the large-scale lifelines (Figure 4.6). The pulses in stirring speed are well captured and provide the same peak-valley frequencies as is expected at the large-scale. The concentrations that the microbes would experience are similar as in the large-scale bioreactor within the peaks and valleys. For example, for CO and H_2 in the 5 $\mathrm{g\,L^{-1}}$ cases the upper concentrations are always in the same order of magnitude and the experienced valleys are very similar to the ones in the large-scale reactor (Figure 4.6a, b). For the cases with high c_x it is more challenging to represent the deep concentration valleys well ($c_{L,i} \ll 1 \times 10^{-3}\,\mathrm{mol\,m^{-3}}$) since the increased c_x generally requires more mass transfer in the valleys. Since the impact of such concentrations on the q_i is small (Figure 4.5), negligible influence of this was expected.

The rate of increase in dissolved gas concentration during the transition from a valley to a peak in the scale-down simulator is very similar to that in the large-scale bioreactor: instantaneously the microbes experience concentration increases up to around 1 – 2 orders of magnitude in a matter of seconds (1 – 5 s). The decrease of the slope at the beginning of the peaks in $c_{L,\mathrm{CO}}$ can equally be identified in some of the peaks of the CFD lifelines. In the large-scale this rapid increase is due to the microorganism travelling instantly into a zone with high mass transfer and thus dissolved gas concentrations, while in the scale-down simulator the mass transfer increase responds to the step increase in stirring speed.

The transition from the peak to the valley was found to be more problematic to reproduce in the bench-scale reactor for the cases with 10 and 25 $\mathrm{g\,L^{-1}}$. Although the dissolved gas concentration decay is more plug flow-like at the large-scale, immediate decreases back to a representative "valley-baseline" were observed in the scale-down simulator. Simulating a ramped decrease in stirring speed could be helpful to obtain a more realistic decay in concentrations.

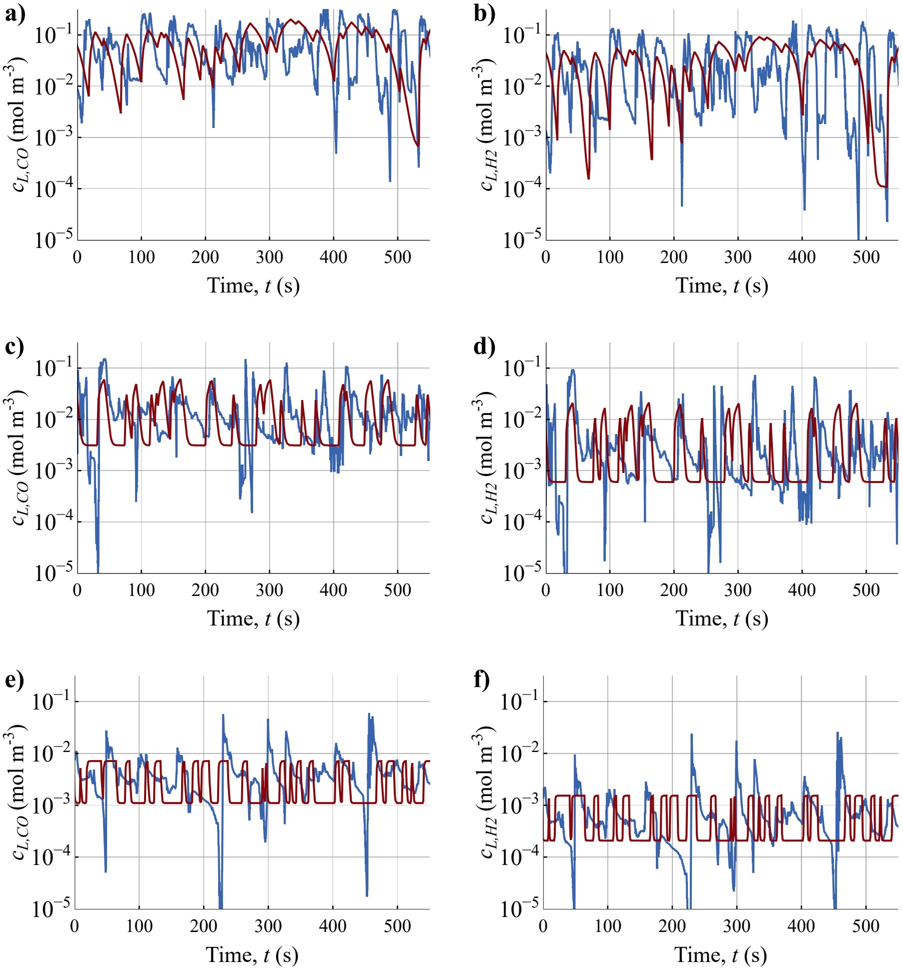

Figure 4.6: Microbial lifelines obtained from the simulation of the EL-GLR (blue) and the scale-down simulator (red), for CO and H_2, and the varying biomass concentrations in the large-scale reactor: a, b) 5 g L^{-1}; c, d) 10 g L^{-1}; e, f) 25 g L^{-1}. Random lifelines were chosen from the CFD simulation (blue) and a random time span of the lifelines in the scale-down simulator

A major factor varying between the two scales is the frequency and magnitude of cellular exposure to shear forces. This was quantified with the energy dissipation/circulation function ($EDCF = \frac{P_{\text{total}}}{V_{\text{eff}}} \frac{1}{t_c}$) [213, 214] while approximating t_c as $\frac{1}{4} t_m$ [71]. In the scale-down simulator there is highly varying exposure to shear between peaks and valleys when the cells are close to the impellers ($EDCF$ varies from 50 kW m^{-3} s^{-1} to 1×10^{-4} kW m^{-3} s^{-1}, respectively). In the EL-GLR there is only a high shear region around the gas plume ($EDCF$ ~0.06 kW m^{-3} s^{-1}), without considering bubble burst. The significantly varying $EDCF$

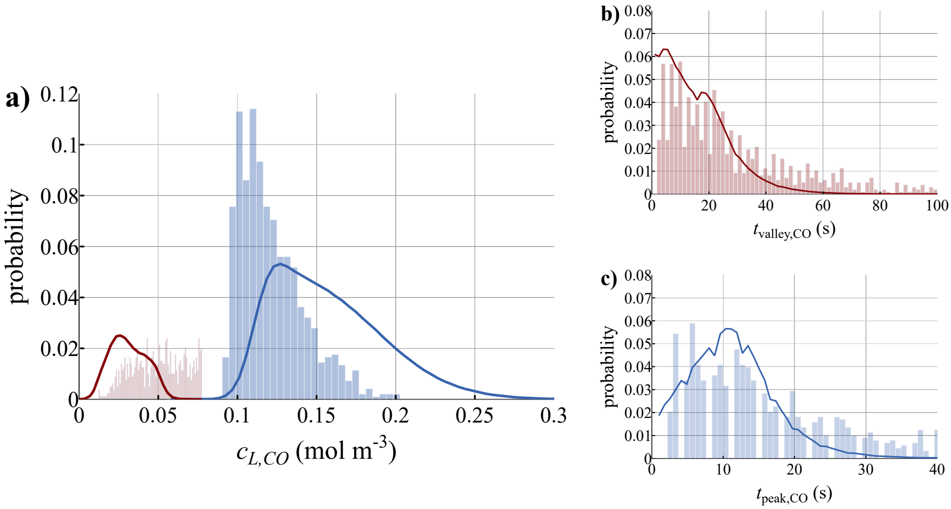

Figure 4.7: Comparison of the probability density functions obtained by the scale-down simulator (bars) with the CFD results (lines). Probability density functions for a) the concentration of dissolved CO during the peaks (blue) and the valleys (red), as well as the residence time in a b) valley or c) peak. Here, the case of CO with 5 g L^{-1} biomass is provided, other cases (H_2 5 g L^{-1}, and both compounds for 10 and 25 g L^{-1}) are provided in Figures C.10-C.14. The scale-down simulator was operated with 2000 peaks.

between two scales could be of impact when *C. autoethanogenum* is shear-sensitive, but this was not expected, due to its small size (around 3 μm) compared to the Kolmogorov scale (~10 µm) [4, 215].

The correspondence of the results of the scale-down simulator with the large-scale reactor was determined by performing a lifeline analysis. In this way, the probability distributions for the residence times and the concentrations in the peaks and valleys could be compared quantitatively (Figure 4.7 and Figures C.10-C.14). Generally, a very good correspondence of the residence time distributions was obtained. To some extent this is logical as CFD results of these are the inputs of the scale-down simulator, although the limitations of a bench-scale reactor do not guarantee good correspondence to be feasible; it indicates the feasibility of imposing rapid stirring speed fluctuations in a well-mixed bench-scale system.

Corresponding concentration distributions were more challenging to obtain since the ranges of the large-scale CO peak concentrations are very large (0.1 – 0.25 mol m^{-3}, Figure 4.7a). In the scale-down simulator the CO peak concentration could not become that high (maximum 0.2 mol m^{-3}) so that a narrower range was obtained, which was more skewed towards the lower concentrations. The assumptions and parameters used in the mass transfer and kinetic models make it challenging, however, to purely rely on quantitative results for the concentration fluctuations in the scale-down setup. Using more accurate mass transfer and kinetic models would increase the reliability of our quantitative predictions and thus our conceptual scale-down simulator.

Despite all these limitations, we showed that with a conceptually relatively simple scale-down simulator, the large-scale dissolved gas concentration gradients for a wide range of biomass concentrations could be reproduced in lab-scale. Model-based tuning of the operational conditions (e.g., stirrer speed, gas flow rate, gas composition) of the scale-down set-up on the probability distribution functions of the large-scale reactor, is a possible strategy to maximise correspondence between the two scales and thereby provide a fruitful basis towards representative scale-down of syngas fermentation.

4.3.4. Outlook

Further improvement of the scale-down simulator could lead to even better representations of the large-scale behaviour. An optimisation routine could help obtaining the best-fit parameters with the CFD-derived data. The ideal scale-down simulator has as few as possible variable parameters and represents the large-scale behaviour for a wide range of conditions. The effect of parameters (e.g., stirrer speed during the start-up phase) could be derived using tools such as principal component analysis during the optimisation and help deciding whether or not to use the parameter in further analyses.

The quantitative results of the CFD study and the proposed scale-down study are strongly dependent on the process conditions (e.g., headspace pressure, gas fraction) as well as on the kinetic model for CO and H_2 uptake. For example, the current models for CO-uptake significantly underestimate the maximum specific growth rate ($\mu_{\mathrm{model}}^{\mathrm{max}}$ = 0.03 h^{-1}) compared to experimental values ($\mu_{\mathrm{exp}}^{\mathrm{max}}$= 0.12 h^{-1}) [45]. As they are parameterised using insufficient data, the accuracy of our simulations is decreased and is therefore a major drawback of the study. Development of accurate kinetic models is crucial for reliably modelling bioreactors, and we hope that our work motivates further research in this area. The MATLAB scripts describing the conceptual scale-down simulator are openly available and can be used for further development with updated sub-models.

Despite the mentioned limitations, the proposed set-up and method are still applicable to a wide range of conditions. Even without using CFD, but an ideal mixing model (Equation 4.8), one can estimate the effect of process variables (e.g., increased mass transfer rates) on the average concentration in the large-scale reactor. In case the reactor is operated in the gas limitation regime ($c_{L,i} < K_{S,i}$), spatial concentration differences of a factor 5 around the mean could be expected based upon our CFD simulations. Since in the scenarios with varying biomass concentrations the residence time distributions in the peaks and valleys does not greatly differ, such differences are neither expected in other operational cases in the limitation regime. A scale-down simulator could then be tuned based upon the estimated concentration differences and the residence time distributions.

Although the developed scale-down simulator is conceptually easy to understand, the practical installation and operation might be challenging. The repeated variations in stirrer speed at high frequencies should be controlled, as well as possible ramp phases when increasing or decreasing the stirring speed. Ideally, rapid-sampling and/or online measurement for CO and H_2 [216, 217] should be applied to make sure that peaks and valleys are obtained in the intentioned manner. As the peaks and valleys are applied in the second-timescale, probe lag should be taken into account when analysing the experimental data. Furthermore, the influence of broth components on $k_L a$ in real fermentations should be considered for better predictions [206]. If the *in situ* concentrations cannot be measured, they could be predicted using a precisely determined $k_L a$ [218].

Our conceptual scale-down simulator makes it possible to simulate a statistically representative lifeline of the EL-GLR within a fraction of the time that it would cost for the CFD model to be run and analysed. Such a lifeline could then be used to study interactions between the extra- and intracellular environment by coupling with a metabolic kinetic model [40]. The obtained response should then be similar to the large-scale response due to the correspondence of both lifelines. By making variations of such lifelines, the peak and valley residence time and concentration distributions can be obtained that could lead to a desired large-scale response (e.g., high ethanol specificity).

Ramp and feast-famine studies in the scale-down set-up could be used to parameterise kinetic models that describe the short-term response of *C. autoethanogenum* [40, 94, 219], by rapid sampling of metabolite and enzyme concentrations. Ramp studies would be helpful to determine whether the instantaneous electron supply in the peaks would indeed lead to increased ethanol production, as was expected from long-term oscillations [204]. If the gas uptake rates are product-independent, then such scale-down simulators could be used for engineered strains to produce higher-value products [9], proteins [220], or for coupled reactions with other microorganisms, such as chain-elongators [221] or PHA production [222]. With the scale-down simulator, the microbe could be adapted to large-scale conditions, so that less scale-up problems might be expected [62].

The analyses of the industrial syngas fermentation process in this and our previous study [197] are all model-based and only slightly tuned based upon the scarcely available literature data of the full-scale LanzaTech operation [8, 10, 111]. To advance the syngas fermentation process, for model validation and the execution of highly representative scale-down simulators, the publication of real industrial data would be required, such as large-scale circulation times, operational $k_L a$ values, a range of dissolved gas concentrations and their gradients. All of this could, for example, enable the utilisation of a broader range of gas compositions, the development of processes towards higher-value products and intensified fermentation equipment.

In our analyses we showed that high biomass concentrations (e.g., $c_x > 10\,\mathrm{g\,L^{-1}}$) might be advantageous for both product yield and gas conversion. Since the highest reported biomass concentration in syngas fermentation reactors is around $9\,\mathrm{g\,L^{-1}}$ [31], experiments should target the influence of increased biomass concentrations and its viability on gas uptake, broth viscosity and mass transfer. The precise operating interval in terms of dissolved gas (CO and H_2) concentrations should be retrieved experimentally, so that the thermodynamically infeasible range can be avoided while operating in the maintenance-dominated regime which would enable high product-to-substrate yields. Our results show that with the currently used syngas composition (20% H_2) and high biomass concentration ($25\,\mathrm{g\,L^{-1}}$), H_2 catabolism may be thermodynamically infeasible, although co-consumption with CO might occur [46]. Thus, in a future with intermittent green hydrogen supply from renewable resources [223], supplementation of hydrogen might be a good option to valorise excess electricity and increase the CO-to-product yield.

4.4. Conclusion

The effect of the biomass concentration and dissolved gas concentration fluctuations in large-scale syngas fermentation was studied with Euler-Lagrangian simulations. Based upon these numerical simulations we recommend the industrial operation at relatively high biomass concentrations, as this would reduce the effects of CO inhibition, could increase the product yield and would provide high operational flexibility. Simulations indicate that in large-scale syngas fermentation *C. autoethanogenum* will experience frequent oscillations (peaks and valleys) in dissolved gas (CO, H_2) concentration of about one order of magnitude, in a timescale of seconds (5 to 30 s). Such concentration fluctuations may occur irrespective of the biomass concentration and were hypothesised to favour the ethanol yield.

The large-scale concentration fluctuations should be simulated during small-scale experiments to study how *C. autoethanogenum* adapts to industrial-scale conditions. We proposed a single-vessel scale-down simulator that theoretically replicates the fluctuations in dissolved gas concentrations by varying the stirrer speed based on the large-scale oscillations. Numerical analysis shows that the duration of the oscillations could be replicated well, but the settings might be adjusted to achieve higher similarities for the variations in concentration. The obtained lifelines in the proposed scale-down simulator represent the large-scale reactor well for a wide range of biomass concentrations and operational conditions.

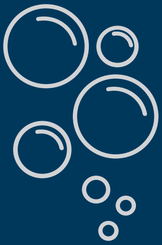

Chapter 5

Influence of the dissolved gas concentration and its gradient

The search for knowledge is not nourished by certainty:
it is nourished by a radical absence of certainty.

Carlo Rovelli

This chapter has been published as:
Puiman, L., Almeida Benalcázar, E., Picioreanu, C., Noorman, H. J., & Haringa, C. (2024). High-resolution computation predicts that low dissolved CO concentrations and CO gradients promote ethanol production at industrial-scale gas fermentation, *Biochemical Engineering Journal*, 109330.

Abstract

Gradients in dissolved gas concentrations are expected to affect the performance of large reactors for anaerobic gas (CO, H_2, CO_2) fermentation. To study how these gradients, and the dissolved gas concentration level itself, influence the productivity of the desired product ethanol and the product spectrum of *C. autoethanogenum*, we coupled a CFD model of an industrial-scale gas fermentor to a metabolic kinetic model for a wide range of metabolic regimes. Our model results, together with literature experimental data and a model with constant dissolved gas concentrations, indicate high ethanol specificity at low dissolved CO concentrations, with acetate reduction to ethanol at very low dissolved CO concentrations and combined ethanol and acetate production at higher CO concentrations. The gradient was predicted to increase both the biomass-specific ethanol production rate and the electron-to-ethanol yield by ~25%. This might be due to intensified ferredoxin and NAD^+ redox cycles, with the rate of the Rnf complex - a critical enzyme for energy conservation – as key driver towards ethanol production, and all at the expense of a reduced flux to acetate. We present improved mechanistic understanding of the gas fermentation process, and novel leads for optimisation and fundamental research, by coupling observations from various down-scaled lab experiments to expected microbial lifelines in an industrial-scale reactor.

Graphical abstract

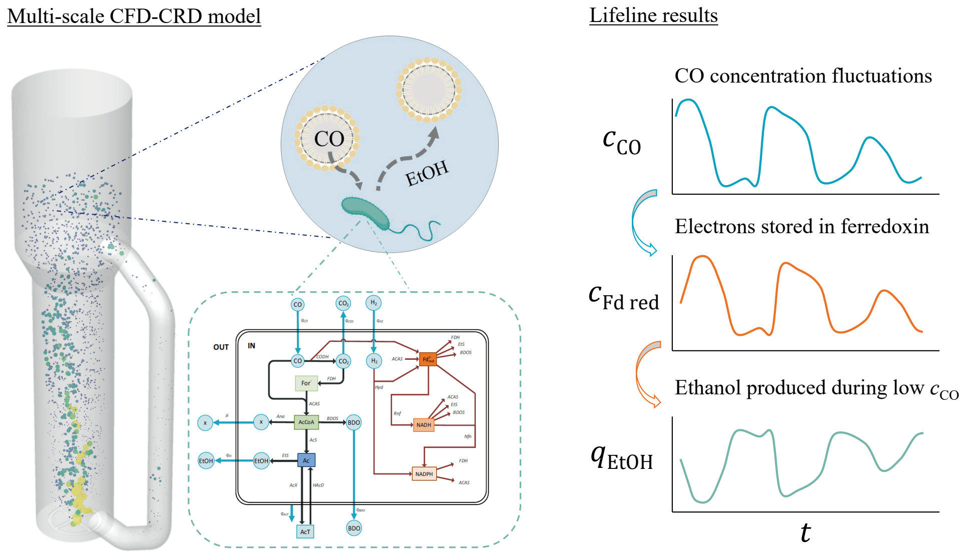
Multi-scale CFD-CRD model
Lifeline results
CO
EtOH
OUT
IN
CO
q_{CO}
CO₂
q_{CO2}
H₂
q_{H2}
CODH
CO₂
H₂
ACAS
Fd^{2-}_{red}
FDH
EtS
BDOS
For⁻
FDH
Hyd
ACAS
Rnf
ACAS
EtS
BDOS
NADH
Nfn
x
μ
x
Ana
AcCoA
BDOS
BDO
AcS
EtOH
q_{Et}
EtOH
EtS
Ac⁻
AcX
HAcD
NADPH
FDH
ACAS
q_{AcT}
AcT
q_{BDO}
BDO
CO concentration fluctuations
c_{CO}
Electrons stored in ferredoxin
$c_{Fd\ red}$
Ethanol produced during low c_{CO}
q_{EtOH}
t

5.1. Introduction

In the last few years, anaerobic gas fermentation (with CO, H_2 and/or CO_2 gas mixtures) has successfully been commercialised by the company LanzaTech for the production of ethanol from industrial waste streams [8, 10]. Ethanol is the product of main interest, since it has an established use as fuel and because it can be upgraded to plastics, textiles, and fine chemicals, while the spent microbial biomass can be used as animal feed [8–11]. The industrial gas fermentation process with the acetogen *Clostridium autoethanogenum* is deployed in external-loop gas-lift reactors (EL-GLR), which has shown potential for achieving high gas-to-liquid mass transfer rates, at least in part due the coalescence-inhibiting properties of the produced ethanol [197, 206].

In large-scale bioreactors (e.g., the mentioned EL-GLR of ~500 m^3), gradients in (amongst others) liquid-phase substrate and dissolved gas concentrations are usually expected when the characteristic time of consumption is smaller than those of liquid circulation and mass transfer, respectively [48, 49]. Moreover, variations in hydrostatic pressure and the gas composition were estimated to result in a gradient of factor 35 [224]. The temporal fluctuations that microorganisms experience as a consequence of these spatial gradients (*lifelines*) were found to enlarge population heterogeneity [97, 98, 202], and often lead to reduced performance [51–53].

Recent works show that spatial dissolved gas concentration gradients are also expected in industrial-scale gas fermentation bioreactors, such as bubble columns [55, 56] and the EL-GLR [224]. From the microbial perspective, the spatial concentration variations in the EL-GLR were predicted to result in frequent and irregular (5 – 30 s) cycles in dissolved gas (CO, H_2) concentrations with one order of magnitude [224]. Long periods (> 70 s) at low CO concentrations ($c_{L,\mathrm{CO}}^{\mathrm{crit}} < 0.003\,\mathrm{mol\,m^{-3}}$) were hypothesised to result into a starvation regime, with transcriptional changes as consequence, and reduced growth rates and product yields [56].

The impact of the concentration gradient on the cellular metabolic activity, and thus its product formation rate, can be studied by coupling a computational fluid dynamics (CFD) model of a bioreactor with a dynamic metabolic model (cellular reaction dynamics, CRD), in an Euler-Lagrangian computational framework. With a one-way coupled approach and kinetics applied to the Eulerian field, the impact of the concentration gradient on the microbial metabolism can relatively quickly be assessed, while with full Euler-Lagrangian two-way coupling the microbial metabolism also impacts the gradient. The first two-way coupled simulations for industrial fermentations were performed by Reuss and co-workers [58, 98], after which follow-up work was done via various methodologies: Morchain et al. [96] used population balance models for microorganisms, while Haringa et al. [99] used a 9-pool dynamic kinetic model [94]. One-way coupled simulations for bubble column reactors were done for *Saccharomyces cerevisiae* [225] and *C. autoethanogenum* [56, 224], and it was found that microorganisms in bubble columns typically experience shorter starvation periods than in stirred-tank reactors [226]. One of the major limitations of this approach is the computational power required for the high-resolution simulations, which can partially be relieved with the use of compartment models [205, 227, 228]. In recent years, the CFD-CRD modelling approach gained widespread attention, as it opens avenues towards more rational scale-up and optimisation of industrial-scale bioreactors [63, 66, 68].

The metabolism of acetogens and the Wood-Ljungdahl pathway have extensively been described before [11, 229, 230]. Carbon (CO and CO_2) is fixed via the Wood-Ljungdahl pathway, which contains two branches: In the carbonyl branch CO is converted into CO_2 to reduce ferredoxins with the reversible carbon monoxide dehydrogenase (CODH) enzyme, while in the methyl branch CO_2 is converted into formate, which is further reduced to an activated methyl group. CO and the methyl group are then combined into acetyl-CoA at the expense of 1 ATP, which is recovered downstream through acetate production [229]. By the establishment of a chemiosmotic gradient, ATP for growth and maintenance is produced: The Rnf complex exports protons via electron transfer from reduced ferredoxin (Fd^{2-}_{red}) to NAD^+ [230, 231]. Ethanol is mainly produced via the AOR pathway (named after the enzyme acetaldehyde:ferredoxin oxidoreductase), which is thermodynamically feasible only when the intracellular acetate concentration passed the threshold of 1000 times the acetaldehyde level [232, 233]. High intracellular acetate concentrations are obtained at low extracellular pH (5.0) and high concentrations of undissociated acetic acid, since this neutral form of the acid can passively diffuse into the cell [233]. H_2-uptake relates to ethanol production, as its electrons are directly stored in Fd^{2-}_{red} and NADPH [45, 46].

A 12-pool CRD model was recently developed that could describe metabolic dynamics upon metabolic-induced self-oscillations [204] of *C. autoethanogenum* in a chemostat culture [40]. This model could explain how extracellular concentrations (of CO, H_2, CO_2, protons and the products acetic acid, ethanol and 2,3-butanediol), and the intracellular carbon (formate, acetyl-CoA, acetate) and electron pools (Fd^{2-}_{red}, NADH, NADPH), change upon fluctuations in any of these. From the self-oscillating culture, it was found that the biomass-specific ethanol production rate, q_{EtOH}, varies proportionally to the uptake rate of the electron donors (CO and H_2) [40]. By varying the redox potential among several batch cultures Grimalt-Alemany et al. [234] observed severe dynamics (within one order of magnitude) in the NAD(H) pool size and the $NADH/NAD^+$ ratio, and that dynamics in the latter positively correlated with the ethanol specificity.

Since the observed dynamics in both studies (in the order of days) are of metabolic origin (no proteomic differences were observed in [204]) and related to thermodynamics, they may help identify how the short-timescale dynamics occurring in the industrial-scale bioreactor (in the order of seconds) affect the metabolism. Based on the dynamics in these experimental studies, we hypothesise that the temporal-variations in dissolved gas concentration as occurring in the industrial-scale EL-GLR, lead to increased q_{EtOH}, compared to a spatially- and temporally homogeneous environment.

In this work, we coupled the CRD model [40] with our previously developed CFD model of an industrial-scale EL-GLR [197, 224] supplied with a gas mix containing 50% CO, 20% H_2 and 30% CO_2, to study how the dissolved gas concentration and its gradient may influence the metabolic behaviour of *C. autoethanogenum* (with focus on the product spectrum, substrate inhibition, and energy conservation mechanisms). Computations were done with several biomass concentrations to study a wide range of fluctuations on dissolved gas concentrations, from conditions with excess mass transfer to severe mass transfer limitations (from over-reduced to significantly under-reduced conditions). By comparing the CFD-CRD model results with those of a model with constant dissolved gas concentrations, the impact of the dissolved gas concentration and its dynamics on the metabolism and product spectrum of *C. autoethanogenum* could be studied. From the results, we could identify which metabolite pools, reactions and enzymes relate to ethanol production, establish several hypotheses for further research, and propose ways for reactor, strain and process optimisation.

5.2. Methods

CFD-CRD coupling approach

The CFD model (geometry, flow pattern and operation conditions) of an external-loop gas-lift reactor (~500 m^3) that was developed in our previous study [197], was complemented with a mass transfer model in [224], and, in the present work, with the CRD model developed in [40]. The hydrodynamic model was validated on pilot-scale data, while mass transfer rates of the EL-GLR corresponded with industrial standards by assuming bubbles with a constant diameter of 3 mm [197], possible due to coalescence inhibition [206].

The CFD simulation including black-box kinetics (with 5 $g_x\,L^{-1}$) and gas-liquid mass transfer, described in [224], was used as an initial condition for the CFD-CRD model described here. 250,000 Lagrangian particles were released at $t = 3000$ s, and mixed for 200 s, to ensure a homogeneous distribution of particles in the reactor at the start of the CFD-CRD simulation. The pH was kept constant at 5.0, while the initial external product and intracellular metabolite and co-factor concentrations were in the range of the ones used for the CRD model calibration [40, 204] (Table D.1).

As soon as the CRD model was activated, two-way reaction coupling was applied for CO, H_2 and CO_2 according to the method described in Haringa et al. [78, 235], so that the metabolic-kinetic model determines the concentration fields and the gas hold-up. A schematic overview of the model structure and solving procedure is provided (Figure 5.1).

The development and parameterisation of the metabolic kinetic model are described extensively in [40] and the relevant parts for two-way coupling in Appendix D.1.1. The MATLAB model, comprising 12 metabolite pools and 12 reactions, was rewritten into C code, and implemented in an Euler-Lagrangian framework using the DPM_SCALAR_UPDATE macro in Ansys FLUENT. This allowed tracking and updating of particle-associated variables, specifically the metabolite concentrations, at every particle time step Δt_p, that was equal or smaller than the flow time step ($\Delta t_p \leq \Delta t_f = 5$ ms).

Since NADH has the lowest turnover time (~1 ms) the metabolic equations were integrated with a fixed – intracellular – time step Δt_{IC} of 0.1 ms. As $\Delta t_{\mathrm{IC}} \ll \Delta t_p$, an integration routine was implemented using the Runge-Kutta 4th order algorithm. After each Δt_{IC}, the concentration vector was updated until Δt_p was completed. The particle position was updated, while the CRD model was integrated again, until the Eulerian time step Δt_f had been completed. At $t + \Delta t_p$, the volumetric source terms for CO, H_2, and CO_2 were computed for each particle within each volume element (VE) during the time step $\tilde{r}_i(p, \Delta t_p)$ using the concentration differences in that particle (Equation 5.1). It was assumed that the amount of Lagrangian particles for which the CRD model was solved, N_p, are evenly distributed in the EL-GLR and that each particle equally contributes to the total biomass concentration. After Δt_f the volumetric source terms for the dissolved species mass balances were computed per VE by summation over each particle and the number of Δt_p required to reach Δt_f.

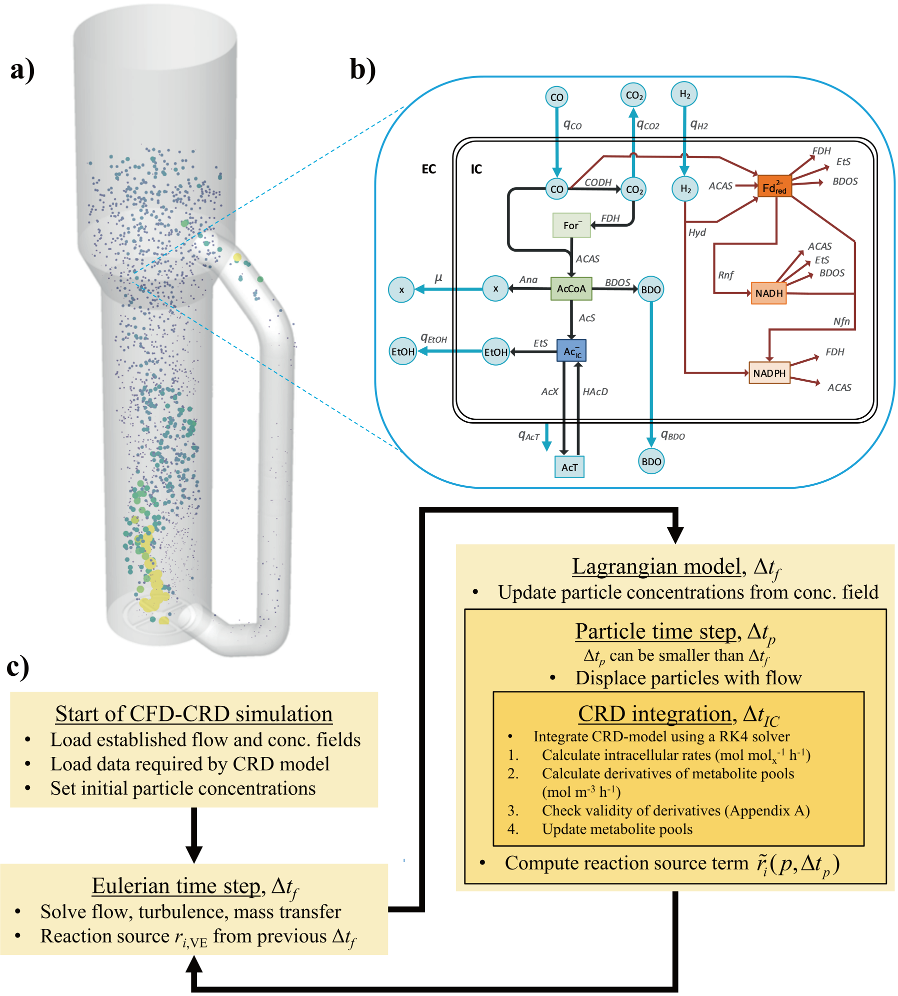
a)
b)
c)
CO
CO$_2$
H$_2$
q_{CO}
q_{CO2}
q_{H2}
EC
IC
CODH
FDH
For$^-$
ACAS
Fd$^{2-}_{red}$
EtS
BDOS
Hyd
Rnf
NADH
Nfn
NADPH
x
μ
Ana
AcCoA
BDO
AcS
EtOH
q_{EtOH}
Ac$^-_{IC}$
AcX
HAcD
q_{AcT}
AcT
q_{BDO}

Start of CFD-CRD simulation
- Load established flow and conc. fields
- Load data required by CRD model
- Set initial particle concentrations

Eulerian time step, Δt_f
- Solve flow, turbulence, mass transfer
- Reaction source $r_{i,\mathrm{VE}}$ from previous Δt_f

Lagrangian model, Δt_f
- Update particle concentrations from conc. field

Particle time step, Δt_p
Δt_p can be smaller than Δt_f
- Displace particles with flow

CRD integration, Δt_{IC}
- Integrate CRD-model using a RK4 solver
1. Calculate intracellular rates (mol mol$_x^{-1}$ h^{-1})
2. Calculate derivatives of metabolite pools (mol m^{-3} h^{-1})
3. Check validity of derivatives (Appendix A)
4. Update metabolite pools

- Compute reaction source term $\tilde{r}_i(p,\Delta t_p)$

Figure 5.1: Overview of the CFD-CRD model and its solving procedure. a) Geometry of the EL-GLR wherein the equations for flow, turbulence and mass transfer are solved, together with the displacement of Lagrangian particles. b) Structure of the metabolic-kinetic model, taken from [40]. c) Step wise solving procedure of the CFD-CRD model.

$$r_{i,\mathrm{VE}} = \frac{\sum\limits_{p=1}^{N_{p,\mathrm{VE}}} \sum\limits_{\Delta t_p}^{\Delta t_f} \tilde{r}_i(p,\Delta t_p)}{V_{L,\mathrm{VE}}} \quad \text{with} \quad \tilde{r}_i(p,\Delta t_p) = \frac{c_i|_{t+\Delta t_p} - c_i|_t}{\Delta t_p} \frac{V_{L,\mathrm{reactor}}}{N_p} \tag{5.1}$$

The metabolic model is based on lin-log kinetics, which is a good approximation of typical hyperbolic kinetics close to a given reference state [236, 237], but leads to inaccurate and unstable behaviour in extreme regions [236, 238]. Thus, results obtained with lin-log based metabolic models are most accurate within a rather narrow range of concentrations (typically one order of magnitude around the reference state). Such behaviour could therefore be expected when the CRD model is solved outside its range of calibration, for example at very low dissolved gas concentrations ($c_{L,\mathrm{CO}} < 0.025\,\mathrm{mol\,m^{-3}}$). As wide concentration ranges occur in the large-scale reactor, several modifications have been made to the solving procedure of the metabolic-kinetic model to increase solution stability (Appendix D.1.2). This comprises rate reversibility and a rate-limitation mechanism based on a given set of minimum concentrations $c_{i,\mathrm{min}}$, preventing unrealistic rates and negative intracellular concentrations.

Model convergence and solution

During Δt_p the metabolite concentrations get updated, while the mass balances of the extracellular gas species only get updated after solving one flow time step Δt_f. As we assumed $c_{i,\mathrm{IC}} = c_{i,\mathrm{EC}}$ for the gases, their extracellular concentrations should be updated as often as possible to preserve the mass balances, requiring very short Δt_f. This implies that the integrated gas uptake rate of a particle during Δt_p, $r_{i,p} = \frac{c_i|_{t+\Delta t_p} - c_i|_t}{\Delta t_p}$, should be equal to the derivative at the beginning of that time step, $r_{i,p} = \left.\frac{dc_i}{dt}\right|_t$ (Equations D.3-D.5). As the flow time step directly affects the total simulation duration, we set Δt_f to 5 ms, a compromise between simulation accuracy and computational efficiency; N_p was fixed at 80,000 on similar grounds (Appendix D.1.5, Figures D.3, D.4).

The CFD-CRD model was solved for 1000 s flow time using Ansys Fluent 2021R2 for three biomass concentration cases, with c_x of 100, 150 and 200 $\mathrm{mol\,m^{-3}}$ (2.5, 3.75 and 5 $\mathrm{g\,L^{-1}}$). Computations were done using the Snellius supercomputer with 128 cores of AMD Rome 7H12 CPU's, with an estimated simulation duration of 530 h per case.

Carbon and electron balance closure (relative error < 5%) for the lifelines were checked for model verification after completion of the CFD-CRD simulations. This was done for *i)* the original, unmodified ("raw"), CRD model (model α), *ii)* the CRD model with rate-limiting modifications (model β), and *iii)* by not considering the values obtained for $c_{L,\mathrm{CO}} < 0.025\,\mathrm{mol\,m^{-3}}$ (model γ).

Post-processing

The following data was exported from FLUENT every 75 ms: the concentrations of each metabolite pool, the q_i of CO, H_2, CO_2, acetate and ethanol, and the position and the local number of particles $N_{p,\mathrm{VE}}$ were written (for 4000 particles, to prevent excessive data transport and storage). With this data, concentration profiles, derivatives and rates could be reconstructed by solving the CRD model for each moment in time in MATLAB, this approach was checked by additionally writing the derivatives for 20 particles. Lifeline data was analysed after removing the first 100 s (approximately one 95% mixing time). For visualisation, the data was smoothed using MATLAB's smoothdata function, according to the moving mean algorithm with smoothing factor of 0.05.

Average particle metabolite concentrations and their derivatives were stored in every VE, according to a rolling-average routine. The number of particles that was present in each VE was registered and used to calculate the rolling average of these variables.

Model with constant concentrations

In order to determine the actual influence of the concentration gradients in the CFD-CRD model, the CRD model was also solved at constant dissolved gas concentrations. This was done for a wide range of fixed dissolved CO and H_2 concentrations. The CO concentration range was determined from the lifeline averages for each c_x, while $c_{L,\mathrm{H_2}}$ was found to be correlated to $c_{L,\mathrm{CO}}$ and determined via linear regression (Figure D.6); the CO_2 concentration was kept constant (Table D.4). The model was integrated with the same Runge-Kutta scheme as the CFD-CRD model, resetting the dissolved gas concentrations after each Δt_{IC} of 0.1 ms. The CRD model was solved for an interval of 1000 s (~1.5 min per simulation). This duration of 1000 s was chosen to be comparable with the CFD-CRD simulations, even if after this time the metabolism does not reach steady state.

5.3. Results and discussion

The results of our modelling study are presented first in terms of mass- and electron balances, to check the influence of the model modifications (section 5.3.1). We look into the global reactor performance, in sections 5.3.2-5.3.4, by analysing energy conservation, characteristic times and averages of individual lifelines. Then in section 5.3.5, we zoom in to discuss the metabolic behaviour and the role of key cellular reactions (particularly the Rnf complex). Several hypotheses that emerged from the study are discussed in section 5.3.6, while in the last section, 5.3.7, practical recommendations are provided for further optimising gas fermentors.

5.3.1. Mass balances in the biomass phase

After solving the CFD-CRD model, we examined mass- and electron balance closure for various model modifications (Figure 5.2). This analysis reveals that the electron balance never closed for the unmodified CRD model (α), with gaps of 10 to 20%. Implementation of the rate-limiting mechanism (model β) damped excessive rates (most prominently in J_{FDH}, J_{CODH}, J_{EtS} and J_{Rnf}). The mechanism ensured mass balance closure (within 5%) and resulted in a substantial reduction in q_{EtOH} from $0.4\,\mathrm{mol\,mol_x^{-1}\,h^{-1}}$ to a more realistic $0.15\,\mathrm{mol\,mol_x^{-1}\,h^{-1}}$.

The lin-log structure of the CRD model induced a numerical depletion of formate, at concentrations outside the range of calibration (Figure D.5). The rate-limiting mechanism dampens the formate depletion (cf. model α with β), although it could not entirely be avoided, due to the high minimum concentration that was required to solve the formate pool (10^{-4} vs. $<10^{-8}\,\mathrm{mol\,m^{-3}}$ for other metabolites). As the rate-limiting modifications were only activated at low $c_{L,\mathrm{CO}}$, the numerically generated formate escalated ethanol production rates (q_{EtOH} increased from 0.09 to $0.15\,\mathrm{mol\,mol_x^{-1}\,h^{-1}}$, cf. β and γ). This results in uncertainty in the model predictions in the low CO concentration range. As both direct CO_2 reduction to formate ($CO_2 + H_2 \longrightarrow \mathrm{For}^- + H^+$) [239], and a formic acid import and formate export mechanism were not included in the CRD model, and as net CO_2 consumption was never observed, inclusion of these reactions in future work could improve the physical reliability of the model at lower $c_{L,\mathrm{CO}}$.

Irrespective of the used model, clear trends in the rates were observed: for example, at increased c_x higher q_{EtOH} was observed at the expense of acetate production ($\mathrm{Ac}^-_{\mathrm{IC}}$ + AcT), while this was partly due to extracellular acetate consumption at increased c_x. As substantial parts of the reactor are operated under low CO conditions, removal or modification of these values from the lifelines would severely affect the magnitude and interpretation of the lifeline results. We hence proceed with model β in further analyses, considering the uncertainty in the model results at low CO concentrations.

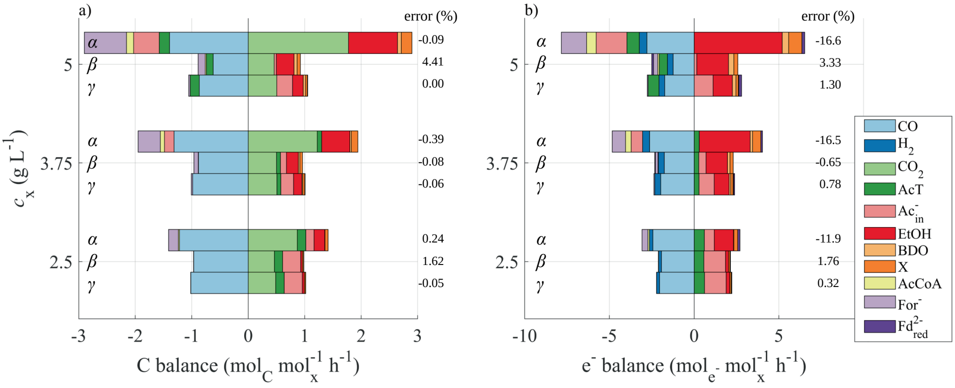

Figure 5.2: Influence of the CRD model choice on the balances (denoted via metabolic rates) of post-processed lifelines. The a) carbon and b) electron mass balances are provided for the three c_x cases with the α: unmodified CRD model; β: CRD model with rate-limiting modifications; γ: model β applied for $c_{L,\mathrm{CO}} > 0.025\,\mathrm{mol\,m^{-3}}$. These low $c_{L,\mathrm{CO}}$ occurred in all c_x cases (62% of data at $5\,\mathrm{g\,L^{-1}} < 0.025\,\mathrm{mol\,m^{-3}}$, 29% at $3.75\,\mathrm{g\,L^{-1}}$ and 10% with $2.5\,\mathrm{g\,L^{-1}}$.). Metabolic rates (colouring in legend) were averaged for 4000 lifelines during 900 s and balanced according to their respective carbon and electron contents. The relative mass balance error was calculated via the difference between the sum of positive and negative rates (as %).

5.3.2. Spatial distribution of energy conservation

In line with the gas hold-up profile in the EL-GLR, there is a clear spatial gradient in dissolved CO concentration, $c_{L,\mathrm{CO}}$, of around one order of magnitude between the high and low concentration zones (Figure 5.3a,b). Similar ε_G and $c_{L,\mathrm{CO}}$ distributions were obtained in our previous study with Haldane-type CO-uptake kinetics [224], indicating that such simulation results are largely insensitive to the model choice. High $c_{L,\mathrm{CO}}$ is observed in locations with high ε_G, such as in the gas plume that is being pushed towards the left side due to the liquid flow exiting the downcomer, and in the gas plume that tends to converge towards the middle of the column. A small $c_{L,\mathrm{CO}}$ pocket is present in the downcomer, due to some gas accumulation. The $c_{L,\mathrm{CO}}$ we derived is still significantly higher than the ones reported in [56] due to the severe mass transfer limitations that were adopted in their simulations ($k_L a \approx 40\,\mathrm{h^{-1}}$, here $360\,\mathrm{h^{-1}}$). q_{CO} follows $c_{L,\mathrm{CO}}$ (Figure 5.3b,c) since uptake inhibition related to $c_{L,\mathrm{CO}}$ was not predicted by the CRD model (see sections 5.3.2 and 5.3.5).

Near the sparger, with locally high $c_{L,\mathrm{CO}}$ and q_{CO}, high rates of ferredoxin reduction are observed (Figure 5.3d). This indicates that our model predicts fast uptake (by diffusion) and utilisation of the incoming CO by CODH, and thus rapidly varying ferredoxin reduction rates, as was hypothesised [240] and measured before [241]. Higher up in the riser, $c_{L,\mathrm{CO}}$ and q_{CO} are still high, but moderate reduction and oxidation rates are observed since the cells might be saturated with $\mathrm{Fd}^{2-}_{\mathrm{red}}$. At zones with low $c_{L,\mathrm{CO}}$ and q_{CO} (downcomer, in the riser near the downcomer outlet, and close to the walls near the top

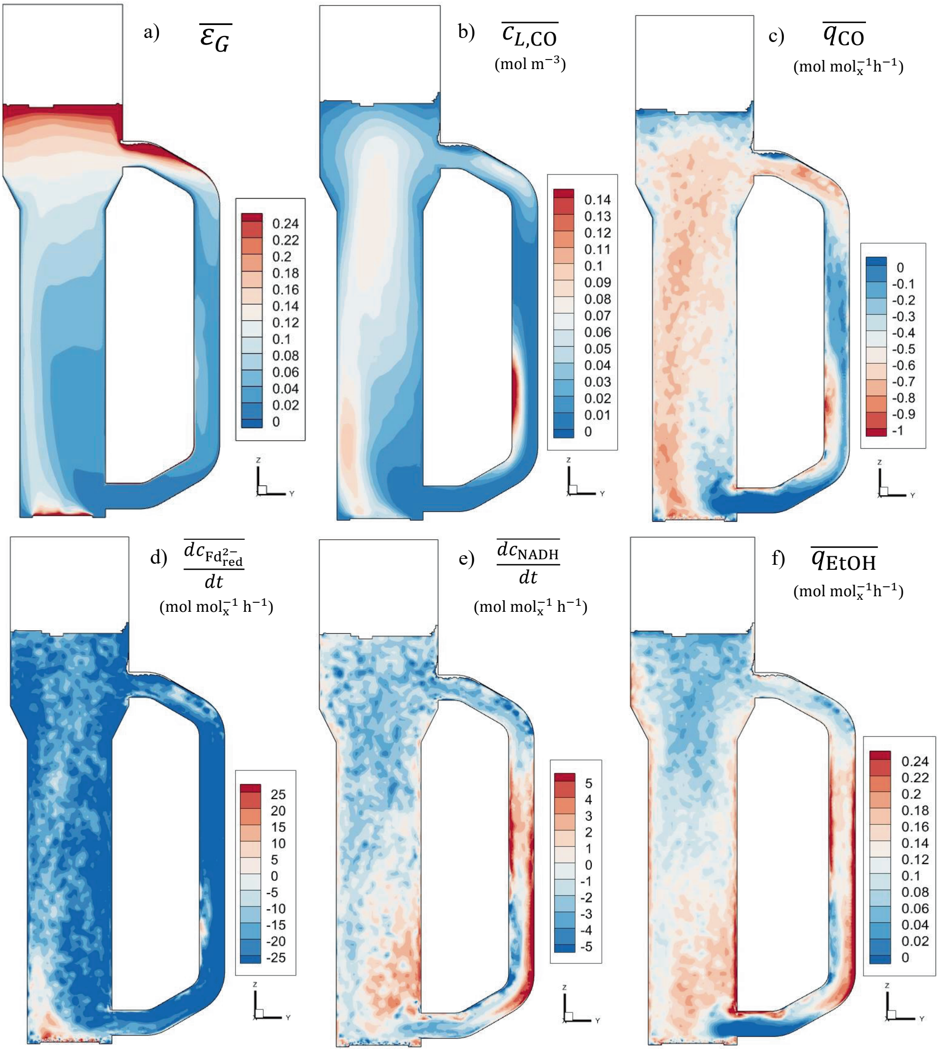

Figure 5.3: Spatial variations in gas hold-up and metabolites in the EL-GLR. Surface plots in the zy-plane (x=0) of the EL-GLR with time-averaged a) ε_G, b) $c_{L,\mathrm{CO}}$, c) q_{CO}, d,e) ferredoxin and NADH reduction rates (red) and oxidation rates (blue) respectively, f) q_{EtOH}. The results are time-averaged during the whole simulation duration of 1000 s, with $c_x = 5\,\mathrm{g\,L^{-1}}$.

separator), high re-oxidation rates of ferredoxin are observed. As soon as $\mathrm{Fd}^{2-}_{\mathrm{red}}$ is oxidised, NAD^+ is reduced and ethanol is produced (Figure 5.3e,f). The model predicts an inverse relationship between the ferredoxin redox state and the ethanol production rate; in zones where ferredoxin is reduced, little ethanol is produced, while ethanol is produced in zones where ferredoxin is oxidised. As a consequence, ethanol is mainly produced in zones with low ε_G and $c_{L,\mathrm{CO}}$ (cf. Figure 5.3b, e). From a microbial point of view, faster variations in dissolved gas concentration are expected to lead to faster ferredoxin oxidation/reduction cycles, and increased variations in q_{EtOH}.

Our model predicts via correlation analysis of lifeline data a significant delay (at least 15 s, with 5 and 3.75 $\mathrm{g_x\,L^{-1}}$, and even 30 s with 2.5 $\mathrm{g_x\,L^{-1}}$) between CO consumption and ethanol production, governed by the dissolved gas concentration gradient: only when $c_{L,\mathrm{CO}}$ (and $c_{\mathrm{Fd^{2-}_{red}}}$), section 5.3.5) decrease, q_{EtOH} increases. This lag time is slightly shorter (~25%) than the circulation time, indicating that ethanol is being produced in a rather short period within the circulation. This is in sharp contrast with results from black-box and genome-scale metabolic models (using dFBA simulations), which both assume metabolic steady-state and show high production rates at locations with high gas uptake rates [75]. In our case the reactor can be subdivided in two zones: (1) a ferredoxin reduction zone and (2) a re-oxidation zone. Video S2 clearly shows the consequential differences in ethanol production zones compared to the black-box model. While further research is required to confirm these predictions, the model suggests a process design and operation that produces multiple, but smaller, of these zones, leading to shorter redox cycles, and improved ethanol productivity.

5.3.3. Analysis of characteristic times

Estimation of characteristic and turnover times is a widely used method for quick assessment of reactor performance and identification of limiting processes [48–50]. From the CFD-CRD model of the EL-GLR becomes clear that mixing and mass transfer are equally slow and generally slower (i.e., higher characteristic time) than CO-uptake (Figure 5.4), indicating that a dissolved CO gradient exist (in the cases with 3.75 and 5 $\mathrm{g_x\,L^{-1}}$), which was confirmed in Figure 5.3b. H_2-uptake is significantly slower than CO-uptake, and its high characteristic time is expected to lead to a spatially well-distributed $c_{L,\mathrm{H_2}}$. The slow H_2-uptake mechanism was expected from experiments [45], as H_2 is thermodynamically the less preferred electron source in a gas mixture [242], and the cell can generate more ATP and reducing equivalents ($\mathrm{Fd^{2-}_{red}}$, NADH, NADPH) per electron from CO than H_2 [243]. The H_2-uptake rates predicted with the CFD-CRD model are significantly lower than the ones that were predicted with the Monod kinetics used in our previous study (Figure D.7), indicating differences between models on the kinetic behaviour of H_2-uptake.

The model predicts that electron storage is done mainly via the ferredoxin pool. The $\mathrm{Fd^{2-}_{red}}$ pool has a similar turnover time compared to CO-uptake, especially in the transport limited regime with 5 $\mathrm{g_x\,L^{-1}}$. The turnover times mainly depend on the concentrations of the metabolite pools, causing that NADH and NADPH show a 100 and 10 time lower turnover time, respectively, which indicate even faster redox cycles of $\mathrm{NAD^+}$ and $\mathrm{NADP^+}$. $\mathrm{Fd^{2-}_{red}}$ can thus be hypothesised as an electron buffer for the cell. As the intracellular concentration of $\mathrm{Fd^{2-}_{red}}$ was never measured, this hypothesis remains to be verified, although low concentrations of NADH and NADPH have indeed been measured before [204].

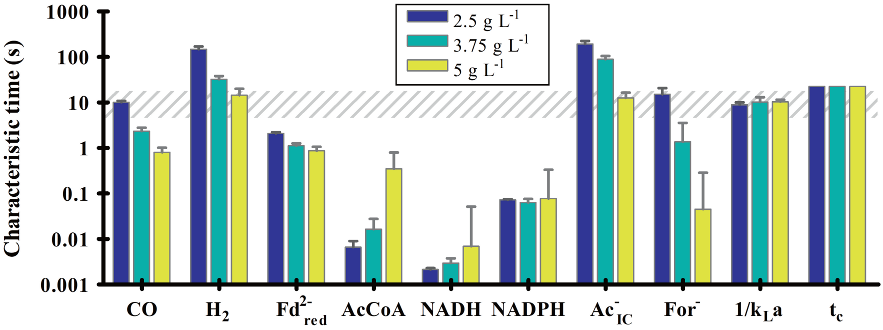

Figure 5.4: Characteristic times for metabolite consumption, mass transfer and mixing. A spatial gradient may be present when the characteristic times are below the dashed grey zone, representing transport limitations. Turnover times of the metabolite pools were computed as the median of the ratio of the metabolite pool size and its depletion rate for 4000 lifelines ($\tau_i = c_i/J_i$). Error bars represent the standard deviation over 4000 lifelines considering a normal distribution. Following the models in [224], $k_L a$ was derived as the 900 s time-and-volume-averaged $k_L a$ of CO, with the error bar representing the standard deviation during that period, while the circulation time t_c was estimated via t_m (1/4 of the 95% mixing time of 90 s in every case [71]).

Similarly, the turnover time of acetate is high, while the other intermediates in the Wood-Ljungdahl pathway (formate and acetyl-CoA) are depleted significantly faster, in the cases with higher c_x. This shows a relatively fast pathway from acetyl-CoA to acetate production, despite the high concentrations of intracellular acetate due to the low pH (5.0) and the high extracellular concentration of acetic acid ($90\,\mathrm{mol\,m^{-3}}$). An interesting observation is the high formate turnover time: In the case with $2.5\,\mathrm{g_x\,L^{-1}}$, formate is overproduced at highly reduced conditions (with very high $c_{\mathrm{Fd^{2-}_{red}}}$, and correspondingly at high $c_{L,\mathrm{CO}}$) (Figure D.9). Formate production has been observed experimentally to relate with pressure [169, 244], or with very low biomass concentrations [41], both resulting into very high $c_{L,\mathrm{CO}}$.

The fast turnover time of CO suggests that the two-way coupling is not needed for the prediction of the $c_{L,\mathrm{CO}}$ gradient, since a one-way coupling routine (with the Haldane kinetics) could also predict a similar gradient and lifelines. The CO- and H_2-uptake rates in the CRD model are, however, predicted by considering the intracellular concentrations, which could lead to an inhibition effect (see section 5.3.5). In order to account for such effects, implementation of a two-way coupling strategy is required.

5.3.4. Influence of dissolved CO on product spectrum

To study the influence of the concentration gradient on the global reactor performance, the results from the CFD-CRD simulations, based on their time-averaged biomass-specific uptake, product formation rates, and observed concentrations, were compared with the results from the model with constant dissolved gas concentrations (Figure 5.5). To check the correspondence of the model predictions with experimental trends and values, we retrieved q_i and calculated $c_{L,\mathrm{CO}}$ for several chemostat experiments. Overall, the trends and the values of the experimental studies corresponded well to those predicted by the model.

The models overestimate the average CO-uptake rate compared to experimental data at high $c_{L,\mathrm{CO}}$ (Figure 5.5a). This led to a rather constant q_{CO} while there was a large spread in $c_{L,\mathrm{CO}}$ in our model, rendering q_{CO} unsuitable for trend analysis. This is partly due to the calibration of the CRD model, which predicted q_{CO} consistently around $1\,\mathrm{mol\,mol_x^{-1}\,h^{-1}}$ while more variation was observed in the experimental data [218]. The (Haldane and Monod-type) kinetic models that have been developed so far (e.g., [34, 40, 208]), are unable to predict the high q_{CO} that is observed experimentally (e.g., [45]). We noticed wide variability in q_{CO} in chemostat experiments with low $c_{L,\mathrm{CO}}$. Due to this variability and the lack of models that adequately link $c_{L,\mathrm{CO}}$ and q_{CO}, we are unable, at this point, to establish any hypotheses or trends based on q_{CO}, and decided to focus our analysis on the role of $c_{L,\mathrm{CO}}$ on the product spectrum.

Acetate production (Figure 5.5b) is slightly underestimated by the model in all scenarios, but the trend clearly corresponds: more acetate is produced at higher $c_{L,\mathrm{CO}}$. The trend of q_{EtOH} and the ethanol-per-electron yield (Figure 5.5c,d) match surprisingly well with the experimental data, and is clearly inverse to the acetate trend: more ethanol is produced at lower $c_{L,\mathrm{CO}}$. This relationship is also visible in the acetate-per-ethanol ratio (Figure 5.5e), where it is clear that $q_{\mathrm{EtOH}} > q_{\mathrm{AcT}}$ at $c_{L,\mathrm{CO}} < 0.1\,\mathrm{mol\,m^{-3}}$. Our model and experimental data suggest that ethanol is produced at the expense of acetate at lower $c_{L,\mathrm{CO}}$, while acetate is produced at the expense of ethanol at high $c_{L,\mathrm{CO}}$.

The CFD-CRD model suggests that the gradients expected at scale benefit ethanol production, since consistently a significant (~25%) higher q_{EtOH} and $q_{\mathrm{EtOH}}/q_{\mathrm{e^-}}$ and lower acetate production are predicted, compared to the results obtained without concentration fluctuations ($p < 10^{-4}$ in all c_x cases using a one-sample t-test, wherein the distribution of lifelines is compared to the mean result of the constant concentration model in that respective range). Section 5.3.5 further explores potential reasons behind this behaviour. Another interesting observation is that at large-scale, population heterogeneity is likely to be observed, visible from the wide scattering of the lifeline-averages in Figure 5.5. The relatively short simulation duration of the CFD-CRD model could be a factor underlying the scattering, but given the currently available computational resources longer two-way coupled simulations with such a resolution are practically unfeasible. For example, to match the long simulation time of the *P. chrysogenum* industrial fermentation (70 hours) with the current model setup, ~14 years of simulations would be required. The development of reduced order models (e.g., compartment models) could be a solution to alleviate this problem [226–228].

Our model, in conjunction with experimental data, indicates that $c_{L,\mathrm{CO}}$ is a key factor influencing the onset of solventogenesis. At high $c_{L,\mathrm{CO}}$, acetogenesis prevails; however, as $c_{L,\mathrm{CO}}$ decreases below ~0.1 $\mathrm{mol\,m^{-3}}$, ethanol production rate surpasses that of acetate production. A phase guided by electron supply shortages and energy starvation has been observed at very low dissolved gas concentrations ($c_{L,\mathrm{CO}} < 0.05\,\mathrm{mol\,m^{-3}}$). In this phase, there is a net consumption of acetate: Acetate is reduced to ethanol, with CO serving as an electron source essential for growth and maintenance (through ATP production via Rnf). As the re-oxidation of the electron carriers occurs via the AOR route, acetate – which freely diffused into the cell as acetic acid – is being converted into ethanol [233, 240]. This phenomenon was also observed in the second reactor in [31], with biomass recycle and high CO conversion and probably very low $c_{L,\mathrm{CO}}$, where both acetate and CO consumption resulted into very high ethanol productivity, although this particular result could also be linked to shortages of essential nutrients as vitamins and metals. It is well known that acetate supplementation enhances the ethanol productivity [39, 41, 199], while it has been demonstrated that exogenously introduced ^{13}C-labelled acetate was converted into ^{13}C-labeled ethanol on CO-grown *C. autoethanogenum* [199]. All these observations lend support to the feasibility of this starvation-induced metabolism at low $c_{L,\mathrm{CO}}$.

A simple thermodynamic analysis could explain why more ethanol is produced at lower $c_{L,\mathrm{CO}}$ (Table D.5). During ethanol production, more ATP is produced compared to acetate production (~2 vs. 1.5 $\mathrm{mol_{ATP}/mol_{product}^{-1}}$) [233, 245], since ethanol production releases more energy ($\mathrm{kJ\,mol_{CO}^{-1}}$) [32], and it is thus not a surprise that ethanol production relates to growth, confirmed both experimentally [45] and in our model (Figure D.12). When more CO is available, acetate might be produced since there is enough carbon and energy resource for growth, relating to the hypothesis of maximum energy dissipation [246]. The resulting acetic acid decreases pH (increasing the proton motive force used for energy generation), safeguarding sustainable growth in the future. From an evolutionary perspective, it might be that this presents a competitive advantage against other microorganisms [247], and thus a survival strategy in nature. Ethanol production via solventogenesis might then only be a (stress) reaction to preserve more energy at low dissolved gas concentrations, while in case with even lower $c_{L,\mathrm{CO}}$, the starvation metabolism is employed for increased energy generation.

As large parts of the data used for the generation of Figure 5.5 were outside the calibrated range of the model (i.e., $c_{L,\mathrm{CO}} < 0.025\,\mathrm{mol\,m^{-3}}$), a similar figure was generated without considering that data in this range (Figure D.10). Obviously, this led to higher average $c_{L,\mathrm{CO}}$ and a lower spread in $c_{L,\mathrm{CO}}$ amongst lifelines. More interestingly is the decreased q_{EtOH} for the 5 $\mathrm{g\,L^{-1}}$ case (as noted in section 5.3.1), while the trends for all compounds remained similar among the complete $c_{L,\mathrm{CO}}$ domain. The gradient still led to significant ($p < 10^{-4}$) increases in q_{EtOH}. The uncertainty in the very low $c_{L,\mathrm{CO}}$ range requires caution for quantitative analysis under these conditions.

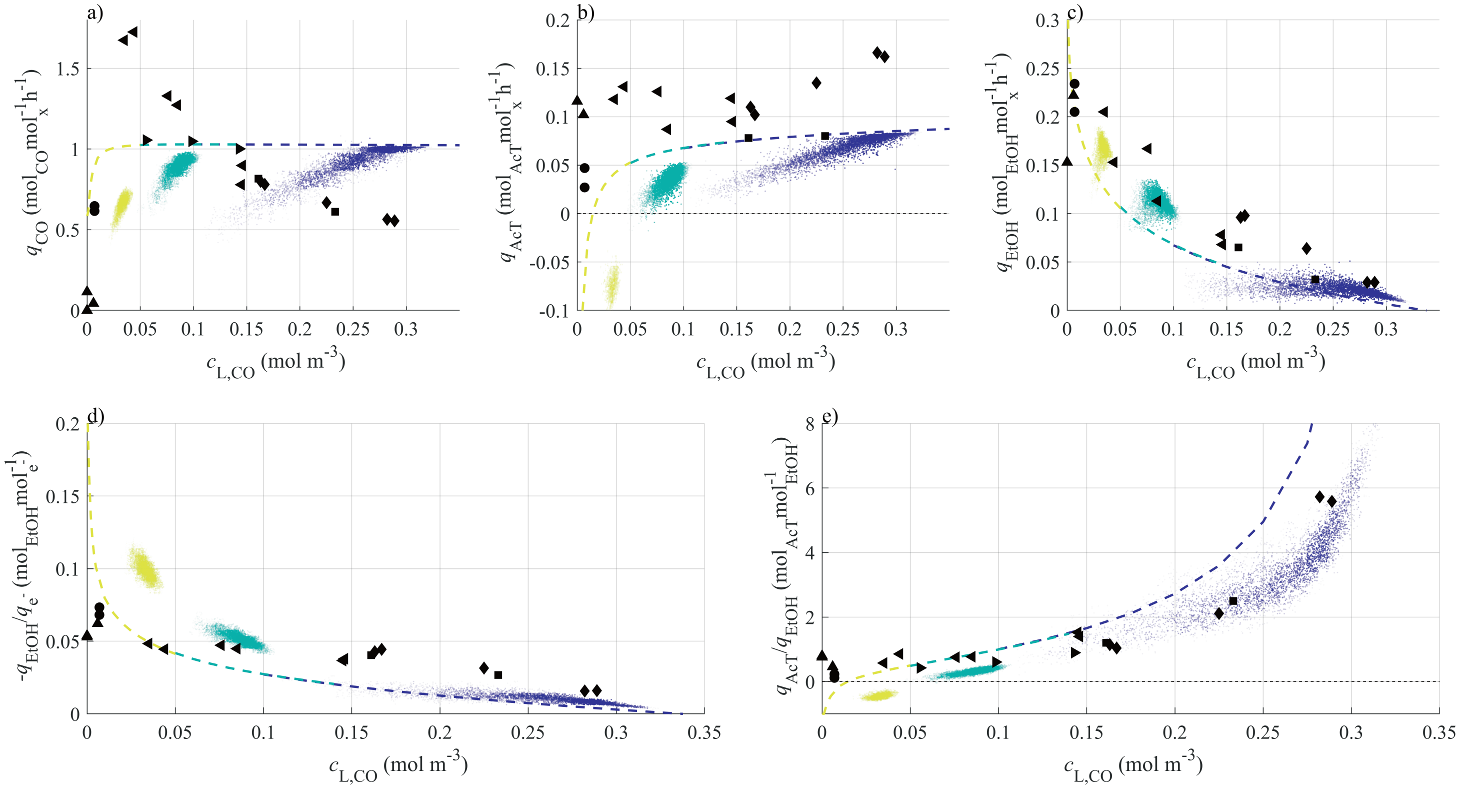

Figure 5.5: Comparison of lifeline-averages from the CFD-CRD model with the constant concentration model and experimental data. The average biomass-specific rates and yields are plotted against the average $c_{L,CO}$: a) q_{CO}, b) q_{AcT}, c) q_{EtOH}, d) the electron-to-ethanol yield q_{EtOH}/q_{e^-} ($q_{e^-} = 1/2(q_{CO} + q_{H_2})$, and e) the acetate-per-ethanol ratio q_{AcT}/q_{EtOH}. The scatters, with varying transparency to reduce overplotting, represent 900 s averages for ~4000 lifelines for each c_x simulation (blue 2.5; green 3.75; yellow 5 g L^{-1}), the dashed line simulations with constant dissolved gas concentrations at the indicated biomass concentrations, and the markers reconciled [218] experimental chemostat data: ◆ [44]; ■ [46] (CO + H_2); • [46] (CO); ▲ [90]; ◀ [45]. $c_{L,CO}$ in ▶ [89], was estimated using their provided $k_L a$

5.3.5. Metabolism during dynamic conditions

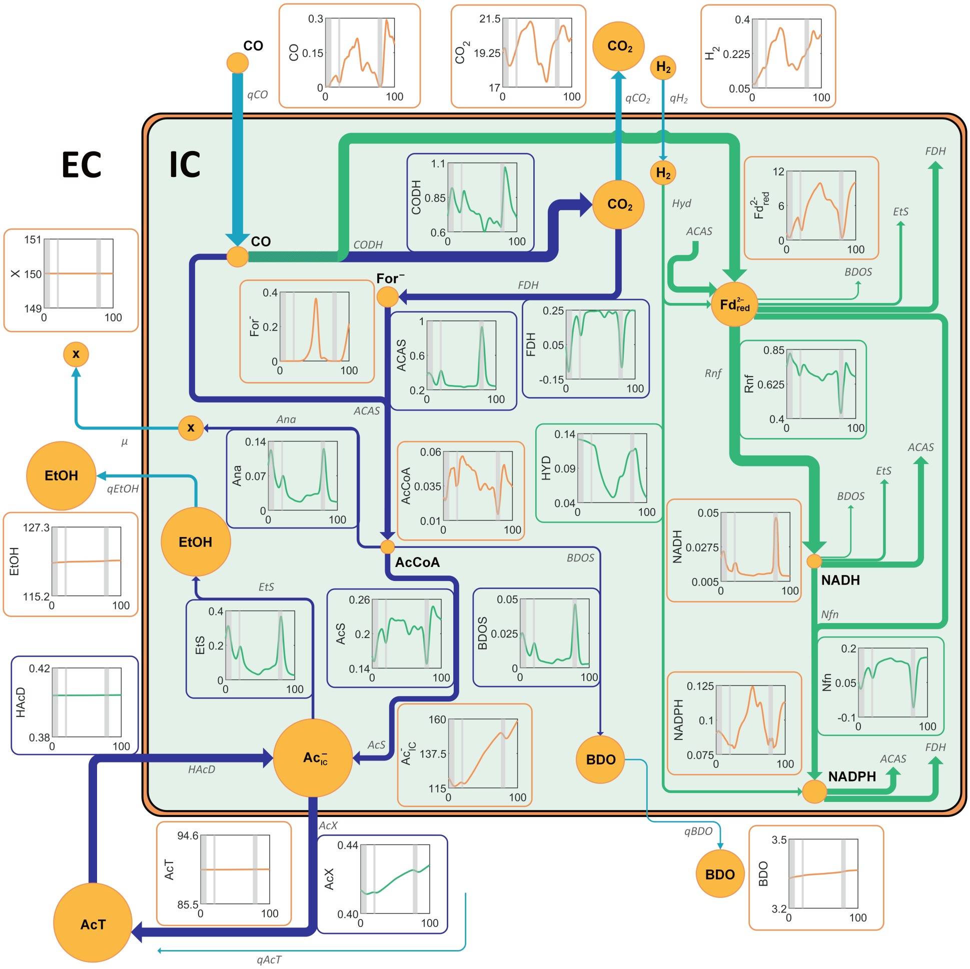
CO
qCO
CO 0.3 0.15 0 0 100
CO2 21.5 19.25 17 0 100
CO2
H2
qCO2
qH2
H2 0.4 0.225 0.05 0 100
EC
IC
H2
CO2
CODH 1.1 0.85 0.6 0 100
CO
CODH
Hyd
ACAS
Fd2- red 12 6 0 0 100
FDH
EtS
BDOS
X 151 150 149 0 100
For−
For- 0.4 0.2 0 0 100
FDH
ACAS 1 0.6 0.2 0 100
FDH 0.25 0.05 -0.15 0 100
Fd2- red
Rnf
Rnf 0.85 0.625 0.4 0 100
x
μ
x
Ana
ACAS
Ana 0.14 0.07 0 0 100
AcCoA 0.06 0.035 0.01 0 100
HYD 0.14 0.09 0.04 0 100
ACAS
EtS
BDOS
EtOH
qEtOH
EtOH
NADH 0.05 0.0275 0.005 0 100
AcCoA
BDOS
NADH
EtOH 127.3 115.2 0 100
EtS
EtS 0.4 0.2 0 0 100
AcS 0.26 0.2 0.14 0 100
BDOS 0.05 0.025 0 0 100
Nfn
Nfn 0.2 0.05 -0.1 0 100
HAcD 0.42 0.38 0 100
NADPH 0.125 0.1 0.075 0 100
AcS
Ac−IC 160 137.5 115 0 100
HAcD
Ac−IC
BDO
ACAS
FDH
NADPH
AcX
qBDO
AcT 94.6 85.5 0 100
AcX 0.44 0.40 0 100
BDO
BDO 3.5 3.2 0 100
AcT
qAcT

Figure 5.6: Metabolism of *C. autoethanogenum* during large-scale gas fermentation. 100 seconds of a lifeline for the case with 3.75 $g_X\,L^{-1}$ is shown with its concentration (in $mol\,m^{-3}$) and rate (in $mol\,mol_X^{-1}\,h^{-1}$) fluctuations. Pool sizes and arrow thickness are approximative to the median concentrations and rates during the whole lifeline. The metabolism in the cases with 2.5 and 5 $g_X\,L^{-1}$ are provided in the supplementary material (Figure D.13 and D.14). Shaded areas in the plots mark zones with $c_{L,CO} < 0.025\,mol\,m^{-3}$.

The effect of the dissolved gas concentration fluctuations in the EL-GLR on the concentrations of metabolites and the modelled rates are schematically depicted in Figure 5.6. This representation allows us to follow the route of the carbon (blue lines) and electrons (green lines) and gives an impression on which processes drive the production of ethanol.

Following the carbon, a direct coupling between CO-uptake and acetate synthesis is seen. The Wood-Ljungdahl pathway, represented with the ACAS flux (J_{ACAS}) in Figure 5.6, is almost always activate with fairly constant rate, although it gets an impulse during a period at low $c_{L,\mathrm{CO}}$ due to the increased NADH availability in the cell. Consequently, the AcCoA concentration follows the peaks of dissolved CO, although it is slightly influenced by the periods at low CO. The net amount of AcCoA slowly decreased during the analysis, a trend also observed in the simulation with constant dissolved gas concentrations (Figure D.2). The rate of acetate formation (J_{AcS}) follows the CO availability, albeit slightly lower than J_{ACAS}, since small amounts of AcCoA are also being used for the formation of biomass and 2,3-BDO. The cell is continuously busy with the acetate import/export cycle: High rates of J_{AcX} and J_{HAcD} were predicted (~0.45 and ~0.40 $\mathrm{mol\,mol_x^{-1}\,h^{-1}}$, respectively), around three times higher than its formation rate via J_{AcS}. Despite these efforts, there is still some acetate accumulation in the cell. In the case with less biomass, there is more acetate export, but also more intracellular acetate accumulation, while lower intracellular acetate concentrations are obtained in the case with more biomass. In the latter case, there is net consumption of acetic acid ($J_{\mathrm{HAcD}} > J_{\mathrm{AcX}}$), which leads to increased ethanol production rates; the starvation-induced metabolism, as explained in the previous section.

Most (~75%) of the consumed CO is being used for electron capture with CODH, thereby producing CO_2 ($J_{\mathrm{CODH}} > J_{\mathrm{FDH}}$), and reducing ferredoxin. $c_{\mathrm{Fd^{2-}_{red}}}$ follows the same profile as $c_{L,\mathrm{CO}}$, but its fluctuations are slower and less steep, showing its electron buffering capacity. Around 70% of the reduced ferredoxin is re-oxidized due to Rnf activity, the enzyme that shuttles the electrons from $\mathrm{Fd^{2-}_{red}}$ to $\mathrm{NAD^+}$ [248], and translocates protons across the cell membrane for the generation of the proton motive force and ATP [231]. NADH, in turn, is mostly used to drive the Wood-Ljungdahl pathway (ACAS) and for the production of the NADPH (via Nfn) that is required for ACAS and FDH.

In a period with low $c_{\mathrm{Fd^{2-}_{red}}}$, $q_{\mathrm{H_2}}$ is increased which relates to increased q_{EtOH} (Figure D.8, D.11). The first observation could relate to inhibition of $q_{\mathrm{H_2}}$ by reduced ferredoxin, while a similar (but weaker) trend was obtained for CO-uptake. This caused that decreased CO- and H_2-uptake rates were actually observed at high reduced ferredoxin concentrations, and not at high CO or H_2 concentrations *per se* (cf. Figure D.7 and D.8). Inhibition of gas uptake could thus, next to binding of CO to hydrogenases, also be explained by a highly reduced intracellular state (i.e., too high intracellular concentrations of electron carriers), as was hypothesised before [249]. Our model results and chemostat experiments [45, 46] show that $q_{\mathrm{H_2}}$ proportionally relates to q_{EtOH}. The ferredoxin that is reduced due to H_2-uptake is probably instantaneously being re-oxidized again to drive EtS and Rnf (Figure 5.6), Because of the temporary lack of reducing equivalents, this mechanism guarantees electron inflow even at $c_{L,\mathrm{CO}}$.

At dynamic conditions, a direct relationship between and $c_{\mathrm{Fd^{2-}_{red}}}$ and $c_{L,\mathrm{CO}}$ ($c_{\mathrm{Fd^{2-}_{red}}}$ increases with $c_{L,\mathrm{CO}}$) is observed (Figure 5.7a), while $c_{\mathrm{Fd^{2-}_{red}}}$ shows an inverse hyperbolic relationship to q_{EtOH} (Figure 5.7b). This indicates that, irrespective of other phenomena occurring in the cell, q_{EtOH} is mostly determined by the temporal $c_{\mathrm{Fd^{2-}_{red}}}$. If other phe-

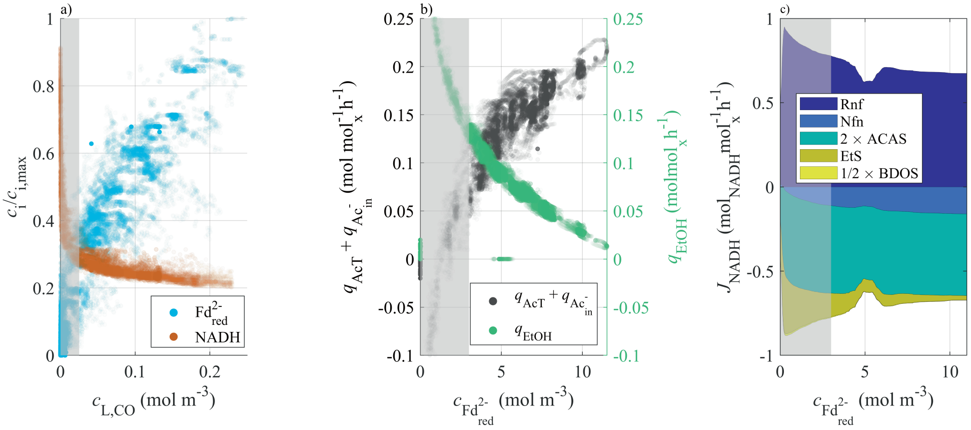

Figure 5.7: Mechanism towards ethanol production in a lifeline. a) The relationship between the concentration of electron carriers Fd^{2-}_{red} (blue) and NADH (orange) is shown and their corresponding $c_{L,CO}$ ($c_{Fd^{2-}_{red},max}$ = 11.5 mol m^{-3}, $c_{NADH,max}$ = 0.04 mol m^{-3}). b) the relationships between acetate production (extracellular + intracellular) (black) and ethanol production (green) with $c_{Fd^{2-}_{red}}$. c) the rates of NADH production (Rnf, darkblue) and consumption (Nfn, light blue; ACAS, green; Ethanol Synthesis, gold; BDO Synthesis; yellow) as function of $c_{Fd^{2-}_{red}}$. The scatters mark temporal observations during a lifeline (between 100 and 1000 s), and their density denotes the probability of occurrence. c) is an energy balance that can be made since $\tau_{NADH} \ll \tau_{Fd^{2-}_{red}}$. Shaded areas mark zones with $c_{L,CO} < 0.025$ mol m^{-3}.

nomena would have influenced q_{EtOH}, a larger spread in q_{EtOH} would be observed at the each $c_{Fd^{2-}_{red}}$. The NADH concentration shows a strong relationship with $c_{Fd^{2-}_{red}}$ (c_{NADH} decreases with $c_{Fd^{2-}_{red}}$), so on its turn c_{NADH} proportionally relates to q_{EtOH}, as was shown experimentally [233, 234, 250]. We could thus predict that, at some point, with low $c_{L,CO}$ and thus low $c_{Fd^{2-}_{red}}$, high amounts of NADH and consequentially increased q_{EtOH} are obtained. The increased q_{EtOH} is due to decreases acetate production (Figure 5.7b), this way conserving mass balances (Figure D.5).

The delay that is observed between CO-uptake and ethanol production (a peak in q_{EtOH} ~50 s; Figure 5.6) is present when $c_{L,CO}$ and, and consequentially $c_{Fd^{2-}_{red}}$, decreased enough to stimulate ethanol production. For example, no clear increase in q_{EtOH} is observed after peaks in $c_{L,CO}$, until $c_{Fd^{2-}_{red}}$ decreases to ~6 mol m^{-3}, when also J_{AcS} slows down, reducing acetate production. Therefore, the delay is caused by the dynamics in the EL-GLR and causes that the microorganisms cycle between two states: one state with high $c_{L,CO}$ and $c_{Fd^{2-}_{red}}$, and thus low c_{NADH} and q_{EtOH}, and another state with low $c_{L,CO}$ and $c_{Fd^{2-}_{red}}$, but with increased c_{NADH} and q_{EtOH}.

Dissolved CO concentration fluctuations (e.g., with increased c_x, Figure D.14) induce the mentioned redox cycling and ethanol production. This happens at the expense of the intracellular acetate pool and J_{AcS}, and in the long term at the expense of the extracellular acetate concentration. The non-linear behaviour of metabolism (here described by lin-log kinetics), the irregular duration and the large variation in $c_{L,\mathrm{CO}}$ in low concentration zones ($< 0.05\,\mathrm{mol\,m^{-3}}$) might cause that non-linear increases in ethanol productivity are observed upon concentration fluctuations. The effect of such variations has never been determined experimentally, a good start for experimental verification would be the developed scale-down simulator in our previous paper [224].

The only reaction that reduces NAD$^+$ to NADH in the CRD model is Rnf, which is active in the whole $c_{\mathrm{Fd}^{2-}_{\mathrm{red}}}$ domain (Figure 5.7c). The resulting NADH is mostly used in the Wood-Ljungdahl pathway (by ACAS), while a small fraction is used for NADPH generation, which is also required in ACAS. At lower $c_{L,\mathrm{CO}}$ and $c_{\mathrm{Fd}^{2-}_{\mathrm{red}}}$, Rnf activity increases while the majority of the resulting NADH is re-oxidized via the Ethanol Synthesis pathway. Thus, the increased Rnf activity at lower $c_{\mathrm{Fd}^{2-}_{\mathrm{red}}}$, can be associated to increases in q_{EtOH}. Metabolic models have previously predicted that increased Rnf activity relates with increased ethanol production in syngas fermenting *Clostridium spp.* [44, 45, 90, 243], although such relationships have never been observed experimentally. A proportional relationship between Rnf and ethanol production was found, however, in *C. thermocellum* grown on cellobiose [251].

The CFD-CRD model also predicts a coupling between ethanol production and growth rate. At higher growth rates, more ethanol is produced (Figure D.12) which complies with experimental observations (e.g., [45]). This might be because growth happens when there is more ATP available and that is the case when Rnf is more active as Rnf increases the proton motive force. No relation, however, between acetate production (q_{AcT}) and growth rate was observed (Figure D.12), which might explain the contrasting experimental data regarding growth rate.

5.3.6. Emerging hypotheses

By mathematically modelling syngas fermentation, we derived a mechanistic understanding on how the dissolved gas concentration (and its fluctuations) influence the product spectrum of *C. autoethanogenum*, which we could support with experimental evidence. Thus far, experimentalists made statements that, for example, *i)* higher dilution rates increase q_{EtOH} [45, 240], *ii)* that lower mass transfer rates result in lower $c_{L,\mathrm{CO}}$ [41], or *iii)* that increased pressure leads to increased formate production [169]. But, by linking $c_{L,\mathrm{CO}}$ (and potentially q_{CO}) to the product spectrum, we could merge such statements into one overarching explanation, by suggesting that *i)* q_{EtOH} is increased at lower $c_{L,\mathrm{CO}}$, *ii)* that acetogenesis occurs at increased $c_{L,\mathrm{CO}}$ and that *iii)* formate accumulates in over-reduced situations (very high $c_{L,\mathrm{CO}}$ and $c_{\mathrm{Fd}^{2-}_{\mathrm{red}}}$). In practice, this might mean that, for example, the faster growth in [45], coupled to high q_{CO}, might have let to the fall in $c_{L,\mathrm{CO}}$ so that q_{EtOH} is increased. The inverse relationship between q_{CO} and $c_{L,\mathrm{CO}}$ indicates a very low K_S (supported by thermodynamics [32]) and low inhibition constant K_I for Haldane kinetics, consistent with the experimentally expected fast CO-uptake [33, 45, 229]. Meanwhile, the increased acetate concentration should be noted in the discussion [39, 41]. To test our observations, the influence of $c_{L,\mathrm{CO}}$ on q_{CO} and q_{EtOH} should be studied in chemostats with CO measurements (e.g., using the protocol in [252] or estimated following [218]) and with fixed operating conditions (i.e., constant growth rates and liquid phase concentrations). As a result, researchers on gas fermentation should link their results to microbial experiences, and thus dissolved gas concentration, and not to operational factors at the reactor-level such as pressure, dilution, or mass transfer rate (e.g., governed by stirrer speed).

The trends in Figure 5.7b might seem remarkable, from a steady-state point of view. For example, in chemostats it has been observed that increased electron (or dissolved gas) uptake rates increase q_{EtOH} [45, 240]. As electron uptake is associated to reduction of ferredoxin, which should lead to increased c_{NADH} and thus q_{EtOH}, it might seem controversial that, in our results, high q_{EtOH} is only obtained at low $c_{\mathrm{Fd}^{2-}_{\mathrm{red}}}$. We identified four hypotheses why we observed this trend in Figure 5.7b.

The first *i)* is that $c_{\mathrm{Fd}^{2-}_{\mathrm{red}}}$ is around 100 times higher than c_{NADH}, causing that each NAD^+ molecule needs to be reduced and re-oxidized 100 times in order to re-oxidize 100 ferredoxin molecules. This might cause that NAD^+ is the limiting component in the Rnf reaction. This hypothesis might be tested by determining the $c_{\mathrm{Fd}^{2-}_{\mathrm{red}}}/c_{\mathrm{NADH}}$ ratio during over-reduced and under-reduced conditions, although it is experimentally very challenging and never done so far in gas fermenting bacteria.

Another hypothesis *ii)* might be related to the thermodynamics of the AOR pathway (acetate to ethanol reduction) as discussed in [234], where was stated that – at constant $c_{\mathrm{Fd}^{2-}_{\mathrm{red}}}$, due to long-lasting batch conditions – there is a linear relationship between the $\mathrm{NADH}/\mathrm{NAD}^+$ ratio and the ethanol-to-acetate ratio (similar to our results, since q_{AcT} decreases when q_{EtOH} increases). If the $\mathrm{Fd}^{2-}_{\mathrm{red}}/\mathrm{Fd}_{\mathrm{red}}$ ratio is increased in their model, at a constant ethanol-to-acetate ratio, a lower $\mathrm{NADH}/\mathrm{NAD}^+$ ratio may be expected, similar to our model results in Figure 5.7.

Furthermore *iii)*, the time scale in a chemostat (order of days) is significantly longer than that of liquid circulation and mass transfer (usually > 20 s) and intracellular metabolite and uptake (< 1 s; Figure 5.4), which could lead to concentration gradients at lab-scale and similar $c_{\mathrm{Fd}^{2-}_{\mathrm{red}}}/c_{\mathrm{NADH}}$ fluctuations.

The last hypothesis *iv)* relates to binding of dissolved CO to iron-sulfur complexes present in Rnf [248, 253] or in ferredoxins [230], similarly to its binding to the Fe-S complexes in hydrogenases [11, 254, 255], and thereby inhibiting Rnf activity. When $c_{L,\mathrm{CO}}$ (and $c_{\mathrm{Fd}^{2-}_{\mathrm{red}}}$) decreases, less Rnf inhibition might be obtained causing that its rate could be increased.

Clearly, too little is known at this moment on the metabolism of acetogens at low dissolved gas concentrations, and during dynamic conditions. To improve our understanding, experiments should be performed wherein *C. autoethanogenum* is exposed to short (5 – 30

s) shortages in $c_{L,\mathrm{CO}}$, so that the effect of a metabolic stall can be studied, which can be used for model updates. Development of measurement methods for $c_{\mathrm{Fd}^{2-}_{\mathrm{red}}}$ and $c_{L,\mathrm{CO}}$ at such conditions would be highly relevant. The ratio of reduced-to-oxidized ferredoxin was estimated to be high during batch fermentations, while the NADH/NAD$^+$ ratio was more dynamic [234], although such results have not yet been obtained from chemostats or during conditions with dynamic gas supply, such as in the scale-down simulator described in [224].

We realise that the lin-log structure of the CRD-model bears several limitations. Results of lin-log models are good estimations around the reference conditions (i.e., around which they have been calibrated) [236], but in the CFD-CRD model, intra- and extracellular conditions far away from the reference concentration occur (see Table D.1). Despite the implemented rate-limitation modifications that were required for model stability, the CFD-CRD model still contained, although significantly dampened, numerical errors (Figure 5.2). We would therefore *not* recommend to use the lin-log structure for CRD models if they are to be coupled with CFD models, but instead stick to hyperbolic equations, analogous to [93, 94, 256] using mechanistic rate equations for intracellular reactions. Another limitation is the ultra-long simulation time of our CFD-CRD model, due to the large number of particles simulated (N_p = 80,000), the short Δt_{IC} (0.1 ms) for integration, and poor parallelisation of the particle-based metabolic model. As a consequence, our simulations had a significant power consumption and environmental burden (~0.45 MWh and ~200 kg CO_2). The development and parameterisation time of the kinetic model took one year, and incorporation in the CFD model lasted around 6 months, so that development of CFD-CRD models should not be considered to be trivial. This demonstrates the balancing act between model purpose, complexity and resource availability (section 1.4).

Lastly, the CRD model could be improved by implementing several additional reactions. An export and back-diffusion cycle for formate should be added, together with the reaction for CO_2 reduction to formate with H_2. Furthermore, there is some evidence that hydrogen can be produced from formate, using a NADP$^+$-based hydrogenase [249], which might be the cause of the simultaneous formate and hydrogen production in [41]. The parameters regarding the acetate export cycle are probably not well calibrated in the CRD model, since the model at low c_x predict large intracellular accumulation of acetate (Figure D.2). Implementation of an ATP balance or maintenance might also improve the model in this respect.

The clear spatial discrepancy between ethanol and acetate production zones might result in significant pH variations, in turn affecting the local $q_{\mathrm{AcT}}/q_{\mathrm{EtOH}}$ ratio. Metabolic models that can predict variations in extracellular pH should be developed, and coupled with CFD to minimise the effect of non-ideal mixing and improve pH buffering.

5.3.7. Towards better gas fermentation bioreactors

The presented CFD-CRD model and its results could enable ways towards rational optimisation of gas fermentation, by adjusting operating conditions, the reactor geometry, and by strain engineering.

In terms of reactor operation, mass transfer limitations are desired: In case there are no mass transfer limitations, CO inhibition prevails, leading to low CO and H_2 conversion rates, while lower $c_{L,\mathrm{CO}}$ and higher conversion rates are obtained when there are mass transfer limitations [224]. In order to sustainably obtain high q_{EtOH} at industrial-scale, the average $c_{L,\mathrm{CO}}$ as experienced by the microorganisms should be kept in a narrow range, around the predicted optimum $c_{L,\mathrm{CO}}$ of $0.05\,\mathrm{mol\,m^{-3}}$ according to our model (Figure 5.5e). A lower $c_{L,\mathrm{CO}}$ will induce too much acetate consumption, while at higher $c_{L,\mathrm{CO}}$ acetate will be produced at the expense of ethanol. When operating in a mass transfer-limited regime, high operational flexibility regarding $c_{L,\mathrm{CO}}$ can be obtained via the incoming gas flow rate, as this directly influences the gas hold-up and thus the mass transfer rate. For example, when there is too much acetate production ($c_{L,\mathrm{CO}}$ is too high), one could decrease the gas flow rate, which would decrease $c_{L,\mathrm{CO}}$, so that produced acetate might be consumed again, leading to high ethanol productivities.

In terms of reactor geometry, clear zonation was obtained in the EL-GLR (Figure 5.3), with CO-uptake and ferredoxin reduction in one zone, and the ferredoxin re-oxidation and ethanol production in the other zone. As both processes can happen quite fast (order of seconds), and cellular transition between the zones was found advantageous for ethanol production, forced zonation can be an interesting way to increase ethanol productivity. To improve industrial-scale reactor design, future (lab and modelling) research could focus on determination of the ideal residence times in both zones, which can be implemented by altering the interior and exterior reactor geometry, and related operation conditions.

Lastly, increases in J_{Rnf} were found to be directly related to increases in q_{EtOH} (Figure 5.7c). Overexpression of Rnf (with deletion of hydrogenase) has been proven as a viable method to increase ethanol production in *C. thermocellum* [251]. Overexpressing Rnf may be a method to amplify J_{Rnf} at high $c_{\mathrm{Fd_{red}^{2-}}}/c_{\mathrm{NADH}}$ and might increase q_{EtOH} even further in *C. autoethanogenum*.

5.4. Conclusion

In this work, we coupled a CFD model of an industrial-scale reactor for gas fermentation to a metabolic kinetic model to study the influence of the dissolved CO concentration and its gradient on the productivity and product spectrum of *C. autoethanogenum*. By comparing our model results with experimental data, we uncovered that the $c_{L,\mathrm{CO}}$ (and potentially q_{CO}) is a major factor steering the product spectrum: Very low $c_{L,\mathrm{CO}}$ ($< 0.05\,\mathrm{mol\,m^{-3}}$) result in high ethanol production rates by reducing extracellular acetic acid, in a starvation-induced metabolism, slightly higher concentrations ($0.05 < c_{L,\mathrm{CO}} < 0.1\,\mathrm{mol\,m^{-3}}$) were related to solventogenesis (CO to ethanol conversion), while high concentrations ($c_{L,\mathrm{CO}} > 0.1\,\mathrm{mol\,m^{-3}}$) were associated with acetate production. The gradient at industrial-scale led to a ~25% increase in ethanol production rate and yield, at the expense of acetate production. This increase was explained by redox cycles of ferredoxin and NAD+, which are imposed when there is a gradient in $c_{L,\mathrm{CO}}$. Due to the gradient, the concentration of reduced ferredoxin gradually decreases, while c_{NADH} increases due to Rnf activity. The re-oxidation of the resulting NADH caused led to enhanced ethanol production rates. We identified several hypotheses to support these results, made suggestions for follow-up research and developed a mechanistic understanding on the gas fermentation process.

Chapter 6

Conclusions

A nice adaptation of conditions will make almost any hypothesis agree with the phenomena. This will please the imagination but not advance our knowledge.

Joseph Black

Gas fermentation has been described as a process dominated by multiple multi-scale phenomena. We characterised a commercial-scale bioreactor for gas fermentation (**Chapter 2**), to investigate the gas and liquid flow pattern and the global mass transfer rate (at the metre-scale). We hypothesised that the production of ethanol by the microbes would lead to significantly reduced bubble diameters, thereby facilitating high mass transfer rates. This led us zoom-in into the world of bubbles (**Chapter 3**) (millimetre-scale), and how they are influenced by the specific compounds, such as ethanol and the mineral medium (< 1 nanometre), and the biomass concentration, in the fermentation broth. The impact of the biomass concentration, while considering small bubbles, on the dissolved gas concentration gradient was estimated in **Chapter 4**. This was used to develop a conceptual scale-down simulator, that could be used to mimic the concentration fluctuations from the large-scale in a lab-scale bioreactor (centimetre-scale). Such a system can be used to examine how these concentration fluctuations influence microbial metabolism. We developed several hypotheses for this by coupling a metabolic model of *C. autoethanogenum* (micrometre-scale) to the model of the large-scale reactor (**Chapter 5**). The dissolved gas concentration was identified as an influential factor regarding the product spectrum. The gradient resulted in increased ethanol production rates, which correlated with the activity of the Rnf-complex (at the nanometre-scale).

All these phenomena indicate that in a complex multi-scale process such as gas fermentation, the seamless integration of length scales and associated time scales is critical for bioprocess understanding and scale-up. Such a comprehensive approach is essential to assess the potential for bioprocess improvement from a broad physics- and biology-based mechanistic perspective.

Section 1.5 introduces several research questions which were aimed to be answered in this thesis. These answers will be briefly discussed below.

Mass Transfer

- What are the factors that should be considered to achieve sufficient mass transfer rates for successful operation of a commercial-scale gas fermentation process?

A CFD model was developed, and validated on pilot-scale experimental data, to predict the gas and liquid flow pattern in industrial-scale external-loop gas-lift reactors (Chapter 2). Based on the predicted hydrodynamic conditions, it was found that very small bubbles (≤ 2 mm) were required to obtain the reported industrial-scale $k_L a$ ($650 - 750\,\mathrm{h^{-1}}$) and mass transfer capacity ($7.5 - 8\,\mathrm{g L^{-1} h^{-1}}$). Such small bubbles may be due to the produced ethanol as it could suppress bubble coalescence and also increase (potentially >30%) the gas hold-up. The produced ethanol was therefore hypothesised to be the major contributor to high mass transfer performance at industrial-scale syngas fermentation.

This hypothesis was tested in Chapter 3 by adding $50\,\mathrm{g L^{-1}}$ of ethanol (the expected concentration at industrial-scale) to water, fermentation medium (without biomass) and fermentation broths (including biomass), in a lab-scale bubble column. From determining the bubble size distribution, a structural decrease in bubble diameter (in d_{32}) was obtained upon the addition of ethanol: from ~3 mm in demineralized water and ~2 mm in salt-containing medium and fermentation broths, to ~1 mm with ethanol. In all cases, a more than 30% increase in gas hold-up was obtained after the addition of ethanol, although a decrease in mass transfer coefficient k_L was observed by adding ethanol or biomass. In these analyses, significant increases were obtained in $k_L a$: up to 6 times in pure water, and up to 4 times in fermentation broths and mineral medium. By measuring the properties of all the mixtures, it was concluded that the typical engineering correlations (based on air-water mixtures) that are used for bioreactor scale-up, are not suitable for fermentation broths with high salt, alcohol and biomass concentrations. Therefore, lab-scale experiments should be carried out to investigate the specific mass transfer properties of (expected) broths.

Pressure and temperature are operational variables that directly affect the solubility and $k_L a$ of gaseous species (via ε_G) (Figure 1.3). In Chapter 2 and 3, the influence of the operating temperature was examined. A substantial (~ 40%) increase in $k_L a$ was observed with a temperature increase from 20 to 37 °C, irrespective of the ethanol concentration, corresponding to commonly-used correlations. The effect of the headspace pressure on $k_L a$ and mass transfer capacity (MTC) was examined in Chapter 2. When the inlet gas mass flow $\dot{m}_G$ is kept constant, a proportional decrease in $u_{G,s}$ is observed, leading to a decreased ε_G and a, while a proportional increase in solubility is obtained. The result was that the headspace pressure had no significant effect on MTC. When $\dot{m}_G$ is adjusted with pressure, MTC increases proportionally (but at higher operational costs).

In biotic operation at commercial-scale, mass transfer limitations were identified as desirable in gas fermentation. Mass transfer (with small bubbles) and microbial gas consumption were implemented in the CFD model of the large-scale reactor in Chapter 4. In cases with excess mass transfer a high dissolved CO concentration led to inhibition of CO and H_2-uptake and low gas conversion. With mass transfer limitations, however, increased gas conversion rates were obtained due to the absence of CO inhibition. Gas consumption in these cases led to lower (~33%) ε_G and thus $k_L a$. This demonstrates the potential of the multi-scale coupling approach to investigate the effects of microbial gas consumption and mass transfer on the global reactor performance.

Across this thesis, the influence of several factors on mass transfer in gas fermentations has been investigated, such as pressure, temperature, reaction rate and, most importantly, the broth composition. The concentration of the produced ethanol has been pinpointed as a key factor for successful operation of commercial-scale gas fermentation.

Downscaling gas fermentation

- What is an effective way to represent industrial-scale gas fermentation conditions at bench-scale?

After evaluating how high mass transfer rates could be obtained in the EL-GLR, the dissolved gas concentration and gradient were estimated for a wide range of conditions (Chapter 4). Based on lifeline analysis, microorganisms were likely to experience irregular fluctuations (between 5 and 30 s) in dissolved gas concentration (of around 1 order of magnitude), although with a wide spread in residence time in both peaks (moments with high concentration) and valleys.

To investigate how these concentration fluctuations affect the metabolism of acetogens, a conceptual scale-down simulator was designed. By imposing dissolved gas concentration fluctuations to a chemostat cultivation by irregularly modulating the stirring speed (with similar time distributions as in the large-scale reactor), similar concentration fluctuations can be experienced at both scales. By measuring metabolic properties like the gas consumption and product formation rates in both cases (chemostat with and without varied stirring speed), the influence of the gradient on variables such as q_{EtOH} could be determined.

The scale-down simulator was developed using the unstructured kinetic model for both CO and H_2-uptake. The structured model (Chapter 5) predicted a lower H_2-uptake rate than the unstructured model. This resulted in the absence of a dissolved H_2 gradient, although this was predicted with the other model. For successful development of a scale-down simulator regarding H_2-uptake, more information on its kinetics should be obtained.

Lastly, it can be argued that the experiments done in Chapter 3 are scale-down studies with respect to mass transfer. With easy and standard methods, the influence of industrial-scale conditions (the ethanol concentration) on gas-liquid mass transfer was studied in a lab-scale bubble column. To do this more rigorously, a wider (> 0.15 cm [196]) and taller (> 1 m [26]) column should be used, while considering the relevant medium composition and biomass concentrations. Despite these features, this study gave good estimations how mass transfer could be enhanced at industrial-scale.

Concentration gradient

- What is the influence of the dissolved gas concentration and its gradient on the metabolism and product spectrum of *C. autoethanogenum*?

The dissolved gas concentration and gradient were identified to be of major importance regarding the product spectrum (Chapter 5). By coupling the developed CFD model of an industrial-scale gas fermentor to a kinetic metabolic (CRD) model, for several biomass concentrations, lifelines with a wide range of relevant dissolved gas concentrations were obtained. The influence of the gradient was examined by comparing the CFD-CRD model results with these obtained from solving the CRD model at constant dissolved gas concentrations.

Via this method was determined that the dissolved CO concentration was a key driver in the product spectrum. By comparing both model results with experimental chemostat data, clear trends with respect to $c_{L,\mathrm{CO}}$ were obtained. Acetogenesis was observed at high $c_{L,\mathrm{CO}}$ ($> 0.1\,\mathrm{mol\,m^{-3}}$), while solventogenesis is expected when ($0.05 > c_{L,\mathrm{CO}} < 0.1\,\mathrm{mol\,m^{-3}}$). A starvation-induced metabolism wherein extracellular acetate is converted into ethanol was predicted at even lower $c_{L,\mathrm{CO}}$.

The gradient was expected to significantly increase the ethanol production rate q_{EtOH} (with ~25%). The model predicted clear zonation in the reactor between the CO concentration and CO-uptake and q_{EtOH}. In zones with high $c_{L,\mathrm{CO}}$ ferredoxin could be reduced, which was found to act as buffer for electron storage. In the zones with low $c_{L,\mathrm{CO}}$, the reduced ferredoxin is re-oxidised, releasing its electrons in NADH which is subsequently used for the conversion of acetate to ethanol. During the moments at low $c_{L,\mathrm{CO}}$ increased rates of the Rnf complex were likely (Rnf transports the electrons from reduced ferredoxin to NADH and translocates protons across the cell membrane, leading to the production of ATP). Several hypotheses were derived to explain this behaviour, and can be tested in further research, for example using the developed scale-down simulator.

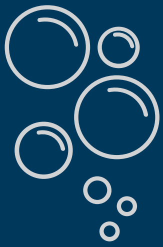

Chapter 7

Moving forwards

More research has to be done in this field.

Every scientist

Last but not least, it is time to discuss the future of gas fermentation. We will do this by gradually zooming in from the role of gas fermentation in the bioeconomy, into the bioreactor and the concentration gradients, into bubbles and mass transfer and lastly into the bacteria. How could we make gas fermentation processes successful?

7.1. The landscape of gas fermentation

Gas fermentation recently gained a lot of industrial attention as many companies (from start-ups to the major chemical producers) are considering it in their process(es). The largest player in the gas fermentation field is LanzaTech, which is collaborating and licensing out their technology to dozens of companies, with various gas feedstocks: off-gases from the steel and ferroalloy industry, oil refineries and chemicals producers, but also gasified orchard wood and municipal solid wastes [103]. Meanwhile, LanzaTech diversifies its product portfolio, as they demonstrated acetone and isopropanol production with high productivity and selectivity at pilot-scale [9]. Many different products have been proposed, ranging from acids (lactic acid and 3-hydroxypropionate), ketones (acetone), alcohols (butanol, 1,3-butanediol, octanol) to dienes (isoprene), using genetic modification of *C. autoethanogenum* or synthetic co-cultures [7, 8, 11].

A preliminary thermodynamic assessment shows that the energy release by anaerobic gas fermentation is very modest, compared to other bioprocesses (Table 7.1). Although Cueto-Rojas et al. [83] mentions CO as a carbon source with high potential for anaerobic processes given its high Gibbs free energy content per electron ($-47\,\mathrm{kJ\,mol_{e^-}^{-1}}$), the low $\Delta_R G^o$ (Table 7.1) requires high catabolic turnover rates for growth. Together with the inherent mass transfer limitations of CO, any non-catabolic process will be a very slow process, leading to poor growth rates and productivities. This causes that genetically modifying *C. autoethanogenum* to introduce a product reaction [11] might not be the way forward for gas utilisation.

Due to the limitations described here (i.e., low free energy release, mass transfer limitations), only short-chain catabolic products may be of relevance in anaerobic gas fermentation processes. Microbiologists should embrace these limitations, produce ethanol or acetate at high selectivity and find good uses for the product. Ethanol and acetate could both be used for production of single-cell protein via high-yield aerobic fermentation [29, 220, 257], or into medium-chain fatty acids [221], while ethanol can chemically be upgraded to (aviation) fuel or plastic. Therefore, anaerobic gas fermentation should be regarded more as a process to utilise waste gases with high global warming potential, and not so much as product-formation platform.

H_2 supplementation to CO gas mixtures improves the sustainability of ethanol formation, since less CO_2 will be produced (Table 7.1). This process is complicated from a bioprocess engineering perspective, since it is more challenging to steer q_{CO} and q_{H_2} in the right ratio than to feed with the specific gas composition (see Section 7.2). CO/H_2 fermentation faces severe competition with catalytic processes (like Fischer-Tropsch), such that its application will be highly dependent on the gas composition (and impurities), and economic and environmental indicators.

If we take the risk to add oxygen to the gas mixture, everything changes drastically, as way more energy becomes available upon oxidation of CO and H_2 (Table 7.1). This is in favour of *knallgas* (CO_2, H_2, O_2) fermentation (for which growth rates up to $0.42\,h^{-1}$ have been achieved, where $k_{L,O_2}a$ was almost $3000\,h^{-1}$(!) [258]). The energy release per mol carbon in this reaction is highly competitive with that of aerobic respiration processes. This explains the high number of start-ups that are currently researching this technology (amongst others, Deep Branch, Solar Foods) for production of protein or PHA [103, 259]. High mass transfer reactor designs ($k_L a > 1000\,h^{-1}$) are required to make up for the very low O_2 content ($< 6.9\%$) that is required to prevent flammable and/or explosive knallgas compositions.

Table 7.1: Thermodynamics of several gas-based bioprocesses [30], with some companies commercialising these processes [29, 103]. Anaerobic gas fermentation is compared with aerobic fermentation of gases and liquid substrates in terms of the Gibbs free energy at standard conditions, per mol reactant and per mol carbon [84].

Substrate	**Reaction**	$\Delta_R G^o$ (kJ mol^{-1})	$\Delta_R G^o$ (kJ mol$_C^{-1}$)	
	Anaerobic gas fermentations			
CO	$4CO + 2H_2O \longrightarrow C_2H_3O_2^- + H^+ + 2CO_2$	-135.0	-33.8	
	$6CO + 3H_2O \longrightarrow C_2H_5OH + 4CO_2$	-224.7	-37.4	
	$2CO + C_2H_3O_2^- + H^+ \longrightarrow C_2H_5OH$	-89.6	-44.8	LanzaTech
CO / H_2	$3CO + 3H_2 \longrightarrow C_2H_5OH + CO_2$	-144.6	-72.3	
	$2CO + 4H_2 \longrightarrow C_2H_5OH + H_2O$	-164.6	-54.9	
H_2 / CO_2	$2CO_2 + 4H_2 \longrightarrow C_2H_3O_2^- + H^+ + 2H_2O$	-104.5	-27.5	
	$2CO_2 + 6H_2 \longrightarrow C_2H_5OH + 3H_2O$	-49.56	-52.3	Synata Bio
	$2H_2 + C_2H_3O_2^- + H^+ \longrightarrow C_2H_5OH + H_2O$	-49.6	-	
	Aerobic gas fermentations			
H_2 / CO_2	$CO_2 + 6H_2 + 2O_2 \longrightarrow CH_2O + 5H_2O$	-922.0	-922.0	Solar Foods
H_2 / CO_2 / CO	$HCOOH + \frac{1}{2}O_2 \longrightarrow CO_2 + H_2O$	-280.6	-280.6	
CO	$CO + \frac{1}{2}O_2 \longrightarrow CO_2$	-55.0	-257.2	
CH_4	$CH_4 + 2O_2 \longrightarrow CO_2 + 2H_2O$	-818.0	-818.0	UniBio
	Aerobic respiration			
Methanol	$CH_3OH + \frac{3}{2}O_2 \longrightarrow CO_2 + 2H_2O$	-1087.8	-1087.8	ICI
Ethanol	$C_2H_5OH + 2O_2 \longrightarrow 2CO_2 + 3H_2O$	-1318.5	-659.3	
Acetate	$C_2H_3O_2^- + H^+ + O_2 \longrightarrow 2CO_2 + 2H_2O$	-893.8	-446.9	
Glucose	$C_6H_{12}O_6 + 6O_2 \longrightarrow 6CO_2 + 6H_2O$	-2872.3	-478.7	Quorn

Anaerobic *gas* fermentation has its name for a reason, and should be treated as such, with preventing greenhouse gas emissions as main application. With the introduction of externality costs (charging for the environmental costs of greenhouse gases via taxes or trading schemes) anaerobic gas fermentation processes become economically more attractive. Interesting gas sources might be industrial off-gases (steel mills, refineries), gasified municipal solid waste streams and (torrified) lignocellulosic biomass wastes. In all scenarios, greenhouse gas emissions are prevented (or the carbon lifeline extended).

The large ethanol market makes it possible to anaerobically convert these gases into useful products for society. Higher-value products might be produced by other fermentation processes, such as glucose or ethanol oxidation, with the knallgas reaction, or with catalytic processes. Gas mixtures derived from air-captured CO_2 and electrolytic hydrogen will possibly be expensive, requiring conversion to facilitate high-value (circular) processes, into e.g., sustainable aviation fuels.

7.2. Bioreactor operation for gas fermentation

Bioreactor design

As the main goal of anaerobic gas fermentation is gas conversion (preventing greenhouse gas emissions), bioreactors should be designed as such. High biomass concentrations and mass transfer limitations will be the desired operational mode, since it prevents inhibition, improves the gas-to-product yield and enables control possibilities. This should be done by implementing methods that control the liquid flow rate and thus the gas hold-up, for example with an axial pump in the downcomer.

Enhancing mass transfer rates (provided its limitations remain by increasing c_x) can be done by increasing both headspace pressure and gas flow rate (at economic costs), by decreasing the inert gas fraction, enlarging the gas inflow, or creating smaller bubbles by changing the medium composition (increase ethanol and salt content [24], risking a lower k_L by creating rigid bubbles).

Implementation of perforated plates might have a profound impact on gas hold-up and bubble size, and thus mass transfer. From simulations of an EL-GLR with perforated plate (15 cm thickness, 20% open area) using a porous medium model (C_2 ~3100 m^{-1}) significantly reduced CO mass flows were expected after passing the plate, compared to a model without plate (Figure 7.1). Overall, the plate increased CO conversion by around 15%, although the 95% mixing time increased from 90 s to 300 s. Future (lab and computational) research should focus on validation of the porous medium model for CFD modelling of perforated plates, and its application in bubble columns since it is a promising method to increase gas conversion.

The downcomer provides several operational advantages (e.g., enabling broth outflow, medium inflow, cooling). It also enlarges riser gas and liquid velocities, which decrease ε_G and $k_L a$ relative to a bubble column operational mode, while friction in the downcomer increases mixing times [108]. An interesting subject for further study might be the influence of the downcomer on axial gas mixing. If the downcomer decreases axial gas mixing, then the gas behaves more like a plug flow in the riser, so that high gas fractions of CO and H_2 are obtained at locations with high hydrostatic pressure, while a well-mixed

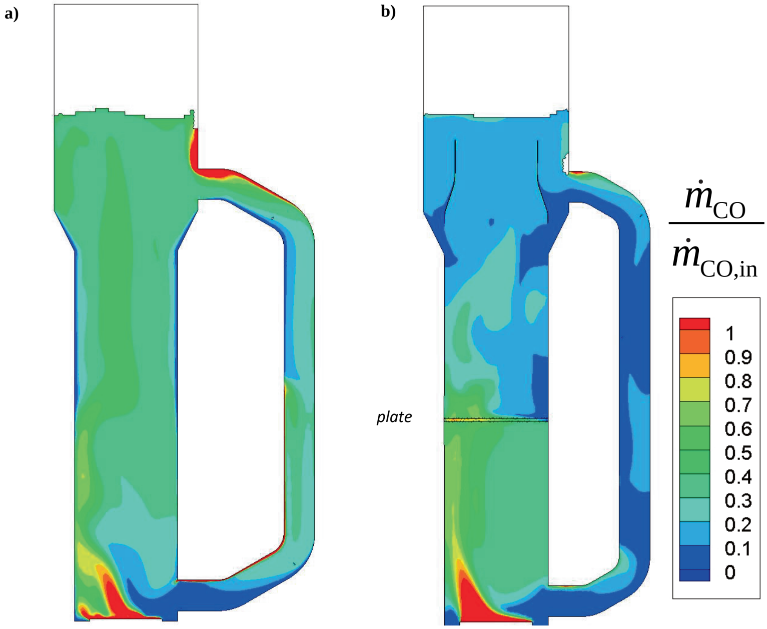

Figure 7.1: Influence of a perforated plate on the CO mass flow in EL-GLRs. a) CFD-simulation without perforated plates, b) simulation with a perforated plate. See Chapter 4 for the configuration of the CFD simulations ($c_x = 10\,\mathrm{g\,L^{-1}}$).

gas phase will lead to decreased y_{CO} and y_{H_2}, which in turn might decrease MTC. Biotic and abiotic lab studies with gases (other than air) might be interesting for finding out when (depending on gas composition and gas flow rates) an external downcomer leads to increased mass transfer.

Gas composition

As discussed in the previous section, H_2 supplementation increases the biomass-specific ethanol production rate q_{EtOH}, and is an attractive method to increase the sustainability of the process. Operationally, it is not straightforward to match q_{CO} and q_{H_2} in the right ratios, due to varying mass transfer coefficients, Henry coefficients and the strong effect of CO inhibition on q_{H_2}. With the ideal-mixing model of the EL-GLR (Chapter 4) a quick assessment was done to estimate the optimal gas composition for ethanol production and to minimise CO_2 production.

From this assessment it turns out that the best gas composition for ethanol production is rich in H_2 (> 90%) and only has small traces (~5%) of CO and CO_2 (Figure 7.2). If more CO_2 is added to the gas, it accumulates in the liquid-phase due to its high solubility and is simply not converted. To obtain net zero CO_2 production a gas mixture with 40% CO and 60% H_2 should be used, different from the ratio in Table 7.1 (33.3% and 66.7%). The

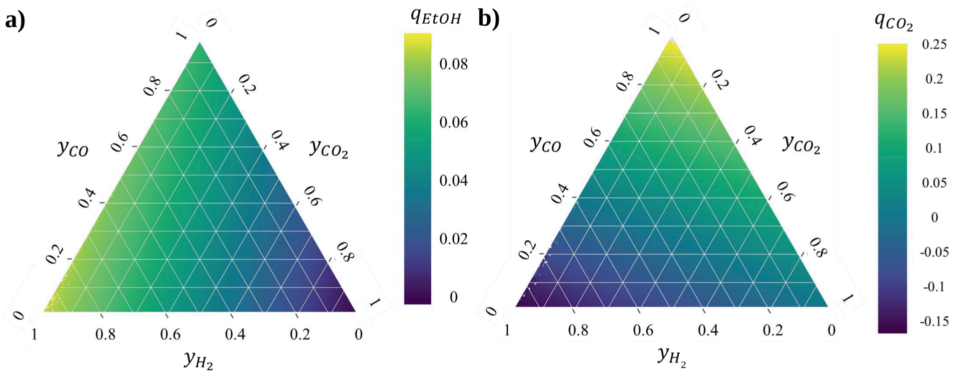

Figure 7.2: Influence of the gas composition y_i on q_{EtOH} and $q_{\mathrm{CO_2}}$. For a wide range of gas compositions the biomass-specific production rates for a) ethanol and b) CO_2 (negative for consumption) were estimated using the ideal-mixing model of a large-scale reactor for gas fermentation (Chapter 4) with mass transfer limitations ($k_{L,\mathrm{CO}}a = 180\,\mathrm{h^{-1}}$, $c_x = 25\,\mathrm{g\,L^{-1}}$), $q_{\mathrm{CO_2}} = \frac{4}{6} q_{\mathrm{CO}} - \frac{1}{3} q_{\mathrm{H_2}}$. No inert gas fraction was assumed.

results are clearly influenced by the high $q_{\mathrm{H_2}}^{\mathrm{max}}$ since the q_{EtOH} can be almost 50% higher in a H_2-rich gas compared to CO-rich gas.

An interesting path for future research would be to perform such analyses with more detailed models for ethanol and CO_2 production, such as the metabolic model in [40] and considering the dynamic conditions in large-scale reactors, since the concentration gradient has a substantial influence on the product spectrum (Chapter 5).

Ethanol concentration

Product inhibition is a frequently observed phenomenon in fermentation processes (see Straathof et al. [63]). Alcohols were found to be a substantial inhibitor to growth of *Bacillus subtilis*, as function of carbon chain length [260]. If this effect would also hold for *C. autoethanogenum* then the ethanol concentration would be an important variable in process design as it directly affects the costs of downstream processing (via heating duty in distillation columns) [16]. Thus, high c_{EtOH} decrease downstream processing costs, would increase mass transfer rates due to coalescence inhibition (Chapter 3), while increased reactor volumes are required due to the decreased productivity and q_{CO}.

Ethanol inhibition was studied before in gas-fermenting *Clostridium* spp., although the mechanism is still unclear. A linear relationship between growth and c_{EtOH} (up to $35\,\mathrm{g\,L^{-1}}$) was obtained for *C. carboxidivorans* grown on CO [35], while [261] did not find any inhibitory effects up to $15\,\mathrm{g\,L^{-1}}$ for syngas-grown *C. ljungdahlii*. Based on long-term culture data with high c_{EtOH} up to $50\,\mathrm{g\,L^{-1}}$ with *C. ljungdahlii* [262], de Medeiros et al. [208] fitted a hyperbolic model for ethanol inhibition.

For successful process design, and determination of kinetic parameters for gas uptake, ethanol inhibition has to be studied more rigorously. Crucial parameters that need to be determined are the critical inhibition concentration, the range of concentrations at which inhibition does not play a role regarding growth, and how ethanol inhibition can be mathematically described (linear, hyperbolic or exponential). This could be studied in chemostats with *C. autoethanogenum* with step changes in c_{EtOH} in the feed. Directed evolution studies might be a possible way to alleviate the effect of high c_{EtOH} in the long term. With clearance on the ethanol inhibition mechanism, integrated bioprocess design studies can be done to find out the optimal conditions for both the upstream and downstream processes.

7.3. Concentration gradients and scale-down

CO and H_2 concentration gradients were expected in the EL-GLR of roughly one order of magnitude (e.g., 0.02 – 0.2 $\mathrm{mol\,m^{-3}}$, depending on c_x) with irregular peak and valley duration in the order of seconds (5 – 30 s). With the proposed scale-down simulator in Chapter 4, the impact of such concentration gradients can be studied at lab-scale.

Future work should employ the proposed scale-down CSTR bioreactor with variable stirrer speed to investigate whether the concentration gradient is of any advantage to ethanol production (see Chapter 5). With the data obtained from the scale-down setup, metabolic models could be parameterised (preferably based on hyperbolic enzyme kinetics), which can in turn be used to improve the CFD-CRD model and our understanding on gas fermentation dynamics. Such work could also shed light on the ideal duration in high and low concentration zones, which could in turn be used for improved bioreactor design, at both pilot and full-scale.

At lab-scale, despite the typical ideal mixing assumption, dissolved gas concentration gradients might also be obtained. This is most probably due to the specific flow pattern in the reactor, fast reaction kinetics and the very low gas flow rates (usually varying between 0.01 vvm in [41] and 0.1 vvm in [45]) gas fermentations. Even at pilot [9] and full-scale (Chapter 2) low gas flow rates <0.1 vvm were expected.

Based on short-cut CFD simulations of a typical lab-scale bioreactor [45], a $c_{L,\mathrm{CO}}$ gradient was expected between 0.02 – 0.05 $\mathrm{mol\,m^{-3}}$ within a 0.75 L bioreactor (12 cm liquid height) (Figure 7.3a). Although this gradient is less significant than the one at larger scales, this was not expected with the ideal-mixing approximation. It was hypothesised that this non-ideal mixing may have a positive impact on q_{EtOH}.

The gradient arises probably due to depletion of CO from gas bubbles, and the fast reaction rate compared to mass transfer and mixing. In Figure 7.3b is visible that closer to the sparger the bubbles contain more CO than the ones near the walls and headspace. The consumed CO is partly replaced by the produced CO_2. To decrease the CO gradient, axial mixing should be improved, for example by changing to an axial impeller.

By compiling data from several lab-studies, q_{EtOH} was found to be increased when reaction is faster than mixing (Figure 7.3c). As was hypothesised that q_{EtOH} may be increased to the $c_{L,\mathrm{CO}}$ gradient (Chapter 5), the conclusions obtained from these studies may be influenced by the gradient. Future research should focus on the existence of concentration gradients at lab-scale gas fermentations, and efforts should be made to diminish their impact when it is not the main topic of research.

One interesting method to obtain constant concentrations, is using microfluidic bioreactors [263, 264]. In microfluidic chips, the dissolved CO concentration can be controlled via regulated mixing with a fully saturated flow (e.g., [265]) or via a fully controlled gas chamber (e.g., [266]). In the microfluidic chip, acetogens can be cultivated at constant or dynamic conditions (following a lifeline [267]), and used to study the influence of $c_{L,\mathrm{CO}}$ on gas uptake kinetics, the product spectrum, and their reaction to concentration gradients. In the future (when cheap microfluidic chip fabrication is available), microfluidic cultivation is potentially an effective tool for strain selection and screening in scale-down studies.

7.4. Gas-to-liquid mass transfer

In this work was highlighted that the medium composition had a significant impact on mass transfer. In a follow-up review paper by Volger et al. [24], the influence of a wide range of broth constituents (e.g., salts, proteins, biomass, products, antifoam) on bubble column hydrodynamics and mass transfer was assessed. This made clear that the combined effects of broth components is barely understood, as the scientific literature is more focused on individual compounds. This all could lead to unexpected deviations in

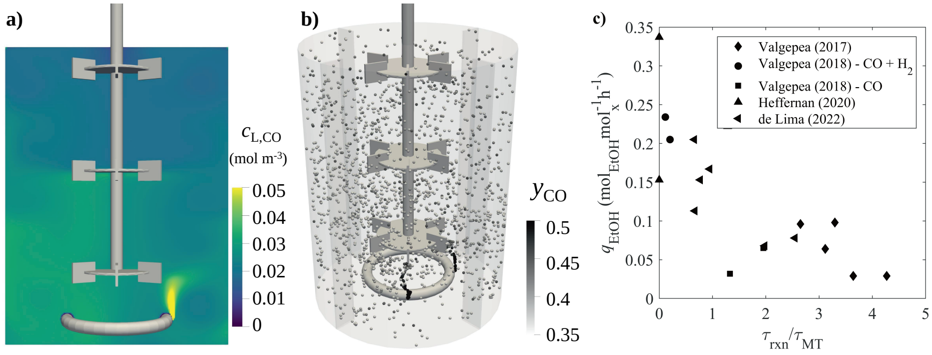

Figure 7.3: Gradients in lab-scale gas fermentations. a) Time-averaged $c_{L,\mathrm{CO}}$ obtained using a short-cut Lattice-Boltzmann CFD simulation (in M-Star) of a 0.75 L reactor with operating conditions based on [45] (1160 rpm, 72 mL min^{-1}, 1 mm bubbles, k_L via Equation 2.5 and reaction as modelled in Chapter 4). b) Bubble dispersion in that reactor, the bubbles are coloured with their y_{CO}. c) Compilation of experimental data depicting the relationship between q_{EtOH} and the ratio between reaction and mass transfer time (values below 1 indicate faster consumption than transfer).

variables important for mass transfer, with respect to the typical engineering correlations.

Industrialists and academics working on gas fermentation should study $k_L a$ of their reactor with water and broth. This is required for successful scale-up, and can be used to calculate dissolved gas concentrations which can not yet be measured. Comparison of broth $k_L a$ with water $k_L a$ should provide proper estimations, as is common practice in wastewater treatment [185]. This can, for example, be done using the relatively simple and cheap methods used in Chapter 3.

The large amount of $k_L a$ data in literature, could make it possible to develop databases with broth compositions, for example via AI-based literature-scraping tools [268]. Pattern recognition may indicate how specific components interact and influence broth $k_L a$.

In gas fermentation experiments, significantly higher $k_L a$ were predicted from the gas consumption rate (Equation 7.1) than the one expected from the gas inflow rate and the amount of bubbles (Equation 7.2) (Figure 7.4a). For example, in a lab-scale reactor operated with 0.1 vvm [45] around 2000 bubbles were expected from simulations (Figure 7.3b) and Equation 7.2, resulting in a $(k_{L,\mathrm{CO}}a)_{\mathrm{abiotic}}$ around $3\,\mathrm{h}^{-1}$ ($d_b = 1\,\mathrm{mm}$, $k_L = 1\times10^{-4}\,\mathrm{m\,s^{-1}}$, bubble residence time $\tau_b = 1\,\mathrm{s}$). This is significantly lower than the minimum biotic $k_L a$ in [45] of $180\,\mathrm{h}^{-1}$. Only with very extreme assumptions such high $(k_{L,\mathrm{CO}}a)_{\mathrm{abiotic}}$ could be obtained ($d_b = 0.1\,\mathrm{mm}$, $k_L = 3\times10^{-4}\,\mathrm{m\,s^{-1}}$, $\tau_b = 3\,\mathrm{s}$). Therefore, it would be interesting to determine how such high mass transfer rates are obtained at lab-scale, despite the small gas flow rates.

$$(k_{L,\mathrm{CO}}a)_{\mathrm{biotic}} = \frac{r_{\mathrm{CO}}}{c^{\mathrm{sat}}_{L,\mathrm{CO}} - c_{L,\mathrm{CO}}} = \frac{q_{\mathrm{CO}}c_x}{c^{\mathrm{sat}}_{L,\mathrm{CO}} - c_{L,\mathrm{CO}}} > \frac{q_{\mathrm{CO}}c_x}{c^{\mathrm{sat}}_{L,\mathrm{CO}} - 0} \gg \frac{q_{\mathrm{CO}}c_x}{H_{\mathrm{CO}}\,p\,y_{\mathrm{CO,in}} - 0} \tag{7.1}$$

$$(k_{L,\mathrm{CO}}a)_{\mathrm{abiotic}} = k_{L,\mathrm{CO}}\cdot a_b\cdot N_b = k_{L,\mathrm{CO}}\cdot\frac{4\pi d_b^2}{V_L}\cdot\frac{F_{G,\mathrm{in}}}{\frac{1}{6}\pi d_b^3}\tau_b = 6k_{L,\mathrm{CO}}\frac{F_{G,\mathrm{in}}}{V_L d_b}\tau_b \tag{7.2}$$

One possibility might be that the mass transfer coefficient k_L is significantly enhanced, hinting at bubble boundary layer effects, as was extensively described in [269]. Such enhancement could be due to the presence of a cell layer around the bubble and by gas consumption in the boundary film layer. Very strong boundary layer effects (high Hatta number) would reduce CO availability in the bulk liquid and thus underpredict q_{CO}. This might explain the fourfold increase in $q^{\mathrm{max}}_{\mathrm{CO}}$ as predicted based on recent experiments [270] relative to the one used in kinetic models (Table 4.1).

One method to measure biotic mass transfer enhancement during continuous gas fermentation might be by mass transfer of inert gases. For example, dynamic measurement of dissolved nitrogen[1] concentration after step changes in $y_{\mathrm{N_2}}$ [195] might reveal the abiotic $k_{L,\mathrm{N_2}}a$, which can be converted into an abiotic $k_{L,\mathrm{CO}}a$ via their diffusion coefficients (Equation 4.13). This can then be compared with the biotic $k_{L,\mathrm{CO}}a$ as calculated using Equation 7.1.

---

[1] possibly via Hach Orbisphere 315xx Nitrogen Sensors.

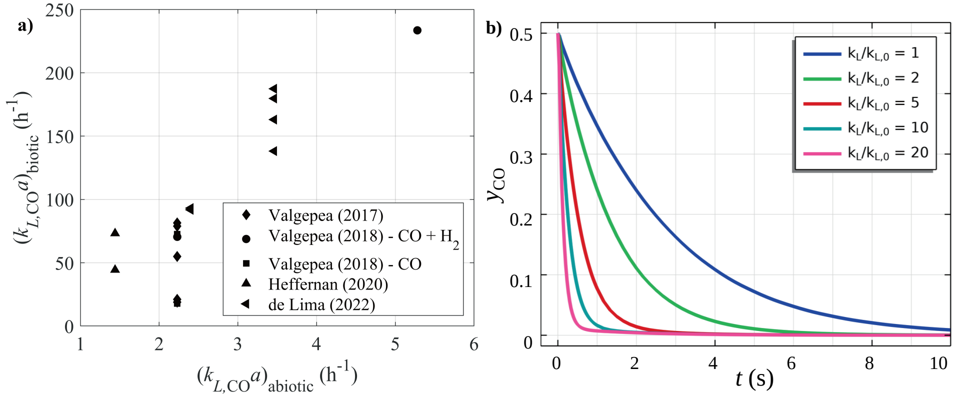

Figure 7.4: Mass transfer uncertainties at lab-scale. a) Comparison of the minimum biotic k_La (Equation 7.1) and estimations of abiotic k_La (Equation 7.2) for various experimental conditions. b) Gas depletion from a bubble over time, calculated for various k_L values. Abiotic k_La was estimated by assuming $d_b = 1$ mm, $k_L = 1 \times 10^{-4}$ m s^{-1}, $\tau_b = 1$ s. Results in b) were obtained using a diffusion-reaction model around a 1 mm gas bubble with initial y_{CO} of 0.5, a boundary layer thickness of 2.71×10^{-5} m, and strong turbulent diffusion in the liquid ($D_{\mathrm{turb}} = 1 \times 10^{-3}$ m^2 s^{-1}), kinetics as in Chapter 4, c_x of 1.56 g L^{-1} [45].

Gas bubbles are depleted faster due to mass transfer enhancement. With a diffusion-reaction model was predicted that a twofold increased k_L would reduce y_{CO} by 50% within 1 s (Figure 7.4b). A tenfold higher k_L would even lead to 95% CO depletion within that second. The 20-times increases in consumption rate (as predicted above), were not expected with this model. The large discrepancies between $y_{\mathrm{CO,in}}$ and $y_{\mathrm{CO,out}}$ (for example in [41]) challenge the estimation of CO solubility and thus k_La and $c_{L,\mathrm{CO}}$, so that the value obtained with Equation 7.1 is at the lower side.

All in all, the high gas conversion rates in lab-scale gas fermentations with low gas flows raise several questions that remain unanswered. Development of online dissolved CO sensors is paramount for further research on this topic. A good first step is the approach used by Mann et al. [252].

7.5. Gas fermenting bacteria

As mentioned throughout this work, there is a clear knowledge gap regarding gas uptake kinetics of acetogens. Although there are several experimental [33, 34] and modelling [40, 208] works that propose gas uptake kinetics, there are big discrepancies between the derived kinetic models and experimental results. The reason for this may be that many conditions influence gas uptake rates (e.g., the concentrations of dissolved CO, H_2, acetate and intracellular reduced ferredoxin).

Future experiments to determine gas uptake kinetics should apply the dissolved CO measuring technique from [252], while keeping product concentrations constant (possibly by supplying them in the inflow). A good approach to determine q^{max} is the one used in [270] (with smaller gas headspace volumes to shorten the cycles), while steady chemostat experiment with varying $y_{i,\mathrm{in}}$ could be done to study K_S and K_I. Dissolved gas gradients should be prevented by increasing axial mixing in the reactor and by working with high volumetric gas flow rates.

As H_2-uptake is inhibited by CO, the measurement of H_2-uptake kinetics becomes even more challenging. One interesting study could be to perturb CO_2 and H_2-grown chemostat cultures with increasing amounts of CO and measure the variations in H_2-uptake rates from the off-gas.

In Chapter 5 several hypotheses were provided on the relationship between $c_{\mathrm{Fd}^{2-}_{\mathrm{red}}}$ and q_{EtOH}. At this moment no methods are available for measurement of $c_{\mathrm{Fd}^{2-}_{\mathrm{red}}}$ [271], so that a direct proof cannot be obtained.

Interesting studies can be done, however, on the Rnf complex, which rate was found to be related to ethanol production. For example, in chemostat cultures with varying $c_{L,\mathrm{CO}}$ (using the approach of [252]), next to obviously q_{CO} and q_{EtOH}, the concentrations of NADH and NAD^+ should be determined (e.g., [234]) as well as the Rnf activity (e.g., [249]). This may identify whether the Rnf rate does indeed relate to q_{EtOH} as was hypothesised in Chapter 5.

Studies with cell extracts, similar to [249], could shed light on the inhibiting effect of CO on Rnf, for example by varying y_{CO} in the headspace or by saturation of demineralized water with CO. Such studies might also reveal whether Rnf is more sensitive to variations in $\mathrm{Fd}^{2-}_{\mathrm{red}}/\mathrm{Fd}_{\mathrm{ox}}$ compared to $\mathrm{NADH}/\mathrm{NAD}^+$, as the latter one was expected to change more frequently during concentration fluctuations.

7.6. The end in mind

In this outlook chapter, we discussed the future of research on gas fermentation. The topic is very dynamic, and although commercial-scale processes are established, there are still too many unknowns compared to the more traditional fermentation processes. For successful scale-up of this technology, the main research gap are the kinetics of acetogens and their reaction to dynamically varying components (dissolved gases and products). With increased understanding on the effect of the broth and the biotic enhancement effect on mass transfer, the accuracy of CFD simulations can be improved.

With detailed kinetics and metabolic models, and increased understanding on gas-to-liquid mass transfer, gas fermentation bioprocesses and operating conditions can be optimised according to specific gas composition and desired end-products. Advances in AI and computer hardware (and availability) will drastically speed-up CFD-CRD simulations. Hydrodynamic-metabolic simulations might be run as a digital twin (fed with off-gas data) to enable real-life control.

Gas fermentation with air-captured CO_2 and electrolytic H_2 could lead to carbon-neutral production of commodities (fuels and chemicals) and even carbon-negative production of materials (plastics). Fast development of gas fermentation processes is crucial to combat climate change.

The future of gas fermentation is bright. Let’s make it happen!

References

[1] Bailey, J. E. (1998). Mathematical modeling and analysis in biochemical engineering: Past accomplishments and future opportunities. *Biotechnology Progress*, *14*(1), 8–20.

[2] Klasson, K. T., Ackerson, M. D., Clausen, E. C., & Gaddy, J. L. (1991). Bioreactor design for synthesis gas fermentations. *Fuel*, *70*(5), 605–614.

[3] Vega, J. L., Prieto, S., Elmore, B. B., Clausen, E. C., & Gaddy, J. L. (1989). The Biological Production of Ethanol from Synthesis Gas. *Applied Biochemistry and Biotechnology*, *20*(21), 781–797.

[4] Abrini, J., Naveau, H., & Nyns, E. J. (1994). Clostridium autoethanogenum, sp. nov., an anaerobic bacterium that produces ethanol from carbon monoxide. *Archives of Microbiology*, *161*(4), 345–351.

[5] Tanner, R. S., Miller, L. M., & Yang, D. (1993). Clostridium ljungdahlii sp. nov., an acetogenic species in clostridial rRNA homology group I. *International Journal of Systematic Bacteriology*, *43*(2), 232–236.

[6] Calvo, D. C., Luna, H. J., Arango, J. A., Torres, C. I., & Rittmann, B. E. (2022). Determining global trends in syngas fermentation research through a bibliometric analysis. *Journal of Environmental Management*, *307*, 114522.

[7] Diender, M., Stams, A. J., & Sousa, D. Z. (2016). Production of medium-chain fatty acids and higher alcohols by a synthetic co-culture grown on carbon monoxide or syngas. *Biotechnology for Biofuels*, *9*(1), 1–11.

[8] Köpke, M., & Simpson, S. D. (2020). Pollution to products: recycling of 'above ground' carbon by gas fermentation. *Current Opinion in Biotechnology*, *65*, 180–189.

[9] Liew, F. E., Nogle, R., Abdalla, T., Rasor, B. J., Canter, C., Jensen, R. O., Wang, L., Strutz, J., Chirania, P., De Tissera, S., Mueller, A. P., Ruan, Z., Gao, A., Tran, L., Engle, N. L., Bromley, J. C., Daniell, J., Conrado, R., Tschaplinski, T. J., Giannone, R. J., Hettich, R. L., Karim, A. S., Simpson, S. D., Brown, S. D., Leang, C., Jewett, M. C., & Köpke, M. (2022). Carbon-negative production of acetone and isopropanol by gas fermentation at industrial pilot scale. *Nature Biotechnology 2022 40:3*, *40*(3), 335–344.

[10] Fackler, N., Heijstra, B. D., Rasor, B. J., Brown, H., Martin, J., Ni, Z., Shebek, K. M., Rosin, R. R., Simpson, S. D., Tyo, K. E., Giannone, R. J., Hettich, R. L., Tschaplinski, T. J., Leang, C., Brown, S. D., Jewett, M. C., & Köpke, M. (2021). Stepping on the Gas to a Circular Economy: Accelerating Development of Carbon-Negative Chemical Production from Gas Fermentation. *Annual Review of Chemical and Biomolecular Engineering*, *12*, 439–470.

[11] Liew, F. M., Martin, M. E., Tappel, R. C., Heijstra, B. D., Mihalcea, C., & Köpke, M. (2016). Gas Fermentation-A flexible platform for commercial scale production of low-carbon-fuels and chemicals from waste and renewable feedstocks. *Frontiers in Microbiology*, *7*, 1–28.

[12] Ail, S. S., & Dasappa, S. (2016). Biomass to liquid transportation fuel via Fischer Tropsch synthesis - Technology review and current scenario. *Renewable and Sustainable Energy Reviews*, *58*, 267–286.

[13] Perret, L., Lacerda de Oliveira Campos, B., Herrera Delgado, K., Zevaco, T. A., Neumann, A., & Sauer, J. (2022). COx Fixation to Elementary Building Blocks: Anaerobic Syngas Fermentation vs. Chemical Catalysis. *Chemie-Ingenieur-Technik*, *94*(11), 1667–1687.

[14] Abubackar, H. N., Veiga, M. C., & Kennes, C. (2011). Biological conversion of carbon monoxide: Rich syngas or waste gases to bioethanol. *Biofuels, Bioproducts and Biorefining*, *5*(1), 93–114.

[15] Munasinghe, P. C., & Khanal, S. K. (2010). Biomass-derived syngas fermentation into biofuels: Opportunities and challenges. *Bioresource Technology*, *101*, 5013–5022.

[16] Janković, T., Straathof, A. J. J., & Kiss, A. A. (2023). Advanced downstream processing of bioethanol from syngas fermentation. *Separation and Purification Technology*, *322*(124320), 1–13.

[17] Sun, X., Atiyeh, H. K., Huhnke, R. L., & Tanner, R. S. (2019). Syngas fermentation process development for production of biofuels and chemicals: A review. *Bioresource Technology Reports*, (100279), 1–6.

[18] Xu, D., Tree, D. R., & Lewis, R. S. (2011). The effects of syngas impurities on syngas fermentation to liquid fuels. *Biomass and Bioenergy*, *35*, 2690–2696.

[19] Chisti, M. Y., Halard, B., & Moo-Young, M. (1988). Liquid circulation in airlift reactors. *Chemical Engineering Science*, *43*(3), 451–457.

[20] Merchuk, J. C., & Siegel, M. H. (1988). Air-lift reactors in chemical and biological technology. *Journal of Chemical Technology & Biotechnology*, *41*(2), 105–120.

[21] Yasin, M., Jang, N., Lee, M., Kang, H., Aslam, M., Bazmi, A. A., & Chang, I. S. (2019). Bioreactors, gas delivery systems and supporting technologies for microbial synthesis gas conversion process. *Bioresource Technology Reports*, *7*, 100207.

[22] Elisiário, M. P., Wever, H. D., Hecke, W. V., Noorman, H., & Straathof, A. J. J. (2021). Membrane bioreactors for syngas permeation and fermentation. *Critical Reviews in Biotechnology*, (pp. 1–17).

[23] Asimakopoulos, K., Gavala, H. N., & Skiadas, I. V. (2018). Reactor systems for syngas fermentation processes: A review. *Chemical Engineering Journal*, *348*, 732–744.

[24] Volger, R., Puiman, L., & Haringa, C. (2024). Bubbles and Broth: A review on the impact of broth composition on bubble column bioreactor hydrodynamics. *Biochemical Engineering Journal*, *201*(October 2023), 109124.

[25] Garcia-Ochoa, F., & Gomez, E. (2009). Bioreactor scale-up and oxygen transfer rate in microbial processes: An overview. *Biotechnology Advances*, *27*(2), 153–176.

[26] Heijnen, J. J., & Van't Riet, K. (1984). Mass transfer, mixing and heat transfer phenomena in low viscosity bubble column reactors. *The Chemical Engineering Journal*, *28*(2), B21–B42.

[27] Burgard, A., Burk, M. J., Osterhout, R., Van Dien, S., & Yim, H. (2016). Development of a commercial scale process for production of 1,4-butanediol from sugar. *Current Opinion in Biotechnology*, *42*, 118–125.

[28] Crater, J., Galleher, C., & Lievense, J. (2017). Consultancy on Large-Scale Submerged Aerobic Cultivation Process Design - Final Technical Report: February 1, 2016 – June 30, 2016. Tech. rep., National Renewable Energy Laboratory (NREL), Golden, CO (United States).

[29] Litchfield, J. H. (1982). Single-Cell Proteins. *Science*, *219*, 740–741.

[30] Woern, C., & Grossmann, L. (2023). Microbial gas fermentation technology for sustainable food protein production. *Biotechnology Advances*, *69*(April), 108240.

[31] Richter, H., Martin, M. E., & Angenent, L. T. (2013). A two-stage continuous fermentation system for conversion of syngas into ethanol. *Energies*, *6*(8), 3987–4000.

[32] Benalcázar, A. E., Noorman, H., Maciel Filho, R., & Posada, J. A. (2020). Modeling ethanol production through gas fermentation: a biothermodynamics and mass transfer-based hybrid model for microbial growth in a large-scale bubble column bioreactor. *Biotechnology for Biofuels*, *13*(59), 1–19.

[33] Mayer, A., Schädler, T., Trunz, S., Stelzer, T., & Weuster-Botz, D. (2018). Carbon monoxide conversion with Clostridium aceticum. *Biotechnology and Bioengineering*, *115*(11), 2740–2750.

[34] Mohammadi, M., Mohamed, A. R., Najafpour, G. D., Younesi, H., & Uzir, M. H. (2014). Kinetic studies on fermentative production of biofuel from synthesis gas using clostridium ljungdahlii. *The Scientific World Journal*, *2014*, 1–8.

[35] Fernández-Naveira, , Abubackar, H. N., Veiga, M. C., & Kennes, C. (2016). Carbon monoxide bioconversion to butanol-ethanol by Clostridium carboxidivorans: kinetics and toxicity of alcohols. *Applied Microbiology and Biotechnology*, *100*(9), 4231–4240.

[36] Straathof, A. J. J. (2023). Modelling of end-product inhibition in fermentation. *Biochemical Engineering Journal*, *191*(September 2022), 108796.

[37] Keitel, G., & Onken, U. (1982). THE EFFECT OF SOLUTES ON BUBBLE SIZE IN AIR-WATER DISPERSIONS. *Chemical Engineering Communications*, *17*(1-6), 85–98.

[38] Ramió-Pujol, S., Ganigué, R., Bañeras, L., & Colprim, J. (2015). How can alcohol production be improved in carboxydotrophic clostridia? *Process Biochemistry*, *50*(7), 1047–1055.

[39] Schulz, S., Molitor, B., & Angenent, L. T. (2023). Acetate augmentation boosts the ethanol production rate and specificity by Clostridium ljungdahlii during gas fermentation with pure carbon monoxide. *Bioresource Technology*, *369*(October 2022), 128387.

[40] Almeida Benalcázar, E. (2023). *Modeling the anaerobic fermentation of CO, H2 and CO2 mixtures at large and micro-scales [doctoral dissertation]*. Ph.D. thesis, Delft University of Technology.

[41] Elisiário, M. P., Van Hecke, W., De Wever, H., Noorman, H., & Straathof, A. J. J. (2023). Acetic acid, growth rate, and mass transfer govern shifts in CO metabolism of Clostridium autoethanogenum. *Applied Microbiology and Biotechnology*, *107*(17), 5329–5340.

[42] Klask, C. M., Kliem-Kuster, N., Molitor, B., & Angenent, L. T. (2020). Nitrate Feed Improves Growth and Ethanol Production of Clostridium ljungdahlii With CO2 and H2, but Results in Stochastic Inhibition Events. *Frontiers in Microbiology*, *11*(May), 1–15.

[43] Shen, S., Gu, Y., Chai, C., Jiang, W., Zhuang, Y., & Wang, Y. (2017). Enhanced alcohol titre and ratio in carbon monoxide-rich off-gas fermentation of Clostridium carboxidivorans through combination of trace metals optimization with variable-temperature cultivation. *Bioresource Technology*, *239*, 236–243.

[44] Valgepea, K., de Souza Pinto Lemgruber, R., Meaghan, K., Palfreyman, R. W., Abdalla, T., Heijstra, B. D., Behrendorff, J. B., Tappel, R., Köpke, M., Simpson, S. D., Nielsen, L. K., & Marcellin, E. (2017). Maintenance of ATP Homeostasis Triggers Metabolic Shifts in Gas-Fermenting Acetogens. *Cell Systems*, *4*(5), 505–515.

[45] de Lima, L. A., Ingelman, H., Brahmbhatt, K., Reinmets, K., Barry, C., Harris, A., Marcellin, E., Köpke, M., & Valgepea, K. (2022). Faster Growth Enhances Low Carbon Fuel and Chemical Production Through Gas Fermentation. *Frontiers in Bioengineering and Biotechnology*, *10*, 1–14.

[46] Valgepea, K., de Souza Pinto Lemgruber, R., Abdalla, T., Binos, S., Takemori, N., Takemori, A., Tanaka, Y., Tappel, R., Köpke, M., Simpson, S. D., Nielsen, L. K., & Marcellin, E. (2018). H2 drives metabolic rearrangements in gas-fermenting Clostridium autoethanogenum. *Biotechnology for Biofuels*, *11*(1), 55.

[47] Köpke, M., Mihalcea, C., Liew, F. M., Tizard, J. H., Ali, M. S., Conolly, J. J., Al-Sinawi, B., & Simpson, S. D. (2011). 2,3-Butanediol production by acetogenic bacteria, an alternative route to chemical synthesis, using industrial waste gas. *Applied and Environmental Microbiology*, *77*(15), 5467–5475.

[48] Lara, A. R., Galindo, E., Ramírez, O. T., & Palomares, L. A. (2006). Living with heterogeneities in bioreactors. *Molecular Biotechnology 2006 34:3*, *34*(3), 355–381.

[49] Nadal-Rey, G., McClure, D. D., Kavanagh, J. M., Cornelissen, S., Fletcher, D. F., & Gernaey, K. V. (2021). Understanding gradients in industrial bioreactors. *Biotechnology Advances*, *46*, 107660.

[50] Sweere, A. P., Luyben, K. C. A., & Kossen, N. W. (1987). Regime analysis and scale-down: Tools to investigate the performance of bioreactors. *Enzyme and Microbial Technology*, *9*(7), 386–398.

[51] Löffler, M., Simen, J. D., Jäger, G., Schäferhoff, K., Freund, A., & Takors, R. (2016). Engineering E. coli for large-scale production – Strategies considering ATP expenses and transcriptional responses. *Metabolic Engineering*, *38*, 73–85.

[52] Olughu, W., Deepika, G., Hewitt, C., & Rielly, C. (2019). Insight into the large-scale upstream fermentation environment using scaled-down models. *Journal of Chemical Technology and Biotechnology*, *94*(3), 647–657.

[53] Sandoval-Basurto, E. A., Gosset, G., Bolivar, F., & Ramírez, O. T. (2005). Culture of Escherichia coli under dissolved oxygen gradients simulated in a two-compartment scale-down system: Metabolic response and production of recombinant protein. *Biotechnology and Bioengineering*, *89*(4), 453–463.

[54] Baart, G. J., & Martens, D. E. (2012). Genome-scale metabolic models: Reconstruction and analysis. *Methods in Molecular Biology*, *799*, 107–126.

[55] Li, X., Griffin, D., Li, X., & Henson, M. A. (2019). Incorporating hydrodynamics into spatiotemporal metabolic models of bubble column gas fermentation. *Biotechnology and Bioengineering*, *116*(1), 28–40.

[56] Siebler, F., Lapin, A., Hermann, M., & Takors, R. (2019). The impact of CO gradients on C. ljungdahlii in a 125m3 bubble column: Mass transfer, circulation time and lifeline analysis. *Chemical Engineering Science*, *207*, 410–423.

[57] Haringa, C., Tang, W., Deshmukh, A. T., Xia, J., Reuss, M., Heijnen, J. J., Mudde, R. F., & Noorman, H. J. (2016). Euler-Lagrange computational fluid dynamics for (bio)reactor scale down: An analysis of organism lifelines. *Engineering in Life Sciences*, *16*(7), 652–663.

[58] Lapin, A., Müller, D., & Reuss, M. (2004). Dynamic behavior of microbial populations in stirred bioreactors simulated with Euler-Lagrange methods: Traveling along the lifelines of single cells. *Industrial and Engineering Chemistry Research*, *43*(16), 4647–4656.

[59] Humphrey, A. (1998). Shake flask to fermentor: What have we learned? *Biotechnology Progress*, *14*(1), 3–7.

[60] Shaikh, A., & Al-Dahhan, M. (2013). Scale-up of bubble column reactors: A review of current state-of-the-art. *Industrial and Engineering Chemistry Research*, *52*(24), 8091–8108.

[61] Stocks, S. M. (2013). Industrial enzyme production for the food and beverage industries: process scale up and scale down. *Microbial Production of Food Ingredients, Enzymes and Nutraceuticals*, (pp. 144–172).

[62] Noorman, H. J., & Heijnen, J. J. (2017). Biochemical engineering's grand adventure. *Chemical Engineering Science*, *170*, 677–693.

[63] Straathof, A. J., Wahl, S. A., Benjamin, K. R., Takors, R., Wierckx, N., & Noorman, H. J. (2019). Grand Research Challenges for Sustainable Industrial Biotechnology. *Trends in Biotechnology*, *37*(10), 1042–1050.

[64] Delvigne, F., Takors, R., Mudde, R., van Gulik, W., & Noorman, H. (2017). Bioprocess scale-up/down as integrative enabling technology: from fluid mechanics to systems biology and beyond. *Microbial Biotechnology*, *10*(5), 1267–1274.

[65] Neubauer, P., & Junne, S. (2010). Scale-down simulators for metabolic analysis of large-scale bioprocesses. *Current Opinion in Biotechnology*, *21*(1), 114–121.

[66] Hartmann, F. S., Udugama, I. A., Seibold, G. M., Sugiyama, H., & Gernaey, K. V. (2022). Digital models in biotechnology: Towards multi-scale integration and implementation. *Biotechnology Advances*, *60*, 108015.

[67] Wang, G., Haringa, C., Noorman, H., Chu, J., & Zhuang, Y. (2020). Developing a Computational Framework To Advance Bioprocess Scale-Up. *Trends in Biotechnology*, *38*(8), 846–856.

[68] Wang, G., Haringa, C., Tang, W., Noorman, H., Chu, J., Zhuang, Y., & Zhang, S. (2020). Coupled metabolic-hydrodynamic modeling enabling rational scale-up of industrial bioprocesses. *Biotechnology and Bioengineering*, *117*(3), 844–867.

[69] Hofmann, S., Weiland, C., Fitschen, J., von Kameke, A., Hoffmann, M., & Schlüter, M. (2022). Lagrangian sensors in a stirred tank reactor: Comparing trajectories from 4D-Particle Tracking Velocimetry and Lattice-Boltzmann simulations. *Chemical Engineering Journal*, *449*(137549).

[70] Box, G. E. P. (1976). Science and Statistics. *Journal of the American Statistical Association*, *71*(356), 791–799.

[71] van't Riet, K., & van der Lans, R. G. (2011). Mixing in Bioreactor Vessels. *Comprehensive Biotechnology, Second Edition*, *2*, 63–80.

[72] Deckwer, W. D., Burckhart, R., & Zoll, G. (1974). Mixing and mass transfer in tall bubble columns. *Chemical Engineering Science*, *29*(11), 2177–2188.

[73] Luttmann, R., Thoma, M., Buchholz, H., & Schügerl, K. (1983). Model development, parameter identification, and simulation of the SCP production process in air lift tower bioreactors with external loop-I. Generalized distributed parameter model. *Computers and Chemical Engineering*, *7*(1), 43–50.

[74] Van der Lans, R. (1985). *Hydrodynamics of a bubble column loop reactor*. Ph.D. thesis, Delft University of Technology, Delft.

[75] Li, X., & Henson, M. A. (2019). Metabolic modeling of bacterial co-culture systems predicts enhanced carbon monoxide-to-butyrate conversion compared to monoculture systems. *Biochemical Engineering Journal*, *151*, 107338.

[76] Haringa, C. (2022). An analysis of organism lifelines in an industrial bioreactor using Lattice-Boltzmann CFD. *Engineering in Life Sciences*, *23*(1), 1–16.

[77] Andersson, B., Andersson, R., Håkansson, L., Mortensen, M., Sudiyo, R., & Van Wachem, B. (2011). *Computational fluid dynamics for engineers*, vol. 9781107018. Cambridge University Press.

[78] Haringa, C., Noorman, H. J., & Mudde, R. F. (2017). Lagrangian modeling of hydrodynamic–kinetic interactions in (bio)chemical reactors: Practical implementation and setup guidelines. *Chemical Engineering Science*, *157*, 159–168.

[79] ANSYS Inc. Ansys Fluent Theory Guide.

[80] Besagni, G., Varallo, N., & Mereu, R. (2023). Computational Fluid Dynamics Modelling of Two-Phase Bubble Columns: A Comprehensive Review. *Fluids*, *8*(3).

[81] Khan, I., Wang, M., Zhang, Y., Tian, W., Su, G., & Qiu, S. (2020). Two-phase bubbly flow simulation using CFD method: A review of models for interfacial forces. *Progress in Nuclear Energy*, *125*(April), 103360.

[82] Shu, S., Vidal, D., Bertrand, F., & Chaouki, J. (2019). Multiscale multiphase phenomena in bubble column reactors: A review. *Renewable Energy*, *141*, 613–631.

[83] Cueto-Rojas, H. F., van Maris, A. J., Wahl, S. A., & Heijnen, J. J. (2015). Thermodynamics-based design of microbial cell factories for anaerobic product formation. *Trends in Biotechnology*, *33*(9), 534–546.

[84] Kleerebezem, R., & Van Loosdrecht, M. C. M. (2010). A generalized method for thermodynamic state analysis of environmental systems. *Critical Reviews in Environmental Science and Technology*, *40*(1), 1–54.

[85] Pirt, S. J. (1965). The maintenance energy of bacteria in growing cultures. *Proceedings of the Royal Society of London. Series B. Biological Sciences*, *163*(991), 224–231.

[86] Monod, J. (1949). The Growth of Bacterial Cultures. *Annual Reviews in Microbiology*, *3*(Xl), 371–394.

[87] Marcellin, E., Behrendorff, J. B., Nagaraju, S., Detissera, S., Segovia, S., Palfreyman, R. W., Daniell, J., Licona-Cassani, C., Quek, L. E., Speight, R., Hodson, M. P., Simpson, S. D., Mitchell, W. P., Köpke, M., & Nielsen, L. K. (2016). Low carbon fuels and commodity chemicals from waste gases – systematic approach to understand energy metabolism in a model acetogen. *Green Chemistry*, *18*(10), 3020–3028.

[88] Norman, R. O., Millat, T., Schatschneider, S., Henstra, A. M., Breitkopf, R., Pander, B., Annan, F. J., Piatek, P., Hartman, H. B., Poolman, M. G., Fell, D. A., Winzer, K., Minton, N. P., & Hodgman, C. (2019). Genome-scale model of C. autoethanogenum reveals optimal bioprocess conditions for high-value chemical production from carbon monoxide. *Engineering Biology*, *3*(2), 32–40.

[89] Chen, J., Daniell, J., Griffin, D., Li, X., & Henson, M. A. (2018). Experimental testing of a spatiotemporal metabolic model for carbon monoxide fermentation with Clostridium autoethanogenum. *Biochemical Engineering Journal*, *129*, 64–73.

[90] Heffernan, J. K., Valgepea, K., de Souza Pinto Lemgruber, R., Casini, I., Plan, M., Tappel, R., Simpson, S. D., Köpke, M., Nielsen, L. K., & Marcellin, E. (2020). Enhancing CO2-Valorization Using Clostridium autoethanogenum for Sustainable Fuel and Chemicals Production. *Frontiers in Bioengineering and Biotechnology*, *8*, 1–17.

[91] Henson, M. A., & Hanly, T. J. (2014). Dynamic flux balance analysis for synthetic microbial communities. *IET Systems Biology*, *8*(5), 214–229.

[92] Henson, M. A., Müller, D., & Reuss, M. (2002). Cell population modelling of yeast glycolytic oscillations. *Biochemical Journal*, *368*(2), 433–446.

[93] Lao-Martil, D., Schmitz, J. P., Teusink, B., & van Riel, N. A. (2023). Elucidating yeast glycolytic dynamics at steady state growth and glucose pulses through kinetic metabolic modeling. *Metabolic Engineering*, *77*(September 2022), 128–142.

[94] Tang, W., Deshmukh, A. T., Haringa, C., Wang, G., van Gulik, W., van Winden, W., Reuss, M., Heijnen, J. J., Xia, J., Chu, J., & Noorman, H. J. (2017). A 9-pool metabolic structured kinetic model describing days to seconds dynamics of growth and product formation by <i>Penicillium chrysogenum</i>. *Biotechnology and Bioengineering*, *114*(8), 1733–1743.

[95] Fredrickson, A. G., Megee, R. D., & Tsuchiya, H. M. (1970). Mathematical Models for Fermentation Processes. *Advances in Applied Microbiology*, *13*(C), 419–465.

[96] Morchain, J., Gabelle, J.-C., & Cockx, A. (2013). Coupling of biokinetic and population balance models to account for biological heterogeneity in bioreactors. *AIChE Journal*, *59*(2), 369–379.

[97] Pigou, M., & Morchain, J. (2015). Investigating the interactions between physical and biological heterogeneities in bioreactors using compartment, population balance and metabolic models. *Chemical Engineering Science*, *126*, 267–282.

[98] Lapin, A., Schmid, J., & Reuss, M. (2006). Modeling the dynamics of E. coli populations in the three-dimensional turbulent field of a stirred-tank bioreactor-A structured-segregated approach. *Chemical Engineering Science*, *61*(14), 4783–4797.

[99] Haringa, C., Tang, W., Wang, G., Deshmukh, A. T., van Winden, W. A., Chu, J., van Gulik, W. M., Heijnen, J. J., Mudde, R. F., & Noorman, H. J. (2018). Computational fluid dynamics simulation of an industrial P. chrysogenum fermentation with a coupled 9-pool metabolic model: Towards rational scale-down and design optimization. *Chemical Engineering Science*, *175*, 12–24.

[100] Wei, P., Haringa, C., Portela, L. M., & Noorman, H. J. (2023). Metabolic-fluid dynamics model construction and scale-down design for an industrial penicillin chrysogenum fermentation with combined dissolved oxygen and glucose concentration dynamics. *Chemical Engineering Science*, *276*(April), 118770.

[101] Du, Y. H., Wang, M. Y., Yang, L. H., Tong, L. L., Guo, D. S., & Ji, X. J. (2022). Optimization and Scale-Up of Fermentation Processes Driven by Models. *Bioengineering*, *9*(9), 1–18.

[102] Xia, J., Wang, G., Fan, M., Chen, M., Wang, Z., & Zhuang, Y. (2021). Understanding the scale-up of fermentation processes from the viewpoint of the flow field in bioreactors and the physiological response of strains. *Chinese Journal of Chemical Engineering*, *30*, 178–184.

[103] Teixeira, L. V., Moutinho, L. F., & Romão-Dumaresq, A. S. (2018). Gas fermentation of C1 feedstocks: commercialization status and future prospects. *Biofuels, Bioproducts and Biorefining*, *12*(6), 1103–1117.

[104] Li, X., Cossey, B., & Trevethick, S. (2017). Fermentation of gaseous substrates.

[105] Chisti, M. Y., & Moo-Young, M. (1987). Airlift Reactors: Characteristics, Applications and Design Considerations. *Chemical Engineering Communications*, *60*(1-6), 195–242.

[106] Jakobsen, H. A. (2014). *Bubble Column Reactors.* Cham: Springer.

[107] Weiland, P., & Onken, U. (1981). Fluid dynamics and mass transfer in an airlift fermenter with external loop. *German Chemical Engineering*, *4*, 42–50.

[108] Verlaan, P., Vos, J. C., & Van 't Riet, K. (1989). Axial dispersion and oxygen transfer in the transition from bubble column to airlift-loop reactor. *Journal of Chemical Technology & Biotechnology*, *45*(3), 181–190.

[109] Bredwell, M., Srivastava, P., & Worden, R. (1999). Reactor Design Issues for Synthesis-Gas Fermentations. *Biotechnology Progress*, *15*(5), 834–844.

[110] Yasin, M., Jeong, Y., Park, S., Jeong, J., Lee, E. Y., Lovitt, R. W., Kim, B. H., Lee, J., & Chang, I. S. (2015). Microbial synthesis gas utilization and ways to resolve kinetic and mass-transfer limitations. *Bioresource Technology*, *177*, 361–374.

[111] Köpke, M., Mihalcea, C., Bromley, J. C., & Simpson, S. D. (2011). Fermentative production of ethanol from carbon monoxide. *Current Opinion in Biotechnology*, *22*(3), 320–325.

[112] Hernández-Calderón, O. M., González-Llanes, M. D., Rios-Iribe, E. Y., Jiménez-Lam, S. A., Del Carmen Chavez-Parga, M., & Escamilla-Silva, E. M. (2017).

Hydrodynamics and mass transfer simulation in airlift bioreactor with settler using computational fluid dynamics. *International Journal of Chemical Reactor Engineering*, *15*(4).

[113] Van Hecke, W., Bockrath, R., & De Wever, H. (2019). Effects of moderately elevated pressure on gas fermentation processes. *Bioresource Technology*, *293*(122129).

[114] Bello, R. A., Robinson, C. W., & Moo-Young, M. (1985). Gas holdup and overall volumetric oxygen transfer coefficient in airlift contactors. *Biotechnology and Bioengineering*, *27*(3), 369–381.

[115] Chisti, M., Fujimoto, K., & Moo-Young, M. (1986). Hydrodynamic and oxygen mass transfer studies in bubble columns and airlift bioreactors. In *Paper 117a presented at AIChE Annual Meeting*. Miami Beach.

[116] Deckwer, W. D., Nguyen-Tien, K., Kelkar, B. G., & Shah, Y. T. (1983). Applicability of axial dispersion model to analyze mass transfer measurements in bubble columns. *AIChE Journal*, *29*(6), 915–922.

[117] Jackson, M. L., & Shen, C. 1978). Aeration and mixing in deep tank fermentation systems. *AIChE Journal*, *24*(1), 63–71.

[118] Akita, K., & Yoshida, F. (1973). Gas Holdup and Volumetric Mass Transfer Coefficient in Bubble Columns. Effects of Liquid Properties. *Industrial and Engineering Chemistry Process Design and Development*, *12*(1), 76–80.

[119] Nakanoh, M., & Yoshida, F. (1980). Gas Absorption by Newtonian and Non-Newtonian Liquids in a Bubble Column. *Industrial and Engineering Chemistry Process Design and Development*, *19*(1), 190–195.

[120] Kawase, Y., Halard, B., & Moo-Young, M. (1987). Theoretical prediction of volumetric mass transfer coefficients in bubble columns for Newtonian and non-Newtonian fluids. *Chemical Engineering Science*, *42*(7), 1609–1617.

[121] Uchida, S., Tsuyutani, S., & Seno, T. (1989). Flow regimes and mass transfer in counter-current bubble columns. *The Canadian Journal of Chemical Engineering*, *67*(5), 866–869.

[122] Vatai, G. Y., & Tekić, M. N. (1989). Gas hold-up and mass transfer in bubble columns with pseudoplastic liquids. *Chemical Engineering Science*, *44*(10), 2402–2407.

[123] Kawase, Y., & Hashiguchi, N. (1996). Gas - Liquid mass transfer in external-loop airlift columns with newtonian and non-newtonian fluids. *Chemical Engineering Journal and the Biochemical Engineering Journal*, *62*(1), 35–42.

[124] Van Benthum, W. A., Van Den Hoogen, J. H., Van Der Lans, R. G., Van Loosdrecht, M. C., & Heijnen, J. J. (1999). The biofilm airlift suspension extension reactor. Part I: Design and two-phase hydrodynamics. *Chemical Engineering Science*, *54*(12), 1909–1924.

[125] Heijnen, J. J., Hols, J., Van Der Lans, R. G., Van Leeuwen, H. L., Mulder, A., & Weltevrede, R. (1997). A simple hydrodynamic model for the liquid circulation velocity in a full-scale two- and three-phase internal airlift reactor operating in the gas recirculation regime. *Chemical Engineering Science*, *52*(15), 2527–2540.

[126] Znad, H., Báleš, V., Markoš, J., & Kawase, Y. (2004). Modeling and simulation of airlift bioreactors. *Biochemical Engineering Journal*, *21*(1), 73–81.

[127] Higbie, R. (1935). The Rate of Absorption of a Pure Gas into a Still Liquid during Short Periods of Exposure. *Transactions of the AIChE*, *31*, 365–389.

[128] Calderbank, P. H., & Moo-Young, M. B. (1961). The continuous phase heat and mass-transfer properties of dispersions. *Chemical Engineering Science*, *16*(1-2), 39–54.

[129] Kaštánek, F. (1977). The volume mass transfer coefficient in a bubble bed column. *Collection of Czechoslovak Chemical Communications*, *42*(8), 2491–2497.

[130] Linek, V., Kordač, M., & Moucha, T. (2005). Mechanism of mass transfer from bubbles in dispersions part II: Mass transfer coefficients in stirred gas-liquid reactor and bubble column. *Chemical Engineering and Processing: Process Intensification*, *44*(1), 121–130.

[131] Lamont, J. C., & Scott, D. S. (1970). An eddy cell model of mass transfer into the surface of a turbulent liquid. *AIChE Journal*, *16*(4), 513–519.

[132] Kawase, Y., & Moo-Young, M. (1990). Mathematical models for design of bioreactors: Applications of. Kolmogoroff's theory of isotropic turbulence. *The Chemical Engineering Journal*, *43*(1), B19–B41.

[133] Karcz, J., Musiał, M., Bitenc, M., & Domański, M. (2013). CFD Modelling of the Fluid Flow Characteristics in an External-Loop Air-Lift Reactor. *Chemical Engineering Transactions*, *32*, 1435–1440.

[134] Moudoud, N., Rihani, R., Bentahar, F., & Legrand, J. (2018). Global hydrodynamic of hybrid external loop airlift reactor: Experiments and CFD modelling. *Chemical Engineering and Processing - Process Intensification*, *129*, 118–130.

[135] Roy, S., Dhotre, M. T., & Joshi, J. B. (2006). CFD simulation of flow and axial dispersion in external loop airlift reactor. *Chemical Engineering Research and Design*, *84*(8 A), 677–690.

[136] Teli, S. M., & Mathpati, C. S. (2021). Experimental and Numerical Study of Gas-Liquid Flow in a Sectionalized External-Loop Airlift Reactor. *Chinese Journal of Chemical Engineering*, *32*, 39–60.

[137] Dhanasekharan, K. M., Sanyal, J., Jain, A., & Haidari, A. (2005). A generalized approach to model oxygen transfer in bioreactors using population balances and computational fluid dynamics. *Chemical Engineering Science*, *60*(1), 213–218.

[138] de Medeiros, E. M., Noorman, H., Maciel Filho, R., & Posada, J. A. (2020). Production of ethanol fuel via syngas fermentation: Optimization of economic performance and energy efficiency. *Chemical Engineering Science: X*, *5*, 100056.

[139] Young, M. A., Carbonell, R. G., & Ollis, D. F. (1991). Airlift bioreactors: Analysis of local two-phase hydrodynamics. *AIChE Journal*, *37*(3), 403–428.

[140] Laborde-Boutet, C., Larachi, F., Dromard, N., Delsart, O., & Schweich, D. (2009). CFD simulation of bubble column flows: Investigations on turbulence models in RANS approach. *Chemical Engineering Science*, *64*(21), 4399–4413.

[141] Krevelen, D., & Hoftijzer, P. (1950). Studies on gas bubble formation - calculation of interfacial area in bubble contactors. *Chemical Engineering Progress*, *46*, 19–35.

[142] Reid, R. C., Prausnitz, J. M., & Poling, B. E. (1987). *The properties of gases and liquids*. New York: McGraw-Hill, 4th ed.

[143] Cussler, E. L. (2011). *Diffusion: mass transfer in fluid systems*. Cambridge; New York: Cambridge University Press, 3 ed.

[144] Sander, R. (2015). Compilation of Henry's law constants (version 4.0) for water as solvent. *Atmos. Chem. Phys*, *15*, 4399–4981.

[145] Voncken, R. M., Holmes, D. B., & den Hartog, H. W. (1964). Fluid flow in turbine-stirred, baffled tanks-III. Dispersion during circulation. *Chemical Engineering Science*, *19*(3), 209–213.

[146] Verlaan, P., Vos, J. C., & Van 't Riet, K. (1989). Hydrodynamics of the flow transition from a bubble column to an airlift-loop reactor. *Journal of Chemical Technology & Biotechnology*, *45*(2), 109–121.

[147] Verlaan, P., Van Eijs, A. M., Tramper, J., Van 't Riet, K., & Luyben, K. C. A. (1989). Estimation of axial dispersion in individual sections of an airlift-loop reactor. *Chemical Engineering Science*, *44*(5), 1139–1146.

[148] Zuber, N., & Findlay, J. A. (1965). Average volumetric concentration in two-phase flow systems. *Journal of Heat Transfer*, *87*(4), 453–468.

[149] Choi, K. H., & Lee, W. K. (1993). Circulation liquid velocity, gas holdup and volumetric oxygen transfer coefficient in external-loop airlift reactors. *Journal of Chemical Technology & Biotechnology*, *56*(1), 51–58.

[150] Ziegenhein, T., Zalucky, J., Rzehak, R., & Lucas, D. (2016). On the hydrodynamics of airlift reactors, Part I: Experiments. *Chemical Engineering Science*, *150*, 54–65.

[151] Zhang, T., Wei, C., Feng, C., Ren, Y., Wu, H., & Preis, S. (2019). Advances in characteristics analysis, measurement methods and modelling of flow dynamics in airlift reactors. *Chemical Engineering and Processing - Process Intensification*, *144*, 107633.

[152] Heijnen, J. J., Mulder, A., Weltevrede, R., Hols, J., & van Leeuwen, H. L. J. M. (1991). Large Scale Anaerobic-Aerobic Treatment of Complex Industrial Waste Water Using Biofilm Reactors. *Water Science and Technology*, *23*(7-9), 1427–1436.

[153] Choi, K. H., & Lee, W. K. (1990). Recirculation and flow structures of gas in downcomer section of a concentric cylindrical airlift reactor. *Journal of Chemical Technology & Biotechnology*, *48*(1), 81–95.

[154] Menzel, T., Kantorek, H. J., Franz, K., Buchholz, R., & Onken, U. (1985). Zur Strömungsstruktur in Airlift-Schlaufenreaktoren. *Chemie Ingenieur Technik*, *57*(2), 139–141.

[155] Zlokarnik, M. (1980). Koaleszenzphänomene im System gasförmig/flüssig und deren Einfluß auf den O2-Eintrag bei der biologischen Abwasserreinigung. *Korrespondenz Abwasser*, *27*(11), 728–734.

[156] Besagni, G., Inzoli, F., De Guido, G., & Pellegrini, L. A. (2016). Experimental investigation on the influence of ethanol on bubble column hydrodynamics. *Chemical Engineering Research and Design*, *112*, 1–15.

[157] Jamialahmadi, M., & Müller-Steinhagen, H. (1992). Effect of alcohol, organic acid and potassium chloride concentration on bubble size, bubble rise velocity and gas hold-up in bubble columns. *The Chemical Engineering Journal*, *50*(1), 47–56.

[158] Oels, U., Schügerl, K., & Todt, J. (1976). Gasanteil, Stofftransportgeschwindigkeitskoeffizient und spezifische Phasengrenzfläche in Gleichstrom-Blasensäulen. *Chemie Ingenieur Technik*, *48*(1), 73–73.

[159] Rollbusch, P., Becker, M., Ludwig, M., Bieberle, A., Grünewald, M., Hampel, U., & Franke, R. (2015). Experimental investigation of the influence of column scale, gas density and liquid properties on gas holdup in bubble columns. *International Journal of Multiphase Flow*, *75*, 88–106.

[160] Krishna, R., Urseanu, M. I., & Dreher, A. J. (2000). Gas hold-up in bubble columns: influence of alcohol addition versus operation at elevated pressures. *Chemical Engineering and Processing: Process Intensification*, *39*(4), 371–378.

[161] Azher, N. E., Gourich, B., Vial, C., Soulami Bellhaj, M., Bouzidi, A., Barkaoui, M., & Ziyad, M. (2005). Influence of alcohol addition on gas hold-up, liquid circulation velocity and mass transfer coefficient in a split-rectangular airlift bioreactor. *Biochemical Engineering Journal*, *23*(2), 161–167.

[162] Kojić, P. S., Tokić, M. S., Šijački, I. M., Lukić, N. L., Petrović, D. L., Jovičević, D. Z., & Popović, S. S. (2015). Influence of the Sparger Type and Added Alcohol on the Gas Holdup of an External-Loop Airlift Reactor. *Chemical Engineering and Technology*, *38*(4), 701–708.

[163] Maximiano Raimundo, P., Cloupet, A., Cartellier, A., Beneventi, D., & Augier, F. (2019). Hydrodynamics and scale-up of bubble columns in the heterogeneous regime: Comparison of bubble size, gas holdup and liquid velocity measured in 4 bubble columns from 0.15m to 3m in diameter. *Chemical Engineering Science*, *198*, 52–61.

[164] Gimbun, J., Rielly, C. D., & Nagy, Z. K. (2009). Modelling of mass transfer in gas-liquid stirred tanks agitated by Rushton turbine and CD-6 impeller: A scale-up study. *Chemical Engineering Research and Design*, *87*(4), 437–451.

[165] Kuschel, M., & Takors, R. (2020). Simulated oxygen and glucose gradients as a prerequisite for predicting industrial scale performance a priori. *Biotechnology and Bioengineering*, *117*(9), 2760–2770.

[166] Roels, J. A., & Heijnen, J. J. (1980). Power dissipation and heat production in bubble columns: Approach based on nonequilibrium thermodynamics. *Biotechnology and Bioengineering*, *22*(11), 2399–2404.

[167] Gaddy, J. L., Arora, D. K., Ko, C.-W., Phillips, J. R., Basu, R., Wikstrom, C. V., & Clausen, E. C. (2001). Methods for increasing the production of ethanol from microbial fermentation.

[168] Simpson, S. D., Forster, R. L. S., Rowe, M. J., Tran, P. L., & Collet, C. (2008). Alcohol production process.

[169] Oswald, F., Stoll, I. K., Zwick, M., Herbig, S., Sauer, J., Boukis, N., & Neumann, A. (2018). Formic Acid Formation by Clostridium ljungdahlii at Elevated Pressures of Carbon Dioxide and Hydrogen. *Frontiers in Bioengineering and Biotechnology*, *6*, 1–10.

[170] Schumpe, A., Saxena, A. K., & Fang, L. K. (1987). Gas/liquid mass transfer in a slurry bubble column. *Chemical Engineering Science*, *42*(7), 1787–1796.

[171] Vazirizadeh, A., Bouchard, J., & Chen, Y. (2016). Effect of particles on bubble size distribution and gas hold-up in column flotation. *International Journal of Mineral Processing*, *157*, 163–173.

[172] Merchuk, J. C., & Stein, Y. (1981). Local hold-up and liquid velocity in air-lift reactors. *AIChE Journal*, *27*(3), 377–388.

[173] Shchukarev, S. A., & Tolmacheva, T. A. (1968). Solubility of oxygen in ethanol — Water mixtures. *Journal of Structural Chemistry 1968 9:1*, *9*(1), 16–21.

[174] Häusler, E. B., van der Wielen, L. A., & Straathof, A. J. (2016). Evaluation of gas supply configurations for microbial product formation involving multiple gaseous substrates. *Bioresources and Bioprocessing*, *3*(1), 1–12.

[175] Jourdin, L., & Burdyny, T. (2021). Microbial Electrosynthesis: Where Do We Go from Here? *Trends in Biotechnology*, *39*(4), 359–369.

[176] Cabau-Peinado, O., Straathof, A. J. J., & Jourdin, L. (2021). A General Model for Biofilm-Driven Microbial Electrosynthesis of Carboxylates From CO2. *Frontiers in Microbiology*, *12*, 1–17.

[177] Stone, K. A., Hilliard, M. V., He, Q. P., & Wang, J. (2017). A mini review on bioreactor configurations and gas transfer enhancements for biochemical methane conversion. *Biochemical Engineering Journal*, *128*, 83–92.

[178] Orgill, J. J., Atiyeh, H. K., Devarapalli, M., Phillips, J. R., Lewis, R. S., & Huhnke, R. L. (2013). A comparison of mass transfer coefficients between trickle-bed, Hollow fiber membrane and stirred tank reactors. *Bioresource Technology*, *133*, 340–346.

[179] Galaction, A. I., Cascaval, D., Oniscu, C., & Turnea, M. (2004). Prediction of oxygen mass transfer coefficients in stirred bioreactors for bacteria, yeasts and fungus broths. *Biochemical Engineering Journal*, *20*(1), 85–94.

[180] Lessard, R. R., & Zieminski, S. A. (1971). Bubble Coalescence and Gas Transfer in Aqueous Electrolytic Solutions. *Industrial and Engineering Chemistry Fundamentals*, *10*(2), 260–269.

[181] Prins, A., & van't Riet, K. (1987). Proteins and surface effects in fermentation: foam, antifoam and mass transfer. *Trends in Biotechnology*, *5*(11), 296–301.

[182] Zieminski, S. A., Caron, M. M., & Blackmore, R. B. (1967). Behavior of air bubbles in dilute aqueous solutions. *Industrial and Engineering Chemistry Fundamentals*, *6*(2), 233–242.

[183] Zlokarnik, M. (1981). Verfahrenstechnische Grundlagen der Reaktorgestaltung. *Acta Biotechnologica*, *1*(4), 311–325.

[184] Lizardi-Jiménez, M. A., López-Ordáz, P., González-Brambila, M. M., Linares-Morales, A., & Melgarejo-Torres, R. (2018). Effect of Biomass Concentration on Oxygen Mass Transfer, Power Consumption, Interfacial Tension and Hydrodynamics in a Multiphase Partitioning Bioreactor. *International Journal of Chemical Reactor Engineering*, *16*(10), 1–10.

[185] Rosso, D., Larson, L. E., & Stenstrom, M. K. (2008). Aeration of large-scale municipal wastewater treatment plants: state of the art. *Water Science and Technology*, *57*(7), 973–978.

[186] APHA/AWWA/WEF (1999). Standard methods for the examination of water and wastewater. In *Standard Methods*. 20 ed.

[187] Bi, Y. H., Hill, G. A., & Sumner, R. J. (2001). Enhancement of the overall volumetric oxygen transfer coefficient in a stirred tank bioreactor using ethanol. *The Canadian Journal of Chemical Engineering*, *79*(3), 463–467.

[188] Bin, A. K., & Smith, J. M. (1982). CHEMICAL ENGINEERING COMMUNICATIONS MASS TRANSFER IN A PLUNGING LIQUID JET ABSORBER. *CHEMICAL ENGINEERING COMMUNICATIONS*, *15*, 367–383.

[189] Miyahara, T., & Nagatani, N. (2009). Influence of alcohol addition on liquid-phase volumetric mass transfer coefficient in an external-loop airlift reactor with a porous plate. *Journal of Chemical Engineering of Japan*, *42*(10), 713–719.

[190] Munasinghe, P. C., & Khanal, S. K. (2010). Syngas fermentation to biofuel: Evaluation of carbon monoxide mass transfer coefficient (kLa) in different reactor configurations. *Biotechnology Progress*, *26*(6), 1616–1621.

[191] De Kok, S., Meijer, J., Van Loosdrecht, M. C., & Kleerebezem, R. (2013). Impact of dissolved hydrogen partial pressure on mixed culture fermentations. *Applied Microbiology and Biotechnology*, *97*(6), 2617–2625.

[192] McClure, D. D., Lamy, M., Black, L., Kavanagh, J. M., & Barton, G. W. (2017). An experimental investigation into the behaviour of antifoaming agents. *Chemical Engineering Science*, *160*, 269–274.

[193] Bandyopadhyay, B., Humphrey, A. E., & Taguchi, H. (1967). Dynamic measurement of the volumetric oxygen transfer coefficient in fermentation systems. *Biotechnology and Bioengineering*, *9*(4), 533–544.

[194] Linek, V., Sinkule, J., & Beneš, P. (1991). Critical assessment of gassing-in methods for measuring kla in fermentors. *Biotechnology and Bioengineering*, *38*(4), 323–330.

[195] Van't Riet, K. (1979). Review of Measuring Methods and Results in Nonviscous Gas-Liquid Mass Transfer in Stirred Vessels. *Industrial & Engineering Chemistry Process Design and Development*, *18*(3), 357–364.

[196] Wilkinson, P. M., Spek, A. P., & van Dierendonck, L. L. (1992). Design parameters estimation for scale-up of high-pressure bubble columns. *AIChE Journal*, *38*(4), 544–554.

[197] Puiman, L., Elisiário, M. P., Crasborn, L. M., Wagenaar, L. E., Straathof, A. J., & Haringa, C. (2022). Gas mass transfer in syngas fermentation broths is enhanced by ethanol. *Biochemical Engineering Journal*, *185*, 108505.

[198] Phillips, J. R., Huhnke, R. L., & Atiyeh, H. K. (2017). Syngas Fermentation: A Microbial Conversion Process of Gaseous Substrates to Various Products. *Fermentation 2017, Vol. 3, Page 28*, *3*(2), 28.

[199] Xu, H., Liang, C., Chen, X., Xu, J., Yu, Q., Zhang, Y., & Yuan, Z. (2020). Impact of exogenous acetate on ethanol formation and gene transcription for key enzymes in Clostridium autoethanogenum grown on CO. *Biochemical Engineering Journal*, *155*, 107470.

[200] McClure, D. D., Kavanagh, J. M., Fletcher, D. F., & Barton, G. W. (2016). Characterizing bubble column bioreactor performance using computational fluid dynamics. *Chemical Engineering Science*, *144*, 58–74.

[201] Haringa, C., Deshmukh, A. T., Mudde, R. F., & Noorman, H. J. (2017). Euler-Lagrange analysis towards representative down-scaling of a 22 m3 aerobic S. cerevisiae fermentation. *Chemical Engineering Science*, *170*, 653–669.

[202] Kuschel, M., Siebler, F., & Takors, R. (2017). Lagrangian Trajectories to Predict the Formation of Population Heterogeneity in Large-Scale Bioreactors. *Bioengineering*, *4*(4), 27.

[203] Greene, J., Daniell, J., Köpke, M., Broadbelt, L., & Tyo, K. E. (2019). Kinetic ensemble model of gas fermenting Clostridium autoethanogenum for improved ethanol production. *Biochemical Engineering Journal*.

[204] Mahamkali, V., Valgepea, K., de Souza Pinto Lemgruber, R., Plan, M., Tappel, R., Köpke, M., Simpson, S. D., Nielsen, L. K., & Marcellin, E. (2020). Redox controls metabolic robustness in the gas-fermenting acetogen Clostridium autoethanogenum. *Proceedings of the National Academy of Sciences of the United States of America*, *117*(23), 13168–13175.

[205] Nadal-Rey, G., McClure, D. D., Kavanagh, J. M., Cassells, B., Cornelissen, S., Fletcher, D. F., & Gernaey, K. V. (2021). Development of dynamic compartment models for industrial aerobic fed-batch fermentation processes. *Chemical Engineering Journal*, *420*, 130402.

[206] Puiman, L., Abrahamson, B., van der Lans, R. G., Haringa, C., Noorman, H. J., & Picioreanu, C. (2022). Alleviating mass transfer limitations in industrial external-loop syngas-to-ethanol fermentation. *Chemical Engineering Science*, *259*, 117770.

[207] Zanghi, A., Lin, D., Balsara, T., Young, L., Wolf, B., & Huang, P. (2017). Increased efficiency and product quality with the UniVessel ® Single Use bioreactor for CHO fed-batch cultures.

[208] de Medeiros, E. M., Posada, J. A., Noorman, H., & Filho, R. M. (2019). Modeling and Multi-Objective Optimization of Syngas Fermentation in a Bubble Column Reactor. *Computer Aided Chemical Engineering*, *46*, 1531–1536.

[209] De Jong, T., Fernandes, C., D'Ambruoso, A., & Koechlein, D. (2019). Scalability in Laboratory Bioreactors Based on Constant Volumetric Mass Transfer Coefficient (kLa).

[210] Gaugler, L., Mast, Y., Fitschen, J., Hofmann, S., Schlüter, M., & Takors, R. (2022). Scaling-down biopharmaceutical production processes via a single multi-compartment bioreactor (SMCB). *Engineering in Life Sciences*.

[211] Oosterhuis, N. (1984). *Scale-up of bioreactors: A scale-down approach*. Ph.D. thesis, Delft University of Technology, Delft.

[212] Wang, G., Tang, W., Xia, J., Chu, J., Noorman, H., & van Gulik, W. M. (2015). Integration of microbial kinetics and fluid dynamics toward model-driven scale-up of industrial bioprocesses. *Engineering in Life Sciences*, *15*(1), 20–29.

[213] Esperança, M. N., Buffo, M. M., Mendes, C. E., Rodriguez, G. Y., Béttega, R., Badino, A. C., & Cerri, M. O. (2022). Linking maximal shear rate and energy dissipation/circulation function in airlift bioreactors. *Biochemical Engineering Journal*, *178*, 108308.

[214] Smith, J. J., Lilly, M. D., & Fox, R. I. (1990). The effect of agitation on the morphology and penicillin production of Penicillium chrysogenum. *Biotechnology and Bioengineering*, *35*(10), 1011–1023.

[215] Nienow, A. W. (2021). The Impact of Fluid Dynamic Stress in Stirred Bioreactors – The Scale of the Biological Entity: A Personal View. *Chemie-Ingenieur-Technik*, *93*(1-2), 17–30.

[216] Dang, J., Wang, N., & Atiyeh, H. K. (2021). Review of Dissolved CO and H2 Measurement Methods for Syngas Fermentation. *Sensors 2021, Vol. 21, Page 2165*, *21*(6), 2165.

[217] Mann, M., Hüser, A., Schick, B., Dinger, R., Miebach, K., & Büchs, J. (2021). Online monitoring of gas transfer rates during CO and CO/H2 gas fermentation in quasi-continuously ventilated shake flasks. *Biotechnology and Bioengineering*, *118*(5), 2092–2104.

[218] Benalcázar, E. A., Noorman, H., Filho, R. M., & Posada, J. (2022). A systematic approach for the processing of experimental data from anaerobic syngas fermentations. *Computer Aided Chemical Engineering*, *51*, 1303–1308.

[219] de Jonge, L. P., Buijs, N. A., ten Pierick, A., Deshmukh, A., Zhao, Z., Kiel, J. A., Heijnen, J. J., & van Gulik, W. M. (2011). Scale-down of penicillin production in Penicillium chrysogenum. *Biotechnology Journal*, *6*(8), 944–958.

[220] Marcellin, E., Angenent, L. T., Nielsen, L. K., & Molitor, B. (2022). Recycling carbon for sustainable protein production using gas fermentation. *Current Opinion in Biotechnology*, *76*, 102723.

[221] Diender, M., Parera Olm, I., Gelderloos, M., Koehorst, J. J., Schaap, P. J., Stams, A. J., & Sousa, D. Z. (2019). Metabolic shift induced by synthetic co-cultivation promotes high yield of chain elongated acids from syngas. *Scientific Reports*, *9*(1), 1–11.

[222] Lagoa-Costa, B., Abubackar, H. N., Fernández-Romasanta, M., Kennes, C., & Veiga, M. C. (2017). Integrated bioconversion of syngas into bioethanol and biopolymers. *Bioresource Technology*, *239*, 244–249.

[223] Ishaq, H., Dincer, I., & Crawford, C. (2022). A review on hydrogen production and utilization: Challenges and opportunities. *International Journal of Hydrogen Energy*, *47*(62), 26238–26264.

[224] Puiman, L., Almeida Benalcázar, E., Picioreanu, C., Noorman, H. J., & Haringa, C. (2023). Downscaling Industrial-Scale Syngas Fermentation to Simulate Frequent and Irregular Dissolved Gas Concentration Shocks. *Bioengineering*, *10*(5), 1–22.

[225] McLeod, A., Jefferson, B., & McAdam, E. J. (2016). Toward gas-phase controlled mass transfer in micro-porous membrane contactors for recovery and concentration of dissolved methane in the gas phase. *Journal of Membrane Science*, *510*, 466–471.

[226] Nadal-Rey, G., Kavanagh, J. M., Cassells, B., Cornelissen, S., Fletcher, D. F., Gernaey, K. V., & McClure, D. D. (2023). Modelling of industrial-scale bioreactors using the particle lifeline approach. *Biochemical Engineering Journal*, *198*(June), 108989.

[227] Haringa, C., Tang, W., & Noorman, H. J. (2022). Stochastic parcel tracking in an Euler–Lagrange compartment model for fast simulation of fermentation processes. *Biotechnology and Bioengineering*, *119*(7), 1849–1860.

[228] Le Nepvou De Carfort, J., Pinto, T., & Krühne, U. (2024). An Automatic Method for Generation of CFD-Based 3D Compartment Models: Towards Real-Time Mixing Simulations. *Bioengineering*, *11*(2), 1–17.

[229] Ragsdale, S. W., & Pierce, E. (2008). Acetogenesis and the Wood-Ljungdahl pathway of CO2 fixation. *Biochimica et Biophysica Acta - Proteins and Proteomics*, *1784*(12), 1873–1898.

[230] Schuchmann, K., & Müller, V. (2014). Autotrophy at the thermodynamic limit of life: A model for energy conservation in acetogenic bacteria. *Nature Reviews Microbiology*, *12*(12), 809–821.

[231] Mock, J., Zheng, Y., Mueller, A. P., Ly, S., Tran, L., Segovia, S., Nagaraju, S., Köpke, M., Dürre, P., & Thauer, R. K. (2015). Energy conservation associated with ethanol formation from H2 and CO2 in Clostridium autoethanogenum involving electron bifurcation. *Journal of Bacteriology*, *197*(18), 2965–2980.

[232] Liu, Z. Y., Jia, D. C., Zhang, K. D., Zhu, H. F., Zhang, Q., Jiang, W. H., Gu, Y., & Li, F. L. (2020). Ethanol metabolism dynamics in Clostridium ljungdahlii grown on carbon monoxide. *Applied and Environmental Microbiology*, *86*(14).

[233] Richter, H., Molitor, B., Wei, H., Chen, W., Aristilde, L., & Angenent, L. T. (2016). Ethanol production in syngas-fermenting Clostridium ljungdahlii is controlled by thermodynamics rather than by enzyme expression. *Energy & Environmental Science*, *9*(7), 2392–2399.

[234] Grimalt-Alemany, A., Etler, C., Asimakopoulos, K., Skiadas, I. V., & Gavala, H. N. (2021). ORP control for boosting ethanol productivity in gas fermentation systems and dynamics of redox cofactor NADH/NAD + under oxidative stress. *Journal of CO2 Utilization*, *50*, 101589.

[235] Haringa, C., Mudde, R. F., & Noorman, H. J. (2018). From industrial fermentor to CFD-guided downscaling: what have we learned? *Biochemical Engineering Journal*, *140*, 57–71.

[236] Heijnen, J. J. (2005). Approximative kinetic formats used in metabolic network modeling. *Biotechnology and Bioengineering*, *91*(5), 534–545.

[237] Visser, D., & Heijnen, J. J. (2003). Dynamic simulation and metabolic re-design of a branched pathway using linlog kinetics. *Metabolic Engineering*, *5*(3), 164–176.

[238] del Rosario, R. C., Mendoza, E., & Voit, E. O. (2008). Challenges in lin-log modelling of glycolysis in Lactococcus lactis. *IET Systems Biology*, *2*(3), 136–149.

[239] Schuchmann, K., & Müller, V. (2013). Direct and reversible hydrogenation of CO2 to formate by a bacterial carbon dioxide reductase. *Science*, *342*(6164), 1382–1385.

[240] Allaart, M. T., Diender, M., Sousa, D. Z., & Kleerebezem, R. (2023). Overflow metabolism at the thermodynamic limit of life: How carboxydotrophic acetogens mitigate carbon monoxide toxicity. *Microbial Biotechnology*, *16*(4), 697–705.

[241] Seravalli, J., Kumar, M., Lu, W. P., & Ragsdale, S. W. (1997). Mechanism of carbon monoxide oxidation by the carbon monoxide dehydrogenase/acetyl-CoA synthase from Clostridium thermoaceticum: Kinetic characterization of the intermediates. *Biochemistry*, *36*(37), 11241–11251.

[242] Hu, Q., Yang, H., Xu, H., Wu, Z., Lim, C. J., Bi, X. T., & Chen, H. (2018). Thermal behavior and reaction kinetics analysis of pyrolysis and subsequent in-situ gasification of torrefied biomass pellets. *Energy Conversion and Management*, *161*, 205–214.

[243] Hermann, M., Teleki, A., Weitz, S., Niess, A., Freund, A., Bengelsdorf, F. R., & Takors, R. (2020). Electron availability in CO2, CO and H2 mixtures constrains flux distribution, energy management and product formation in Clostridium ljungdahlii. *Microbial Biotechnology*, *13*(6), 1831–1846.

[244] Kantzow, C., & Weuster-Botz, D. (2016). Effects of hydrogen partial pressure on autotrophic growth and product formation of Acetobacterium woodii. *Bioprocess and Biosystems Engineering*, *39*(8), 1325–1330.

[245] Bertsch, J., & Müller, V. (2015). Bioenergetic constraints for conversion of syngas to biofuels in acetogenic bacteria. *Biotechnology for Biofuels*, *8*(1), 1–12.

[246] Niebel, B., Leupold, S., & Heinemann, M. (2019). An upper limit on Gibbs energy dissipation governs cellular metabolism. *Nature Metabolism*, *1*(1), 125–132.

[247] Fredrickson, A. G., & Stephanopoulos, G. (1981). Microbial competition. *Science*, *213*(4511), 972–979.

[248] Biegel, E., Schmidt, S., González, J. M., & Müller, V. (2011). Biochemistry, evolution and physiological function of the Rnf complex, a novel ion-motive electron transport complex in prokaryotes. *Cellular and Molecular Life Sciences*, *68*(4), 613–634.

[249] Wang, S., Huang, H., Kahnt, H. H., Mueller, A. P., Köpke, M., & Thauer, R. K. (2013). NADP-Specific electron-bifurcating [FeFe]-hydrogenase in a functional complex with formate dehydrogenase in clostridium autoethanogenum grown on CO. *Journal of Bacteriology*, *195*(19), 4373–4386.

[250] Panneerselvam, A., Wilkins, M. R., DeLorme, M. J., Atiyeh, H. K., & Huhnke, R. L. (2010). Effects of various reducing agents on syngas fermentation by clostridium ragsdalei. *Biological Engineering*, *2*(3), 135–144.

[251] Lo, J., Olson, D. G., Murphy, S. J. L., Tian, L., Hon, S., Lanahan, A., Guss, A. M., & Lynd, L. R. (2017). Engineering electron metabolism to increase ethanol production in Clostridium thermocellum. *Metabolic Engineering*, *39*, 71–79.

[252] Mann, M., Miebach, K., & Büchs, J. (2021). Online measurement of dissolved carbon monoxide concentrations reveals critical operating conditions in gas fermentation experiments. *Biotechnology and Bioengineering*, *118*(1), 253–264.

[253] Biegel, E., & Müller, V. (2010). Bacterial Na+-translocating ferredoxin: NAD+ oxidoreductase. *Proceedings of the National Academy of Sciences of the United States of America*, *107*(42), 18138–18142.

[254] Krasna, A. I. (1979). Hydrogenase: Properties and applications. *Enzyme and Microbial Technology*, *1*(3), 165–172.

[255] Perec, L., Krasna, A. I., & Rittenberg, D. (1962). The Inhibition of Hydrogenase by Carbon Monoxide and the Reversal of this Inhibition by Light. *Biochemistry*, *1*(2), 270–275.

[256] Tang, W. (2022). *Structured Kinetic Modeling for Rational Scale-down and Design Optimization of Industrial Fermentations.* Ph.D. thesis.

[257] Vlaeminck, E., Uitterhaegen, E., Quataert, K., Delmulle, T., Kontovas, S. S., Misailidis, N., Ferreira, R. G., Petrides, D., De Winter, K., & Soetaert, W. K. (2023). Single-Cell Protein Production from Industrial Off-Gas through Acetate: Techno-Economic Analysis for a Coupled Fermentation Approach. *Fermentation*, *9*(8).

[258] Tanaka, K., Ishizaki, A., Kanamaru, T., & Kawano, T. (1995). Production of PoIy(D-3-Hydroxybutyrate) from COP, H2, and O2 by High Cell Density Autotrophic Cultivation of Alcaligenes eutrophus. *Biotechnology and Bioengineering*, *45*, 268–275.

[259] Jones, S. W., Karpol, A., Friedman, S., Maru, B. T., & Tracy, B. P. (2020). Recent advances in single cell protein use as a feed ingredient in aquaculture. *Current Opinion in Biotechnology*, *61*, 189–197.

[260] Dagley, S., & Hinshelwood, C. N. (1938). 365. Physicochemical aspects of bacterial growth. Part III. Influence of alcohols on the growth of Bact. lactis aerogenes. *Journal of the Chemical Society (Resumed)*, (pp. 1942–1948).

[261] Ramió-Pujol, S., Ganigué, R., Bañeras, L., & Colprim, J. (2018). Effect of ethanol and butanol on autotrophic growth of model homoacetogens. *FEMS Microbiology Letters*, *365*(10), 1–4.

[262] Phillips, J. R., Klasson, K. T., Clausen, E. C., & Gaddy, J. L. (1993). Biological production of ethanol from coal synthesis gas - Medium development studies. *Applied Biochemistry and Biotechnology*, *39-40*(1), 559–571.

[263] Dusny, C., & Grünberger, A. (2020). Microfluidic single-cell analysis in biotechnology: from monitoring towards understanding. *Current Opinion in Biotechnology*, *63*, 26–33.

[264] Täuber, S., Schmitz, J., Blöbaum, L., Fante, N., Steinhoff, H., & Grünberger, A. (2021). How to perform a microfluidic cultivation experiment—a guideline to success. *Biosensors*, *11*(12).

[265] Täuber, S., Blöbaum, L., Steier, V., Oldiges, M., & Grünberger, A. (2022). Microfluidic single-cell scale-down bioreactors: A proof-of-concept for the growth of Corynebacterium glutamicum at oscillating pH values. *Biotechnology and Bioengineering*, *119*(11), 3194–3209.

[266] Kasahara, K., Leygeber, M., Seiffarth, J., Ruzaeva, K., Drepper, T., Nöh, K., & Kohlheyer, D. (2023). Enabling oxygen-controlled microfluidic cultures for spatiotemporal microbial single-cell analysis. *Frontiers in Microbiology*, *14*.

[267] Blöbaum, L., Haringa, C., & Grünberger, A. (2023). Microbial lifelines in bioprocesses: From concept to application. *Biotechnology Advances*, *62*, 108071.

[268] Swain, M. C., & Cole, J. M. (2016). ChemDataExtractor: A Toolkit for Automated Extraction of Chemical Information from the Scientific Literature. *Journal of Chemical Information and Modeling*, *56*, 1894–1904.

[269] Garcia-Ochoa, F., & Gomez, E. (2005). Prediction of gas-liquid mass transfer coefficient in sparged stirred tank bioreactors. *Biotechnology and Bioengineering*, *92*(6), 761–772.

[270] Allaart, M. T. (2023). *Poison to Products: On harnessing the power of microorganisms to convert waste streams into new chemicals.* Ph.D. thesis, Delft University of Technology.

[271] Heffernan, J. K., Mahamkali, V., Valgepea, K., Marcellin, E., & Nielsen, L. K. (2022). Analytical tools for unravelling the metabolism of gas-fermenting Clostridia. *Current Opinion in Biotechnology*, *75*, 102700.

[272] Bishop, C. M. (2006). *Pattern Recognition and Machine Learning*. New York: Springer, 1 ed.

[273] Press, W. H., Teukolsky, S. A., Vetterling, W. T., & Flannery, B. P. (1992). *Numerical Recipes in C. The Art of Scientific Computing*. Cambridge University Press, 2nd ed.

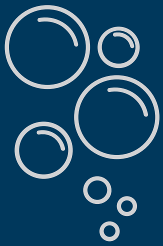

Appendix A

Supplement Chapter 2

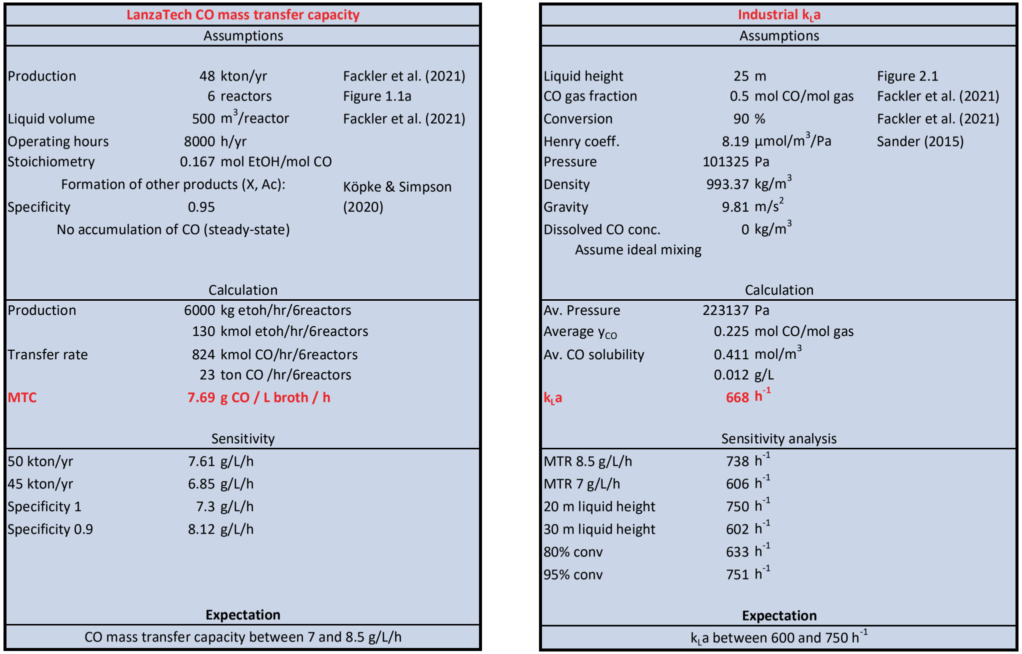

LanzaTech CO mass transfer capacity			
Assumptions			
Production	48	kton/yr	Fackler et al. (2021)
	6	reactors	Figure 1.1a
Liquid volume	500	m^3/reactor	Fackler et al. (2021)
Operating hours	8000	h/yr	
Stoichiometry	0.167	mol EtOH/mol CO	
Formation of other products (X, Ac):			Köpke & Simpson (2020)
Specificity	0.95		
No accumulation of CO (steady-state)			
Calculation			
Production	6000	kg etoh/hr/6reactors	
	130	kmol etoh/hr/6reactors	
Transfer rate	824	kmol CO/hr/6reactors	
	23	ton CO /hr/6reactors	
MTC	**7.69**	**g CO / L broth / h**	
Sensitivity			
50 kton/yr	7.61	g/L/h	
45 kton/yr	6.85	g/L/h	
Specificity 1	7.3	g/L/h	
Specificity 0.9	8.12	g/L/h	
Expectation			
CO mass transfer capacity between 7 and 8.5 g/L/h			

Industrial k_La			
Assumptions			
Liquid height	25	m	Figure 2.1
CO gas fraction	0.5	mol CO/mol gas	Fackler et al. (2021)
Conversion	90	%	Fackler et al. (2021)
Henry coeff.	8.19	µmol/m^3/Pa	Sander (2015)
Pressure	101325	Pa	
Density	993.37	kg/m^3	
Gravity	9.81	m/s^2	
Dissolved CO conc.	0	kg/m^3	
Assume ideal mixing			
Calculation			
Av. Pressure	223137	Pa	
Average y_{CO}	0.225	mol CO/mol gas	
Av. CO solubility	0.411	mol/m^3	
	0.012	g/L	
k_La	**668**	**h^{-1}**	
Sensitivity analysis			
MTR 8.5 g/L/h	738	h^{-1}	
MTR 7 g/L/h	606	h^{-1}	
20 m liquid height	750	h^{-1}	
30 m liquid height	602	h^{-1}	
80% conv	633	h^{-1}	
95% conv	751	h^{-1}	
Expectation			
k_La between 600 and 750 h^{-1}			

Figure A.1: Preliminary calculations based upon publicly available data to estimate the CO mass transfer capacity (MTC) and $k_L a$ from the LanzaTech syngas fermentation process.

Table A.1: Parameters and variables for determining $k_L a$ via the relationships in Table 2.1. 1: calculated using [25] for EL-GLRs. 2: calculated using [114]. Flow rates for one EL-GLR.

Variable	**Symbol**	**Value**	**Unit**
Riser diameter	D_r	5	m
Riser surface area	A_r	20	$\mathrm{m^2}$
Downcomer diameter	D_d	1.5	m
Downcomer surface area	A_d	1.8	$\mathrm{m^2}$
Dispersion height	H_D	25	m
Headspace pressure	p_{head}	101325	Pa
Bottom pressure	p_{bot}	344949	Pa
CO inflow	$\dot{n}_{\mathrm{CO,in}}$	136	$\mathrm{kmol_{CO}\,h^{-1}}$
Syngas composition	y_i	50% CO, 50% N_2	$\mathrm{mol_i\,mol_G^{-1}}$
Syngas molar inflow	$\dot{n}_{G,\mathrm{in}}$	272	$\mathrm{kmol_G\,h^{-1}}$
Gas molar volume at bottom	$V_{\mathrm{G},m,\mathrm{bot}}$	0.0075	$\mathrm{m_G^3\,mol_G^{-1}}$
Syngas inflow	$F_{\mathrm{G,bot}}$	2031	$\mathrm{m_G^3\,h^{-1}}$
Superficial gas velocity	$u_{G,s,\mathrm{in}}$	0.028	$\mathrm{m\,s^{-1}}$
Power-to-volume ratio[1]	P/V_D	257	$\mathrm{W\,m_L^{-3}}$
Gas hold-up[2]	ε_G	0.126	$\mathrm{m_G^3\,m_L^{-3}}$
Liquid hold-up	ε_L	0.874	$\mathrm{m_L^3\,m_L^{-3}}$
Concentration of solids	c_{solids}	0	$\mathrm{kg\,m_L^{-3}}$
Physical constants			
Universal gas constant	R	8.314	$\mathrm{J\,mol^{-1}\,K^{-1}}$
Gravity	g	9.81	$\mathrm{m\,s^{-2}}$
Density	ρ_L	993.37	$\mathrm{kg\,m_L^{-3}}$
Temperature	T	310.15	K
Broth viscosity	η_L	7.074×10^{-4}	Pa s
CO diffusion coefficient	$D_{L,\mathrm{CO}}$	2.71×10^{-9}	$\mathrm{m^2\,s^{-1}}$
Surface tension	σ	0.072	$\mathrm{N\,m^{-1}}$

Table A.2: Dimensionless numbers used for the determining $k_L a$ in the relations given in Table 2.1, based on the definitions proposed by [25].

Name	**Equation**	**Estimated value**
Schmidt	$Sc = \frac{\eta_L}{\rho_L D_{L,\mathrm{CO}}}$	~260
Eötvös	$Eo = \frac{\rho_L g D_r^2}{\sigma}$	$\sim 3.38 \times 10^6$
Galileo	$Ga = \frac{\rho_L^2 g D_r^3}{\eta_L^2}$	$\sim 2.40 \times 10^{15}$
Froude	$Fr = \frac{u_{G,s,\mathrm{in}}}{g D_r}$	$\sim 40 \times 10^{-3}$
Reynolds	$Re = \frac{\rho_L u_{G,s,\mathrm{in}} D_r}{\eta_L}$	$\sim 1.9 \times 10^5$
Sherwood	$Sh = \frac{k_L D_r}{D_{L,\mathrm{CO}}}$	-

Table A.3: Results of the mesh refinement study. $k_L a$ and MTC (100 s time-averaged) were determined for the three meshes with three different k_L-relations from Table 2.2. For the calculations, bubbles of 3 mm diameter were assumed as well as the hold-up increasing effect of ethanol and operation at 37 °C.

	Mesh 1		**Mesh 2**		**Mesh 3**	
Cells	370764		1688085		1929575	
Relation	$k_L a$ (h^{-1})	MTC ($\mathrm{gL}^{-1}\mathrm{h}^{-1}$)	$k_L a$ (h^{-1})	MTC ($\mathrm{gL}^{-1}\mathrm{h}^{-1}$)	$k_L a$ (h^{-1})	MTC ($\mathrm{gL}^{-1}\mathrm{h}^{-1}$)
1	672	5.86	624	5.68	620	5.69
2	688	5.82	637	5.68	632	5.70
5	480	4.13	461	4.30	469	4.35

Table A.4: Discretization schemes and relaxation factors used for the different CFD models. The gradient was solved via the least-square cell-based scheme.

	Pilot-scale		**Large-scale**	
Variable	Discretization scheme	Relaxation factor	Discretization scheme	Relaxation factor
Pressure	PRESTO!	0.3	PRESTO!	0.3
Density	First order upwind	1.0	First order upwind	1.0
Body Forces	-	1.0	-	1.0
Momentum	Second order upwind	0.2	First order upwind	0.7
Volume fraction	First order upwind	0.5	First order upwind	0.5
Turbulent kinetic energy	First order upwind	0.5	First order upwind	0.8
Turbulent dissipation rate	First order upwind	0.5	First order upwind	0.8
Turbulent viscosity (eq.)	-	1	-	1
Tracer mass fraction	First order upwind	1	-	-

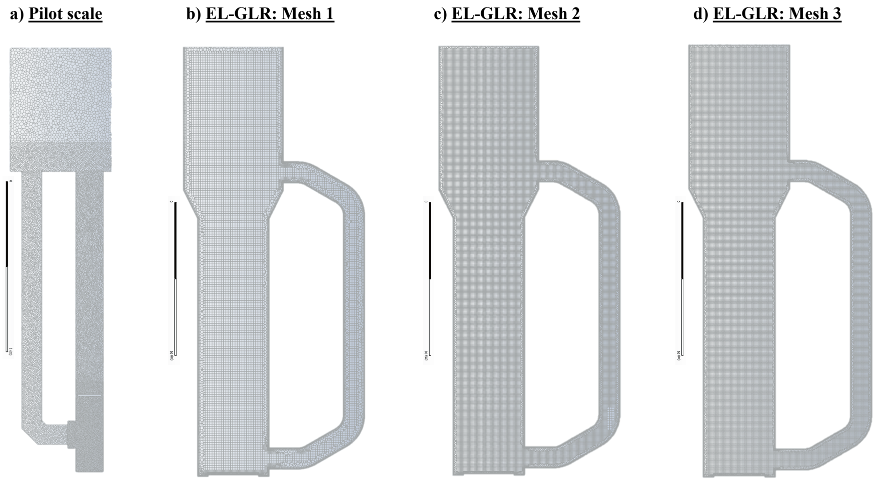

Figure A.2: Meshes used for CFD modelling. a) the mesh for the pilot-scale reactor model (grid size = 0.008 m). b-d) meshes for the industrial EL-GLR (grid size = 0.20 m, 0.15 m, 0.10 m, respectively).

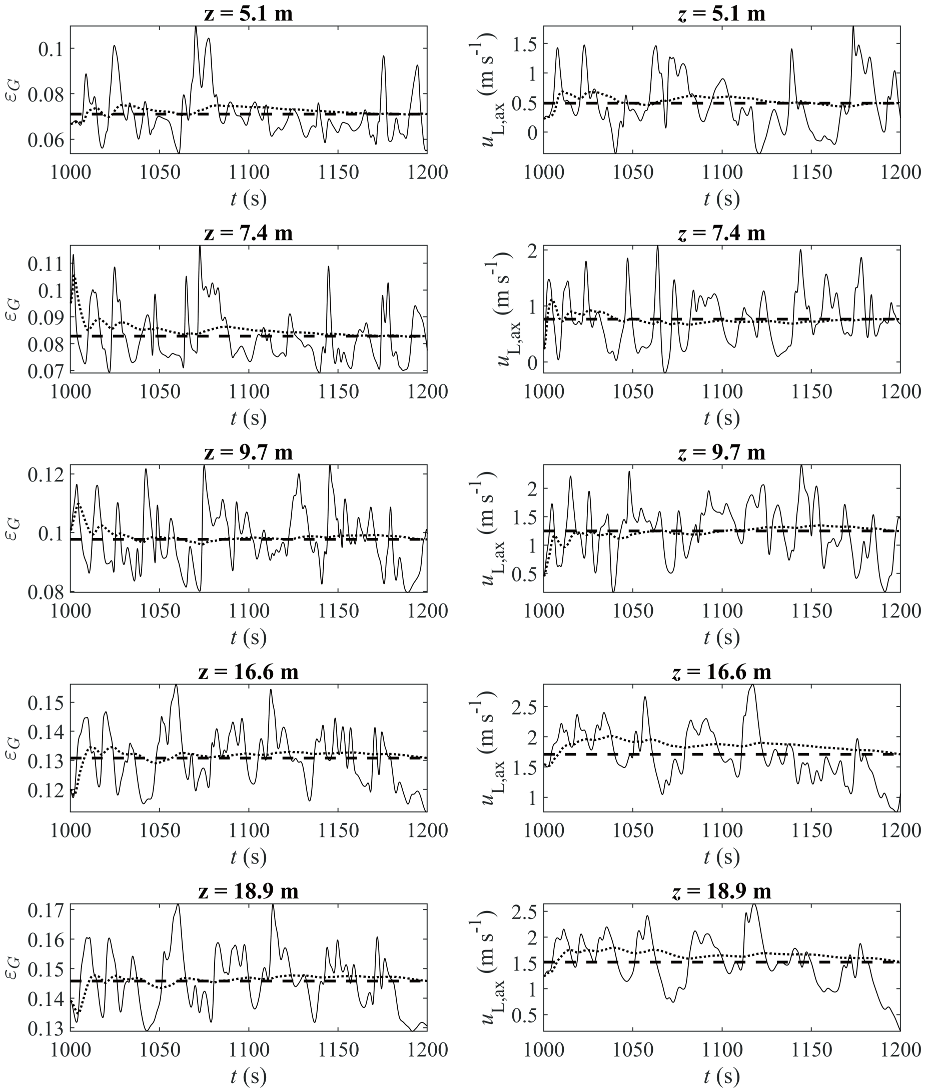

Figure A.3: Dynamic variations in gas hold up and axial liquid velocity at the EL-GLR riser centreline at several axial positions. Full line: transient values; dotted lines: rolling averages; dashed lines; 200 s time-averaged values.

Table A.5: Results from the pilot-scale reactor used by Young et al. [139] and the predictions made by the CFD model. Given are the average values and the standard deviation along the radial direction, as well as the relative difference in the value as predicted by the CFD model.

$u_{G,s}$	$\mathrm{cm\,s^{-1}}$		**8.4**			**4.7**	
		Pilot	CFD	dev	Pilot	CFD	dev
$u_{L,\mathrm{ax,r}}$	$\mathrm{m\,s^{-1}}$	0.85 ± 0.24	0.54 ± 0.31	-36%	0.62 ± 0.18	0.44 ± 0.24	-29%
I_r	%	34.7 ± 6.4	22.2 ± 7.8	-36%	33.3 ± 6.6	15.9 ± 4.23	-52%
$u_{L,\mathrm{ax,d}}$	$\mathrm{m\,s^{-1}}$	0.87 ± 0.44	0.93 ± 0.37	+6%	0.67 ± 0.34	0.80 ± 0.32	+19%
I_d	%	10.3 ± 2.7	12.1 ± 2.2	+17%	8.80 ± 1.4	13.9 ± 3.35	+58%
$u_{G,\mathrm{ax,r}}$	$\mathrm{m\,s^{-1}}$	0.96 ± 0.20	0.72 ± 0.40	-24%	0.79 ± 0.20	0.62 ± 0.34	-21%
$\varepsilon_{G,r}$		0.12 ± 0.01	0.11 ± 0.01	-3%	0.09 ± 0.01	0.07 ± 0.00	-17%

$u_{G,s}$	$\mathrm{cm\,s^{-1}}$		**2.1**			**0.96**	
		Pilot	CFD	dev	Pilot	CFD	dev
$u_{L,\mathrm{ax,r}}$	$\mathrm{m\,s^{-1}}$	0.46 ± 0.17	0.32 ± 0.18	-31%	0.31 ± 0.14	0.24 ± 0.13	-23%
I_r	%	36.4 ± 8.63	24.3 ± 12.5	-33%	34.6 ± 10.5	16.61 ± 6.14	-52%
$u_{L,\mathrm{ax,d}}$	$\mathrm{m\,s^{-1}}$	0.53 ± 0.27	0.60 ± 0.25	+14%	0.42 ± 0.21	0.45 ± 0.18	+7%
I_d	%	8.48 ± 1.29	12.9 ± 4.75	+53%	8.12 ± 1.72	13.3 ± 3.62	+63%
$u_{G,\mathrm{ax,r}}$	$\mathrm{m\,s^{-1}}$	0.64 ± 0.17	0.50 ± 0.27	-23%	0.54 ± 0.14	0.42 ± 0.23	-23%
$\varepsilon_{G,r}$		0.05 ± 0.01	0.04 ± 0.00	-15%	0.02 ± 0.01	0.02 ± 0.00	-4%

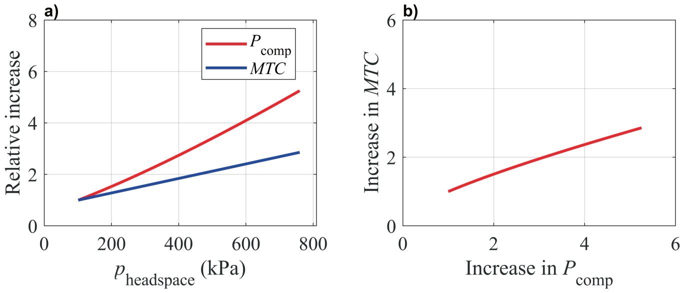

Figure A.4: Influence of the absolute headspace pressure on MTC (Equation 2.7) and power consumption [113] by the compressor. b) Relation between the relative increases in compressor power consumption and MTC. MTC and P_{comp} are compared to a base-case with 101 kPa headspace pressure, considering that the gas-inflow rate is increased proportional to the headspace pressure to obtain constant k_La.

Table A.6: For two sparger configurations, k_La and MTC are compared for three k_L relations. Provided are the 200 s time- and volume-averaged values, while the difference was calculated relative to the bottom-plate sparger. Assumed are d_b = 3 mm, a 30% increase in gas-hold up compared to water due to the presence of ethanol and a temperature of 37 °C. The gas hold-up in the configuration with sparger above the downcomer was calculated to be 11% lower, explaining the difference in k_La values

	Bottom sparger		**Higher sparger**		**Difference (%)**	
	k_La	MTC	k_La	MTC	k_La	MTC
	$(\mathrm{h^{-1}})$	$(\mathrm{g L^{-1} h^{-1}})$	$(\mathrm{h^{-1}})$	$(\mathrm{g L^{-1} h^{-1}})$	$(\mathrm{h^{-1}})$	$(\mathrm{g L^{-1} h^{-1}})$
Higbie [127]	673	5.84	503	4.59	-10.8	-6.22
Calderbank and Moo-Young [128]	689	5.86	515	4.61	-10.9	-6.20
Lamont and Scott [131]	485	4.18	376	3.37	-7.49	-3.95

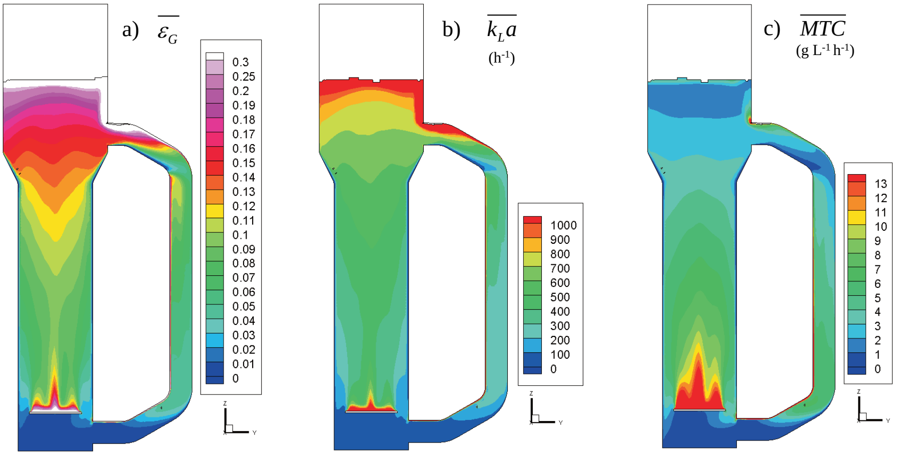

Figure A.5: Surface plots at the zy-plane (x=0) of the EL-GLR with the sparger 0.5 m above the downcomer outlet, a) the 200 s time-averaged gas hold-up, b) $k_L a$ and c) MTC as determined via the Higbie relation, assuming d_b = 3 mm, a 30% increase in gas-hold up and a temperature of 37 °C

CFD simulations with higher positioned sparger

Methods

An alternative geometry has been developed with the spider sparger (Figure 2.1b) positioned 0.5 m above the downcomer outlet, and meshed with 370,000 cells and 0.3 orthogonal quality. In ANSYS Fluent, interpolation has been performed using the established flow field from the bottom-plate sparger (replace zone-option). Initialization has been performed by setting all directions of the liquid and gas velocities as well as the gas hold-up to zero, at 0.5 m above and below the sparger. Convergence (residuals < $O(10^{-3})$) was obtained with the following time stepping strategy: 0.01 s for 2 time steps, 0.02 s for 5 steps, 0.05 s for 5 steps and was then increased to 0.1 s, while decreasing the momentum under-relaxation factor to 0.4 (raised back to 0.7 after 120 s). Results were obtained by exporting data for 200 s (every 2.5 s) after 350 s simulation time, when a stable flow field was obtained.

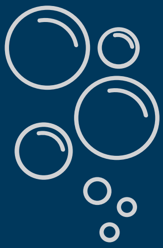

Appendix B

Supplement Chapter 3

Relations used for $k_L a$ determination by physical properties

Table B.1: Relations used for the prediction of $k_L a$ in bubble column reactors. Constants: $D_r = 0.07$ m, $u_{G,s} = 1.8\,\mathrm{mm\,s^{-1}}$, $D_{L,O_2} = 2.1 \times 10^{-9}\,\mathrm{m^2\,s^{-1}}$, $g = 9.18\,\mathrm{m\,s^{-2}}$.

Dimensionless relations	**Equation**
Akita and Yoshida [118]	$(Sh)\,a \cdot D_r = 0.6 Eo^{0.62} Ga^{0.3} Sc^{0.5} \varepsilon_G^{1.1}$
Kawase et al. [120]	$(Sh)\,a \cdot D_r = 0.452 Eo^{0.62} Ga^{0.3} Sc^{0.5} Fr^{1} Re^{1}$
Nakanoh and Yoshida [119]	$(Sh)\,a \cdot D_r = 0.09 Eo^{0.75} Ga^{0.4} Sc^{0.5} Fr^{1}$
Uchida et al. [121]	$(Sh)\,a \cdot D_r = 0.17 Eo^{0.62} Ga^{0.3} Sc^{0.5} \varepsilon_G^{1.1}$
Vatai and Tekić [122]	$(Sh)\,a \cdot D_r = 0.031 Eo^{0.75} Ga^{0.4} Sc^{0.5} Fr^{1}$
Dimensionless numbers	**Equation**
Schmidt	$Sc = \frac{\eta_L}{\rho_L D_{L,O2}}$
Eötvös	$Eo = \frac{\rho_L g D_r^2}{\sigma}$
Galileo	$Ga = \frac{\rho_L^2 g D_r^3}{\eta_L^2}$
Froude	$Fr = \frac{u_{G,s,\mathrm{in}}}{g D_r}$
Reynolds	$Re = \frac{\rho_L u_{G,s,\mathrm{in}} D_r}{\eta_L}$
Sherwood	$Sh = \frac{k_L D_r}{D_{L,O2}}$

Cultivation strategies and media composition

Fermentation broth 1 was effluent resulting from a CO fermentation by *Clostridium autoethanogenum* (DSM 10061) in a continuous stirred-tank reactor (CSTR). The cultivation was carried out in a 1.5 L glass jacketed chemostat (Applikon, The Netherlands) with a working volume of 1 L. The temperature was controlled at 37 °C, the agitation rate was set to 500 rpm and the pH was maintained at 5.9. The bioreactor was continuously supplied with a gas phase consisting of CO ($6\,\mathrm{mL\,min^{-1}}$) and N_2 ($6\,\mathrm{mL\,min^{-1}}$). The sterile growth media (composition reported in Table B.2) was supplied continuously at the dilution rate of $0.024\,\mathrm{h^{-1}}$. The fermentation effluent was continuously sparged with 100% N_2 to maintain anaerobic conditions, kept at room temperature (~20 °C) and collected anaerobically in a glass bottle during 4 days, and then used for the mass transfer experiments.

Fermentation broth 2 was the effluent resulting from CO fermentations by *C. autoethanogenum* (DSM 10061) in a custom-built rotor-stator spinning disc reactor (RS-SDR) coupled to a buffer tank. The fermentation broth was cultivated in a 600 mL glass mixed buffer vessel (300 mL working volume) and recirculated though the RS-SDR (60 mL working volume), made of polymethyl methacrylate. The reactor was operated in a sequential batch mode, with a cycle time of 24 hours. Each cycle, 10 mL of fermentation broth in the buffer tank was exchanged by the same volume of fresh sterile feed medium (composition reported in Table B.2). The headspace of the buffer tank (300 mL) was completely refreshed with 100% CO once a day and kept at 1.5 bar of absolute pressure. The buffer tank was placed on a heating stirring plate. The temperature was controlled between 35 and 37 °C, the broth was agitated at 200 rpm with a magnetic stirrer and the pH was maintained between 5.3 and 5.8. The fermentation broth was recirculated through the RS-SDR at a recirculation liquid flow rate of 120 $\mathrm{mL\,min^{-1}}$. The RS-SDR operated at varying rotation speeds (100, 500, 1000 or 1500 rpm). After 72 hours of cultivation, the fermentation effluent was collected in 1 L plastic bottles and stored in the fridge (~2 °C). The effluent of 8 consecutive independent fermentations was stored (during a maximum 4 weeks), mixed and then used for the mass transfer experiments.

Fermentation broth 3 was the effluent of a mixed culture converting CO into H_2 and acetate in a continuous stirred tank reactor (CSTR). The cultivation was carried out in a 500 mL chemostat with a working volume of 400 mL. The temperature was controlled at 30 °C, the agitation rate was set to 800 rpm and the pH was maintained at 7.0. The bioreactor was continuously supplied with a gas phase consisting of CO (2 $\mathrm{mL\,min^{-1}}$), N_2 (1.06 $\mathrm{mL\,min^{-1}}$) and CO_2 (0.27 $\mathrm{mL\,min^{-1}}$). The sterile growth media (composition reported in Table B.2) was supplied continuously to maintain the dilution rate of 0.014 $\mathrm{h^{-1}}$. The fermentation effluent was collected anaerobically into 1 L serum glass bottles sealed with butyl rubber stoppers and aluminium caps, under N_2/CO_2 (80:20 v%) headspace, at 1.4 bar of absolute pressure. The effluent was stored at room temperature (~20 °C) during 5 days, and then used in the mass transfer experiments.

Fermentation broth 4 was produced by the fermentation of CO by *C. autoethanogenum* (DSM 10061) in batch bottles. The cultivation medium (which composition is reported in Table B.2) was dispersed into 1 L glass bottles (300 mL working volume) sealed with butyl rubber stoppers and aluminium caps. The headspace of each bottle (700 mL) was filled with 100% CO to a final absolute pressure of 1.5 bar, using an anaerobic gas-exchange system. The bottles were sterilised in a autoclave immediately after preparation, for 20 minutes at 121 °C. Each bottle was inoculated with 1% (v/v) of exponential growing inoculum, at initial pH of 5.9 and incubated without shaking at 37 °C until reaching optical density at 660 nm (OD660) of 0.2. The fermentation broth from each bottle was then collected and mixed, and used for bubble size characterisation (Figure B.1, Table B.3).

Table B.2: Media composition used for the cultivation of the fermentation broths. Media compounds concentrations are reported in $\mathrm{g\,L^{-1}}$ ($\mathrm{mg\,L^{-1}}$ in the case of metal trace elements and vitamins).

	Mineral media	**Broth-1**	**Broth-2**	**Broth-3**	**Broth-4**
	($\mathrm{g\,L^{-1}}$)	($\mathrm{g\,L^{-1}}$)	($\mathrm{g\,L^{-1}}$)	($\mathrm{g\,L^{-1}}$)	($\mathrm{g\,L^{-1}}$)
Ammonium chloride	0.9	0.9	0.3	0.3	0.3
Sodium chloride	0.9	0.9	0.3	0.3	0.3
Magnesium sulfate heptahydrate	0.2	0.2	0.1	0.03	0.03
Monopotassium phosphate	0.7	0.7	0.408	0.408	0.408
Dipotassium phosphate	1.5	1.5	-	-	-
Sodium phosphate dibasic dihydrate	-	-	0.534	-	-
Calcium chloride dihydrate	0.02	0.02	0.11	0.11	0.11
Sodium bicarbonate	-	-	4.0	4.0	4.0
Resazurin sodium salt	0.0005	0.0005	0.0005	0.0005	0.0005
Yeast extract	0.5	0.5	1.0	0.1	0.1
Triptone	-	-	1.0	-	-
L-cysteine hydrochloride monohydrate	-	0.75	0.5	0.1	0.1
Sodium sulfide nonahydrate	-	-	0.24	-	0.24
Metal trace elements	($\mathrm{mg\,L^{-1}}$)	($\mathrm{mg\,L^{-1}}$)	($\mathrm{mg\,L^{-1}}$)	($\mathrm{mg\,L^{-1}}$)	($\mathrm{mg\,L^{-1}}$)
Iron(II) chloride tetrahydrate	1.50	1.50	1.50	1.50	1.50
Iron(III) chloride hexahydrate	2.50	2.50	-	-	-
Zinc chloride	0.07	0.07	0.07	0.07	0.07
Manganese(II) chloride tetrahydrate	0.10	0.10	0.10	0.10	0.10
Boric acid	0.006	0.006	0.062	0.062	0.062
Cobalt(II) chloride hexahydrate	0.190	0.19	0.119	0.119	0.119
Copper(II) chloride dihydrate	0.002	0.002	0.017	0.017	0.017
Nickel(II) chloride hexahydrate	0.024	0.024	0.024	0.024	0.024
Sodium molybdate dihydrate	0.040	0.040	0.024	0.024	0.024
Sodium selenite	0.004	0.004	0.017	0.017	0.017
Sodium tungstate dihydrate	0.200	0.200	0.033	0.033	0.033
Vitamins	($\mathrm{mg\,L^{-1}}$)	($\mathrm{mg\,L^{-1}}$)	($\mathrm{mg\,L^{-1}}$)	($\mathrm{mg\,L^{-1}}$)	($\mathrm{mg\,L^{-1}}$)
Biotin	0.02	0.02	0.02	0.02	0.02
Nicotinamide	0.20	0.20	0.20	0.20	0.20
P-aminobenzoic acid	0.10	0.10	0.10	0.10	0.10
Thiamine	0.20	0.20	0.20	0.20	0.20
Pantothenic acid	0.10	0.10	0.10	0.10	0.10
Pyridoxamine	0.50	0.50	0.50	0.50	0.50
Cyanocobalamin	0.10	0.10	0.10	0.10	0.10
Riboflavin	0.10	0.10	0.10	0.10	0.10

Bubble size method cross-validation

With broth-4, and in the same conditions as used with the other mixtures, bubbles were obtained that could be analysed using both methods (the one designed for the small bubbles with the photo-optical probe (SOPAT) and the one for the larger bubbles with the CANON EOS 200D camera). The resulting bubble size distributions (BSDs) are given in Figure B.1. As can be seen, the resulting BSDs are very similar, with the exception that the method used for the small bubbles is not able to capture bubbles bigger than 1.3 mm and that it has a slightly higher probability peak between 0.5 - 0.75 mm. As the obtained average bubble diameters, Sauter mean bubble diameters and standard deviations (Table B.3) were similar, it was concluded that both methods could be used for bubble size comparison purposes.

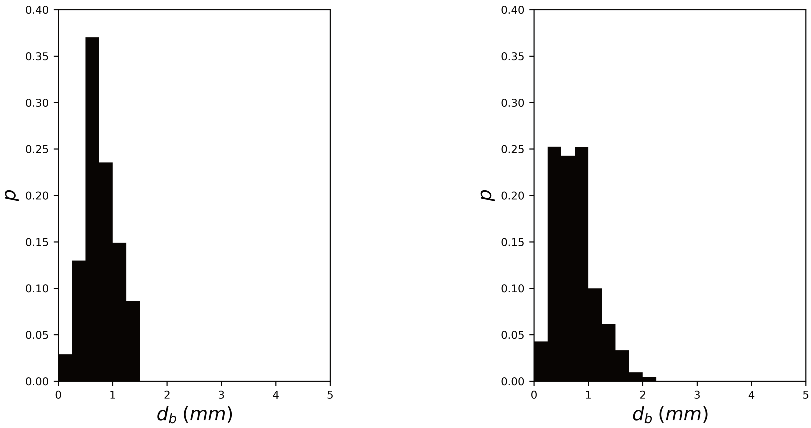

Figure B.1: Bubble size distributions obtained using the method designed for a) the smaller bubbles, and b) the larger bubbles.

Table B.3: Bubble diameter method cross-validation. For broth-4, the average bubble diameters, Sauter mean bubble diameter, and the standard deviation of the bubble diameter were determined via both methods.

	SOPAT method	**CANON method**
$\overline{d_b}$ (mm)	0.78	0.77
d_{32} (mm)	0.98	1.11
σ_{d_b} (mm)	0.29	0.36

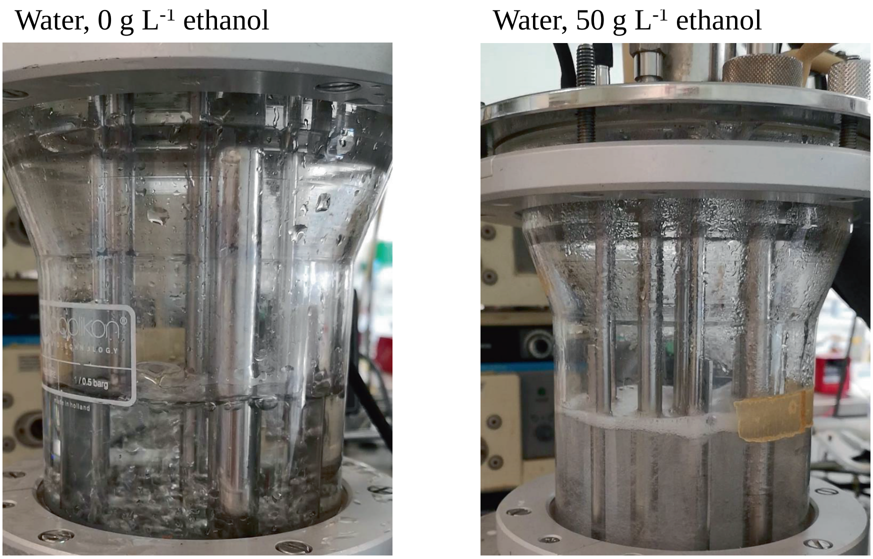

Water, 0 g L^{-1} ethanol

Water, 50 g L^{-1} ethanol

Figure B.2: Photographs of bubbles in the STR with and without supplemented ethanol.

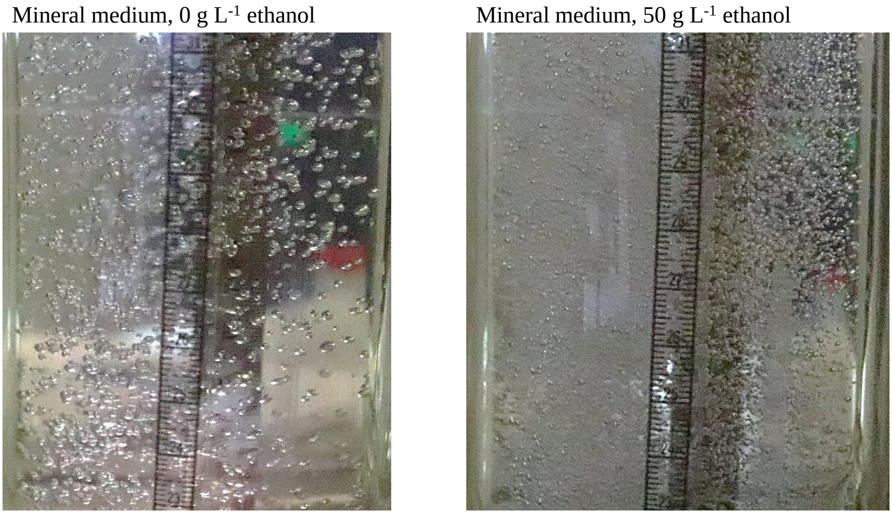

Mineral medium, 0 g L^{-1} ethanol

Mineral medium, 50 g L^{-1} ethanol

Figure B.3: Photographs of bubbles in the BCR with mineral medium with and without supplemented ethanol. In the solution without ethanol, small but less stable, wobbling, bubbles were observed, while the ethanol leads to rigid, spherical, bubbles.

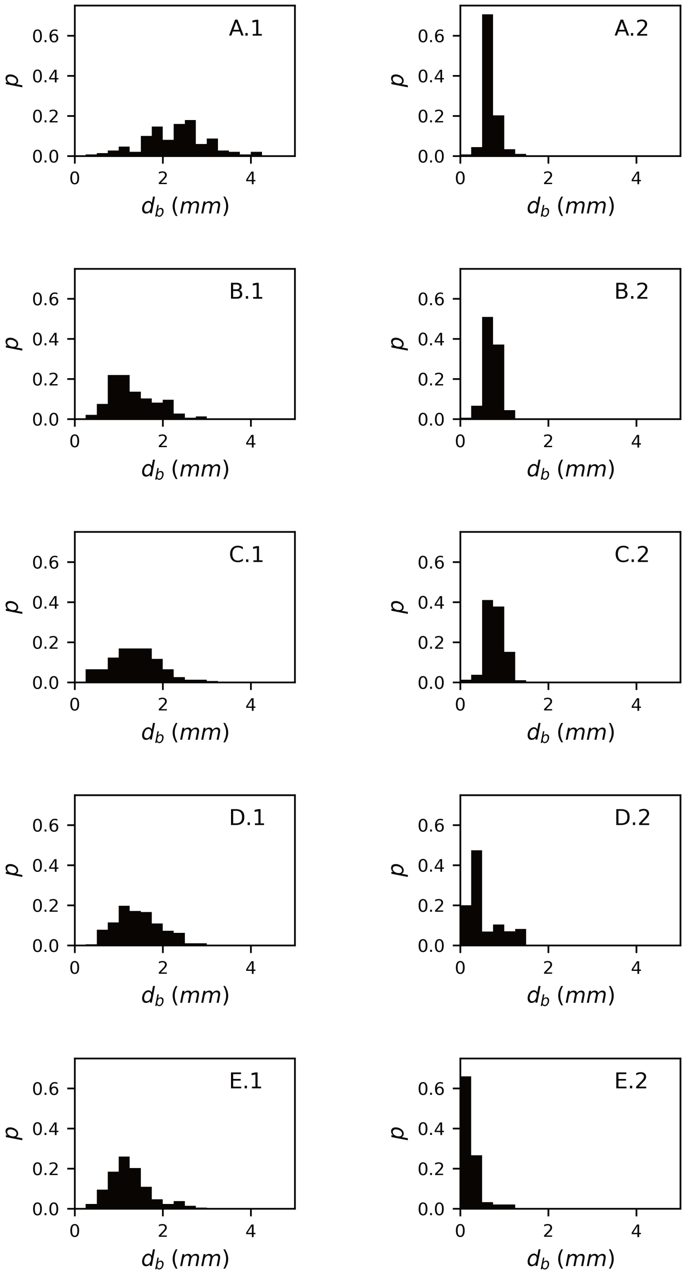

Figure B.4: Bubble size distributions obtained for the different mixtures. A: water, B: mineral medium, C: broth-1, D: broth-2, E: broth-3, 1: without ethanol, 2: with ethanol.

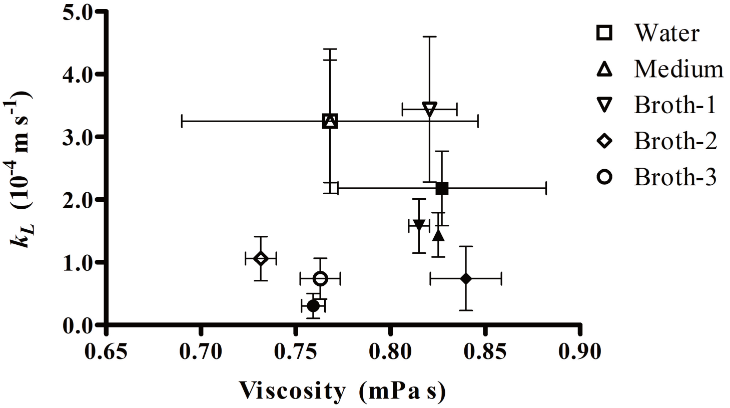

Figure B.5: k_L as a function of the mixture viscosity. Error bars: standard deviations. Filled symbols: mixtures with ethanol, empty symbols: mixtures without ethanol.

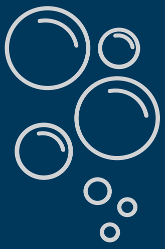

Appendix C

Supplement Chapter 4

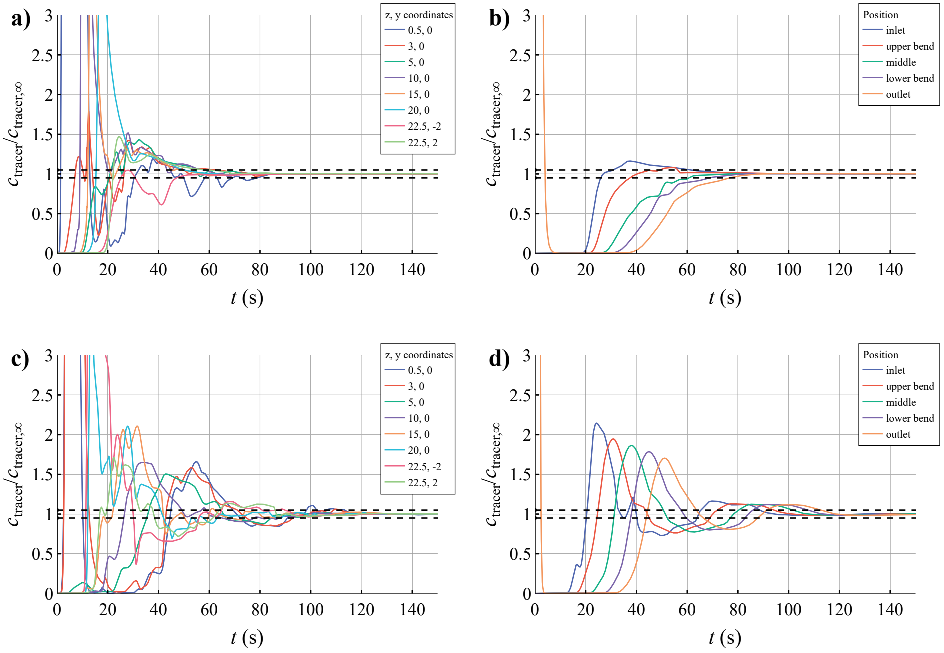

Figure C.1: Mixing study in the EL-GLR. A tracer with the same properties as the fluid phase was injected at the outlet of the downcomer and its normalised concentration recorded at several positions in the riser (a, c – coordinates in m) and downcomer (b, d). The 95% mixing time t_m is obtained when all curves are within the dashed lines representing a 5% deviation around the final tracer concentration. t_m was recorded for a case without reaction (only the hydrodynamic model was enabled) (a, b) and a case including mass transfer and reaction at 25 $\mathrm{g\,L^{-1}}$ biomass without CO_2 production (c, d). t_m without reaction is around 80 s, while with reaction it is around 115 s. This difference is explained by the lower gas hold-up in the case with reaction since the syngas is consumed. The circulation time t_c is estimated from the mixing time as $t_m \sim 3-5t_c$ [71].

Table C.1: Characteristics of the scale-down simulator [25, 207].

Reactor type and dimensions	Applikon 3L Glass bioreactor
Volume reactor (L)	3
Height (m)	0.234
Diameter (m)	0.13
Impeller diameter, d_{imp} (m)	0.06
Power number, N_{Po}	1.5
Liquid volume, V_L (L)	2
Mass transfer parameters	
α	0.783
β	0.459
Fixed operating conditions	
Temperature (°C)	37
Pressure (kPa)	101
pH	5 (for solventogenesis)
Ethanol concentration ($\mathrm{g\,L^{-1}}$)	50 (if possible because of inhibition)
Acetate concentration ($\mathrm{g\,L^{-1}}$)	12
Dilution rate ($\mathrm{h^{-1}}$)	0.021
Gas flow rate (vvm)	0.05

Statistical analysis of lifelines

It was determined how many lifelines were required to obtain statistically independent probability density distributions of the residence time in peaks and valleys. This was done by calculating the Kullback-Leibler divergence D_{KL} (Equation C.1) or the relative entropy for the variables of interest (e.g., the residence time distribution in peaks and valleys for CO and H_2). D_{KL} is a common tool in data sciences to measure dissimilarity between two probability distributions [272] . By minimising D_{KL} of a distribution with respect to a given (“true”) distribution, it can be determined how close a distribution is to the true distribution [118, 272]. As a “true" distribution (with $N_p, N_{t_c} \to \infty$) was not available, it was assumed that the distribution obtained with all peaks and valleys, $P\left(N_p N_{t_c}\right)_\infty$, is sufficiently representative of the “true” distribution.

$$D_{KL}\left(P\left(N_p N_{t_c}\right)_\infty || P\left(N_p N_{t_c}\right)\right) = \sum_{i=1}^{k} P_i\left(N_p N_{t_c}\right)_\infty \ln\left[\frac{P_i\left(N_p N_{t_c}\right)_\infty}{P_i\left(N_p N_{t_c}\right)}\right] \tag{C.1}$$

From the analysis became clear that with $N_p N_{t_c} \sim O(10^5)$ D_{KL} approaches zero (Figure C.2) for the probability distributions describing the duration of a peak in CO concentration. One could argue that even around $\sim O(10^4)$ the information gain by extending the set of lifelines is small. These results give an indication of the required number of particles and run time for lifeline analysis of environmental fluctuations, which is considerably lower than the numbers typically applied for such analysis (e.g. $O(10^6)$ [56, 57, 165]. As an exception, McClure et al. [200] only used $\sim O(10^4)$ while obtaining statistically satisfactory results. It must be noted that our analysis is only applicable when particles act as passive tracers. When the simulated biomass particles affect the Eulerian flow or concentration field (e.g., two-way coupling with metabolic models) [58, 99], a higher N_p is required to achieve a sufficiently homogeneous spatial biomass distribution [78]. In syngas fermentation modelling, this could be applicable if one wants to study the effect of local microbial CO_2 production or consumption, using a detailed kinetic metabolic model.

By calculating D_{KL}, we saved a significant amount of simulation and data processing time: the analyses with 10 and 25 $\mathrm{g\,L^{-1}}$ (650 s and 40,000 particles) only required 20 GB of data instead of 200 GB with the 5 $\mathrm{g\,L^{-1}}$ case (1000 s and 160,000 particles). Next to checking whether the Lagrangian averages matches the Eulerian average [56], which is – in case of sufficient mixing – usually after 3 mixing times per particle, we suggest calculating D_{KL} as well to check variability of the results.

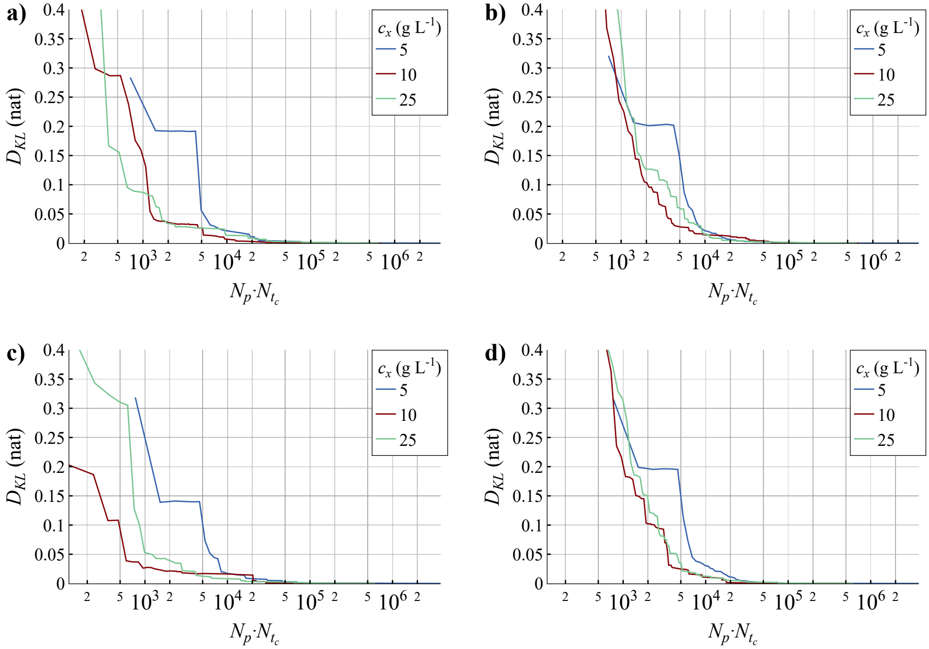

Figure C.2: Kullback-Leibler divergence D_{KL} determined using an increasing $N_p N_{t_c}$ of the residence time distribution a) in a CO peak, b) CO valley, c) H_2 peak, and d) H_2 valley. Blue: D_{KL} obtained from distributions derived from lifelines with 5 $\mathrm{g\,L^{-1}}$ biomass with $(N_p N_{tc})_\infty \sim 3 \times 10^6$, green (10 $\mathrm{g\,L^{-1}}$) and red (25 $\mathrm{g\,L^{-1}}$) with $(N_p N_{tc})_\infty \sim 6 \times 10^5$.

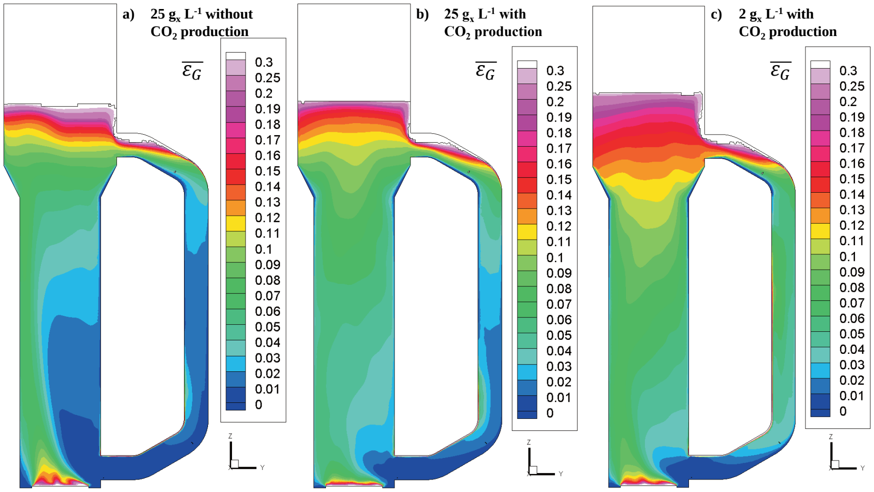

Figure C.3: Surface plots of the 200 s time-averaged gas hold-up in the zy-plane ($x = 0$) of the EL-GLR, obtained with a) 25 g L^{-1} biomass without CO$_2$ production, b) 25 g L^{-1} biomass while including CO$_2$ production and c) 2 g L^{-1} biomass without CO$_2$ production.

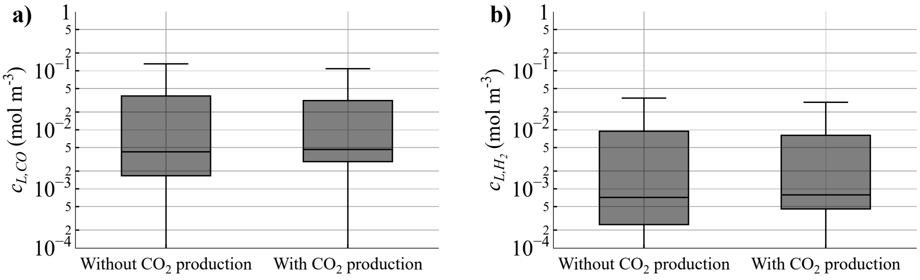

Figure C.4: Variation of a) dissolved CO and b) dissolved H$_2$ concentrations within the EL-GLR reactor volume in the cases without and with CO$_2$ production (with 25 g L^{-1} biomass). In the boxplot each quartile represents 25% of the dispersion volume with a specific concentration.

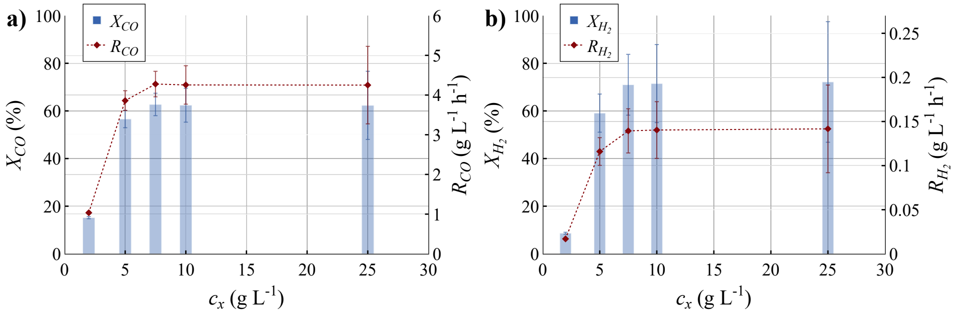

Figure C.5: For the varying biomass concentrations the Eulerian results for a) CO and b) H_2 conversion (blue bars) and consumption rates (red markers) are given.

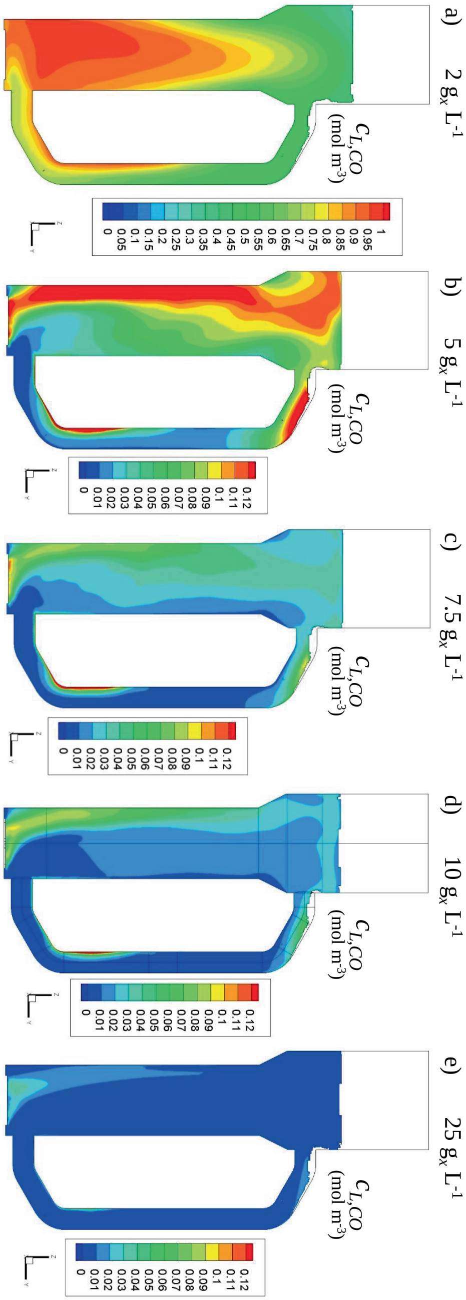

Figure C.6: Surface plots of the dissolved CO concentration in the zy-plane ($x = 0$) of the EL-GLR, for several concentrations of biomass (2, 5, 7.5, 10, 25 g L^{-1}) (a-e).

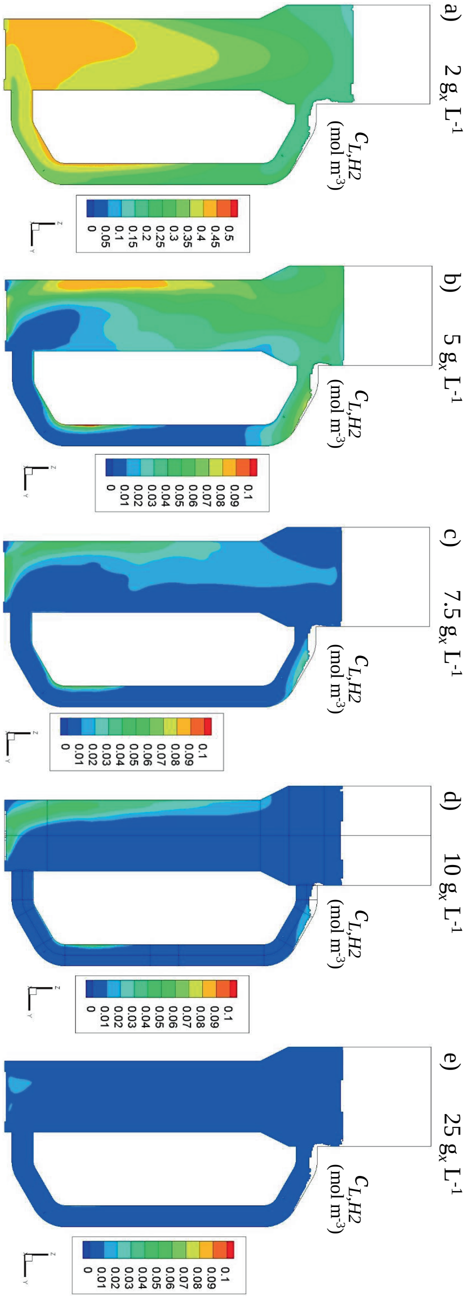

Figure C.7: Surface plots of the dissolved H_2 concentration in the zy-plane ($x = 0$) of the EL-GLR, for several concentrations of biomass (2, 5, 7.5, 10, 25 $\mathrm{g\,L^{-1}}$) (a-e).

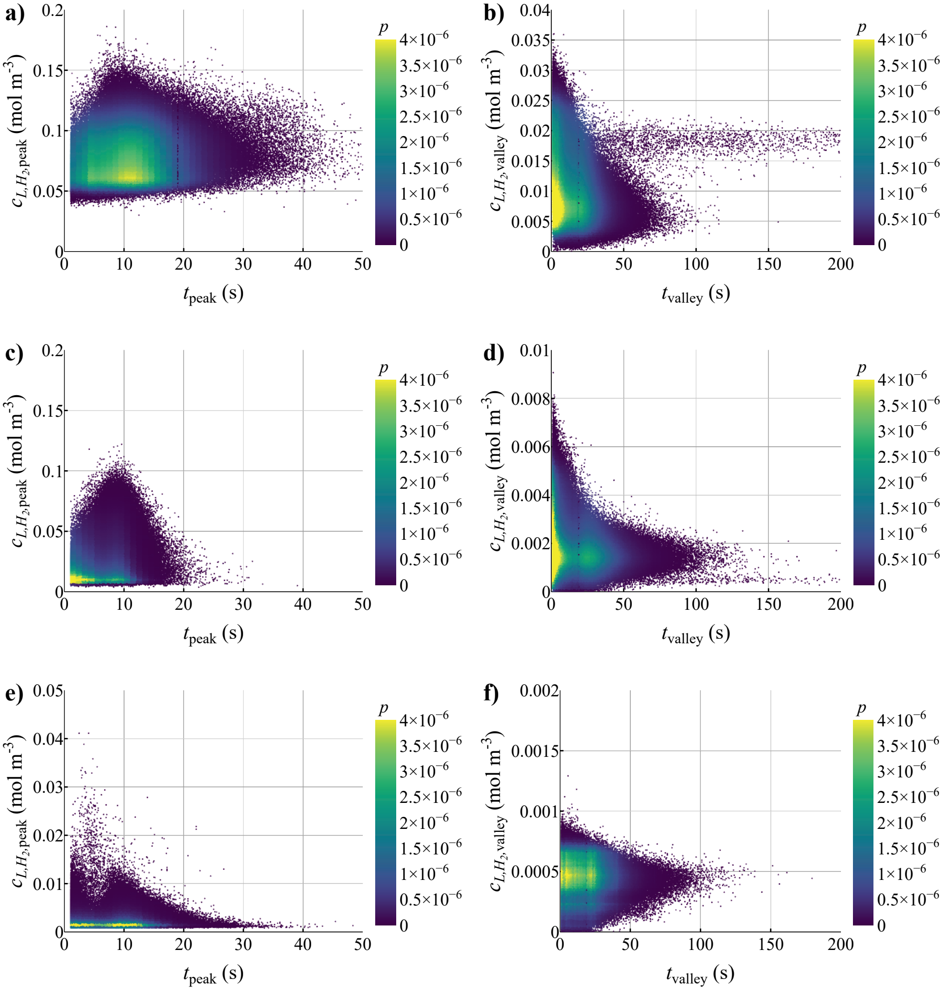

Figure C.8: The probability of a microbe to experience a specific H_2 concentration peak or valley. Each dot represents a peak or valley with such a concentration and time, and is coloured by the probability of occurrence. Each row represents data obtained with a specific concentration: (a, b) 5, (c, d) 10 and (e, f) 25 g L^{-1}. Peaks are in the left column of plots (a, c, e) and the valleys are at the right (b, d, f).

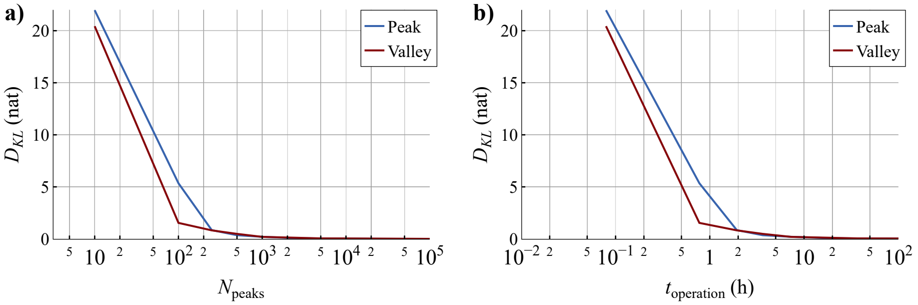

Figure C.9: Minimisation of the Kullback-Leibler divergence for a) the number of peaks used as input for the scale-down simulator, and b) the operational time of the scale-down simulator. D_{KL} was calculated by comparing the probability distribution of the residence time in the peak (blue line) or valley (red line) from the scale-down simulator with their respective CFD-derived counterpart. The probability distributions from the scale-down simulator were derived without assuming mass transfer and reaction.

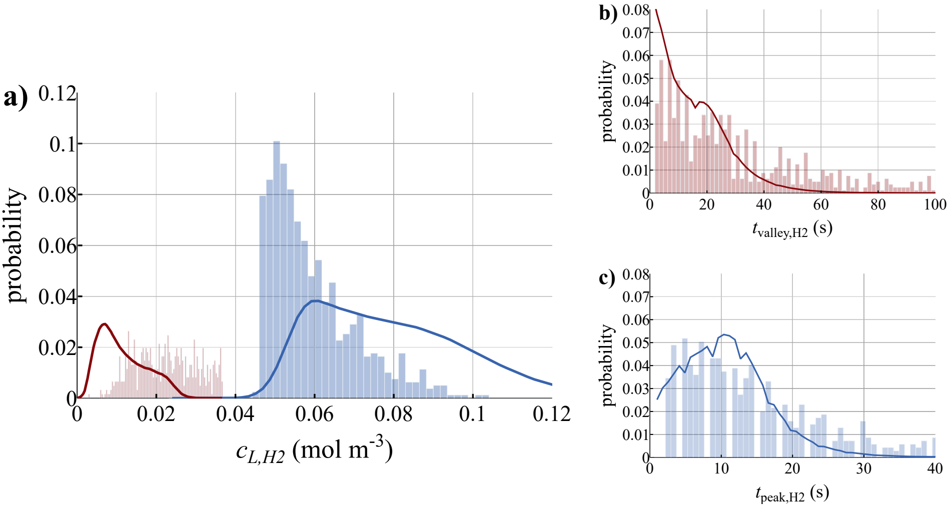

Figure C.10: Comparison of the probability density functions obtained by the scale-down simulator (bars) with the CFD results (lines). Probability density functions for a) the concentration of dissolved H_2 during the peaks (blue) and the valleys (red), as well as the residence time in a b) valley or c) peak, obtained with 5 $g L^{-1}$ biomass and simulating 2000 peaks.

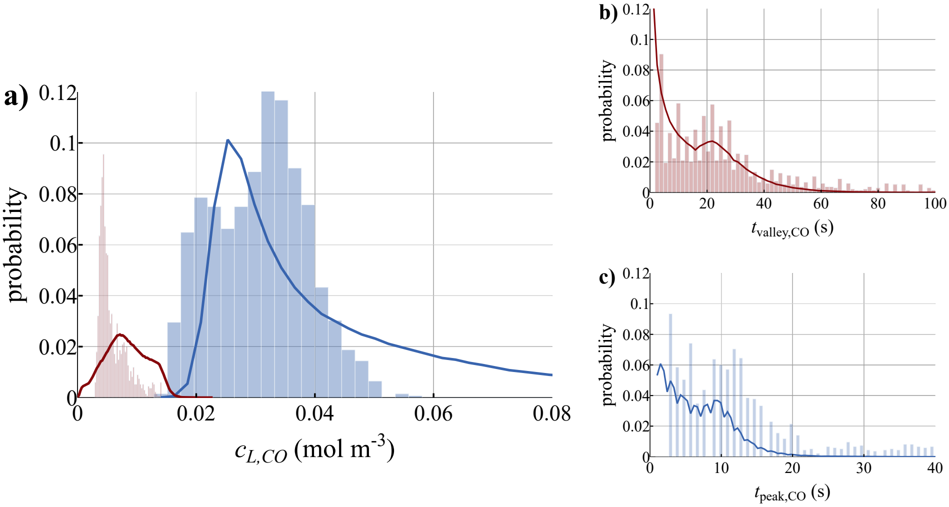

Figure C.11: Comparison of the probability density functions obtained by the scale-down simulator (bars) with the CFD results (lines). Probability density functions for a) the concentration of dissolved CO during the peaks (blue) and the valleys (red), as well as the residence time in a b) valley or c) peak, obtained with 10 $\mathrm{g\,L^{-1}}$ biomass and simulating 2000 peaks.

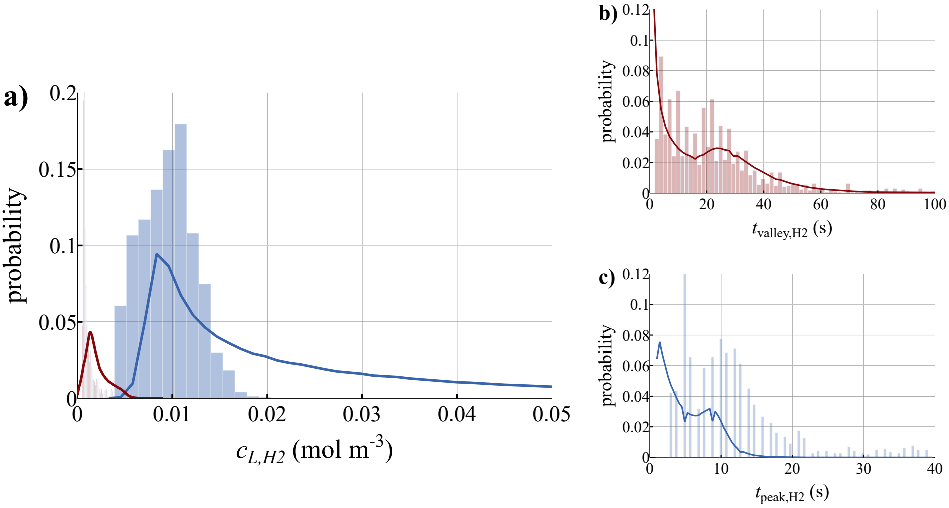

Figure C.12: Comparison of the probability density functions obtained by the scale-down simulator (bars) with the CFD results (lines). Probability density functions for a) the concentration of dissolved H_2 during the peaks (blue) and the valleys (red), as well as the residence time in a b) valley or c) peak, obtained with 10 $\mathrm{g\,L^{-1}}$ biomass and simulating 2000 peaks.

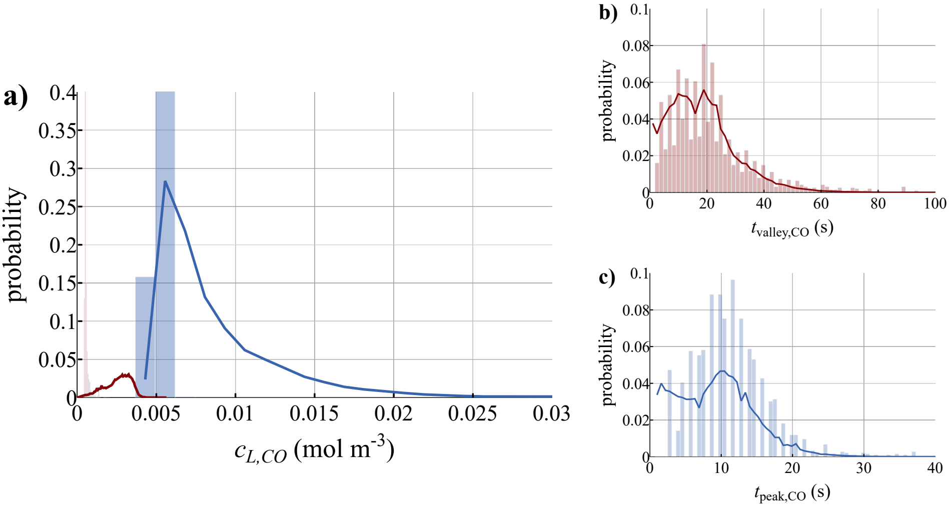

Figure C.13: Comparison of the probability density functions obtained by the scale-down simulator (bars) with the CFD results (lines). Probability density functions for a) the concentration of dissolved CO during the peaks (blue) and the valleys (red), as well as the residence time in a b) valley or c) peak, obtained with 25 gL^{-1} biomass and simulating 2000 peaks.

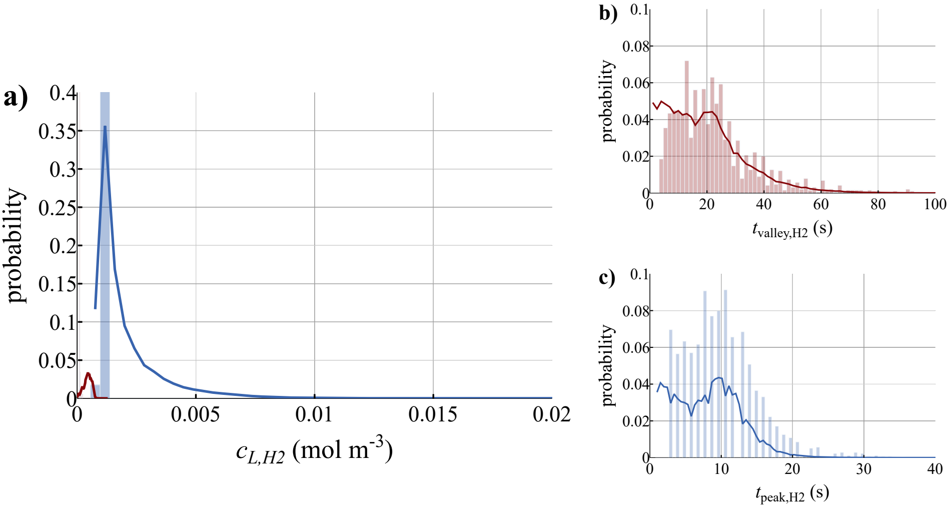

Figure C.14: Comparison of the probability density functions obtained by the scale-down simulator (bars) with the CFD results (lines). Probability density functions for a) the concentration of dissolved H_2 during the peaks (blue) and the valleys (red), as well as the residence time in a b) valley or c) peak, obtained with 25 gL^{-1} biomass and simulating 2000 peaks.

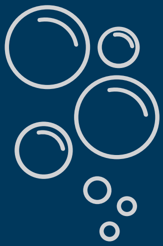

Appendix D

Supplement Chapter 5

D.1. Detailed CRD model description

D.1.1. Metabolic kinetic model

The kinetic model describes the microbial biomass, six metabolites that are in exchange with the cellular environment (CO, H_2, CO_2, acetic acid, ethanol and 2,3-butatendiol), and six intracellular compounds (formate, acetyl-CoA, intracellular acetate, reduced ferredoxin, NADH and NADPH). Transport across the cell membrane is regarded as instantaneous (i.e., the concentration of CO in the cell equals the concentration outside the cell and its import does not require energy), except for intracellular acetate, which is actively excreted while extracellular acetic acid passively diffuses back into the cell. The acid-base equilibrium of acetate is considered so that the total extracellular acetic acid concentration equals the dissociated acetate concentration and the undissociated acetate concentration ($\mathrm{AcT} = \mathrm{HAc} + \mathrm{Ac}^-_{\mathrm{IC}}$). An overview of the metabolites, their reference concentrations, the provided initial concentrations and the minimum concentrations, which are required for model stability in case the concentrations get too low, are provided in Table D.1. The minimum concentrations prevent negative results of the ODE system, and were used in a correction scheme to prevent excessive rates in case lower concentrations were obtained.

With the lin-log based kinetic model, 11 intracellular rates were calculated (Table D.2), with which the metabolite pools were updated. These rates were calculated using a given set of reference concentrations and rates from the steady-state model, and a state-independent elasticity matrix (Table D.3) [40]. Some of the rates were considered irreversible, in line with their physical relation, to increase model stability and to prevent nonphysical model results.

For a given set of concentrations c_i in the particle (based upon their environment and history), the intracellular, lin-log corrected flux J (in $\mathrm{mol\,mol_x^{-1}\,h^{-1}}$) for reaction j, was calculated using Equation D.1, in which r_j^{ll} is the dimensionless lin-log-correction term. The back-diffusion rate of acetic acid into the cell was calculated using Equation D.2 (with the cell surface area, a_x ($321\,\mathrm{m^2\,mol_x^{-1}}$), and the acetic acid diffusivity, $k_{\mathrm{HAC,D}}$ ($3.8 \times 10^{-5}\,\mathrm{m\,h^{-1}}$)). It should be noted that the lin-log formulation may decrease the accuracy of reaction rates far away from the reference concentration [236]. To minimise model exceptions, such as negative concentrations and excessive rates in such regions,

Table D.1: The metabolites and their characteristic concentrations for solving the CFD-CRD model.

Compound i	**Reference concentration** c_i^{ref} ($\mathrm{mol\,m^{-3}}$)	**Initial concentration** $c_{i,0}$ ($\mathrm{mol\,m^{-3}}$)	**Minimum concentration** $c_{i,\mathrm{min}}$ ($\mathrm{mol\,m^{-3}}$)
CO	0.157	0.1	10^{-10}
H_2	0.155	0.08	10^{-10}
CO_2	9.21	9	0.1
AcT	110	90.	0.1
EtOH	63.4	119.7	0.1
BDO	1.28	3.2	0.1
AcCoA	0.21	0.041	10^{-8}
NADH	0.011	0.01	10^{-12}
NADPH	0.184	0.133	10^{-12}
$\mathrm{Ac}_{\mathrm{IC}}$	34.8	70	10^{-12}
For^{-}	18.6	1	10^{-4}
$\mathrm{Fd}^{2-}_{\mathrm{red}}$	9.13	6	10^{-12}

Table D.2: The modelled reactions in the CFD-CRD model. Reversibility is noted with 1, irreversibility with 0. *a*: After the simulations we realised that Rnf could be a reversible reaction. We have not observed a tendency of Rnf towards zero, so we do not expect major variations in our results because of its modelling as an irreversible reaction.

Reaction name	**Abbreviation** j	**Reversibility**	**Reference rate** r_j^{ref} ($\mathrm{mol\,mol_x^{-1}\,h^{-1}}$)
Formate dehydrogenase	FDH	1	0.182
AcCoA synthesis	ACAS	0	0.182
CO dehydrogenase	CODH	1	0.686
Fd-NADPH-Hydrogenase	Hyd	1	0.01
Acetate synthesis	AcS	0	0.16
Ethanol synthesis	EtS	1	0.078
2,3-butanediol synthesis	BDOS	1	0.003
Nfn complex	Nfn	1	0.131
Rnf complex^{a}	Rnf	0	0.575
Anabolism	Ana	0	0.039
Acetate export	AcX	0	0.426

the concentrations used in Equation D.1 were constrained at the minimum concentration (Table D.1).

$$J_j = r_j^{\mathrm{ref}} \cdot r_j^{ll} = r_j^{\mathrm{ref}} \left(1 + \sum_{i=1}^{n} \varepsilon_{ji} \ln \left[\frac{\max\left(c_i, c_{i,\mathrm{min}}\right)}{c_i^{\mathrm{ref}}} \right] \right) \tag{D.1}$$

$$r_{\mathrm{HAc,D}} = a_x k_{\mathrm{HAc,D}} c_{\mathrm{HAc,o}} \text{ with } c_{\mathrm{HAc,EC}} = c_{\mathrm{AcT}} \frac{10^{\mathrm{pK_a}}}{10^{\mathrm{pH_{EC}}} + 10^{\mathrm{pK_a}}} \tag{D.2}$$

With the known intracellular fluxes and the calculated acetate back-diffusion rates, the volumetric rates and intracellular balances were then solved according to Equations D.3 – D.14. The derivatives of the compounds that are in exchange with the environment (Equations D.3 – D.8) are calculated as function of the local liquid volume (units in

Table D.3: Elasticity matrix used for solving the CRD model. Elasticity coefficients $\varepsilon_{i,j}$ are provided for each metabolite i in reaction j.

ε_{ij} $j \backslash i$	CO	H_2	CO_2	AcT	EtOH	BDO	AcCoA	NADH	NADPH	Ac^-_{IC}	For^-	Fd^{2-}_{red}
FDH	0	0	0.16	0	0	0	0	0	1.11	0	-0.15	0.98
ACAS	0.49	0	0	0	0	0	-0.47	3.81	-0.57	0	-0.004	0.45
CODH	0.26	0	0.02	0	0	0	0	0	0	0	0	-0.45
Hyd	0	-0.96	-0.11	0	0	0	0	-0.65	0.02	0	-0.97	-0.08
AcS	0	0	0	0	0	0	0.6	0	0	0.98	0	0
EtS	0	0	0	0	-0.51	0	0	1.41	0	0.07	0	-0.77
BDOS	0	0	0.7	0	0	1.66	-0.46	10.2	0	0	0	1.08
Nfn	0	0	0	0	0	0	0	-0.98	0.07	0	0	0.01
Rnf	0	0	0	0	0	0	0	-0.81	0	0	0	-0.37
Ana	0	0	0	0	0	0	-0.01	0.5	0.79	0	0	-0.81
AcX	0	0	0	0.99	0	0	0	0	0	0.13	0	0

$\mathrm{mol\,m_L^{-3}\,h^{-1}}$), while for the intracellular metabolite pools (Equations D.10 – D.14), for which dilution by cell growth is considered, the derivatives are calculated in $\mathrm{mol\,m_x^{-3}\,h^{-1}}$, considering the molar volume of bacteria, V_x ($5.89 \times 10^{-5}\ \mathrm{m^3\,mol_x^{-1}}$). The anabolism flux was regarded as the growth rate ($\mu = J_{\mathrm{Ana}}$).

$$\frac{dc_{\mathrm{CO}}}{dt} = -\left(J_{\mathrm{ACAS}} + J_{\mathrm{CODH}}\right) c_x \tag{D.3}$$

$$\frac{dc_{\mathrm{H_2}}}{dt} = -2 J_{\mathrm{Hyd}} c_x \tag{D.4}$$

$$\frac{dc_{\mathrm{CO_2}}}{dt} = \left(J_{\mathrm{CODH}} - J_{\mathrm{FDH}}\right) c_x \tag{D.5}$$

$$\frac{dc_{\mathrm{AcT}}}{dt} = \left(J_{\mathrm{AcX}} - r_{\mathrm{HAc,D}}\right) c_x \tag{D.6}$$

$$\frac{dc_{\mathrm{EtOH}}}{dt} = J_{\mathrm{EtS}} c_x \tag{D.7}$$

$$\frac{dc_{\mathrm{BDO}}}{dt} = J_{\mathrm{BDOS}} c_x \tag{D.8}$$

$$\frac{dc_{\mathrm{AcCoA}}}{dt} = \left(J_{\mathrm{ACAS}} - J_{\mathrm{ACS}} - 2J_{\mathrm{BDOS}} - \frac{1}{2} J_{\mathrm{Ana}}\right) \frac{1}{V_x} - \mu c_{\mathrm{AcCoA}} \tag{D.9}$$

$$\frac{dc_{\mathrm{NADH}}}{dt} = \left(J_{\mathrm{Rnf}} - 2J_{\mathrm{ACAS}} + J_{\mathrm{ETS}} - \frac{1}{2} J_{\mathrm{BDOS}} - J_{\mathrm{Nfn}}\right) \frac{1}{V_x} - \mu c_{\mathrm{NADH}} \tag{D.10}$$

$$\frac{dc_{\mathrm{NADPH}}}{dt} = \left(J_{\mathrm{Hyd}} + 2J_{\mathrm{Nfn}} - \frac{1}{2} J_{\mathrm{FDH}} - J_{\mathrm{ACAS}}\right) \frac{1}{V_x} - \mu c_{\mathrm{NADPH}} \tag{D.11}$$

$$\frac{dc_{\mathrm{Ac^-_{in}}}}{dt} = \left(J_{\mathrm{AcS}} + r_{\mathrm{HAc,D}} - J_{\mathrm{EtS}} - J_{\mathrm{AcX}}\right) \frac{1}{V_x} - \mu c_{\mathrm{Ac^-_{in}}} \tag{D.12}$$

$$\frac{dc_{\mathrm{For}}}{dt} = \left(J_{\mathrm{FDH}} - J_{\mathrm{ACAS}}\right) \frac{1}{V_x} - \mu c_{\mathrm{For}} \tag{D.13}$$

$$\frac{dc_{\mathrm{Fd^{2-}_{red}}}}{dt} = \begin{pmatrix} -\frac{1}{2} J_{\mathrm{FDH}} + J_{\mathrm{ACAS}} + J_{\mathrm{CODH}} + J_{\mathrm{Hyd}} \\ - J_{\mathrm{EtS}} - J_{\mathrm{BDOS}} - J_{\mathrm{Nfn}} - J_{\mathrm{Rnf}} \end{pmatrix} \frac{1}{V_x} - \mu c_{\mathrm{Fd^{2-}_{red}}} \tag{D.14}$$

D.1.2. Increasing the model stability

After calculation of the volumetric derivatives (Equations D.3 – D.14), their physical correctness is checked (i.e., is there enough metabolite/dissolved gas available). This is done by calculating a maximum rate, considering that the concentrations cannot be lower than the minimum one and that multiple Lagrangian particles could be present in the current volume element $N_{p,\mathrm{VE}}$, decreasing the substrate availability per particle (this term is not included for the intracellular compounds).

This was done by calculating the maximum rate to be $\left.\frac{dc_i}{dt}\right|_{\mathrm{max}} = \frac{c_i - 0.9c_{i,\mathrm{min}}}{N_{p,\mathrm{VE}}\Delta t_{IC}}$ with t_{IC} as the integration time step of 0.1 ms, while a factor 0.9 was used to prevent zero-divisions when $c_i = c_{i,\mathrm{min}}$. In the case that for one of the other metabolites j the maximum rate is exceeded, $\frac{dc_j}{dt} > \left.\frac{dc_j}{dt}\right|_{\mathrm{max}}$, the entire metabolism is proportionally scaled to maintain model stability without violation of the mass balance (Equation D.15). When for multiple metabolites the maximum rates are exceeded, this re-scaling is conducted based on the rate that had the smallest relative excess.

$$\frac{\frac{dc_i}{dt}}{\frac{dc_j}{dt}} = \frac{\left.\frac{dc_i}{dt}\right|_{\mathrm{cor}}}{\left.\frac{dc_j}{dt}\right|_{\mathrm{max}}} \quad \text{thus} \quad \left.\frac{dc_i}{dt}\right|_{\mathrm{cor}} = \left.\frac{dc_j}{dt}\right|_{\mathrm{max}} \cdot \frac{\frac{dc_i}{dt}}{\frac{dc_j}{dt}} \tag{D.15}$$

After integration via the Runge-Kutta 4th order algorithm using a fixed integration time step Δt_{IC}, the viability of the results were checked by comparing the updated concentration with a predicted range of values determined by the forward Euler method. In case the new concentrations determined by the Runge-Kutta integration method are more than 100 times outside the predicted range from the forward Euler method, the concentrations are not updated (0.15% of the particles). In the case that computations caused invalid (nan) results (0.5%), then no changes in concentration were considered during that particle time step. These steps were required for solving the CFD-CRD model in a highly parallelised environment supercomputer with 128 CPU cores. Solving the model on a less parallelised system lasted significantly longer, but was computationally more stable.

From the obtained lifelines the rates could be back-calculated considering the modifications, by solving a system of linear equations. In this case the equations D.3–D.14 are considered as a system of linear equations, which could be solved for the reaction rates J_j using the known concentrations, stoichiometry's, and derivatives in MATLAB.

D.1.3. Model verification as a batch process

Several simulations have been performed to check whether the implementation of the kinetic model in Ansys FLUENT was done correctly. The original kinetic model was written in MATLAB, then it was rewritten into C and subsequently adjusted to use with Ansys FLUENT's DPM_SCALAR_UPDATE macro. Its validity was checked by calculating the concentration trajectory in a 50 s liquid-phase "batch" fermentation from the initial concentrations (Table D.1), in MATLAB, the C code and the FLUENT code, for which simulations were performed in the Snellius supercomputing infrastructure. In C and FLUENT, the system was integrated using the Runge-Kutta 4^{th} order algorithm as described above, while in MATLAB the system was integrated using ode15s.

From the metabolite trajectories (Figure D.1) became clear that there are two distinctive regions during the batch fermentation. In the first region (0 to ~3.5 s) all the models produced the same results and the model was found to be applicable to solve kinetic interactions. But in the other region, the lin-log model was found not to be applicable so that the results were determined by the imposed modifications. In order to prevent nonphysical results, the additional modifications imposed in the Ansys FLUENT script cause that nothing changes (the cell is on "stand-by").

The ode15s solver in MATLAB was unable to provide results in the region with low concentrations. Although tests were done with other ODE solvers in the C-script (i.e., the explicit Runge-Kutta-Cash-Karp and the Bulirsch-Stoer algorithms with adaptive time stepping as well as the implicit Kaps-Rentrop and the semi-implicit extrapolation methods [273]), they did not increase stability in the region of instability, nor changed the results of the simulation during the first ~3.5 s. The poor validity of the lin-log model structure in regions with low concentrations, should be kept in mind when developing kinetic models that have to be coupled with CFD simulations.

The modifications imposed in the FLUENT script and the supercomputing infrastructure probably caused smaller deviations from the endpoint at 3.5 s, compared to the C-script, wherein larger acetate and H_2 consumption rates are predicted. The imposed minimum concentrations (min $O(10^{-12})$), and the numerical error ($O(10^{-16})$) can result into derivatives of $O(10^4)$, which might lead to excessive rates, which were in turn limited as much as possible using the rate-limitation mechanism described above.

Currently, experimental data regarding the impact of short-term (order of seconds) fluctuations on *C. autoethanogenum* metabolism are unavailable; such results are required to validate the model predictions under the simulated conditions. The kinetic model, was however, parameterised on an experimental data set with metabolic oscillations in the time-scale of hours [40, 204]. Our model predictions should thus be regarded as a hypothesis regarding cellular response under large-scale conditions, which are to be explored further.

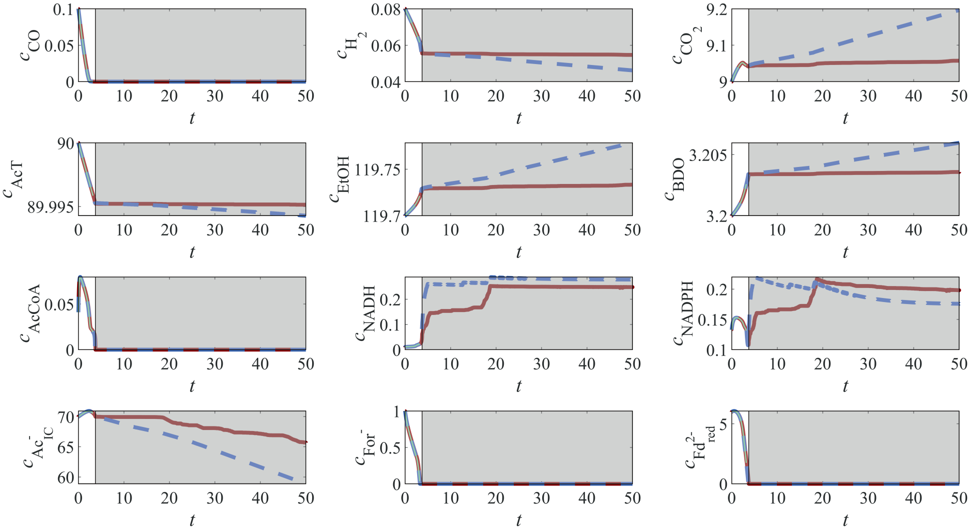

Figure D.1: Verification of the model implementation strategies, by comparing metabolite concentration (in mol/m^3) trajectories during a batch (t in s) fermentation in the liquid phase, with $c_x = 5\,\mathrm{g\,L^{-1}}$. Based on the provided initial concentrations (Table D.1) the three implementations of the metabolic-kinetic models in MATLAB (green line), C (blue dashed line) and Ansys FLUENT (red line) were solved. The three models produce the same results in the uncoloured region (hence the overlapping lines), while the predictive capacity of the model becomes more limited in regions with lower metabolite concentrations (shaded with grey), where the MATLAB model was unable to provide results.

D.1.4. Lifeline reconstruction in C and comparison with constant concentration case

To check the influence of the computing infrastructure on the metabolite concentrations, a lifeline obtained from the CFD-CRD model, was reconstructed via the C-script (Figure D.2). The dissolved CO, H_2 and CO_2 concentrations were used as input parameters for this model, as well as the local number of particles (required for the rate-limitation mechanism). As the data export resolution was 750 times higher than Δt_{IC}, linear interpolation between two subsequent data points was done. Generally, a pretty good overlap is observed between the CFD results (red) and the reconstructed CFD-results (black lines). Negligible deviations only occurred in the cases with very low dissolved gas concentrations for AcCoA, NADH and NADPH. This made us conclude that our modelling algorithms and workflow were well implemented and suitable for metabolism predictions on dissolved gas concentration fluctuations.

To inspect how the metabolite behaviour with $2.5\,\mathrm{g\,L^{-1}}$ biomass deviates from a case with constant dissolved gas concentrations, the model with constant dissolved gas concentrations was applied at the average CO concentration during that lifeline of $0.29\,\mathrm{mol\,m^{-3}}$. Because the average $c_{L,CO}$ is relatively high and its characteristic time was in the similar order of magnitude as the mass transfer characteristic time, no large spatial gradient was expected in the CFD model. The causes that there is high similarity between the general trend from the CFD-CRD model results and the model with constant dissolved gas concentrations. The fluctuations in $c_{L,\mathrm{CO}}$ have strong effects on the metabolism, as can be seen by the depletion of formate and the increases in ethanol production during moments with low $c_{L,\mathrm{CO}}$.

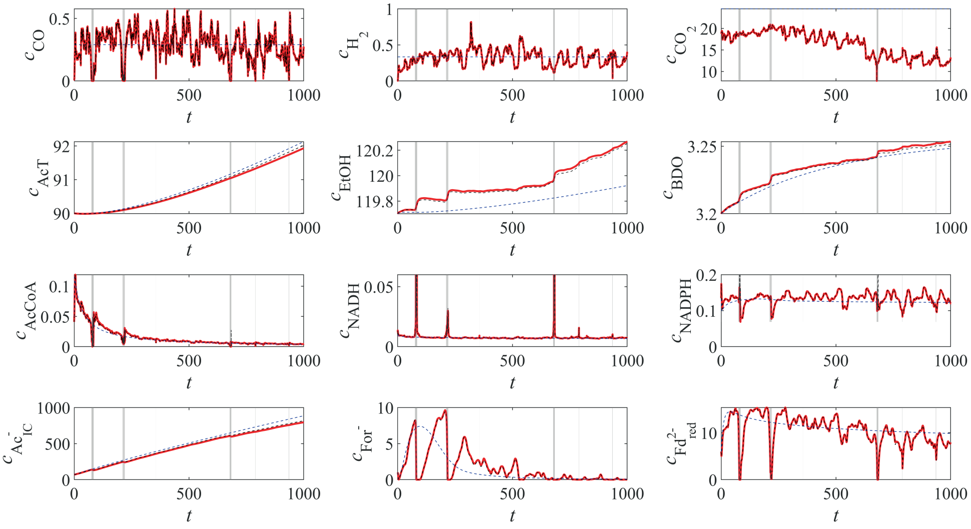

Figure D.2: Comparison of metabolic fluctuations during a lifeline (c in mol m^{-3} and t in s) from the CFD-CRD model (red), its reconstruction in C (black dashed line) and the constant concentration model (blue), c_x = 2.5 g L^{-1}, with an average $c_{L,\mathrm{CO}}$ of 0.29 mol m^{-3}.

D.1.5. Choice of Δt_f and N_p

A considerate decision had to be made regarding the number of particles N_p which the kinetic model was solved for. Simulating more particles could increase accuracy of the solution, but would lead to longer simulations. The build-up of the simulation time per time step was determined for a varying number of particles for which the metabolic model was solved (N_p [0 - 250,000]) (Figure D.3a). Obviously, the simulation time of the flow, species, turbulence and particle displacement models were independent from the number of particles for which the metabolic model was solved for. The total time required to solve the metabolism, increased linearly with the number of particles. Per particle solving the CRD model took around 0.04 ms (with Δt_f = 5 ms and 128 CPUs), which turned out to be the limiting mechanism in terms of simulation time. The cumulative CO and H_2 consumption rates did not vary significantly with more than 80,000 particles. In order to test the accuracy of the simulation results with respect to the number of particles and the Eulerian time step Δt_f, the CO and H_2 uptake rates (volume integral of Equation

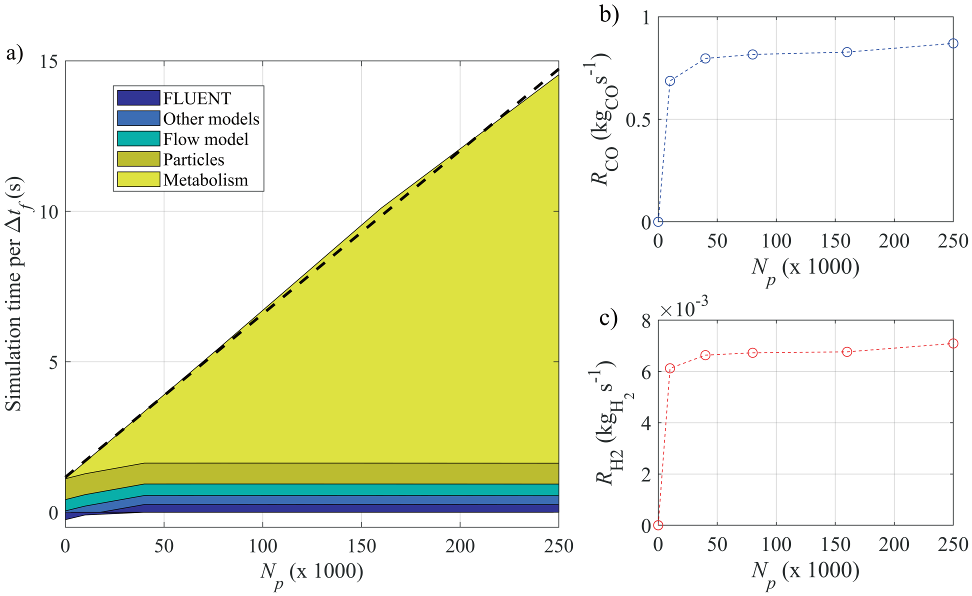

Figure D.3: The influence of the number of simulated particles on simulation time and accuracy. a) The built-up of the simulation time per Eulerian time step (Δt_f) as a function of the number of particles for which the metabolic model was solved. The influence of the number of particles on the b) total CO and c) H_2 consumption rate. The data was obtained using Δt_f of 5 ms and 250,000 well-distributed Lagrangian particles, during 200 flow time steps at 128 CPU cores. FLUENT: leftover between the total wall time and the provided simulation times for all the sub-models, attributed to communication and parallelisation gains and losses; Other models: the species model (for CO, H_2 and CO_2), gas-liquid mass transfer and the turbulence models; Particles: displacement of the 250,000 particles, which time was determined by not solving the metabolism.

5.1, in $\mathrm{kg\,s^{-1}}$) were determined for the cases with 80,000 and 250,000 reacting particles, with varying time steps (1 - 10 ms) (Figure D.3b,c). From the analysis became clear that the accuracy increase between 80,000 and 250,000 particles is very limited, compared to the twofold increase in computation time, rendering it unworthy to use more than 80,000 particles. From the time step variation, the inverse proportional relationship with run time became visible, and consequently we chose to use a 5 ms time step, since that one showed low variations in uptake rates, for an acceptable simulation time.

Large deviations were expected between the uptake rate predicted by the metabolic model at the beginning of the Eulerian time step, $\left.\frac{dc_i}{dt}\right|_{p,t}$, and the one that has been realised at the end of Δt_f, $\left.\frac{c_i|_{t+\Delta t_f} - c_i|_t}{\Delta t_f}\right|_p$, in case of large time steps (since Δt_f » Δt_{IC}). Since the species balances are only calculated at the beginning of the flow time step, and not while solving the metabolic model, one has to be sure that the deviation between these becomes not too big. Using as source term would not guarantee intracellular mass balance closure, and could lead to unstable solutions in cases with low metabolite concentrations. Instead, the cumulative integration term in the source term guarantees mass balance closure and increases model stability, but requires the use of smaller Δt_f. To test the choice of Δt_f, the average percentage of deviation between the two approaches was determined for the examined range of Δt_f (Equation D.16, Figure D.4). The deviations were considered to be small enough (< 10%) using a 5 ms time step.

$$\text{deviation}(\%) = \frac{1}{N_p} \cdot \sum_{p=1}^{N_p} \left\| \frac{\left.\frac{dc_i}{dt}\right|_{p,t} - \left.\frac{c_i|_{t+\Delta t_f} - c_i|_t}{\Delta t_f}\right|_p}{\left.\frac{dc_i}{dt}\right|_{p,t}} \right\| \cdot 100\% \tag{D.16}$$

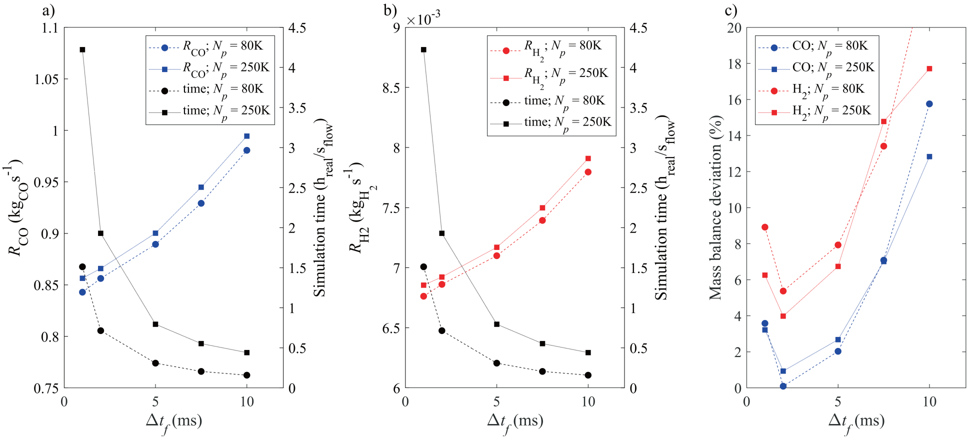

Figure D.4: Influence of the Eulerian time step and the number of particles for which the kinetic model is solved on a, b) the accuracy and run time of the CFD-CRD and c) the mass balance deviation. Accuracy was measured as a) the CO-uptake rate (blue) and b) the H_2 uptake rate (red), while run time (black) was determined as time taken per second simulation time. The mass balance deviation was calculated using Equation D.16. Squares and circles denote the simulations with 250,000 and 80,000 reacting particles, respectively. All uptake rates and run times were based on their average during 0.2 s simulation time.

D.1.6. Mass balance during a lifeline

The carbon and electron balances were computed during lifelines for each c_x case, and analysed as a function of the temporal $c_{L,CO}$ (Figure D.5) in order to determine the mass balance error due to the model correction terms. Generally, the mass balance closes each moment in time, although at low concentrations (the dashed region) there is some intracellular formate generation (see Section 5.3.1).

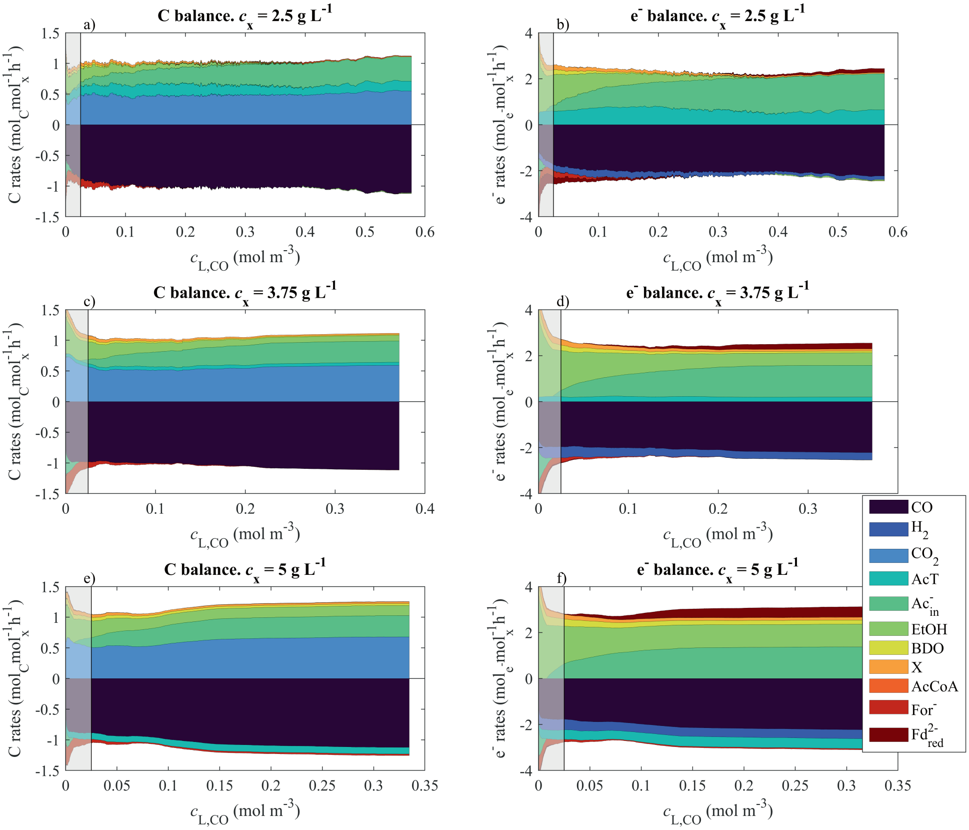

Figure D.5: a, c ,e) Carbon and b, d, f) electron balances during varying $c_{L,CO}$ of a lifeline for varying c_x: a, b) 2.5; c, d) 3.75; e, f) 5 g L^{-1}. The shaded area below the calibrated $c_{L,CO}$ range. The metabolite rates (colouring in legend) were sorted along their respective $c_{L,CO}$ and smoothened using smoothing factor 0.4 for improved visualisation.

D.2. Relationship between dissolved CO and H_2

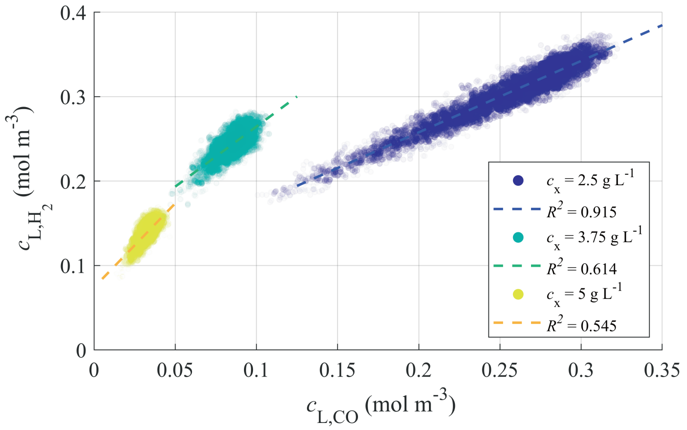

Figure D.6: Relationship between $c_{L,CO}$ and c_{L,H_2}. The scatters represent the average $c_{L,CO}$ and corresponding c_{L,H_2} for 4000 lifelines for each biomass concentration. The resulting linear approximations were determined using linear regression in MATLAB and checked by calculating R^2.

Table D.4: Cases for which the CRD model with constant dissolved gas concentrations was solved for. The CO concentration was varied in a specific range for each biomass concentration, which resulted in a corresponding H_2 concentration. The CO_2 concentration was kept as a constant value, based on its time- and volume-averaged concentration in the EL-GLR during the last 900 seconds of the CFD-CRD simulation.

c_x (g L^{-1})	$c_{L,CO}$ range (mol m^{-3})	c_{L,H_2} (mol m^{-3})	c_{L,CO_2} (mol m^{-3})
5	0.005 — 0.05	1.99 $c_{L,CO}$ + 0.074	21.4015
3.75	0.05 -- 0.12	1.43 $c_{L,CO}$ + 0.110	17.5929
2.5	0.125 -- 0.35	0.846 $c_{L,CO}$ + 0.0885	24.5735

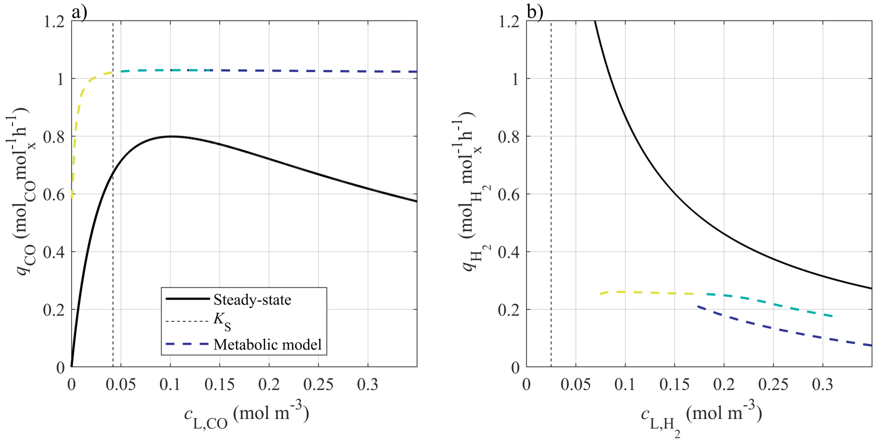

Figure D.7: Comparison of uptake rates for CO and H_2 between the CRD model (Metabolic model) and the steady-state (Monod and Haldane) models as a function of their concentration in the liquid phase. Black line: steady-state kinetics (Table 4.1); dashed black line: K_s according to the steady-state model; coloured dashed lines: results from CRD model with constant dissolved gas concentrations.

D.3. CO and H_2 uptake kinetics and inhibition by ferredoxin

From the models with constant dissolved gas concentrations, q_{CO} and q_{H_2} were determined as function of the dissolved gas concentration (Figure D.7) (considering the ratio between CO and H_2 (Figure D.6)). The CO-uptake rate in the CRD model is slightly higher than the one in the case of Haldane kinetics. The inhibition effect at increased $c_{L,CO}$ is not visible in the CRD model. The H_2-uptake rate is clearly lower than was predicted with the Monod model, and an inhibition effect due to increased $c_{L,CO}$ (and c_{L,H_2}) was observed.

From the lifeline results in the CFD-CRD model, was derived that inhibition of CO- and H_2-uptake could occur due to high concentrations of reduced ferredoxin (Figure D.8). When $c_{Fd^{2-}_{red}}$ is around 5 mol m^{-3}, q_{H_2} starts to decrease significantly, which could indicate a certain inhibition mechanism by reduced ferredoxin. The spread that is observed in the H_2 and CO data regarding H2-uptake at high concentrations, suggests that the inhibition effect is not directly caused by the CO and H_2 concentrations themselves.

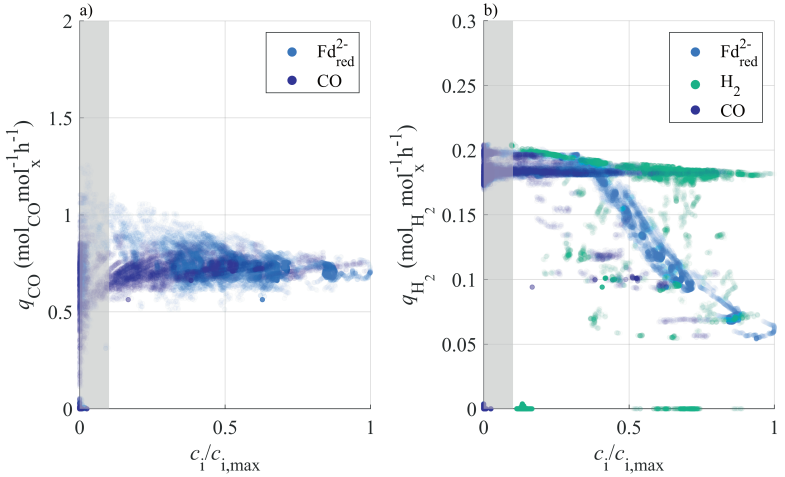

Figure D.8: Relationships between a) dissolved CO and b) H_2 concentration, the reduction state of the cell ($c_{Fd^{2-}_{red}}$), and the uptake rate of the respective gas q_i. The scatters mark temporal observations during a lifeline from the CFD-CRD simulation with $c_x = 5\,\mathrm{g\,L^{-1}}$ (between 100 and 1000 s), the scatter density denotes its probability of occurrence., $c_{L,CO,max} = 0.25\,\mathrm{mol\,m^{-3}}$, $c_{L,H_2,max} = 0.42\,\mathrm{mol\,m^{-3}}$, $c_{Fd^{2-}_{red},max} = 11.25\,\mathrm{mol\,m^{-3}}$. Shaded areas mark zones with $c_{L,CO} < 0.025\,\mathrm{mol\,m^{-3}}$.

D.4. Formate production

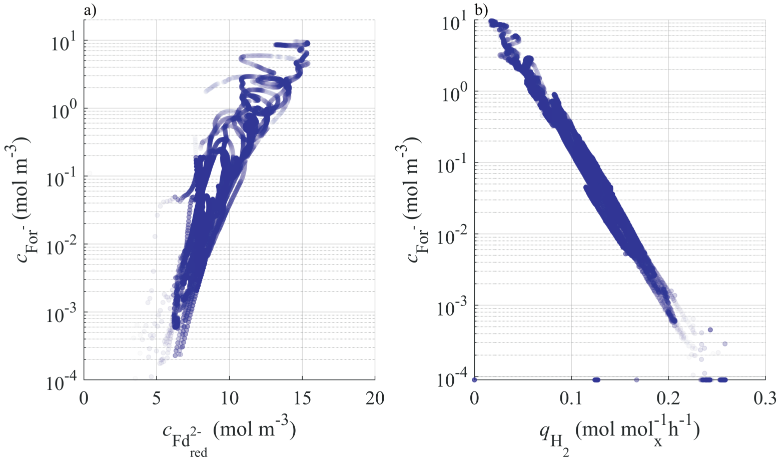

Figure D.9: The relationship between a) $c_{Fd^{2-}_{red}}$ and b) q_{H_2} and the formate concentration. The scatters mark temporal observations during a lifeline from the CFD-CRD simulation with $c_x = 2.5\,\mathrm{g\,L^{-1}}$ (between 100 and 1000 s), their density denote the probability of occurrence.

D.5. Ethanol production during lifelines

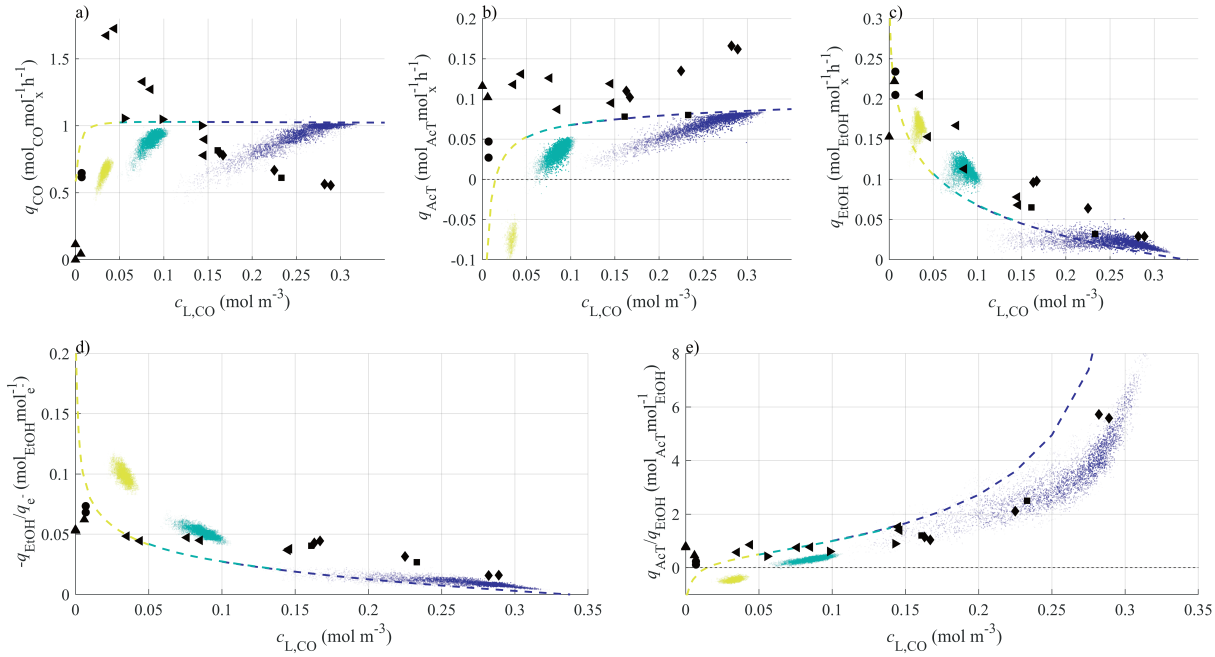

Figure D.10: Comparison of lifeline-averages from the CFD-CRD model (after removing $c_{L,CO} < 0.025\,\text{mol}\,\text{m}^{-3}$) with the constant concentration model and experimental data. The average biomass-specific rates and yields are plotted against the average $c_{L,CO}$: a) q_{CO}, b) q_{AcT}, c) q_{EtOH}, d) the electron-to-ethanol yield q_{EtOH}/q_{e^-} ($q_{e^-} = 1/2(q_{CO} + q_{H_2})$, and e) the acetate-per-ethanol ratio q_{AcT}/q_{EtOH}. The scatters, with varying transparency to reduce overplotting, represent 900 s averages for ~4000 lifelines for each c_x simulation (blue 2.5; green 3.75; yellow $5\,\text{g}\,\text{L}^{-1}$), the dashed line simulations with constant dissolved gas concentrations at the indicated biomass concentrations, and the markers reconciled [218] experimental chemostat data: ♦ [44]; ■ [46] (CO + H_2); • [46] (CO); ▲ [90]; ◄ [45]. $c_{L,CO}$ in ► [89], was estimated using their provided $k_L a$.

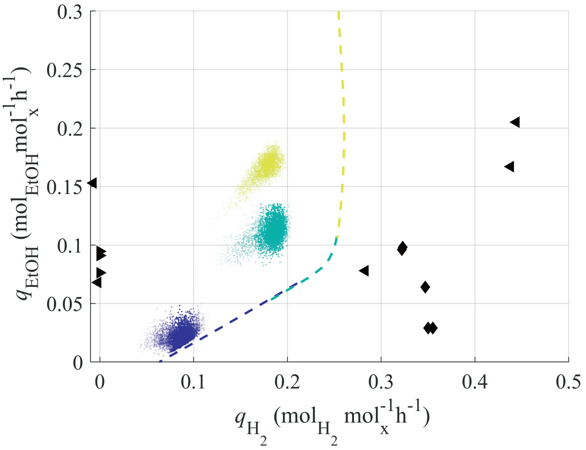

Figure D.11: Relationship between q_{H_2}-uptake and q_{EtOH}. The scatters, with varying transparency to reduce overplotting, represent 900 s averages for ~4000 lifelines for each c_x simulation (blue 2.5; green 3.75; yellow 5 gL^{-1}), the dashed line simulations with constant dissolved gas concentrations at the indicated biomass concentrations, and the markers reconciled [218] experimental chemostat data: ◆ [44]; ■ [46] (CO + H$_2$); • [46] (CO); ▲ [90]; ► [45]. $c_{L,CO}$ in ◄ [89], was estimated using their provided $k_L a$

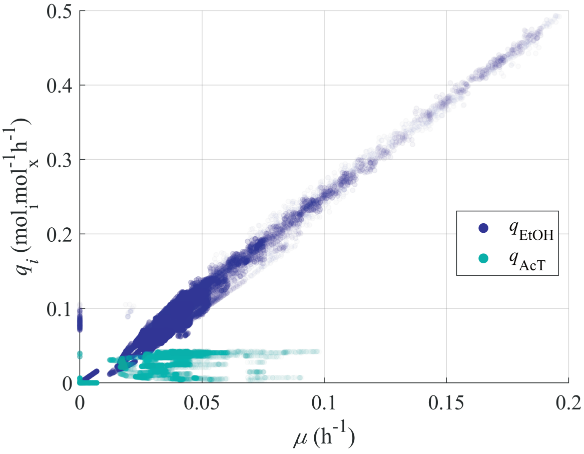

Figure D.12: Relationship between the growth rate μ and q_{EtOH} and q_{AcT}. The scatters mark temporal observations during a lifeline from the CFD-CRD simulation with $c_x = 3.75$ gL^{-1} (between 100 and 1000 s), their density denotes the probability of occurrence.

Table D.5: Catabolic reactions towards ethanol and acetate production from CO, including the Gibbs free energy at standard conditions per mol product and CO [84].

Reaction		$\Delta_r G^o$ (kJ mol$^{-1}_{\text{product}}$)	$\Delta_r G^o$ (kJ mol$^{-1}_{\text{CO}}$)
Acetogenesis	$-4CO - 2H_2O + C_2H_3O_2^- + H^+ + 2CO_2$	-135.04	-33.76
Solventogenesis	$-6CO - 3H_2O + C_2H_5OH + 4CO_2$	-224.66	-37.44
Starvation	$-2CO - C_2H_3O_2^- - H^+ - H_2O + C_2H_5OH + 2CO_2$	-89.62	-44.81

D.6. Metabolism

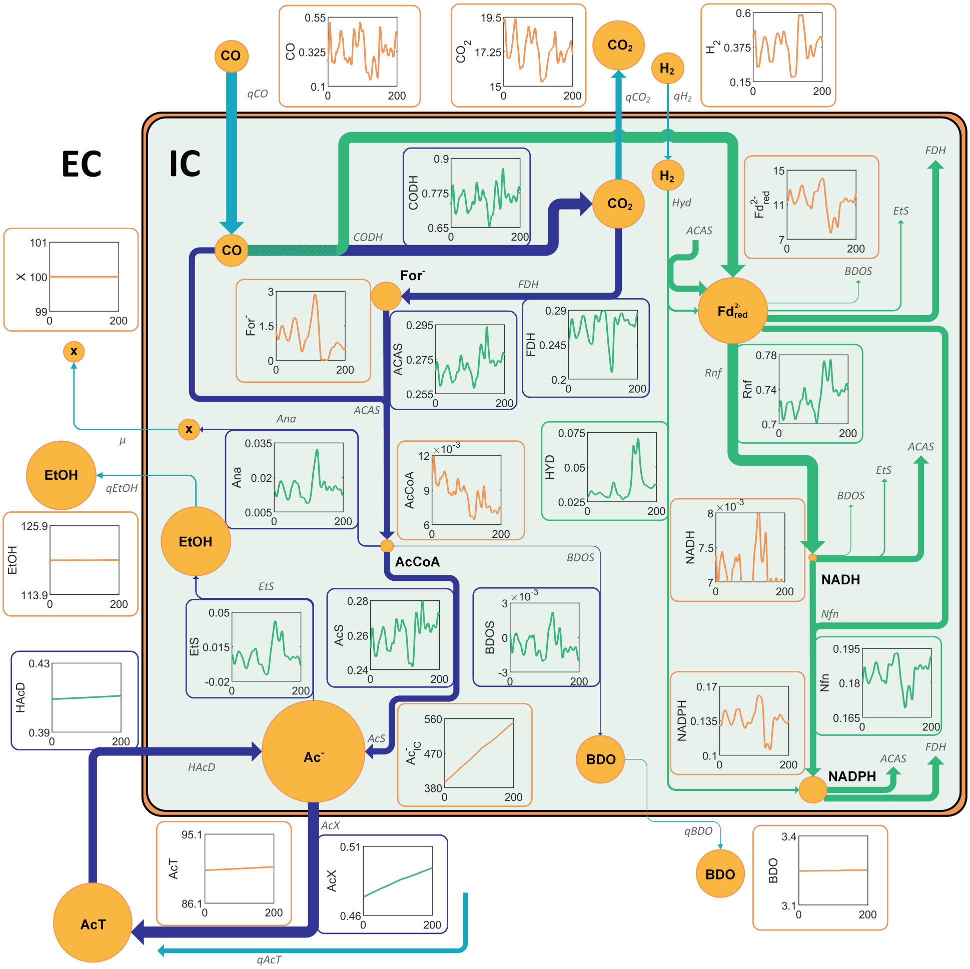
EC
IC
CO
qCO
CO₂
qCO₂
H₂
qH₂
CODH
For⁻
FDH
Hyd
ACAS
Fd²⁻red
FDH
EtS
BDOS
Rnf
Ana
AcCoA
NADH
Nfn
NADPH
X
x
μ
EtOH
qEtOH
HAcD
Ac⁻
AcS
AcX
AcT
qAcT
BDO
qBDO
Ac⁻IC

Figure D.13: Metabolism of *C. autoethanogenum* during large-scale syngas fermentation. 100 seconds of a lifeline of the case with 2.5 $g_x\,L^{-1}$ is shown with its concentration (in mol m^{-3}) and rate (in mol $mol_x^{-1}\,h^{-1}$) fluctuations. Pool sizes and arrow thickness are approximative to the median concentrations and rates during the whole lifeline.

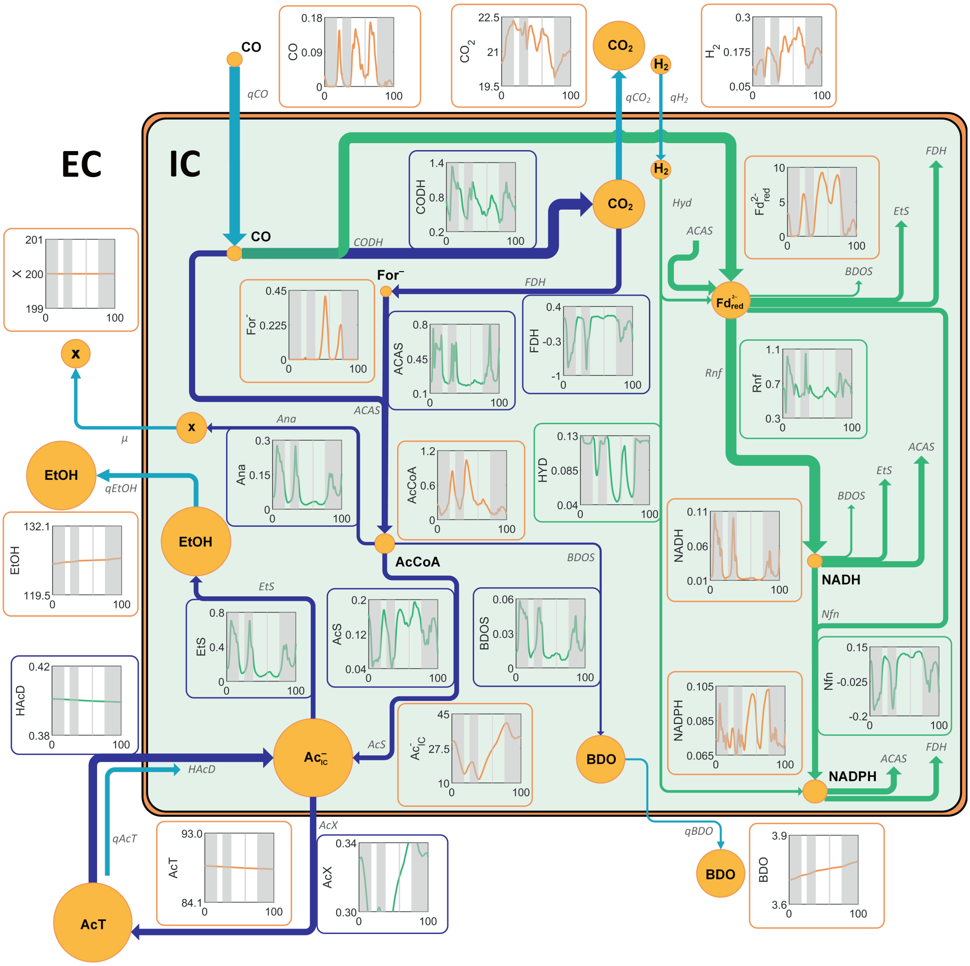
EC
IC
CO
qCO
CO
0.18
0.09
0
0
100
CO2
22.5
21
19.5
0
100
CO2
qCO2
H2
qH2
H2
0.3
0.175
0.05
0
100
CO
CODH
CODH
1.4
0.8
0.2
0
100
CO2
H2
Hyd
ACAS
FDH
Fd2-red
10
5
0
0
100
EtS
BDOS
Fd2-red
X
201
200
199
0
100
For−
For−
0.45
0.225
0
0
100
FDH
ACAS
0.8
0.45
0.1
0
100
FDH
0.4
-0.3
-1
0
100
Rnf
Rnf
1.1
0.7
0.3
0
100
x
x
μ
Ana
ACAS
Ana
0.3
0.15
0
0
100
AcCoA
1.2
0.6
0
0
100
HYD
0.13
0.085
0.04
0
100
ACAS
EtS
BDOS
EtOH
qEtOH
EtOH
EtOH
132.1
119.5
0
100
AcCoA
BDOS
NADH
0.11
0.06
0.01
0
100
NADH
Nfn
EtS
EtS
0.8
0.4
0
0
100
AcS
0.2
0.12
0.04
0
100
BDOS
0.06
0.03
0
0
100
Nfn
0.15
-0.025
-0.2
0
100
HAcD
0.42
0.38
0
100
HAcD
Ac−IC
AcS
Ac−IC
45
27.5
10
0
100
BDO
NADPH
0.105
0.085
0.065
0
100
ACAS
FDH
NADPH
qAcT
AcT
93.0
84.1
0
100
AcX
AcX
0.34
0.30
0
100
qBDO
BDO
BDO
3.9
3.6
0
100
AcT

Figure D.14: Metabolism of *C. autoethanogenum* during large-scale syngas fermentation. 100 seconds of a lifeline of the case with $5\,g_X\,L^{-1}$ is shown with its concentration (in $mol\,m^{-3}$) and rate (in $mol\,mol_X^{-1}\,h^{-1}$) fluctuations. Pool sizes and arrow thickness are approximative to the median concentrations and rates during the whole lifeline.

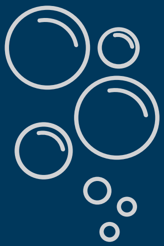

Acknowledgements / Dankwoord

A PhD thesis is not just the accumulated written work of one single person working at one single place. This thesis was written not only behind a (standing) desk in an office, but also in several other places: first at home, during the pandemic, but also in other places, on trains, and planes: in Germany, France, Denmark, Australia and even in a crappy hospital in Liège on a Saturday night. I'm grateful for the advances in modern technology, which enabled running multi-gigabyte simulations from the WiFi on ICE. And then I did not even mention the help obtained from ChatGPT.

But most importantly, finishing a PhD is not a lonely achievement. During the last few years, many people were involved in various ways, probably too many to count, but I would like to start by thanking the people mostly involved:

Henk, you are a true visionary in the field of bioprocess engineering, which has been a great inspiration to me while working together over the past few years. You successfully familiarised the international biotech community with the 'start with the end in mind' mentality. I am very grateful to have been able to work on your ideas and apply them to gas fermentation. All your feedback and advice has helped me to grow and be the best that I can be.

Cristian, when you were teaching the NMST, you lured me into modelling and then into this PhD position. During the PhD I really enjoyed teaching the NMST together and discussing any programming problem. I still think it is a pity that you left TU Delft after the first year, but despite the geographical distance we stayed in touch. While going through your latest paintings and snorkelling experiences, we were met regularly for lunch and a good cup of coffee. Thank you so much for getting me excited about this field and all the great times we have had together.

Cees, I am so glad that you came on board. Not only is your technical guidance of superior quality, also your involvement in the other aspects of the PhD has been valuable. It has been a pleasure to work together and to see the CASE group grow and develop over time. Not only professionally but also on a more personal level, we have had great times. You have become not only an excellent supervisor and co-promotor, but also a friend. Thank you again for inviting us to your wedding on Terschelling. That weekend was the highlight of 2023 and will be remembered forever.

Thank you all for your great contributions to this thesis and all the other feedback, hints and advice you provided. This enabled us to share our work in papers and in many conference talks. I am grateful for all the presentations I could give, with special mention to the one on Heron Island. Thanks for making this once-in-a-lifetime journey possible!

Marina and Eduardo were my closest colleagues during my PhD. **Marina**, without your enthusiasm for science and gas fermentation, and the way you passed it on to me, I might never have started this adventure. I am still very proud of how, in a 30-minute meeting, we combined our skills and wrote a research proposal. A few months later we got it published. We enjoyed many trips and conferences together, we had great times in nightclubs in Nottingham, in the forests near Wageningen, and watching the sunset on the Rheintreppe in Düsseldorf. Thank you for welcoming me to Novozymes and the cold in Copenhagen. It has been a pleasure working with you over the past five years.

Eduardo, thanks for the f*cking model! We have had so much trouble getting it to work and with the analyses, but now we have a cool movie to show. Your love-hate relationship with science is adorable, and your critical attitude towards thermodynamic analyses of metabolic pathways is next level. I have loved the discussions we have had over the last couple of years. We always helped each other to improve our work, but we'll never agree on some philosophical theories (like degrowth). Let's continue discussing them while watching some small bubbles rise.

On a day-to-day basis, **Sam**, you got me through my PhD. I should have spent a bit more energy listening to your cricket stories, as you listened to all my complaints about whatever model did not work. We had a great time living together at the Arthur van Schendelplein, with the traditional *ambachtelijke knakworstlunch* as highlight of the weekend. I will always feel guilty for not being able to attend your defence. Thank you for all your support and friendship .

Thank you, **Sam** and **Marina**, for being my paranymphs. I hope both of you are not spending too much time on it, but I'm sure it will be a day we'll never forget.

Steven, thanks for all the discussions on the wording of the propositions. As the in-house philosopher you taught me the basics how to become one.

Many students worked during their MSc or BSc thesis on topics related to this thesis. First of all, **Britt**, you did a wonderful job by starting up the project, I'm glad that we kept in touch during the last few years. **Héctor**, it was a pleasure to lure you into the project and later into a PhD. It was great working with you, first as a student and then as a colleague. We had amazing discussions (with and without carbonated liquids) and rainy bike rides during which we learnt a lot from each other. I am looking forward to meeting the new colleague you will have to recruit as CFD BOSS 3.O. **Lilo**, you started your project just after a lockdown, your enthusiasm was infectious and pushed the project forward: I'm very proud we got your results published. **Laura**, **Yassine**, **Bram** and **Lucy**, I would also like to thank you for the great time we had during your projects. Coaching and supervising all of you was one of the most enjoyable parts during the PhD.

It has been wonderful to be part of the BPE group. As a group we have done so much together: No group or company could ever compete with such a great working environment. Everyone in the group went through similar highs and lows (some higher, some lower), and sharing these experiences (or: *lifelines*) together paves the way for lifelong friendships. I'm glad to have shared all of these with such a fantastic group of colleagues. During our working days we had many (and perhaps too long) coffee and lunch breaks, usually with snacks or cakes after birthdays or conference trips. It's a shame that some of the breaks were cut short because of ongoing discussions about the monarchy. After work, we ordered beers via Flink, we organised BBQ's, we went to the beach, we (tried to) brew beer, we went out for bike rides, we celebrated birthdays and we even had a month-long beard growth competition, after eating Mexican food with our nasty moustaches.

During this time, I shared the office with Joan, Marina, Rik, Héctor and Tamara. I'm thankful to all of you that I could ask whatever random question that was in my mind. **Joan**, you were an example how to approach the PhD, and I'm glad that your roadmap through Manuscript Earth is still there in the office. **Marina**, we managed to keep each other in the office for way too long to discuss mass transfer limitations or whatever other interesting problem one of us faced. **Rik**, you did a wonderful achievement by convincing me to share code online. I highly enjoyed the discussions we had in the office on whatever topic, ranging from bubbles and broth to the credibility of the executive board. Thanks for all the help in writing code, improving figures and analysing metabolic fluxes. **Héctor**, I enjoyed welcoming you in the office as a colleague, maybe you will become *officemeister* once again. You are such a kind and helpful person. I highly enjoyed organising the many BBQ's together. **Tamara**, you are a scientific bulldog, please take some time to enjoy and reflect on your achievements. Time flew by during our drive back from Enschede, especially with all the nice conversations we had.

Marijn and Oriol, the MES-twins, I hope both of you can celebrate ending this period in good health as soon as possible. We had great parties together, for example after King's Day when you met "the Koning van Delluft". **Oriol**, I loved to discuss and to share the frustrations on COMSOL-modelling together. Let's hope that Catalunya will gain independence soon. It was great spending time together, **Marijn**, when we went to PSV, to Liberation day, or just to Pint Wednesday in de Gist. Next to one of the kindest persons, you are also one of the craziest persons ever: With the same ease as you walk through glass doors, you walked from Wageningen to Veenendaal.

Mariana, you are the living proof that a monarchy actually works, you gained democratic legitimacy as BPE Queen. Thanks for luring me into the PhD committee. **Tiago**, you resemble drive and persistence: it's inspiring to see how you get things done. This is not only demonstrated in the never-ending discussions we had on topics ranging from chromatography modelling, to monarchy and communism, but also by you flying back-and-forth from Milan to celebrate King's Day in Amsterdam. Thanks for all the discussions, your help and advice.

Daphne, as travel buddies we started our holiday's together, after going through the same experiences in the last few months. It was great to follow all your adventures, I'm sure more will come. **Roxana**, thanks for all the nice times we had together, your kindness and patience, for example after the first Oktoberfest party. Herzlichen Dank für deine Hilfe bei den vielen Übersetzungen, ohne dich hätte ich nie gewusst, was eine Blasensäule ist. **Maarten**, you are one of the most practical guys of the group, I love to hear your innovative solutions to some problems. I'm always looking forward to hearing more about your 3D printed Arduino projects. **Tim**, you undergo a transformation after a few drinks, luckily you only drink from small glasses. Thanks for all the sweets you brought to the coffee breaks.

At some point, Cees started hiring like crazy and we ended up with the CASE group. It was amazing to see this group starting to form and to have biweekly meetings, dinners, activities and trips together with the young research group. **Ramon**, thanks for all your efforts in organising the meetings. You kickstarted your PhD with amazing work and you are well on track to give more presentations than me, including an amazing one in Boston to look forward to. **Mariana** and **Miki**, we had great times, from Terschelling to Stuttgart, we had fun. "Well, that's good for you".

Victor, you're a bit of a geographical outlier to the group, but definitely part of it. Thanks for introducing me to DTU and your colleagues and friends, and going out to the sauna, football matches or your neighbours party. I loved the sudden discussions we had on a wide range of topics spanning from CFD modelling to politics.

Meanwhile BPE kept on growing. New faces provide new identities to the group, while keeping older ones. For example, last year the activities committee lifted the Oktoberfest to the next level. Thanks **Maarten**, **Brenda** and **Marika** for keeping such traditions alive. I wish everyone who still has to finish all the best and lots of luck, I am sure we will stay in touch!

I would like to thank **Adrie** for some great dinners, for working together on several projects, and sometimes you were even the first to read my work. I felt a bit sorry all the time to ask for money and other bureaucracies. **Ludo**, it was amazing spending time together in Berlin, your love for your technology is highly motivating and a driver to continue working on whatever you feel you're interested in. Thanks **Rob**, for the sometimes way too lengthy discussions about bubbles. **Kawieta**, for all the logistics to keep our group up and running.

Prior to the defence I want to thank the committee for reading the thesis, with special mention to **Ralf** for the great discussions we had on Heron Island. Surely you gave me the opportunity to present in many conferences, from which I learnt a lot.

My friends, for their support during this whole journey. In particular, **Koen**, **Berend**, **Hessel**, for the great times near the Russian border fence close to Danzig. Let's plan another weekend soon. **Marijn**, for watching rising bubbles in broken beer glasses in Stuttgart. **Lennart**, **Thijs** and **Steven**, for ice skating every Tuesday night.

Maar zonder jullie, **papa en mama**, had ik dit nooit geschreven. Heel erg bedankt voor het altijd beantwoorden van de “waarom dan?”-vraag. Zonder het geduldige antwoord geven op deze vraag was ik nooit zo nieuwsgierig en kritisch geworden dat dit proefschrift er kon komen. **Jort**, heel erg bedankt voor het lezen en voor de oneindige discussies over alles en niets.

Thank you all for making it through this thesis. I'm looking forward to the future and hope to stay in touch with all of you!

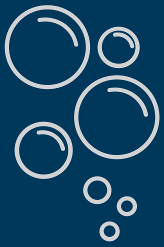

List of Publications

Full papers:

6. Almeida Benalcázar, E., van Winden, W., Puiman, L., Posada, J.A., Jansen, M.L.A., Noorman H.J., & Straathof A.J.J. Bioreactor operation for industrial-scale conversion of ethanol into single-cell protein. *Manuscript in preparation.*

5. Puiman, L., Almeida Benalcázar, E., Picioreanu, C., Noorman, H.J., & Haringa, C. (2024). High-resolution computation predicts that low dissolved CO concentrations and CO gradients promote ethanol production at industrial-scale gas fermentation. *Biochemical Engineering Journal*, 109330, `https://doi.org/10.1016/j.bej.2024.109330`.

4. Volger, R., Puiman, L., & Haringa, C. (2023). Bubbles and Broth: A review on the impact of broth composition on bubble column bioreactor hydrodynamics. *Biochemical Engineering Journal*, 201, 109124, `https://doi.org/10.1016/j.bej.2023.109124`.

3. Puiman, L., Almeida Benalcázar, E., Picioreanu, C., Noorman, H.J., & Haringa, C. (2023). Downscaling Industrial-Scale Syngas Fermentation to Simulate Frequent and Irregular Dissolved Gas Concentration Shocks. *Bioengineering*, 10(5), 518, `https://doi.org/10.3390/bioengineering10050518`.

2. Puiman, L., Elisiário, M. P., Crasborn, L. M., Wagenaar, L.E.C.H., Straathof, A.J.J., & Haringa, C. (2022). Gas mass transfer in syngas fermentation broths is enhanced by ethanol. *Biochemical Engineering Journal*, 185, 108505, `https://doi.org/10.1016/j.bej.2022.108505`.

1. Puiman, L., Abrahamson, B., van der Lans, R. G. J. M., Haringa, C., Noorman, H. J., & Picioreanu, C. (2022). Alleviating mass transfer limitations in industrial external-loop syngas-to-ethanol fermentation. *Chemical Engineering Science*, 259, 117770, `https://doi.org/10.1016/j.ces.2022.117770`.

Conference papers:

2. Eskandari, M., Puiman, L., & Zeitler, J. (2023). Multi-fidelity Bayesian Optimisation of Syngas Fermentation Simulators. peer-reviewed arXiv preprint, `https://doi.org/10.48550/arXiv.2311.05776`.

1. Puiman, L., Maldonado de León, H. A., Noorman, H. J., Picioreanu, C., & Haringa, C. (2022). Intensification of syngas fermentation in industrial-scale bioreactors by implementation of perforated plates: A CFD study. *Chemie Ingenieur Technik*, 94(9), 1242-1242, `https://doi.org/10.1002/cite.202255104`.

Conference contributions (presenting author is underlined):

13. Puiman, L., Almeida Benalcázar, E., Picioreanu, C., Noorman, H.J., & Haringa, C. CFD-CRD predicts metabolic shifts in industrial-scale gas fermentation. *Gas Fermentation conference* (February 2024), Heron Island, Australia. Oral presentation.

12. Eskandari, M., Puiman, L., & Zeitler, J. (2023). Multi-fidelity Bayesian Optimisation of Syngas Fermentation Simulators. *NeurIPS Workshop on Computational Sustainability* (December 2023), New Orleans, USA. Poster presentation.

11. Puiman, L., Almeida Benalcázar, E., Noorman, H.J., & Haringa, C. CFD-CRD in Syngas Fermentation: What can we learn? *Netherlands Biotechnology Conference* (September 2023), Leiden, The Netherlands. Poster presentation.

10. Puiman, L., Elisiário, M.P., Straathof, A.J.J., Picioreanu, C., Noorman, H.J., & Haringa, C. Relieving mass transfer limitations in industrial syngas-to-ethanol fermentation processes. *14th ECCE and 7th ECAB* (September 2023), Berlin, Germany. Oral presentation.

9. Puiman, L., Almeida Benalcázar, E., Noorman, H.J., & Haringa, C. Coupling hydrodynamics and metabolic dynamics in syngas fermentation towards industrial reactor design. *18th Netherlands Process Technology symposium* (July 2023), Enschede, The Netherlands. Oral presentation.

8. Puiman, L., Almeida Benalcázar, E., Noorman, H.J., & Haringa, C. Coupling hydrodynamics and metabolic dynamics in syngas fermentation towards industrial reactor design. *Himmelfahrtstagung on Bioprocess Engineering* (April 2023), Weimar, Germany. Oral presentation.

7. Puiman, L., Maldonado de León, H. A., Noorman, H.J., Picioreanu, & C., Haringa, C. Intensification of syngas fermentation in industrial-scale bioreactors by implementation of perforated plates: a CFD study. *13th ESBES Symposium* (September 2022), Aachen, Germany. Oral presentation.

6. Puiman, L., Elisiário, M.P., Straathof, A.J.J., Haringa, C., Noorman, H.J., & Picioreanu, C. Relieving mass transfer limitations in industrial syngas-to-ethanol fermentation processes. *European Federation of Biotechnology - Spring conference* (May 2022), online. Oral presentation.

5. Maldonado de León, H. A., Puiman, L., Picioreanu, C., & Haringa, C. Unveiling the hydrodynamic effects of internal devices in an external-loop gas lift reactor for syngas fermentation. *17th Netherlands Process Technology symposium* (April 2022), Delft, The Netherlands. Poster presentation.

4. Puiman, L., Elisiário, M.P., Straathof, A.J.J., Haringa, C., Noorman, H.J., & Picioreanu, C. Relieving mass transfer limitations in industrial syngas-to-ethanol fermentation processes. *17th Netherlands Process Technology symposium* (April 2022), Delft, The Netherlands. Oral presentation.

3. Puiman, L., Haringa, C., Noorman, H.J., & Picioreanu, C. Syngas fermentation: a scale-down approach to simulate large-scale concentration gradients. *7th BioProScale* (March 2022) Berlin, Germany. Oral presentation.

2. Puiman, L., Noorman, H.J., & Picioreanu, C. CFD and mass transfer in industrial gas-lift reactors for syngas fermentation. *6th BioProScale* (March 2021), online. Oral presentation.

1. Puiman, L., Elisiário, M.P., De Wever, H., Van Hecke, W., Noorman, H.J., Picioreanu, C. & Straathof, A.J.J., Modelling syngas fermentation hollow fibre membrane bioreactors. *The Carbon Recycling Network conference* (February 2020), Nottingham, UK. Poster presentation.

Als je wint, heb je vrienden
Rijen dik, echte vrienden
Als je wint, nooit meer eenzaam
Zolang je wint

Herman Brood & Henny Vrienten in *Als je wint*

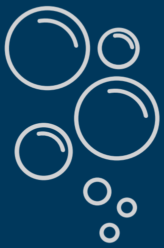

Curriculum Vitae

Lars was born on August 28th, 1995, in Stadskanaal, a ribbon village in the north-east of the Netherlands. He enjoyed his childhood there and later attended Gymnasium at the Ubbo Emmius Lyceum. Inspired by his chemistry teacher, he embarked on a journey into Life Science & Technology (LST) in 2013, a double degree bachelor program shared by Leiden University and Delft University of Technology. In 2015, he took a gap year to serve as secretary for the LST study association, studievereniging LIFE. Following a full-time board year, he undertook a minor in Science & Research Based Business. He completed his bachelor in 2017 with a research project in environmental biotechnology on fluorescent *in situ* hybridisation. Lars moved to Delft and engaged in the Biochemical Engineering master's in 2017, graduating *cum laude* in 2020 with the MSc thesis "Modelling syngas fermentation in hollow fibre membrane reactors". During this time, he also pursued a MSc on Management of Technology, with a thesis on gas fermentation in the business context. Captivated by gas fermentation, he pursued a PhD project under the guidance of Prof. Dr. Ir. Henk J. Noorman, Prof. Dr. Ir. Cristian Picioreanu and Dr. Ir. Cees Haringa, ultimately culminating into this dissertation. After completing his PhD, Lars would like to go abroad to continue working on scale-up of (gas) fermentations. Besides research, Lars finds joy in outdoor activities like long-distance (race) biking, hiking and ice-skating. He enjoys reading and discussing on a wide range of subjects, from sport and politics, to philosophy.